UNIVERSITY OF CALIFORNIA, SAN DIEGO

Fault Segments and Step-overs: Implications for Geohazards and Biohabitats

A dissertation submitted in partial satisfaction of the requirements for the degree

Doctor of Philosophy

in

Earth Sciences

by

Jillian Marie Maloney

Committee in charge:

Neal W. Driscoll, Chair
Alistair J. Harding
Richard Norris
Paul E. Parnell
Larry Smarr
Lisa Tauxe

2013

The Dissertation of Jillian Marie Maloney is approved, and it is acceptable in quality and form for publication on microfilm and electronically:

_____

_____

_____

_____

_____

_____

Chair

University of California, San Diego

2013

To my mom,
“zeeba zeeba zoo”

"I was awakened by a tremendous earthquake, and though I hadn't ever before enjoyed a storm of this sort, the strange thrilling motion could not be mistaken, and I ran out of my cabin, both glad and frightened, shouting, 'A noble earthquake! A noble earthquake,' feeling sure I was going to learn something." - John Muir

Table of Contents

List of Figures

List of Tables

Acknowledgements

I would like to thank my advisor Neal Driscoll for providing opportunities to participate in a wide range of interesting research projects and for trusting me in leadership roles that have helped me grow as a researcher. I especially enjoyed all my time spent on the R/V Point Loma, even when it meant constantly wrangling kelp from the transducers. Neal also showed me that doing science is much more fun when you can share your experience with others. I've learned so much from Neal and our collaborators and had a really great time in the process.

Jeff Babcock and Ernest Aaron contributed immensely to the work on San Diego Bay. It was such a pleasure to spend all those days on the water with you guys taking in the sights of San Diego and learning about our local geology. Thanks also to Ryan Switzer who helped process the San Diego Bay multibeam. The methane seep research was funded through a UC Ship Funds proposal and I'm so glad that Ally Pasulka and Ben Grupe approached me to be a part of that work. It's been awesome making discoveries and learning about the earth with such good friends.

I'd like to thank Graham Kent for his continued support and contribution to my research. Thanks also to Rob Baskin for field support and lots of great conversations on the water. Thanks to my lab mates, past and present, who have made my time at Scripps so much fun. A special thanks to Danny Brothers for giving my research a jump start as a young graduate student and for being a constant source of knowledge and advice.

I'd like to thank my friends and family for their support. I'm so lucky to have such a strong and reliable support system to reach out to for advice, encouragement, and lots of laughs. I especially want to thank my partner, Michelle Lande, who I was lucky enough to meet here at Scripps. I've had long hard days and really exciting moments as a graduate student and she's always there, helping me through frustrations and sharing in the joy.

The text and figures from chapter 2, in full, is a reprint of the material as it appears in: Maloney, J.M., Noble, P.J., Driscoll, N.W., Kent, G.M., Smith, S.B., Schmauder, G.C., Babcock, J.M., Baskin, R.L., Karlin, R., Kell, A.M., Seitz, G.G., Zimmerman, S., Kleppe, J.A., 2013, Paleoseismic history of the Fallen Leaf Segment of the West-Tahoe Fault reconstructed from slide deposits in the Lake Tahoe Basin, California-Nevada: Geosphere, v. 9, p. 1065-1090. The dissertation author was the primary researcher and author and the co-authors listed in this publication directed and supervised the research.

The text and figures from chapter 3 are being prepared for publication in: Maloney, J.M., N.W. Driscoll, G.M. Kent, D.S. Brothers, S. Duke and T. Freeman, In Prep, Segmentation and step-overs along strike slip fault systems in the inner California borderlands: Implications for fault architecture and basin formation. The dissertation author was the primary researcher and author of the manuscript. The co-authors directed and supervised the research that forms the basis for this chapter.

The text and figures from chapter 4 are being prepared for publication in: Maloney, J.M., Driscoll, N.W., Babcock, J.M, Anderson, T. and Parnell, P.E., In Prep, Geological constraints on biohabitats: A geophysical characterization of San Diego Bay and adjacent regions, California: Marine Geology. The dissertation author was the primary researcher and author of the manuscript. The co-authors directed and supervised the research that forms the basis for this chapter.

The text and figures from Appendix A are being prepared for publication in: Maloney, J.M., B.M. Grupe, A. Pasulka, C.A. Frieder, L.A. Levin, K. Dawson, D. Case, and N.W. Driscoll, In Prep, Transpressional segment boundaries in strike-slip fault systems offshore southern California: Implications for fluid expulsion and seep habitats: Geophysical Research Letters. The dissertation author, second author, and third author

were the primary researchers, and the dissertation author was the primary author of the manuscript. The co-authors assisted with the research that forms the basis for this chapter.

The text and figures from Appendix B are being prepared for publication in: Dong, S., G. Ucarkus, S.G. Wesnousky, J. Maloney, N.W. Driscoll, G. Kent, and R. Baskin, In Review, Strike-slip Faulting along the Wassuk Range of the northern Walker Lane, Nevada: Geosphere. The dissertation author was involved in aquisition, processing and interpretation of the data that forms the basis of this chapter.

Vita

2002-2004	Undergraduate Research Assistant Department of Earth Sciences University of Southern California
2004	Bachelor of Science, Geological Sciences University of Southern California
2013	Doctor of Philosophy, Earth Sciences Scripps Institution of Oceanography University of California, San Diego

Publications

Maloney, J.M., Noble, P.J., Driscoll, N.W., Kent, G.M., Smith, S.B., Schmauder, G.C., Babcock, J.M., Baskin, R.L., Karlin, R., Kell, A.M., Seitz, G.G., Zimmerman, S., and Kleppe, J.A., 2013, Paleoseismic history of the Fallen Leaf Segment of the West-Tahoe Fault reconstructed from slide deposits in the Lake Tahoe Basin, California-Nevada: Geosphere, v. 9, p. 1065-1090.

Abstract of the Dissertation

Fault Segments and Step-overs: Implications for geohazards and biohabitats

by

Jillian Marie Maloney

Doctor of Philosophy in Earth Sciences

University of California, San Diego, 2013

Neal W. Driscoll, Chair

This thesis presents research on fault segmentation from regions along the Pacific-North American plate boundary. Geophysical and geological data provide new insights into how fault segments and segment boundaries influence both geohazards and habitat distribution. In the Lake Tahoe basin, Chirp data imaged slide deposits, which could be temporally correlated across multiple basins. The lateral distribution and timing of slide deposits were used to identify seismically triggered slides and reconstruct the paleoseismic history of the basin. The recurrence interval on the basin bounding West Tahoe-Dollar Point Fault is ~3-4 k.y., and it appears that the fault may sometimes rupture only along individual segments, and other times along the entire length of the fault.

Offshore San Diego, geophysical data imaged faulting and deformation in the inner California borderlands geomorphic province. These data highlight changes in major strike slip faults as they approach step overs, define tectonic controls on the topographically high Point Loma peninsula and associated kelp forest, and illustrate that deformation in the borderlands is more consistent with a strike slip model than a regional blind thrust model. Additionally in the region, restraining bends in strike slip faults

appear to play an important role in controlling the distribution of methane seep habitats. Localized fluid seepage from a restraining bend in the offshore San Diego Trough Fault hosts a deep-sea methane seep ecosystem that was explored and characterized with ROV surveys and biological sampling.

In San Diego Bay, multibeam, backscatter, and Chirp data imaged the pronounced anthropogenic influence on sediments and habitats of San Diego Bay. This study revealed both geologic and anthropogenic influence on eelgrass and kelp forest habitats within the bay, and provided a quantitative baseline for assessing future change due to sea level rise. Understanding geologic controls on habitats over multiple time-scales is important for addressing ecosystem response to climate change and sea-level rise. A study on kelp forest habitat migration over a glacial-interglacial sea level cycle addresses these questions using a new approach with geophysical datasets.

1

Introduction

1.1 FAULT SEGMENTATION AND THESIS OVERVIEW

Fault traces are commonly discontinuous at the surface of the earth, and these complex geometries can influence rupture patterns and geomorphology in ways that remain poorly understood. For example, how do fault segments interact? What controls rupture patterns between segments? How do segment boundaries shape geomorphology and habitat distributions? Geophysical, geological, and geochemical data were examined to address these questions, which are important for geohazard assessments and ecosystem management.

Several observations have shown that earthquakes will either propagate across, or terminate at, fault segment boundaries (e.g., King and Nábělek, 1985; Bodin and Brune, 1996; Wesnousky, 2006). Understanding fault segmentation is therefore important for assessing geohazards because earthquake size increases with rupture length (Wells and Coppersmith, 1994). Much of our understanding of rupture patterns and segmentation has been derived from historic earthquake data (e.g., Wesnousky, 2006) and earthquake modeling (e.g., Oglesby, 2005). Marine geophysical data provide an opportunity to study fault segmentation and earthquake rupture patterns over longer time scales.

Chapter 2 presents a new, extended paleoseismic history of the Lake Tahoe Basin using direct (offset strata) and indirect evidence (seismically triggered slide deposits) imaged by Chirp data. Long cores provide important constraints on the timing of the slides deposits, which provides new insights into rupture patterns along the West Tahoe Dollar Point Fault. The recurrence interval for the fault system is ~3-4 k.y., and it appears that in some earthquakes, the entire length of the fault has ruptured, while in others fault segments have ruptured independently.

In Chapter 3, geophysical data from the inner California borderlands images localized compression and extension associated with step overs in strike slip fault systems. Others have proposed that regional blind thrust systems have caused the

compressional deformation observed offshore (Rivero and Shaw, 2000; 2011). Data presented in this chapter demonstrate that deformation associated with the purported blind thrusts is moribund. Furthermore, deformational patterns such as changes in stratigraphic dip, flower structures, and localized compression and extension, are more consistent with a strike-slip setting. These observations are important for geohazard assessment because thrust faults can pose different seismic risks than strike-slip faults (e.g., tsunami hazard).

Fault bends and step-overs also appear to play an important role in controlling the distribution and form of biohabitats. Especially in strike slip systems, fault segmentation has a significant influence on geomorphology. Broadly, releasing steps in strike slip faults generate pull-apart basins and restraining steps generate pop-up structures (McClay and Dooley, 1995; McClay and Bonora, 2001). San Diego Bay is a pull-apart basin formed by a right step from offshore faults to the onshore Rose Canyon Fault zone (Rockwell, 2010). Chapter 3 shows that dip-slip deformation on offshore bounding faults increases as they approach the step-over. As a result, a horst-graben structure is generated in the hanging wall of the Coronado Bank fault zone that is responsible for the topographic high of the Point Loma peninsula. The high standing horst block exposes Cretaceous hardgrounds at the seafloor that provide the substrate for the Point Loma kelp forest. Additionally, the San Diego Bay basin created in a releasing step-over is a structural low dominated by sedimentary habitats (Chapter 4).

Appendix A describes localized fluid expulsion from a restraining bend in the offshore San Diego Trough Fault that hosts a deep-sea methane seep ecosystem. The pop-up created by compression in the bend is localized and dies away abruptly north and south. An actively venting methane seep was discovered near the crest of the anticlinorium that forms the pop-up. Other seeps have been located along restraining bends in the region offshore southern California (Paull, et al., 2008). At restraining bends,

localized tectonic compression may promote fluid migration to the seafloor, and therefore, it is more likely that seeps are located at restraining bends than along releasing bends. These patterns are important for understanding fluid flow processes related to tectonic deformation, as well as for regional ecology. The controls on seep habitat distribution in strike-slip settings differ from convergent margins, which are characterized by extensive regional compaction and deep fluid sources.

Additional appendices describe geophysical datasets in the Walker Lane (Appendix B) and offshore San Diego (Appendix C). At Walker Lake along the eastern side of the Wassuk Range, offshore and onshore data are combined to map previously unknown strike-slip faults and estimate event ages (Appendix B). Combined with onshore normal faults, these strike slip faults are characteristic of strain partitioning, reconcile geologic measurements with geodetic rates, and suggest that low-slip strike-slip faults may produce very large displacement events. Offshore San Diego, high resolution data are used to reconstruct the available habitat space for kelp forests throughout a sea level cycle. Bathymetric data are used to reconstruct the possible depth range for kelp and Chirp data provided constraints on the exposed substrate in the euphotic zone. During the sea level rise between ~11.5 – 6 k.y. BP, the aerial extent of exposed hardgrounds is greater than the present-day distribution, which would be more conducive for kelp forest growth.

In summary, my thesis presents new insights into fault segmentation and how segment boundaries relate to geohazards and biohabitats. These results are important for understanding earthquake rupture patterns and assessing geohazards associated with complex, segmented fault systems. Additionally, understanding geologic controls on biohabitats over multiple time-scales is important for addressing ecosystem response to future change.

1.2 REFERENCES

King, G., and Nábělek, J., 1985, Role of fault bends in the initiation and termination of earthquake ruptures: Science, v. 228, no. 4702, p. 984-987.

McClay, K., and Dooley, T., 1995, Analogue models of pull-apart basins: Geology, v. 23, no. 8, p. 711-714.

McClay, K., and Bonora, M., 2001, Analogue models of restraining stepovers in strike-slip fault systems: AAPG Bulletin, v. 85.2, p. 233-260.

Parnell, P. E., Dayton, P. K., Lennert-Cody, C. E., Rasmussen, L. L., and Leichter, J. J., 2006, Marine reserve design: optimal size, habitats, species affinities, diversity, and ocean microclimate: Ecological Applications, v. 16, no. 3, p. 945-962.

Paull, C. K., W. R. Normark, W. Ussler III, D. W. Caress, and R. Keaten, 2008, Association among active seafloor deformation, mound formation, and gas hydrate growth and accumulation within the seafloor of the Santa Monica Basin, offshore California: Marine Geology, v. 250, p. 258-275.

Oglesby, D.D., 2005, The dynamics of strike-slip step-overs with linking dip-slip faults: Bulletin of the Seismological Society of America, v. 95, no. 5, p. 1604-1622.

Rivero, C., and Shaw, J. H., 2011, Active folding and blind thrust faulting induced by basin inversion processes, inner California borderlands, in Shaw, J. H., and Suppe, J., eds., Thrust fault related folding, Volume AAPG Memoir 94, p. 187-214.

Rivero, C., Shaw, J. H., and Mueller, K., 2000, Oceanside and Thirtymile Bank blind thrusts: Implications for earthquake hazards in coastal southern California: Geology, v. 28, no. 10, p. 891-894.

Rockwell, T., 2010, The Rose Canyon Fault Zone in San Diego, Fifth International Conference on Recent Advances in Geotechnical Earthquake Engineering and Soil Dynamics and Symposium in Honor of Professor I.M. Idriss: San Diego, California.

Wells, D.L., and Coppersmith, K.J., 1994, New Empirical Relationships among Magnitude, Rupture Length, Rupture Width, Rupture Area, and Surface Displacement: Bulletin of the Seismological Society of America, v. 84, no. 4, p.

974-1002.

Wesnousky, S. G., 2006, Predicting the endpoints of earthquake ruptures: Nature, v. 444, p. 358-360.

2

Paleoseismic history of the Fallen Leaf segment of the West Tahoe–Dollar Point fault reconstructed from slide deposits in the Lake Tahoe Basin, California-Nevada

Geosphere, published online on 26 June 2013 as doi:10.1130/GES00877.1

Paleoseismic history of the Fallen Leaf segment of the West Tahoe–Dollar Point fault reconstructed from slide deposits in the Lake Tahoe Basin, California-Nevada

Jillian M. Maloney[1], Paula J. Noble[2], Neal W. Driscoll[1], Graham M. Kent[3], Shane B. Smith[2], Gretchen C. Schmauder[3], Jeffrey M. Babcock[1], Robert L. Baskin[4], Robert Karlin[2], Annie M. Kell[3], Gordon G. Seitz[5], Susan Zimmerman[6], and John A. Kleppe[7]

[1]*Scripps Institution of Oceanography, University of California, San Diego, 9500 Gilman Drive, La Jolla, California 92093, USA*
[2]*Department of Geological Sciences & Engineering, University of Nevada, Reno, Reno, Nevada 89557-0138, USA*
[3]*Nevada Seismological Laboratory, University of Nevada, Reno, Reno, Nevada 89557-0174, USA*
[4]*U.S. Geological Survey, West Valley City, Utah 84119, USA*
[5]*California Geological Survey, 345 Middlefield Road, MS 520, Menlo Park, California 94025, USA*
[6]*Center for Accelerator Mass Spectrometry, Lawrence Livermore National Laboratory, Livermore, California 94550, USA*
[7]*College of Engineering, University of Nevada, Reno, Reno, Nevada 89557-0256, USA*

ABSTRACT

The West Tahoe–Dollar Point fault (WTDPF) extends along the western margin of the Lake Tahoe Basin (northern Sierra Nevada, western United States) and is characterized as its most hazardous fault. Fallen Leaf Lake, Cascade Lake, and Emerald Bay are three subbasins of the Lake Tahoe Basin, located south of Lake Tahoe, and provide an opportunity to image primary earthquake deformation along the WTDPF and associated landslide deposits. Here we present results from high-resolution seismic Chirp (compressed high intensity radar pulse) surveys in Fallen Leaf Lake and Cascade Lake, multibeam bathymetry coverage of Fallen Leaf Lake, onshore Lidar (light detection and ranging) data for the southern Lake Tahoe Basin, and radiocarbon dates from piston cores in Fallen Leaf Lake and Emerald Bay. Slide deposits imaged beneath Fallen Leaf Lake appear to be synchronous with slides in Lake Tahoe, Emerald Bay, and Cascade Lake. The temporal correlation of slides between multiple basins suggests triggering by earthquakes on the WTDPF system. If this correlation is correct, we postulate a recurrence interval of ~3–4 k.y. for large earthquakes on the Fallen Leaf Lake segment of the WTDPF, and the time since the most recent event (~4.5 k.y. ago) exceeds this recurrence time. In addition, Chirp data beneath Cascade Lake image strands of the WTDPF offsetting the lake floor as much as ~7.5 m. The Cascade Lake data combined with onshore Lidar allow us to map the WTDPF continuously between Fallen Leaf Lake and Cascade Lake. This improved mapping of the WTDPF reveals the fault geometry and architecture south of Lake Tahoe and improves the geohazard assessment of the region.

INTRODUCTION

Onshore and offshore research in the Lake Tahoe Basin (northern Sierra Nevada, western United States) has defined the geometry and slip rates of the major faults accommodating active extension across the basin (Brothers et al., 2009; Dingler et al., 2009; Gardner et al., 2000; Karlin et al., 2005; Kent et al., 2005; Schweickert et al., 2004; Seitz et al., 2006, 2005). These faults, the Stateline–North Tahoe fault, Incline Village fault, and the West Tahoe–Dollar Point fault (WTDPF), exhibit down to the east normal displacement (Dingler et al., 2009) (Fig. 1A). Recent work in Fallen Leaf Lake has helped identify the WTDPF as potentially the most hazardous fault in the Lake Tahoe Basin, with the potential to produce M >7.0 earthquakes (Brothers et al., 2009). The WTDPF is a major north-south–striking normal fault, extending >50 km along the western margin of the Lake Tahoe Basin, and is divided by geomorphic discontinuities into three main segments: the southern Fallen Leaf Lake segment, central Rubicon segment, and northern Dollar Point segment (Fig. 1A). The most recent event (MRE) on the Fallen Leaf Lake segment was 4.57–4.85 k.y. ago. The MRE on the Rubicon segment was dated as ca. 5.3–5.6 ka (Smith et al., 2013). A recurrence interval for the WTDPF of ~4.8 k.y. was estimated by Kent et al. (2005) based on slip-rate models, but the paleoseismic record has not been extended past the MREs on the Fallen Leaf Lake and Rubicon segments. Furthermore, rupture timing patterns between the three WTDPF segments, Incline Village fault, and Stateline–North Tahoe fault remain poorly understood.

Historic earthquakes have been shown to trigger mass movements in lacustrine and marine environments (Hampton et al., 1996; Lee et al., 2009); recent studies have used slide deposits observed in sediment cores and seismic reflection data to estimate earthquake recurrence intervals (Goldfinger et al., 2007; Schnellmann et al., 2002; Strasser et al., 2006; Upton and Osterberg, 2007). Several lines of evidence argue for seismic triggering of slide deposits, but the most convincing is a record of synchronous deposits across broad areas and multiple basins. Compressed high intensity radar pulse (Chirp) data beneath the Lake Tahoe subbasins Fallen Leaf Lake, Cascade Lake, and Emerald Bay image several large slide deposits correlated temporally between the three subbasins, as well as with previously dated slides in Lake

Geosphere; August 2013; v. 9; no. 4; doi:10.1130/GES00877.1; 16 figures; 2 tables.
Received 20 October 2012 ♦ Revision received 3 May 2013 ♦ Accepted 16 May 2013 ♦ Published online 26 June 2013

Geosphere, published online on 26 June 2013 as doi:10.1130/GES00877.1

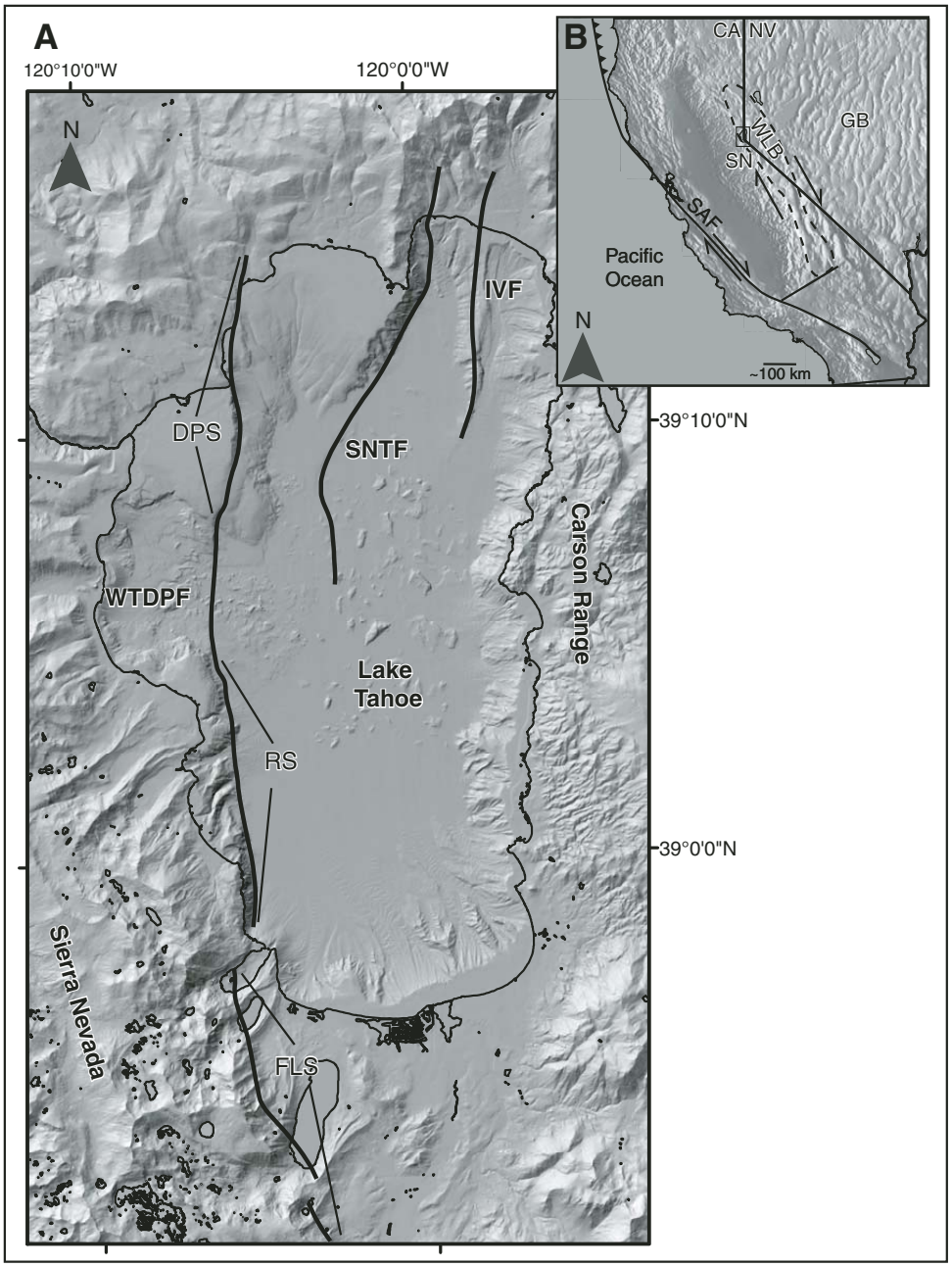

Figure 1. (A) Map of the Lake Tahoe Basin and surrounding area showing generalized fault traces of the West Tahoe–Dollar Point fault (WTDPF), Stateline–North Tahoe fault (SNTF), and Incline Village fault (IVF). Three segments of the WTDPF are also labeled: the northern Dollar Point segment (DPS), central Rubicon segment (RS), and southern Fallen Leaf segment (FLS) (modified from Brothers et al., 2009). (B) Regional plate boundary map showing location of the San Andreas fault (SAF), Walker Lane Belt (WLB), Sierra Nevada Range (SN), and the Great Basin (GB). The Lake Tahoe Basin is located within the northwestern WLB, on the border between California (CA) and Nevada (NV).

Geosphere, published online on 26 June 2013 as doi:10.1130/GES00877.1

Tahoe (Smith et al., 2013). Based on extent and timing, we suggest that four of the slides were triggered by events on the WTDPF; if correct, these coseismic slides extend the paleoseismic record for the WTDPF and provide new insights into the rupture patterns along strike, and possibly between faults. Examination of the extended paleoseismic record yields a recurrence interval of ~3–4 k.y. on the Fallen Leaf Lake segment of the WTDPF; this is vital in assessing geohazards posed by the WTDPF to the populated Lake Tahoe Basin.

BACKGROUND

The Lake Tahoe Basin is located in the northern Walker Lane deformation belt, and is the westernmost basin in a series of north-south–trending basins and mountain ranges bounded by normal faults (Faulds et al., 2005; Unruh et al., 2003). The Walker Lane is located between the Sierra Nevada block and the central Great Basin, and is characterized by transtensional deformation caused by the oblique divergence of the Sierra Nevada–Central Valley microplate and stable North America (Fig. 1B) (Argus and Gordon, 2001; Oldow, 2003; Unruh et al., 2003). Geodetic studies indicate 9–13 mm/yr of dextral shear in the Walker Lane deformation belt, which amounts to ~20%–25% of the total plate motion between the North American and Pacific plates (Bennett et al., 2003; Dixon et al., 2000; Hammond and Thatcher, 2004; Svarc et al., 2002).

The Lake Tahoe Basin is an asymmetric half-graben set between the Sierra Nevada and Carson mountain ranges, and has been tectonically active for at least 3 m.y. (Dingler et al., 2009; Faulds et al., 2005; Hyne et al., 1972; Kent et al., 2005; Schweickert et al., 2004; Surpless et al., 2002). Extension across the basin is accommodated by three primary normal fault systems: the WTDPF, Stateline–North Tahoe fault, and Incline Village fault (Kent et al., 2005), which have vertical slip rates of 0.4–0.8 mm/yr, 0.35–0.6 mm/yr, and 0.18–0.30 mm/yr, respectively (Brothers et al., 2009; Dingler et al., 2009).

Fallen Leaf Lake, Cascade Lake, and Emerald Bay are bounded by lateral Tioga (ca. 30–14 ka; Benson et al., 1998; Bischoff and Cummins, 2001; Clark and Gillespie, 1997; Howle et al., 2012; Phillips et al., 1996; Rood et al., 2011) and Tahoe glacial moraines on their eastern and western shores (Saucedo et al., 2005). Fallen Leaf Lake and Cascade Lake are separated from Lake Tahoe by recessional end moraines, whereas Emerald Bay connects with Lake Tahoe to the north at Emerald Point. Input of modern sediment to Fallen Leaf Lake is sourced mainly from Glen Alpine Creek, which drains an area of ~42 km^2 from the Desolation Wilderness to the south. Additional input to the lake is sourced from Cathedral Creek and several unnamed creeks along the western shore that drain from the mountains to the southwest. Sediment input to Cascade Lake is mainly from Cascade Creek, which drains an area of ~12 km^2. Input to Emerald Bay is mainly from Eagle Creek, which drains an area of ~25 km^2 from the mountains to the southwest. Granitic rocks of the Sierra Nevada batholith and metamorphosed roof pendants characterize the geology of the drainage areas for all three subbasins (Saucedo et al., 2005). Several Pleistocene–Holocene landslide deposits have been mapped onshore near the subbasins (Saucedo et al., 2005). Slides are mapped above the southernmost shores of both Emerald Bay and Cascade Lake and appear to spill into the basins very near the WTDPF (Fig. 2). Two slides are also mapped slightly northwest from Cathedral Creek, above Fallen Leaf Lake.

Debris flow and turbidite deposits have been identified in cores and seismic reflection data in Lake Tahoe sediments, and seismic triggering of the deposits has been suggested (Dingler et al., 2009; Karlin et al., 2005; Kent et al., 2005; Seitz et al., 2006; Smith et al., 2013). Smith et al. (2013) mapped and dated 18 debris flow and turbidite deposits in Lake Tahoe, 4 of which appear to be triggered by events on the Lake Tahoe Basin faults. Three events were triggered by events on the WTDPF: deposit F (4.51–4.07 ka), deposit G (5.60–5.33 ka), and deposit J (7.89–7.19 ka). Several deposits younger than deposit J were also linked to events on faults outside the Lake Tahoe Basin. Older event deposits were also identified and dated as deposits K (9.45–8.77 ka), L (9.73–9.32 ka), M (10.16–9.80 ka), N (11.26–10.48 ka), and O (12.49–11.20 ka), but the triggering earthquake events for these deposits are poorly constrained, and in some cases may be related to motion on the Stateline–North Tahoe fault.

METHODS

Fallen Leaf Lake bathymetric data were collected in July 2010 using a Reson 7125 multibeam system operated at 200 kHz (Fig. 3) with a nominal vertical resolution of ~2.5 cm. Positions were calculated through a dual-differential global positioning system (GPS) system, providing lateral position accuracy to better than 2 m. Data were processed using Caris HIPS and SIPS software (http://www.caris.com/products/hips-sips/), and interpreted with QPS Fledermaus and ArcGIS (http://www.qps.nl/display/fledermaus/main; www.esri.com) software packages. The U.S. Geological Survey (USGS) Fallen Leaf Lake water-level datum of 1944 m (North American Vertical Datum, NAVD88) was used to correlate with onshore Lidar (light detection and ranging) data.

In June 2011, ~45 line km of Chirp seismic data were acquired from Fallen Leaf Lake and Cascade Lake (Figs. 2B, 2C). The Chirp profiler was operated with a 30 ms swept pulse of 1–15 kHz, and provided decimeter vertical resolution and subbottom penetration >50 m. Location accuracy is to within 5 m. Data were processed using SIOSEIS (Henkart, 2003) software and imported to Kingdom Suite (http://www.ihs.com/) and QPS Fledermaus software packages for interpretation. A nominal water and sediment velocity of 1450 m/s was assumed for all depth and sediment thickness conversions.

Piston cores from four locations were acquired in Fallen Leaf Lake during November 2010 using a Kullenberg piston coring system from LaCore (University of Minnesota; Fig. 2C). Core BC1A, taken near the basin depocenter, is 9.8 m long and penetrated the entire Holocene package into the Pleistocene periglacial deposits below. The piston cores were logged for lithology, magnetic susceptibility, and sampled for micropaleontology, geochemistry, and radiocarbon dating (Karlin et al., 2011). Plant macrofossils were extracted from the cores for radiocarbon dating and submitted to the Lawrence Livermore National Laboratory Center for Accelerator Mass Spectrometry (CAMS). Calibrated radiocarbon ages were determined using OxCal v. 4.1.7 (Bronk Ramsey, 2009) with the IntCal 04 calibration curve (Reimer et al., 2004) (Table 1). The ages of the two youngest event deposits in Fallen Leaf Lake were modeled as a sequence in OxCal v. 4.1.7 using bounding dates from three cores taken in 2010 and a core taken in 2006 (PC3; Brothers et al., 2009). Older event deposit ages were calculated based on the overall age model for core BC1A (Karlin et al., 2011) (Table 1). We observe a systematic offset of ~0.5 m between core depth and Chirp depth calculated using a nominal 1450 m/s velocity.

A previously collected piston core (EB2) from Emerald Bay (Dingler et al., 2009) was used to calculate ages for event deposits observed in Emerald Bay Chirp data. Three macrofossil samples were analyzed at the CAMS Laboratory and calibrated radiocarbon ages were determined using OxCal v. 4.1.7 (Bronk Ramsey, 2009) and the IntCal 04 calibration curve (Reimer et al., 2004; Table 1).

RESULTS

Fallen Leaf Lake Bathymetry

The maximum depth of Fallen Leaf Lake as recorded in multibeam data is ~116 m below

Geosphere, published online on 26 June 2013 as doi:10.1130/GES00877.1

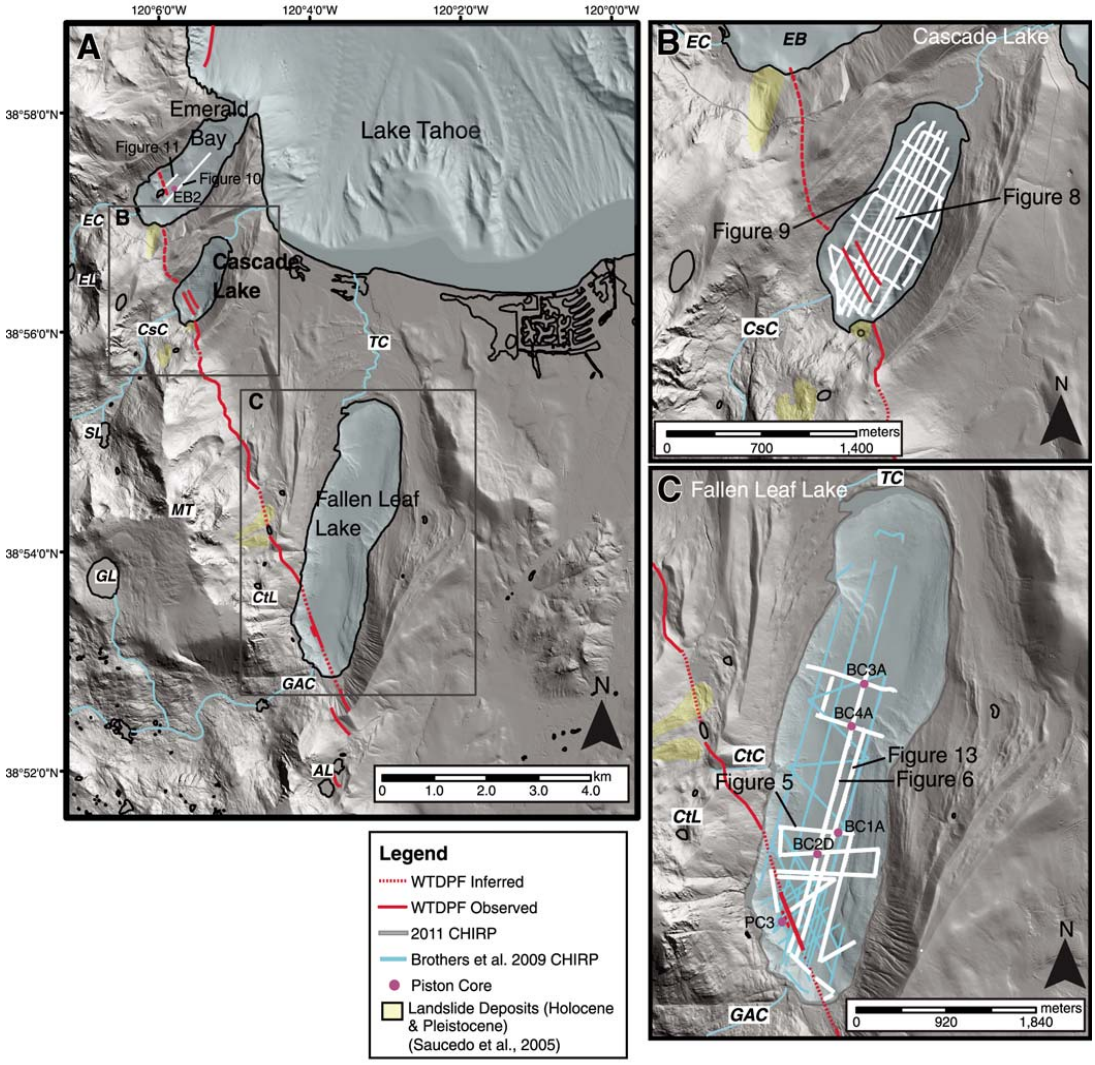

Figure 2. (A) Map of the southern Lake Tahoe Basin including the subbasins Emerald Bay (EB), Cascade Lake, and Fallen Leaf Lake. Bathymetry of Lake Tahoe and Emerald Bay is from Gardner et al. (2000) retrieved from U.S. Geological Survey (2001). Trace of the West Tahoe–Dollar Point fault (WTDPF) beneath Lake Tahoe is from Brothers et al. (2009) and Dingler et al. (2009). Onshore topography is from aerial Lidar (light detection and ranging) surveys (Tahoe Regional Planning Agency, 2010). Bathymetry and topography are 1 m grids shaded from an azimuth of 315° and elevation of 45°. CHIRP—compressed high intensity radar pulse. (B) Enlargement of Cascade Lake area. (C) Enlargement of Fallen Leaf Lake area. See inset legend for further details. Abbreviations: AL—Angora Lakes, CsC—Cascade Creek, CtL—Cathedral Lake, CtC—Cathedral Creek, EL—Eagle Lake, EC—Eagle Creek, GL—Gilmore Lake, GAC—Glenn Alpine Creek, MT—Mount Tallac, SL—Snow Lake, TC—Taylor Creek.

Geosphere, published online on 26 June 2013 as doi:10.1130/GES00877.1

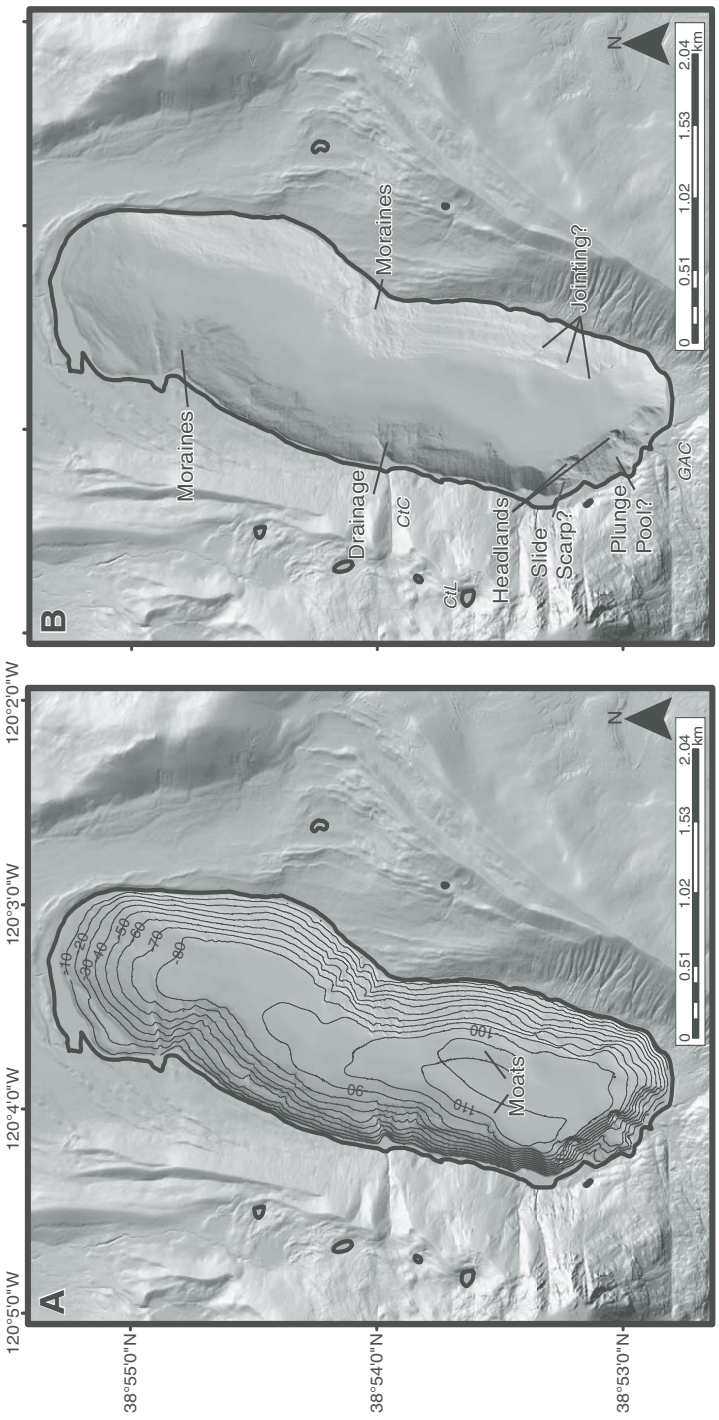

Figure 3. (A) Hillshaded bathymetry of Fallen Leaf Lake from the 2010 multibeam survey with 10 m contours from -10 m to -110 m. Depths are below the U.S. Geological Survey 1944 m lake level. Solid gray areas between the bathymetry and lakeshore are areas of no data. (B) Hillshaded bathymetry without contours to highlight lake floor features. Also shown are Cathedral Creek (CtC) and Glen Alpine Creek (GAC) inputs to the lake. CtL—Cathedral Lake. Labeled features are described in detail in the text. For both figures, the topography is from aerial Lidar (light detection and ranging) surveys. Bathymetry and topography are 1 m grids shaded from an azimuth of 315° and elevation of 45°.

Geosphere, published online on 26 June 2013 as doi:10.1130/GES00877.1

TABLE 1. RADIOCARBON AGES FOR FALLEN LEAF LAKE AND EMERALD BAY CORES

Location	Sample name	Lab sample*	Depth (m)†	$\delta^{13}C$§	Uncalibrated ^{14}C age (yr B.P.)	Calibrated calendar age#	Confidence (%)	Rounded age (k.y ago)**
Core BC1A (FLL)	Bolly-1A3-65	152695	2.285	–25	3735 ± 30	***4155–3983***	93.4	4.0–4.2
						4221–4208	2.0	
	Bolly-1A5-22	152542	4.105	–25	4515 ± 45	***5313–5039***	94.1	5.0–5.3
						4996–4983	1.3	
	Bolly-1A5-142	152696	5.290	–25	6165 ± 30	***7164–6975***	95.4	7.0–7.2
	Bolly-1A6-149	152543	6.860	–25	8045 ± 40	***9032–8768***	94.5	8.8–9.1
						9076-9062	0.9	
	Bolly-1A7-5.5	152544	6.935	–25	8190 ± 45	***9279–9020***	95.4	9.0–9.3
	Bolly-1A8-55	152545	8.940	–25	10335 ± 35	***12251–12037***	71.5	12.0–12.4
						12380–12260	23.9	
Core BC2D (FLL)	Bolly-2D3-46	152688	3.230	–25	4120 ± 30	***4726–4527***	70.4	4.5–4.8
						4815–4753	25.0	
	Bolly-2D4-28	152689	4.410	–25	4630 ± 40	***5471–5291***	94.4	5.3–5.6
						5570–5559	1.0	
	Bolly-2D6-77.5	152702	6.725	–25	6805 ± 35	***7687–7586***	95.4	7.6–7.7
	Bolly-2D8-7.5	152703	8.385	–25	7885 ± 30	***8778–8592***	92.0	8.6–8.9
						8860–8834	2.4	
						8933–8922	0.8	
						8946–8944	0.2	
	Bolly-2D-734††		6.875		7015 ± 45	***7946–7739***	95.4	7.7–7.9
Core BC3A (FLL)	Bolly-3A1-105.5	152707	1.040	–25	2750 ± 35	***2928–2767***	95.4	2.8–2.9
	Bolly-3A2-66	152709	2.185	–25	4980 ± 45	***5763–5604***	77.1	5.6–5.9
						5889–5809	18.3	
	Bolly-3A3-18.25	152710	3.250	–25	6640 ± 35	***7580–7460***	95.4	7.5–7.6
Core PC3 (FLL)	FLL-PC3-110	152721	1.100	–25	3670 ± 30	***4088–3905***	95.4	3.9–4.1
	FLL-PC3-383§§	AA76374	3.830	–25.6	4235 ± 44	***4765–4620***	49.8	4.6–4.9
						4869–4785	45.6	
Core EB2 (EB)	EB2-1	94940	0.880	–25	1995 ± 40	***2056–1865***	95.1	1.8–2.1
						1841–1837	0.3	
	EB2-2	94941	3.765	–25	4280 ± 40	***4967–4815***	89.8	4.7–5.0
						4754–4711	5.6	
	EB2-3	94942	4.260	–25	4610 ± 70	***5480–5211***	67.5	5.0–5.6
						5199–5048	23.5	
						5578–5534	4.3	

Note: FLL—Fallen Leaf Lake; EB—Emerald Bay.

*Sample analysis was performed at the Center for Accelerator Mass Spectrometry at Lawrence Livermore National Laboratory, with the exception of FLL-PC3-383, which was analyzed at the University of Arizona Accelerator Mass Spectrometry Laboratory.

†Measured from top of core.

§ $\delta^{13}C$ values of –25 were not measured, but are the assumed values according to Stuiver and Polach (1977).

#Calibrated ages determined using OxCal version 4.1.7 (Bronk Ramsey, 2009) and IntCal04 atmospheric curve (Reimer et al., 2004). Calibrated ages are reported as yr ago % confidence under the 95% probability distribution. The highest probability calibrated range for each date is shown in bold italics.

**Rounded to nearest 0.1 k.y.

††Tsoyowata Ash age from Bacon (1983).

§§Data from Brothers et al. (2009).

Geosphere, published online on 26 June 2013 as doi:10.1130/GES00877.1

the USGS datum at 1944 m elevation (Fig. 3). Steep slopes bound the basin on the southern, eastern, and western shorelines (~15°–40°), with a more gently dipping slope to the north (<~10°). Several prominent features with high slope and rugosity are observed along the basin slopes. The steep basin slopes change abruptly at the basin floor, which is gently sloping with low rugosity. The deepest areas of the basin are represented by two moats that extend along the base of the eastern and western slopes in the southern basin. The moats encircle a subparallel mound. There are other smaller mounds and depressions on the basin floor, but regionally it slopes gently up to the north.

The expression of the WTDPF is observed on the basin floor as a linear depression that trends ~N20°W. A second splay may also occur along the base of the steeply sloping southern wall. These expressions of the fault on the lake floor align well with traces of the WTDPF splays mapped in Chirp data.

Along the basin slopes, several ridges, interpreted as recessional moraines, extend from the shore to the basin floor. Three prominent ridges are located near the center of the eastern slope and three additional ridges are located along the northwestern slope. The crests range in height between ~1 and 15 m. Several less prominent ridges are located along the western slope. A fan-shaped ridge feature on the eastern slope is offshore the mouth of Cathedral Creek.

Three prominent parallel scarps are located near the base of the eastern slope. The scarps are evenly spaced ~220 m apart, trend ~N20°W, and each exhibits ~10 m of down to the southwest vertical offset of the lake floor at the basinward edge. In Chirp data, we observe a topographic high in the acoustic basement adjacent to these features, but we do not observe evidence for associated faulting of basin sediments, and therefore do not interpret them to be faults.

Along the southern slope, two small headland features slope steeply to the basin floor. Above the southeastern headland is a circular, flat area at ~40 m water depth. Shoreward to the southeast, the plateau is bounded by steeply dipping slopes leading up to the modern shoreline. Shoreward to the northeast a more gently sloping ramp leads up to the shore. The ramp is bordered on the basinward edge by a ridge trending S55°E. The ridge crest is highest (~5 m) nearshore, and decreases as it wraps around the edge of the plateau (~1 m). The ridge ends where it meets the southeastern headland on the slope to the basin floor. The mouth of Glen Alpine Creek empties just to the southeast of the plateau and headland. A small debris fan is adjacent to the northwestern headland and spills slightly out onto the basin floor. Above this fan there are three scarps oriented ~N5°W. The scarps are ~10–15 m high.

Seismic Stratigraphy

Fallen Leaf Lake

Based on acoustic character, we divide Fallen Leaf Lake sediments into two major groups, section I and section II, and one minor group, section III. Section I is further subdivided into units A, B, and C (e.g., Brothers et al., 2009). Section III infills topographic lows in the northern basin and is not observed basin wide. Subhorizontal, parallel reflectors characterize section II; in contrast, section I exhibits a distinct lenticular geometry.

We describe the sequences from oldest to youngest. The acoustic basement is the basal layer imaged by Chirp data and the relief on this surface is shown in Figure 4. Little to no lacustrine sediment is observed on the steep basin walls. The depth to basement is greatest in the southern basin and shoals to the north. In the deepest areas, acoustic basement is not visible in the Chirp profiles, and thus the depth to basement is a minimum estimate (Fig. 4). The acoustic basement is hummocky throughout the basin; several mounds and ridges form complex topography. A large topographic high in the acoustic basement is located adjacent to prominent modern scarps observed on the southeast basin slope in bathymetry data (Figs. 3 and 4). The central basin trends north in a tortuous path and is interrupted by several features. A large mound at the center of the basin has a long axis that extends roughly north-south and its height tapers to the north (Figs. 4 and 5). Other topographic highs in the northern basin form ridges that extend across the basin trending roughly northwest-southeast. The ridges observed in the acoustic basement relief map (Fig. 4) occur near the bathymetric ridges mapped along the eastern slope (Fig. 3). These features divide the basin into a southern and northern zone, and are referred to herein as mid-lake moraines (Figs. 4 and 6). The southern zone is a deep basin with steeply sloping walls and isolated topographic highs. The northern zone is shallower, with more gently sloping walls and highly variable topography in the acoustic basement (Fig. 4).

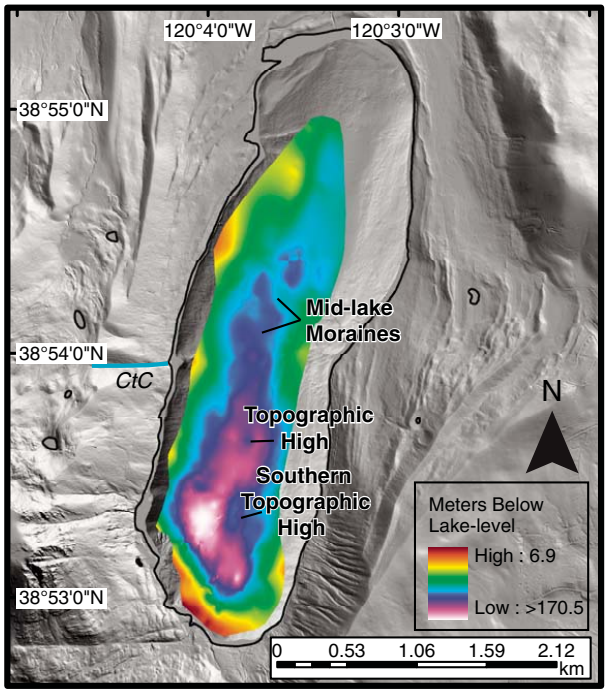

Figure 4. Topography of the acoustic basement traced in, and gridded between, Chirp (compressed high intensity radar pulse) profiles. Labeled features are discussed in the text. CtC—Cathedral Creek.

Geosphere, published online on 26 June 2013 as doi:10.1130/GES00877.1

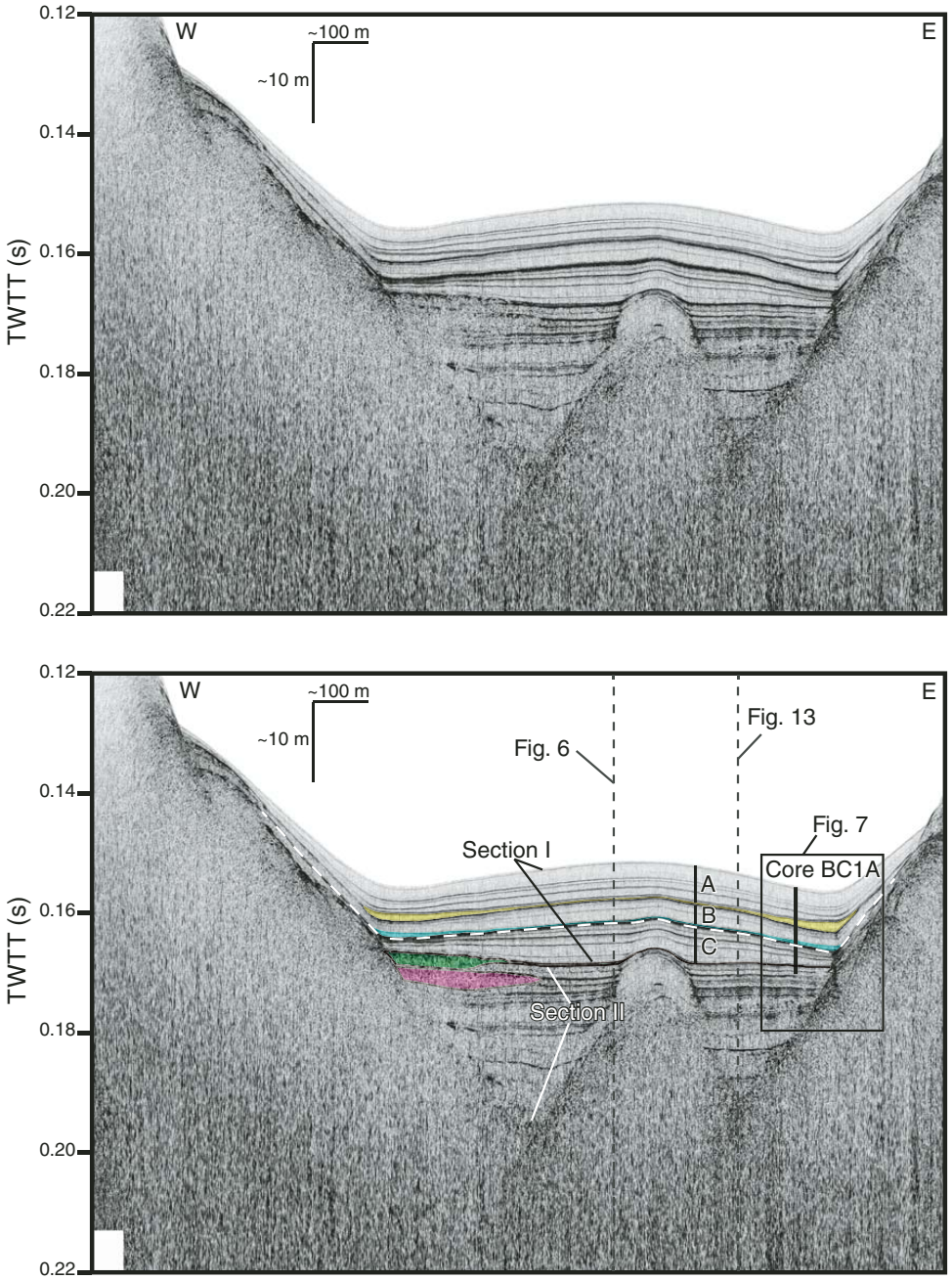

Figure 5. East-west Chirp (compressed high intensity radar pulse) profile showing Fallen Leaf Lake slides FLLS1 (yellow), FLLS2 (blue), FLLS3 (green), and FLLS4 proximal slide (pink). This profile also illustrates the sedimentary packages defined in the text. Section II, section I, and units A, B, and C are labeled. The white dashed horizon represents the Tsoyowata Ash horizon. The enlargement near core BC1A is shown in Figure 7. TWTT—two-way traveltime.

Geosphere, published online on 26 June 2013 as doi:10.1130/GES00877.1

The shape of the acoustic basement in these two zones appears to control sediment dispersal and results in differential deposition between the northern and southern zones.

Section III is observed between the acoustic basement and section I north of the mid-lake moraines. This package is chaotic, with some wavy, high-amplitude, discontinuous reflectors (Fig. 6). The package infills topographic lows and thins onto highs in the acoustic basement topography of the northern basin, particularly around the mid-lake moraine complex. The upper contact of section III is wavy and in some locations hummocky. Generally the unit is more chaotic near the base and systematically exhibits more acoustic reflectors toward the upper contact. There is a marked contrast between section III and the more transparent units of section I above. Section III was beyond the penetration depth for all sediment cores.

Section II is only observed in the southern zone of the basin and has a maximum thickness of >40 m. The section consists of parallel continuous reflectors separating semitransparent layers of varying thickness (Figs. 5 and 6). Both high- and low-amplitude reflectors are observed within section II; there is a large thickness variability between reflectors. The high-amplitude reflectors are vertically farther apart near the base of section II and become more numerous and closely spaced near the upper contact (ranging from ~1 m to several meter spacing). Where visible, the low-amplitude reflectors are very closely spaced (decimeter scale), and appear to be clustered. In the deepest part of the basin, the reflectors remain mostly horizontal, except where offset by the WTDPF. The contact of the reflectors and the steep basin walls is generally a straight, lateral onlap. To the north, reflectors of section II shoal, converge, and eventually onlap the acoustic basement as it slopes upward toward the mid-lake moraines (Fig. 6). The reflectors appear to maintain a constant amplitude signal throughout the southern basin.

The base of section II was identified as the acoustic basement where visible, but it was beyond the penetration depth of the Chirp in the deepest portions of the southern basin. Based on acoustic character, section II is not observed north of the mid-lake moraines. Nevertheless, we cannot rule out that there may be a highly condensed unit of section II that we grouped either with section III or section I. The upper contact of section II marks a change in stratal geometry from flat-lying beds below to lenticular shaped beds in section I above (Fig. 5). This contact was recovered in core BC1A at 8.5 m downcore, where it is marked by a thin turbidite laterally traceable to a slide deposit observed in Chirp data (Fig. 7). The proximal expression of this slide is observed to the west in Chirp data at the upper contact of section II (Fig. 5). The upper contact of section II is placed directly below the turbidite. Lithologically, there is a change in sediment character below the turbidite where it transitions into a 0.6 m interval of laminated silty clay. Below the laminated interval is a thin layer of bluish clay, below which is 0.6 m of glacial silt. The upper contact of section II also marks a change in magnetic susceptibility, which is almost zero at the base of section I, and increases downward through the laminated interval and into the glacial silt unit below the bluish clay layer (Fig. 7). We calculate the age of the upper contact of section II to be ca. 11.24–11.64 ka (95% confidence level) based on our age model with a median age of 11.44 ka (Table 1; Fig. 7).

Section I is divided into three units, separated by slide deposits; units A and B are separated by the FLLS1 slide (FLL is Fallen Leaf Lake) and units B and C are separated by the FLLS2 slide (Fig. 5). The slide deposits are easily identified in Chirp data because they infill topographic lows associated with lenticular deposits that characterize section I (Fig. 5). These topographic lows form moats on the lake floor adjacent to the steep walls (Fig. 3). The slides preferentially infill the moats, obscuring in part their relief, and are used as marker beds for correlation to sediment cores (Fig. 7). The units of section I exhibit lateral variation in thickness across the basin. All three units were recovered in piston cores (Fig. 7). Unit C is characterized by olive and yellow clay with banding partially disturbed by bioturbation. Unit B is characterized by yellowish-olive clay with subtle banding and mottling. The lower section of unit A is similar in lithology to unit B, with an upper section characterized by homogeneous olive mud (Fig. 7). In many cases magnetic susceptibility spikes in the core correspond to high-amplitude reflections in Chirp data. Units A, B, and C exhibit similar acoustic character. Each unit consists of variable thickness transparent layers separated by thin, continuous reflectors of low to high amplitude. Unit C contains more high-amplitude reflectors than units A and B. To the north, the transparent packages for all units thin and the reflectors converge and decrease in amplitude (Fig. 6). Layers within units A, B, and C extend up the basin slopes and onlap the acoustic basement well above the lake floor (Fig. 5). In the southern basin, each unit exhibits a lenticular geometry that is thickest near the basin center and thins toward the eastern and western basin slopes (Fig. 5). In some profiles, the reflectors appear to be truncated by slide deposits (Fig. 5). The lenticular pattern does not extend to the northern basin; instead, the units in the northern basin thin toward highs in topography and are fairly uniform in thickness.

Cascade Lake

The acoustic character of stratigraphic packages in Cascade Lake is similar to that observed in Fallen Leaf Lake, and allows for a stratigraphic correlation between the two basins. The acoustic basement is hummocky, with steep slopes on the southern, eastern, and western sides and a gentler slope up to the north (Figs. 8 and 9). The deepest part of the basin is in the south, near the WTDPF. Based on acoustic character, the stratigraphy can be divided into three sections that have characteristics similar to those of sections I, II, and III in Fallen Leaf Lake (Fig. 8). The oldest sedimentary unit, section III, is chaotic and homogeneous with some discontinuous and wavy low- to high-amplitude reflectors that infill lows and thin onto basement highs. In the deepest area of the basin, the uppermost part of section III is represented by thinly spaced (decimeter scale), high-amplitude, wavy, and mostly continuous reflectors that separate semitransparent layers. The upper contact of section III is a high-amplitude reflector that separates the thinly spaced reflectors below from section II above. Continuous, subparallel, high-amplitude reflectors that separate semitransparent layers of variable thickness (approximately decimeter to meter scale) are characteristic of section II. These beds thin onto highs in topography, but do not extend north beyond the southern depocenter. The high-amplitude reflectors maintain a strong signal throughout the basin. Some thinly spaced (decimeter scale), low-amplitude reflectors are apparent within the semitransparent layers (Fig. 8). The uppermost package, section I, is divided into two units separated by the dashed line in Figure 8.

Semitransparent layers that are separated by high-amplitude reflectors characterize the lower unit. The reflectors become more closely spaced moving upsection. This unit was grouped with section I rather than section II because it drapes over highs in topography away from the southern depocenter, whereas section II onlaps topographic relief and is restricted to the southern depocenter. Within section I, the lower unit is separated from the upper unit by a high-amplitude reflector that maintains acoustic strength throughout the basin. The upper unit of section I is mostly transparent with numerous thinly spaced (decimeter scale), low-amplitude reflectors (Fig. 8). These reflectors decrease in amplitude from south to north. A single high-amplitude reflector is observed in the lower third of section I that appears to correlate with the

Geosphere, published online on 26 June 2013 as doi:10.1130/GES00877.1

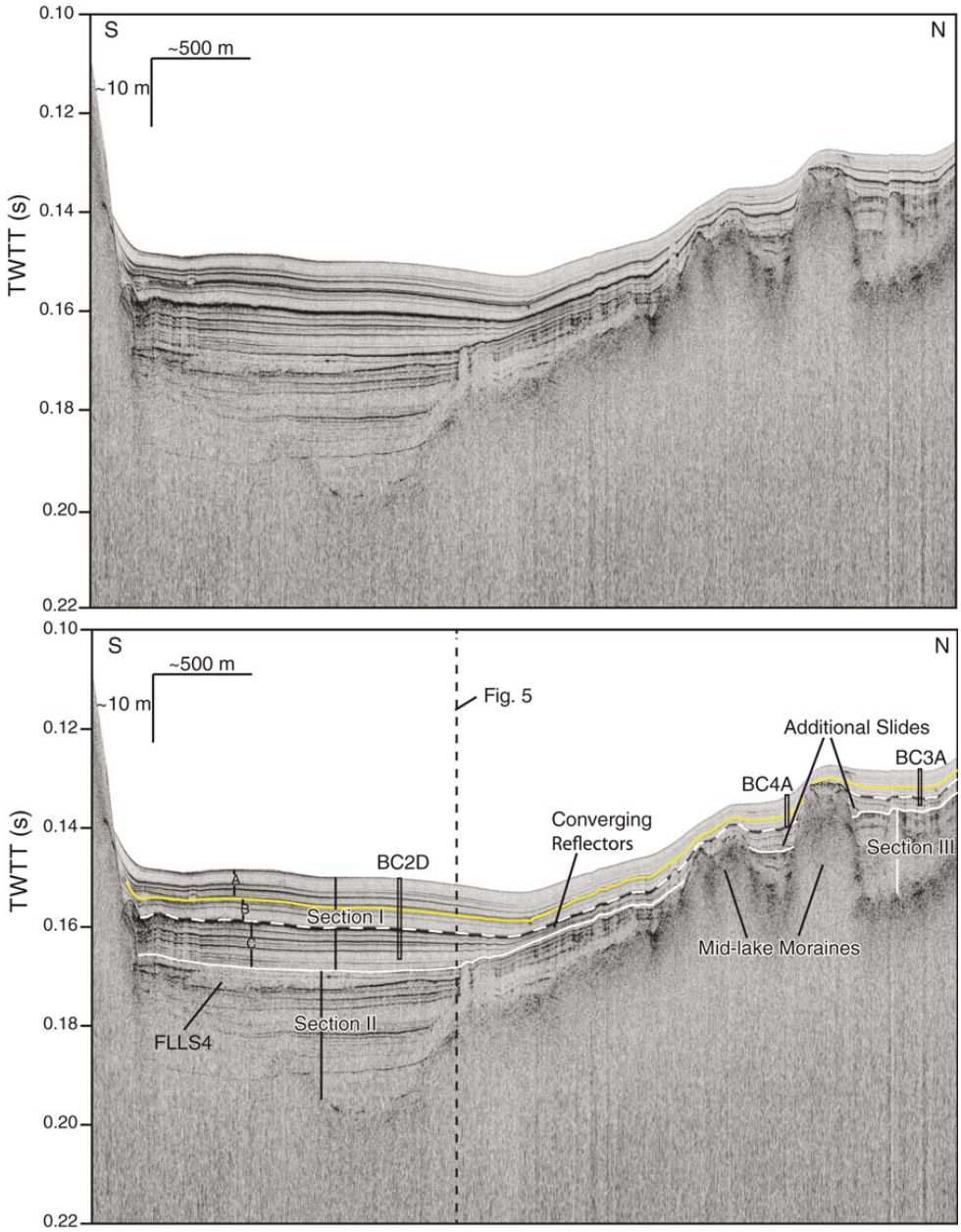

Figure 6. North-south–trending Chirp (compressed high intensity radar pulse) profile showing variability in character of sediment packages between the northern and southern parts of the basin, separated by the mid-lake moraines. The base of section I is marked in white, the Tsoyowata Ash horizon is dashed white, and the most recent event (MRE) horizon is marked in yellow. The Fallen Leaf Lake slide, FLLS1, is also in yellow where resolved. The location and penetration depth of piston cores BC2D, BC4A, and BC3A are illustrated. TWTT—two-way traveltime.

Geosphere, published online on 26 June 2013 as doi:10.1130/GES00877.1

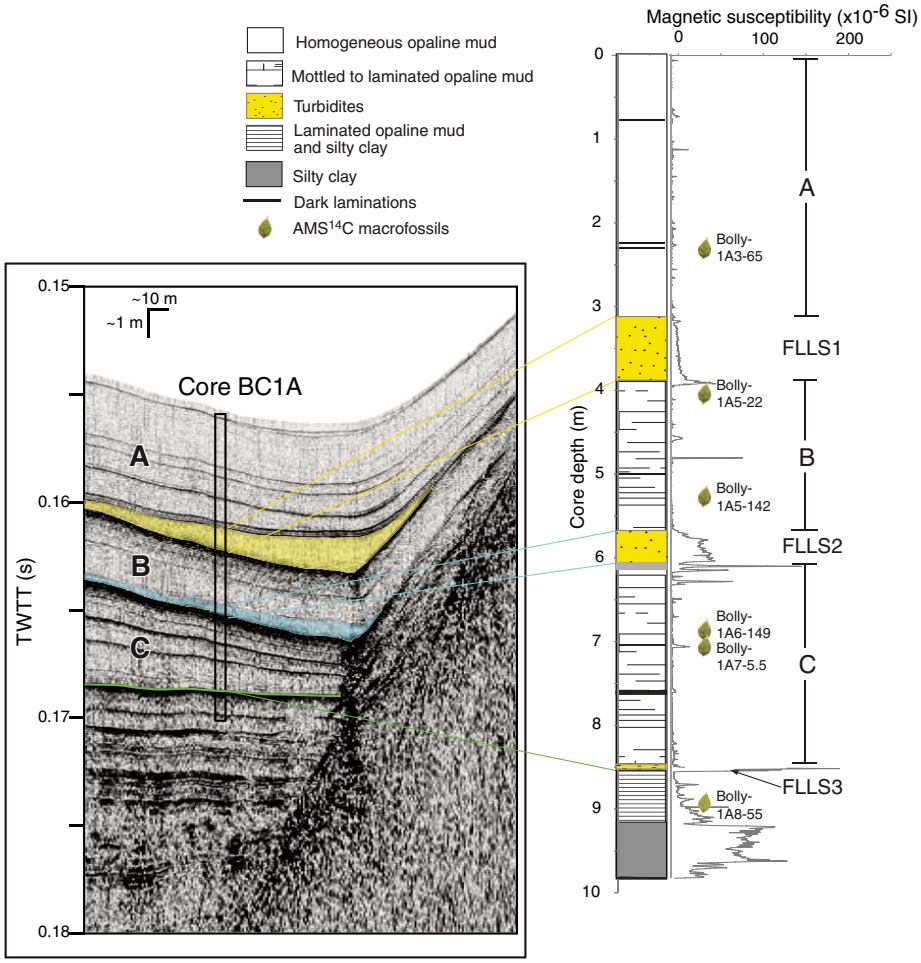

Figure 7. Enlargement of section from Figure 5 Chirp (compressed high intensity radar pulse) profile correlated to piston core BC1A. The three slide deposits observed in the core are easily identified in Chirp data and were used to correlate the core to the Chirp imagery. The three Fallen Leaf Lake slides are FLLS1 (yellow), FLLS2 (blue), and FLLS3 (green). See inset legend for detailed core lithology. Radiocarbon sample names are listed next to macrofossil symbols and correspond to dates from Table 1. TWTT—two-way traveltime; AMS—accelerator mass spectrometry.

base of a slide deposit. This reflector decreases in amplitude away from the slide deposit.

Along the base of the southern slope we observe two major strands of the WTDPF that trend ~N30°W (Fig. 8). The trend of the southern strand appears to extend onshore to the east and correlates with the trace of the WTDPF scarp identified in Lidar data (Fig. 2). Both strands produce offset of the lake floor, which increases downsection to the basement. It is difficult to identify discrete offset of individual reflectors because of antecedent topography on the acoustic basement. However, the maximum observed offset on the northern strand is ~6.7 m at the lake floor and ~21.2 m at the acoustic basement. The maximum offset on the southern strand is ~7.5 m at the lake floor and ~17.8 m at the acoustic basement. Horizons are generally horizontal, but may exhibit some deformation as they approach the fault. The two strands become less well pronounced to the northwest. In the northwestern most northeast-southwest–trending Chirp profile, we do not observe two distinct fault strands with obvious normal displacement, but rather several strands that deform basin sediments (Fig. 9). Some fault strands in this profile are characterized by chevron folds, while some exhibit normal displacement. This Chirp profile is located on the western slope of Cascade Lake and the steep topography may obscure significant offset

Geosphere, published online on 26 June 2013 as doi:10.1130/GES00877.1

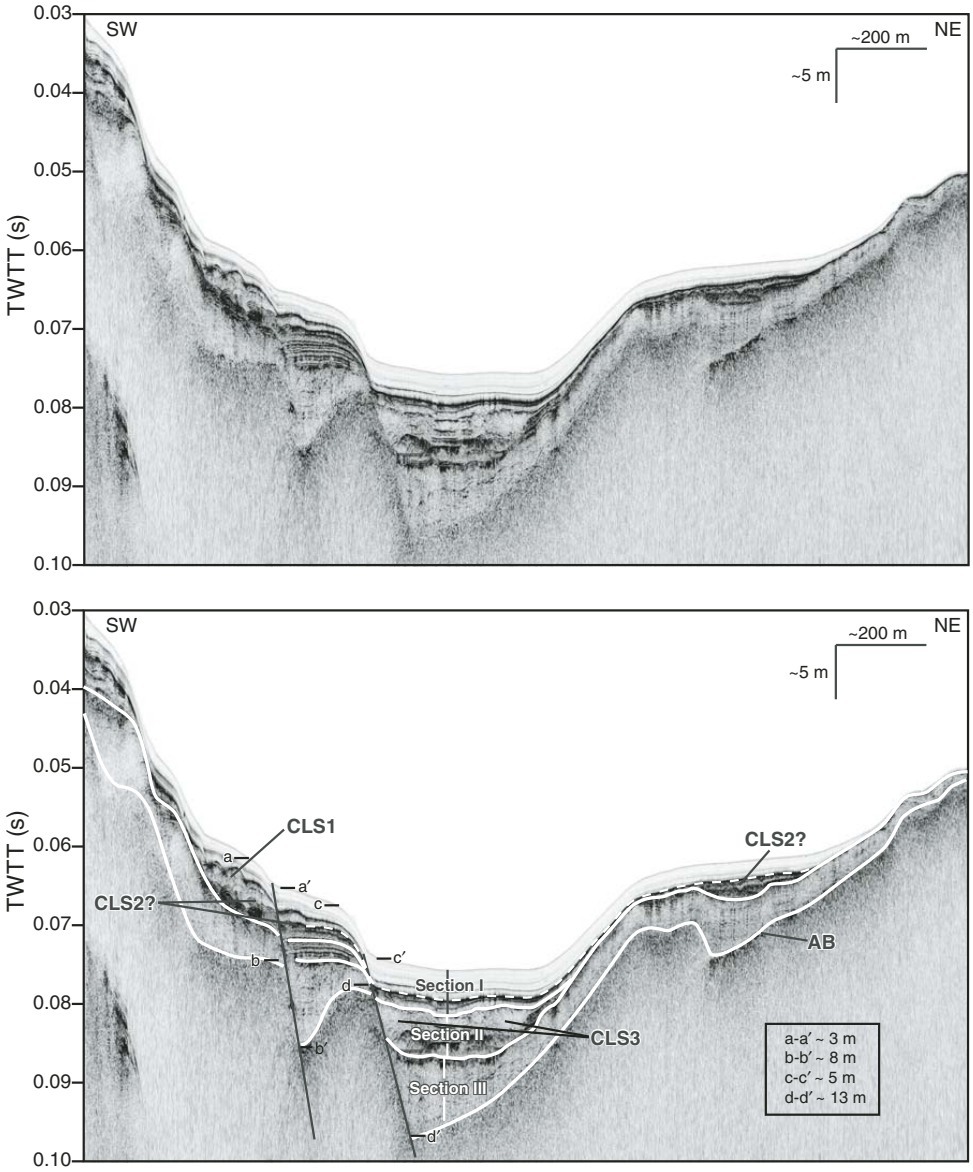

Figure 8. Southwest-northeast–trending Chirp (compressed high intensity radar pulse) profile from Cascade Lake (CL) illustrating two strands of the West Tahoe–Dollar Point fault (WTDPF) (solid black lines), slide deposits (CLS1, CLS2?, and CLS3), and acoustic character of lake stratigraphy. Offset on the two WTDPF strands is measured at the seafloor and the acoustic basement (AB) at locations indicated (a–a′, b–b′, c–c′, and d–d′). The dashed horizon is interpreted to be synchronous with the Tsoyowata Ash horizon. Section boundaries are marked in solid white. TWTT—two-way traveltime.

Geosphere, published online on 26 June 2013 as doi:10.1130/GES00877.1

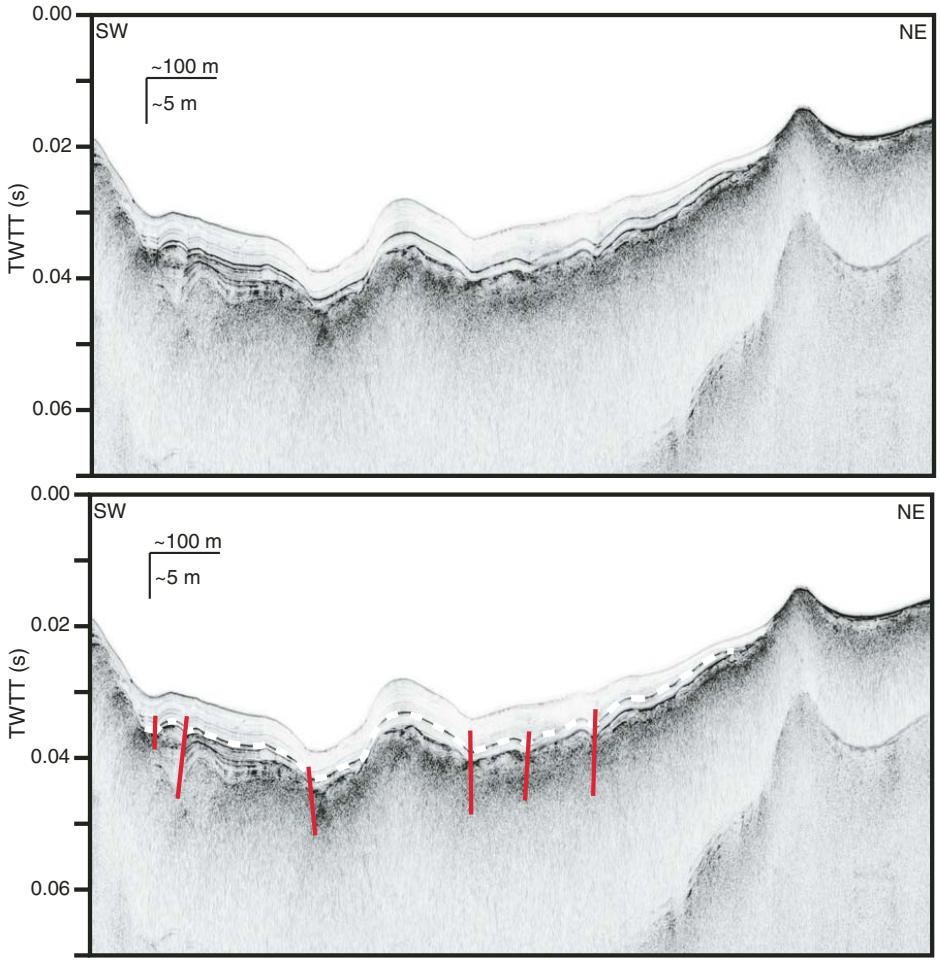

Figure 9. Westernmost Chirp (compressed high intensity radar pulse) profile in Cascade Lake. Strands of the West Tahoe–Dollar Point fault are shown in red. The faults are more distributed than in the central basin, with evidence of transtensional deformation. The dashed white line traces the interpreted Tsoyowata Ash horizon. TWTT—two-way traveltime.

of the acoustic basement observed in eastern profiles. The shallowest horizon deformed by these faults is a low-amplitude reflector within section I, which appears to correlate with a slide deposit (CLS1; CL is Cascade Lake). We did not identify strong evidence for a scarp extending onshore to the west from Cascade Lake in Lidar data (Fig. 2); the distributed nature of offset in Cascade Lake, along with no focused fault scarp observed west of the lake, may represent horsetail splaying of the WTDPF as it dies out to the west, toward Emerald Bay.

Emerald Bay

We use the same acoustic character observations in Fallen Leaf Lake and Cascade Lake to correlate the stratigraphy of Emerald Bay (Fig. 10). In general, section III is the oldest sediment that is characterized in large part by a chaotic acoustic character with some high-amplitude wavy and discontinuous reflectors. The acoustic character of section II is variably spaced low- to high-amplitude reflectors between semitransparent packages. Section I is mostly transparent with many low-amplitude reflectors and a few higher amplitude reflectors. In Emerald Bay, the reflectors of section I generally decrease in amplitude from south to north; however, some locations show more lateral variation in acoustic amplitude.

Sediment core EB2 recovered from Emerald Bay penetrated to a depth of ~5.3 m below the lake floor, and 3 radiocarbon dates were determined (Table 1). We calculate a constant sedimentation rate of ~1 mm/yr between the youngest and oldest dated samples. The dates also suggest an increase in sedimentation rate

Geosphere, published online on 26 June 2013 as doi:10.1130/GES00877.1

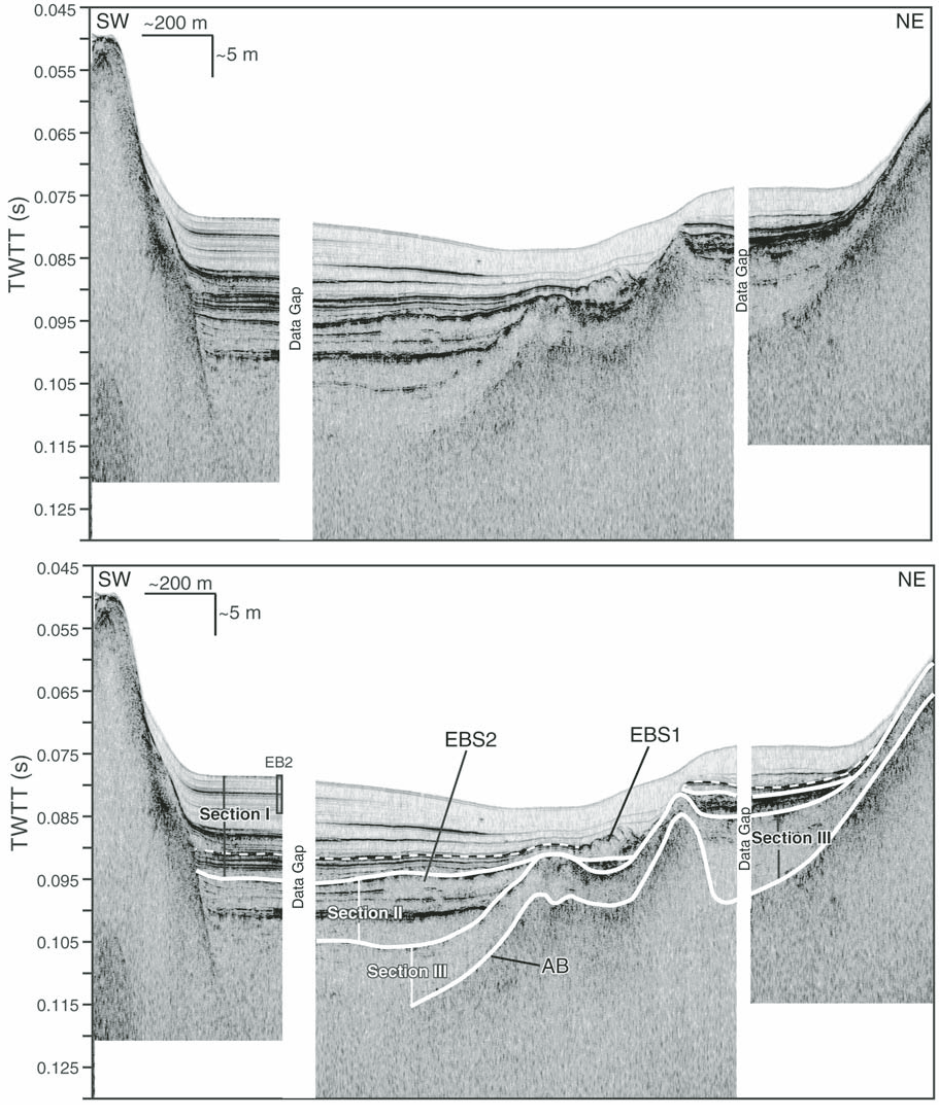

Figure 10. Southwest-northeast–trending Chirp (compressed high intensity radar pulse) profile from Emerald Bay (EB) showing acoustic character of the stratigraphy (sections I–III) and slide deposits (EBS1 and EBS2). The dashed line corresponds to horizon 1 in Figure 11, and is interpreted as the Tsoyowata Ash horizon based on acoustic correlation to Fallen Leaf Lake. Location and approximate penetration depth of piston core EB2 is also shown. Solid white lines mark section boundaries. In the southern basin, section II and III are not differentiated because a distinct boundary is not observed. The depth to acoustic basement (AB) is also not identified in the southern basin. TWTT—two-way traveltime.

Geosphere, published online on 26 June 2013 as doi:10.1130/GES00877.1

with depth. Between the youngest samples, we calculate a sedimentation rate of ~0.99 mm/yr, but the time spanning the oldest samples yields a sedimentation rate as high as ~1.24 mm/yr.

The WTDPF is not readily observed in Chirp data from Emerald Bay (Figs. 10 and 11). Nevertheless, we observe acoustic wipeout to the northeast of the island located in the southern part of the bay (Fig. 11). In a single profile, we observe acoustic reflectors diverging to the south, into the acoustic wipeout (Fig. 11). The diverging beds are not observed in the Chirp lines to the north or south. The youngest horizon that exhibits rotation and divergence into the gas wipeout is horizon 1. Although the sediment package between horizon 1 and horizon 2 thickens toward the gas wipeout, horizon 2 does not dip toward the south where it intersects the gas wipeout. Reflectors above horizon 2 are subhorizontal and do not slope toward the south.

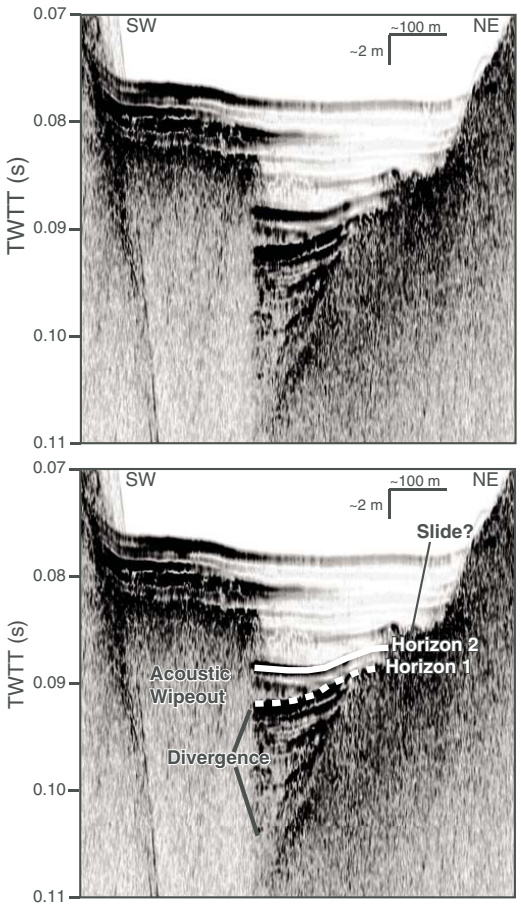

Figure 11. Southwest-northeast–trending Chirp (compressed high intensity radar pulse) profile beneath Emerald Bay images diverging beds. Horizon 1 is correlated to the dashed horizon in Figure 10, and is interpreted as the Tsoyowata Ash horizon. Above horizon 2, divergence is not observed. Acoustic basement at the far left of the profile slopes up toward the island in Emerald Bay. TWTT—two-way traveltime.

Event Deposits

Fallen Leaf Lake

We observe four recurring slide deposits in Chirp data and sediment cores from Fallen Leaf Lake: FLLS1, FLLS2, FLLS3, and FLLS4 (Fig. 12; Table 2). FLLS1 and FLLS2 are morphologically similar; both consist of a proximal and a distal component that have a measurable thickness in Chirp data (Fig. 13). FLLS3 and FLLS4 have proximal components that are discernible in Chirp data (Figs. 12C, 12D), but the distal component is too thin to be resolved. Nevertheless, FLLS3, manifested as a 4-cm-thick turbidite, was recovered in core BC3A and both slides may have distal components represented by high-amplitude reflectors. The proximal slides are identified in Chirp as chaotic, homogeneous units that disrupt previously deposited horizontal reflectors (Figs. 5 and 13). For all four slides, we are able to identify the youngest acoustic horizons disrupted by the proximal slides. These horizons also correlate to the base of the associated distal component for FLLS1 and FLLS2. In all cases, these slides correlate with strong reflectors that can be traced throughout the basin. The tops of the proximal slides are identified by a hummocky surface and a change from chaotic, homogeneous units below to transparent laminated units above (Fig. 13). The bases of the proximal slides are not always apparent due to acoustic attenuation and scattering.

FLLS1 was first identified and described by Brothers et al. (2009), who described the distal portion of the slide as a diverging unit that onlaps bathymetric highs, thickens into lows, and infills accommodation created during the MRE. The proximal slide, sampled by a piston core, is coarse grained and contains several large pieces of wood and smaller twigs. With the addition of new high-resolution Chirp data, we are able to map the extent of the proximal, massive slide deposits in more detail and calculate the thickness of the distal slide (Fig. 12). We observe two apparently synchronous proximal slide deposits located in the southwestern and southeastern corners of the lake. The maximum observed thickness of the proximal FLLS1 is ~3.9 m and the deposits cover a total area of ~0.40 km^2. The youngest acoustic horizon disrupted by FLLS1 is identified as the MRE horizon. The proximal slides appear to grade into the distal slide, which overlies the MRE horizon (Figs. 5 and 13). The distal slide is transparent in Chirp profiles and infills accommodation created by the MRE as well as other topographic lows (Fig. 5). The maximum thickness of the distal slide is ~1.9 m over the mapped extent (~2.08 km^2; Fig. 12). The calculated areal extent is based on where the thickness of the deposit was detectable in

Geosphere, published online on 26 June 2013 as doi:10.1130/GES00877.1

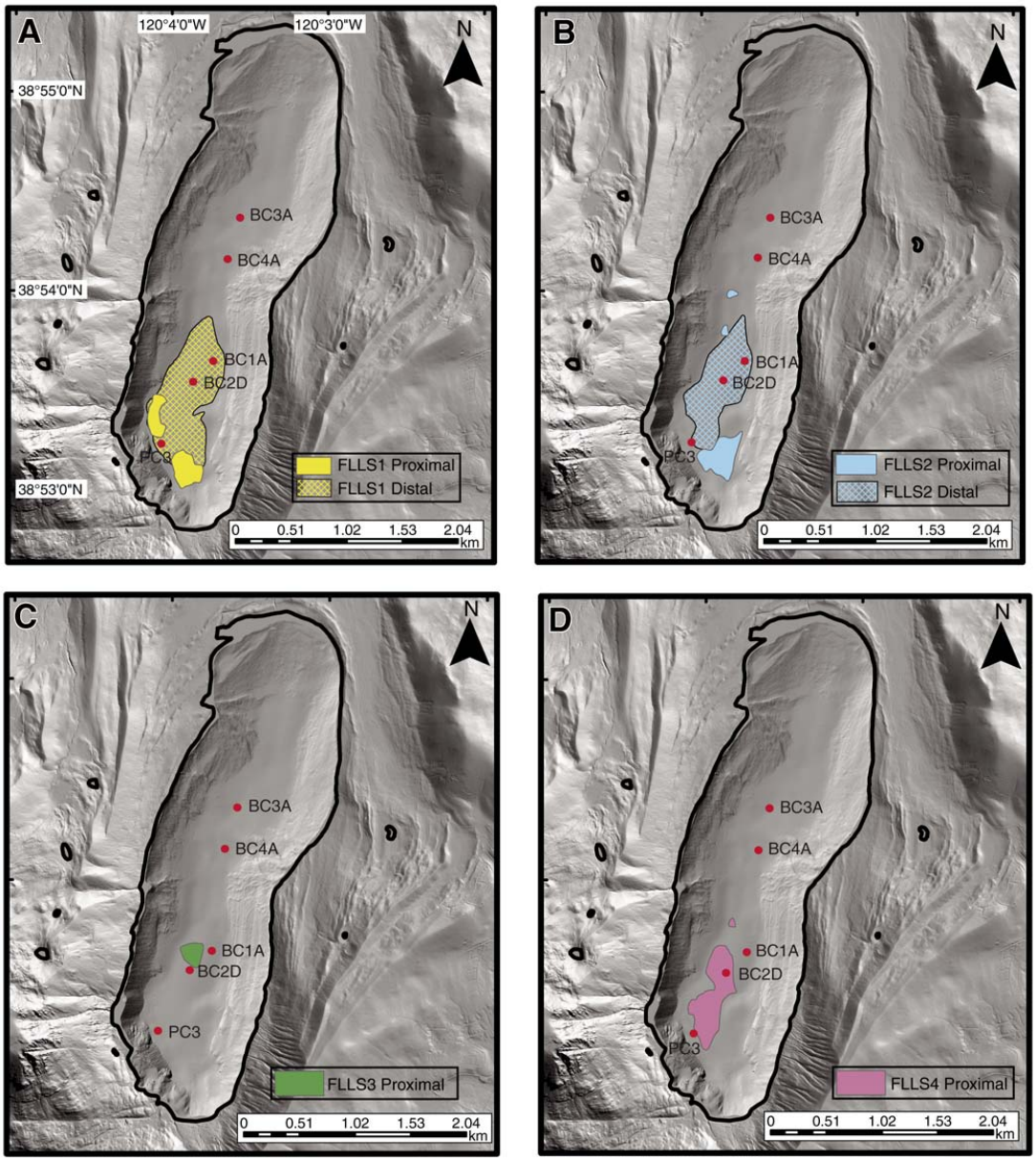

Figure 12. Locations of Fallen Leaf Lake slide deposits. (A) FLLS1. (B) FLLS2. (C) FLLS3. (D) FLLS4. Locations of piston cores are shown as red dots and labeled with core identifications.

Geosphere, published online on 26 June 2013 as doi:10.1130/GES00877.1

TABLE 2. NAMES AND AGES FOR SLIDE DEPOSITS LISTED BY SUBBASIN

Approximate age (ka)	Lake Tahoe*	FLL	Emerald Bay	Cascade Lake
4.5	F	FLLS1	–	–
5.3	G	–	–	CLS1
8	J	FLLS2	EBS1	CLS2?
11.5	O	FLLS3	EBS2	CLS3
13	–	FLLS4	–	–

Note: FLL—Fallen Leaf Lake; dash indicates slide not observed.
*Data from Smith et al. (2013).

Chirp data and is therefore likely an underestimate. For example, the slide is sampled farther north in piston core BC3A, where it was recovered as an ~5-cm-thick deposit, below the Chirp detection limit. The horizon correlated to the base of the distal slide remains highly reflective throughout the basin, indicating that the slide may cover the entire area of the basin.

The FLLS1 distal slide mapped in Chirp data was correlated to piston cores, and radiocarbon dates were acquired for organic material bracketing FLLS1 in four different cores (cores BC3A, BC2D, BC1A, and PC3; Fig. 2; Table 1). The conservative age range of the slide determined from these dates is 2.89–5.69 ka, using the oldest and youngest modeled dates. The preferred age model, which is a composite model for all cores, constrains the age of FLLS1 to 4.57–4.85 ka (Fig. 14).

The FLLS2 slide directly overlies the Tsoyowata Ash marker bed. The Tsoyowata Ash was recovered in piston cores BC1A and BC2D and was correlated to Chirp data and mapped throughout the basin. The ash is 7.7–8.0 ka and was sourced from a Mount Mazama eruption (Bacon, 1983; Sarna-Wojcicki et al., 1991). In the piston cores, the distal portion of FLLS2 was recovered directly on top of the Tsoyowata Ash. In Chirp data, we observe both a massive, proximal slide and the associated distal deposits that were recovered in the cores (Figs. 5, 7, and 13). The proximal slide is located in the southwestern area of Fallen Leaf Lake, covering an area of ~0.35 km^2 (Fig. 12). The chaotic deposit disrupts horizontal reflectors that are folded adjacent to the margin of the deposit. The youngest disrupted horizon is correlated to the Tsoyowata Ash deposit. Although the base of the proximal slide is not always visible due to acoustic scattering and attenuation, the distal margin of the slide disrupts ~7.6 m of previously deposited sediment. In some areas, the slide unit contains fragments of folded and tilted horizons. None of the sediment cores penetrated the proximal section of FLLS2. We also image two local slides near the central basin that were deposited directly above the Tsoyowata Ash horizon (Fig. 12).

Similar to FLLS1, the distal portion of FLLS2 is acoustically transparent and infills topographic lows (Fig. 5). The maximum thickness of the distal slide is ~1.0 m over the mapped extent (~1.37 km^2). The FLLS2 distal slide appears to extend across the entire basin, was recovered as a <5 cm deposit in the northernmost core BC3A, and remains highly reflective throughout the basin.

Modeled radiocarbon ages for FLLS2 yield a conservative age range of 7.06–7.93 ka and a preferred age range of 7.62–7.90 ka (Table 1; Fig. 14). These results are based on dates from three piston cores bracketing the slide. The preferred model is a composite of dates from all three cores.

The proximal slide FLLS3 is imaged in Chirp data covering ~0.12 km^2 with a maximum thickness of ~1.3 m (Figs. 5 and 12). Slide FLLS3 appears to have a distal component that reaches at least 550 m across the lake, was recovered in core BC1A, is dated as ca. 11.24–11.64 ka, and is observed as a strong reflector in Chirp data.

Slide FLLS4 is observed in Chirp data as a massive, proximal slide deposit in the southern lake basin covering an area of ~0.72 km^2 (Figs. 6 and 12). A small slide is also observed along the western slope in the central basin, which may not be directly linked to the southern slide, but appears to have been synchronous (Fig. 12). In some areas, the top of the slide is not well defined by an acoustic reflector, but the base of the slide is often marked by a high-amplitude subhorizontal reflector. The character of the deposit is chaotic and the slide disturbs previously deposited horizontal reflectors. The maximum slide thickness is ~2.8 m. FLLS4 is chaotic, and returns from within the deposit are of lower amplitude than those observed in FLLS1 and FLLS2 proximal slides. FLLS4 is located near the center of the southern basin and along the western basin slope (Fig. 12). The youngest reflector disrupted by the slide can be traced throughout the basin; however, it is below the depth of the deepest penetrating piston core. To date this horizon, we extrapolated sedimentation rates observed in piston core BC1A, which yielded an age of ca. 13.2–16.3 ka (Table 1). The disrupted reflector used in the calculation is at the base of the slide and therefore the slide may be slightly younger than calculated.

We also observed several small, isolated slide deposits in northern Chirp profiles (Fig. 6). These slides do not appear to have a distal component. Stratigraphy is highly condensed in northern lake sediments, making it difficult to trace horizons continuously to the north. The slides are stratigraphically below the FLLS1 and FLLS2 horizons and may correlate with the older slides observed in the southern basin. The slide deposits occur near a distinct transition in the seismic stratigraphy of the northern basin between homogeneous, chaotic units below (section III) and thinly bedded, acoustically transparent layers above (section I). As such the northern slides may be correlated to one another. The combined area covered by these deposits is ~0.15 km^2.

Cascade Lake

We observe two major slide deposits in Cascade Lake (Fig. 8). The youngest slide, CLS1, is located at the base of the steep southern basin slope. The slide is between the two strands of the WTDPF and across the southern strand to the south. Slide CLS1 has a hummocky upper surface below the transparent sediments of section I. The slide covers an area of ~0.1 km^2 and reaches a maximum thickness of ~2.1 m. CLS1 marks the uppermost high-amplitude reflector of section I. Even though the WTDPF makes direct tracing of this horizon difficult, we assume, on the basis of acoustic character, that the horizon north of the WTDPF corresponding to the slide is also the uppermost high-amplitude reflector. This allows us to compare the age of the slide with slide CLS3. Slide CLS3 comprises two apparently synchronous slides (Fig. 8); both have similar acoustic characteristics and so are described as one. CLS3 is stratigraphically lower than CLS1, and is located north of both strands of the WTDPF in the depocenter of the lake. The slide is acoustically chaotic with a hummocky surface. It disturbs several horizons within section II sediments. The uppermost horizon disturbed by CLS3 was used to determine the relative age of the slide. CLS3 covers ~0.09 km^2 and has a maximum thickness of ~3.8 m.

Emerald Bay

We observe two major slide deposits in sediments beneath Emerald Bay (Fig. 10). The youngest slide, EBS1, has a hummocky upper contact with transparent to laminated units above and a maximum thickness of ~4.5 m. The slide is acoustically chaotic, disturbs previously deposited horizons, and covers an area of ~0.06 km^2. The uppermost horizon disturbed by EBS1 is a reflector that maintains a high-amplitude signal throughout the basin, and corresponds to horizon 1 in Figure 11. The slide is located in the central basin near the base of the gently northeast sloping acoustic basement

Geosphere, published online on 26 June 2013 as doi:10.1130/GES00877.1

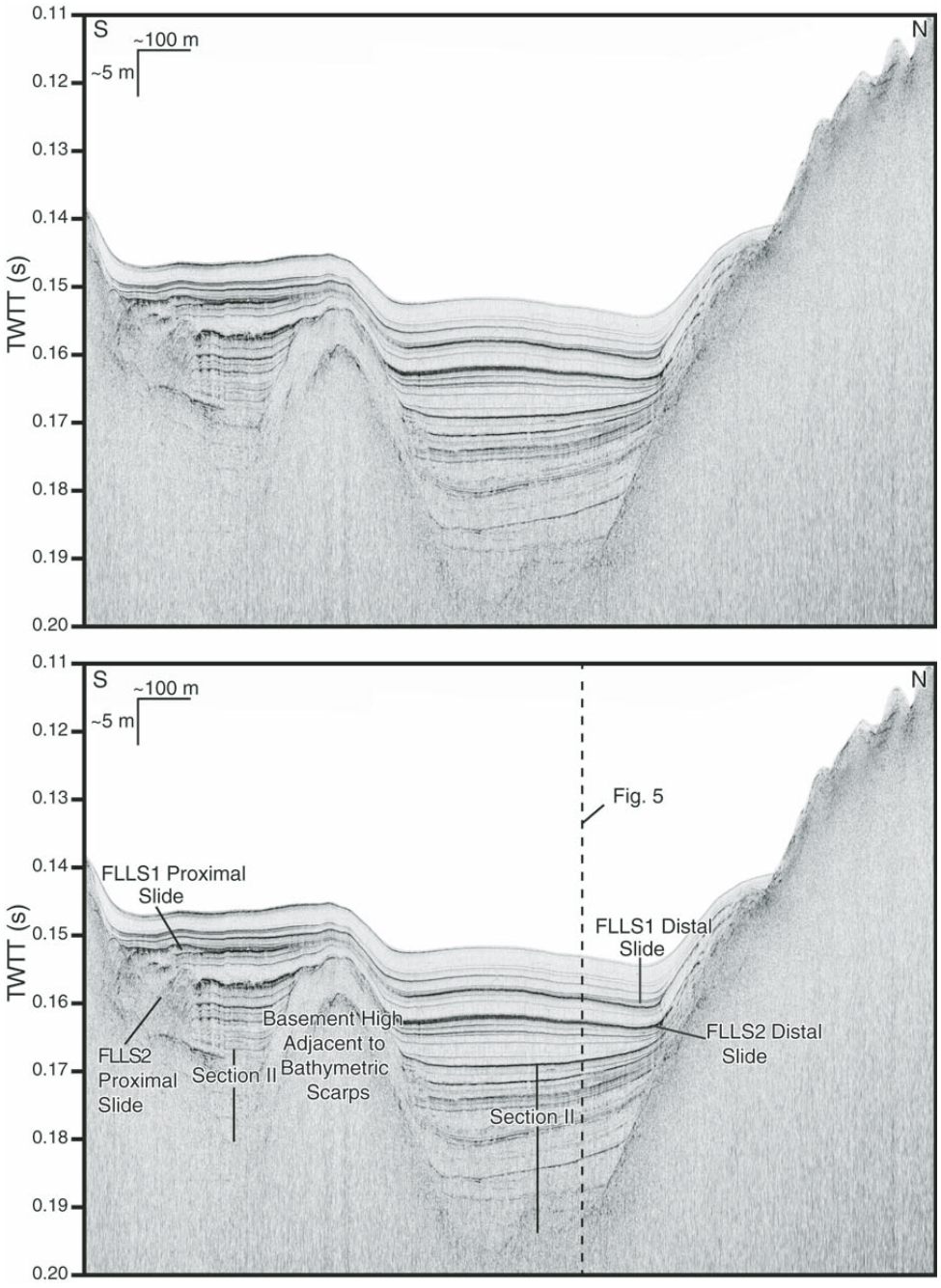

Figure 13. North-south–trending Chirp (compressed high intensity radar pulse) profile from Fallen Leaf Lake showing proximal and distal FLLS1 and FLLS2 slides. TWTT—two-way traveltime.

Geosphere, published online on 26 June 2013 as doi:10.1130/GES00877.1

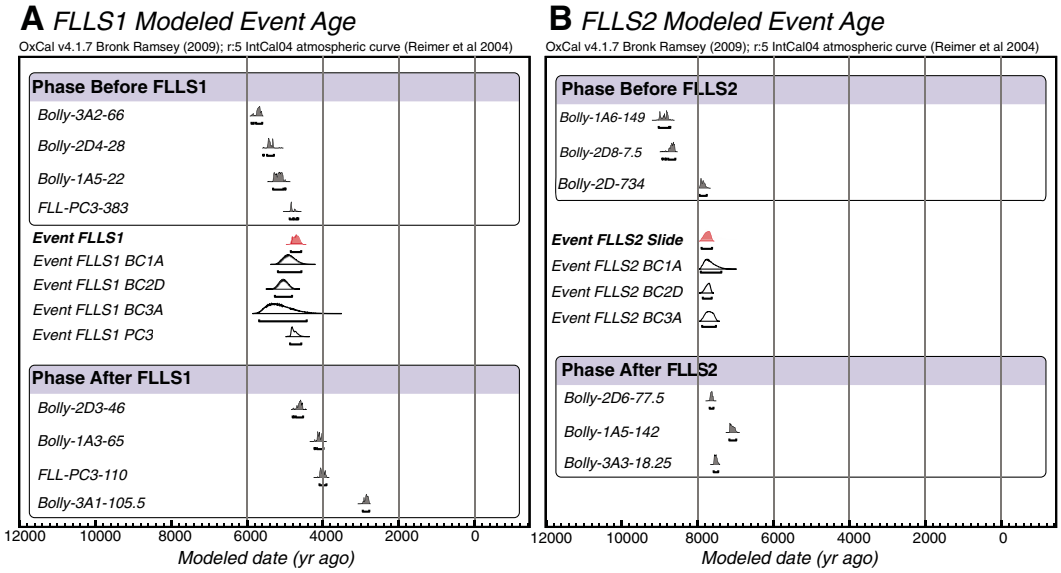

Figure 14. (A) The modeled event age of Fallen Leaf Lake slide FLLS1. (B) The modeled event age of FLLS2. The probability distribution for each radiocarbon date is shown in gray, the modeled dates for individual cores are white, outlined in black, and the combined preferred model is shown in red. Additional information on radiocarbon dates is available in Table 1.

horizon. The older slide, EBS2, is similar in character to EBS1 and is located slightly to the southeast (Fig. 10). The maximum thickness of slide EBS2 is ~2.9 m and it covers an area of ~0.26 km^2.

By extrapolating below the bottom of sediment core EB2 using a 1 mm/yr sedimentation rate and accounting for potential uncertainty due to overpenetration of as much as 0.5 m, we constrain EBS1 as ca. 9.4–10.2 ka, and slide EBS2 as ca. 12.7–13.5 ka. Using the radiocarbon ages from core EB2, we calculate a sedimentation rate of ~0.99 mm/yr between the two youngest dates and an increase in sedimentation rate to ~1.24 mm/yr between the two oldest dates. This increase in sedimentation rates observed downcore should continue, as glacially derived sediment sources would have been closer. In addition, during the Tioga glacial period, glaciers would have eroded previously deposited sediments and ice would have been in contact with the Chirp acoustic basement horizon. A thickness of >25 m of sediment is observed above the acoustic basement at the location of EB2. If the acoustic basement represents the retreat of the last Tioga glacial period (ca. 14 ka), this would require a faster sedimentation rate to account for >25 m of sediment accumulated at this location. Furthermore, we observe an increase in sedimentation rate with depth in Fallen Leaf Lake sediments, and we expect these two basins to have somewhat similar patterns in sedimentation. If we use the increased sedimentation rate of ~1.24 mm/yr below the bottom of core EB2, we obtain age ranges for EBS1 of ca. 8.6–9.3 ka and for EBS2 of ca. 11.2–11.9 ka.

DISCUSSION

Stratigraphic Interpretation

The Tioga glaciation, which lasted from ca. 30 to ca. 14 ka, consisted of several cycles of glacial advance and retreat (Benson et al., 1998; Bischoff and Cummins, 2001; Clark and Gillespie, 1997; Phillips et al., 1996; Rood et al., 2011). The series of arched terminal and recessional Tioga moraines that bound Fallen Leaf Lake, Cascade Lake, and Emerald Bay to the north (Saucedo et al., 2005) delineate the farthest advance of Tioga glaciation. The mid-lake moraine complex, mapped in Fallen Leaf Lake Chirp data, was likely deposited during a stillstand in glacial retreat or a subsequent, less extensive advance. The ridges observed in the Chirp acoustic basement horizon align with ridges observed in lake bathymetry and with mapped Tioga-age moraines onshore. These moraines created topography on the basin floor that has affected sedimentation patterns in Fallen Leaf Lake.

We assume that the glaciers that formed Fallen Leaf Lake, Emerald Bay, and Cascade Lake were in contact with the acoustic basement during the Tioga glaciation. Therefore, the sedimentary packages above the acoustic basement were deposited after the retreat of the glaciers from these lakes at the end of the Tioga glaciation, ca. 14 ka. In Fallen Leaf Lake, the basin also records stalls in the glacial retreat as evidenced by the mid-lake moraines. Section III infills lows created by the mid-lake moraine complex (Fig. 6); we interpret these deposits as subglacial or proglacial deposits. The chaotic and strongly reflective acoustic nature of these deposits is consistent with such a depositional scenario and suggests that they are coarse grained and lack internal structure. Some horizons can be distinguished and may represent coarser material deposited as an outburst flood event (e.g., Uchupi and Ross, 2000). Section III is only observed north of the mid-lake moraines, but similar deposits may be deeper than the penetration capability of Chirp data in the southern basin. We interpret section III as the oldest sedimentary section deposited when the glacier extended to the mid-lake moraines.

Geosphere, published online on 26 June 2013 as doi:10.1130/GES00877.1

Subsequent to deposition of section III, the glacier retreated up the valley, and sedimentation of section II began in the deep accommodation created by the glacier and the WTDPF in the southern basin. We interpret section II as sediment carried by glacial meltwater and deposited in a proglacial lake (Figs. 5, 6, and 7). Sedimentation rates were high during deposition of section II as the rapidly melting glacier carried sediment to the basin. The age of the upper contact of section II is ca. 11.24–11.64 ka and the maximum thickness of section II is >40 m, indicating an average sedimentation rate of ~16 mm/yr. Furthermore, the onlap of layers within section II onto basin slopes is flat and subhorizontal, and horizons maintain a strong acoustic amplitude laterally throughout the section. This may indicate rapid emplacement of gravity flows from glacial outburst floods. Section II sediments are not observed north of the mid-lake moraine complex; however, it is possible that we are not able to separate a highly condensed section II from section I or III. These topographic highs may have acted as depositional barriers for sediments that mainly entered the basin from the south.

The upper contact of section II appears to mark the transition from glacial deposits below to lacustrine sediments in section I above. This transition was captured in core BC1A, where we observe glacial silt and high magnetic susceptibility below the upper contact of section II, and lacustrine sediments and low magnetic susceptibility above the upper contact of section II (Fig. 7). In Chirp data, a change from uniform thickness and flat onlap at basement highs to lenticular deposits that onlap high onto basement walls also suggests a change from glacial to lacustrine deposition (Fig. 5). The diminished acoustic amplitude of reflectors to the north indicates that the source of sediment for section I was primarily from the south.

In Cascade Lake and Emerald Bay, we do not observe the lenticular pattern of section I, but are able to correlate the sections based on acoustic character. Section I in Emerald Bay and Cascade Lake is primarily identified by characteristic onlap high at basin walls. Section I in these basins has high-amplitude reflections near the base, but is mostly transparent in the upper sediments. As with section I in Fallen Leaf Lake, we interpret these deposits to be lacustrine deposits. Section II and section III are considered glacial deposits, similar to those of Fallen Leaf Lake. Section III is the older of the units, and the entire sequence from section III through section II is interpreted to be a transition from subglacial, to proximal proglacial, to distal proglacial deposits.

Character of Slide Deposits

The slide deposits observed in Fallen Leaf Lake sediments are characteristic of debris flow and turbidite deposits. The FLLS1 and FLLS2 slides are indicative of large proximal debris flow deposits with associated distal turbidites. The turbidite deposits are easily identifiable in Fallen Leaf Lake cores as graded beds, and they infill lows in topography created by scour and differential deposition observed in section I. We observe only a proximal debris flow component for FLLS3 and FLLS4 in Chirp data, though both slides correspond to a high-amplitude reflector that maintains strength throughout the basin and may represent the distal components.

The FLLS1 proximal slides appear to be sourced from the southeastern and southwestern corners of Fallen Leaf Lake (Fig. 12). Although we do not observe evidence for well-defined deltas, these are both areas of water and sediment input to the lake. The southeastern slide is located near the Glen Alpine Creek input and the southwestern slide is located near several small, unnamed creeks that drain from the steep slopes of Cathedral Peak (Fig. 2). The southwestern slide may be sourced from the small apron extending slightly onto the basin floor from the slope. Above the slope is a set of ridges that may be scarps from the FLLS1 slide (Fig. 3). The large FLLS2 proximal slide also appears to be sourced from the southeastern area of the lake near the Glen Alpine Creek input (Fig. 12). The southern source area for the FLLS1 and FLLS2 slides is also adjacent to the WTDPF and the steepest basin wall slopes, where slide deposits triggered by an event on the fault would be expected. The two smaller proximal slides associated with the FLLS2 deposits are located near the Cathedral Creek input to the lake on the western shore (Fig. 12). FLLS3 is sourced from the western slope, just south of the input from Cathedral Creek (Fig. 12). FLLS4 extends throughout much of the southern basin. In the south, the source of the slide appears to be the southern slope, whereas to the north the source appears to be the western slope, near Cathedral Creek (Fig. 12). This suggests that the FLLS4 may be two distinct slides that coalesce near the center of the southern basin. Several slides were sourced from the western slope near Cathedral Creek. This is directly below two slide deposits mapped onshore that are adjacent to the WTDPF trace (Saucedo et al., 2005). In Lidar data, the toe of the eastern slide is located on the footwall side of the fault trace (Fig. 2). The westernmost slide is larger and is deposited across the trace. We do not observe a fault trace across the western slide deposit, so either the slide occurred post-MRE, or is difficult to observe across the hummocky, coarse slide deposit. It is also possible that the slide was synchronous with the MRE, but we lack sufficient data to determine an age. We also cannot determine if these slides were synchronous with older slide deposits in Fallen Leaf Lake.

In Emerald Bay, the slide deposits appear sourced from the northwestward-sloping basin wall; this is toward the mouth of the bay. A slide is mapped onshore spilling into the southern part of Emerald Bay (Saucedo et al., 2005), but we do not observe a slide sourced from this area in Chirp data. In Cascade Lake, CLS1 appears to be sourced from the southern slope on the footwall of the WTDPF. CLS3 is deposited in the basin depocenter and appears to be sourced from both the northern and southern basin slopes. An onshore slide is also mapped at the southernmost shore of Cascade Lake (Saucedo et al., 2005). In Lidar data the onshore slide is directly adjacent to the WTDPF on the footwall side of the trace (Fig. 2). With currently available data, it is difficult to determine if the onshore slide is related to any of the slides observed in Chirp data.

Timing of Slide Deposits

Age ranges for the slide deposits observed in Lake Tahoe (Smith et al., 2013), Fallen Leaf Lake, Emerald Bay, and Cascade Lake are plotted in Figure 15. The ages of dated slide deposits in Emerald Bay and Cascade Lake are estimates and more detailed radiocarbon dating is needed to confirm temporal correlations with slides in Fallen Leaf Lake and Lake Tahoe. Although the ages of the Emerald Bay and Cascade Lake slides are estimated from acoustic correlation, we have more confidence in slide deposit dates for Fallen Leaf Lake, which are based on a robust age model (Table 1; Fig. 14).

The age model determined from the 2010 piston cores in Fallen Leaf Lake constrains the age range of FLLS1 as 4.57–4.85 ka. We suggest that FLLS1 in Fallen Leaf Lake is synchronous with the MRE on the WTDPF Fallen Leaf Lake segment and event deposit F in Lake Tahoe (4.07–4.51 ka; Smith et al., 2013). Deposit F is characterized by a debris flow and multiple turbidites that appear to originate from, and are constrained to, the northern Lake Tahoe Basin (Smith et al., 2013). Despite the slight difference in estimated age ranges, we suggest that deposit F and FLLS1 were both triggered by the same seismic event on the Fallen Leaf Lake segment of the WTDPF. Given the preferred age models for deposit F and FLLS1, the age of this event is ca. 4.5 ka. Errors in the modeled age range of FLLS1 or deposit F in Lake Tahoe could be due

Geosphere, published online on 26 June 2013 as doi:10.1130/GES00877.1

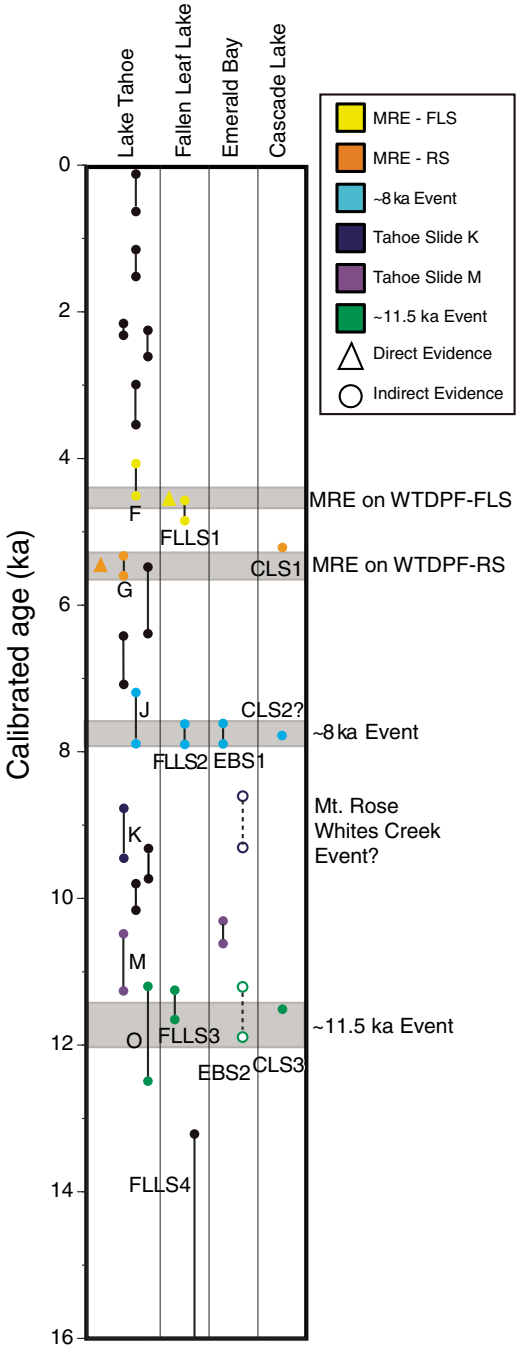

to sparseness of dates in pre-2010 cores, uncertainty in model calculations, or nonuniform deposition rates at the sites. Based on core data and seismic stratigraphy, there is no evidence for a young slide in either Emerald Bay or Cascade Lake that correlates with FLLS1.

The age model for FLLS2 in Fallen Leaf Lake constrains the age of the slide to 7.62–7.90 ka. In sediment cores, the distal component of FLLS2 is observed directly above the Tsoyowata Ash deposit; the ash bed provides a distinct marker bed to correlate with other subbasins. In Lake Tahoe, the age range for the synchronous deposit J is 7.19–7.89 ka (Smith et al., 2013). Deposit J also overlies the Tsoyowata Ash in cores from Lake Tahoe and is characterized by multiple debris flows originating along the southwestern basin and a single turbidite deposit that extends to the central and northern basin. Both FLLS2 and deposit J are characterized by large proximal slides relative to basin

Figure 15. Plot showing timing of direct (fault offset) and indirect (slide deposits) evidence for earthquakes in Lake Tahoe, Fallen Leaf Lake (FLL), Emerald Bay (EB), and Cascade Lake (CL). Where evidence is correlated across basins, the symbols are color coded by event age (see legend; MRE—most recent event; FLS—Fallen Leaf segment; RS—Rubicon segment). Black symbols represent evidence not correlated across multiple basins. The approximate ages for observed direct earthquake deformation on the Fallen Leaf Lake and Rubicon segments of the West Tahoe–Dollar Point fault are shaded in gray and marked with triangles. Proposed events based on synchronous slides across basins are also shaded in gray. All Lake Tahoe slides are modeled event dates (name convention is from Smith et al., 2013). The two youngest Fallen Leaf Lake slides are modeled event dates. The age range of the two oldest slides was calculated by extrapolating the age model for core BC1A. Two models of Emerald Bay event age ranges are shown. The solid symbols represent ages based on stratigraphic interpretation where EBS1 is synchronous with the FLLS2 and assigned the same age range of 7.62–7.90 ka. The EBS2 age is calculated based on a sedimentation rate of 1.24 mm/yr below EBS1. The dashed symbols were determined based on calculated sedimentation rates from core EB2 (see text). Cascade Lake event ages were determined based on acoustic character correlation with Emerald Bay and Fallen Leaf Lake.

Geosphere, published online on 26 June 2013 as doi:10.1130/GES00877.1

size and turbidite deposits that extend laterally in each basin.

Based on a comparison of the stratigraphy between Fallen Leaf Lake, Lake Tahoe, Emerald Bay, and Cascade Lake, it is possible that slides observed in Emerald Bay or Cascade Lake are synchronous with FLLS2 and deposit J. The stratigraphic horizon representing slide EBS1 appears to mark a transition in acoustic character. Below the slide, we observe alternating semitransparent layers and high-amplitude reflectors. Above the slide we observe a more transparent unit with low-amplitude reflectors and a few high-amplitude reflectors (Fig. 10). In Lake Tahoe, Chirp data interpreted by Smith et al. (2013) illustrates that deposit J (7.19–7.89 ka) marks this same acoustic transition. In Fallen Leaf Lake, the transition to acoustically transparent units is less clear; we observe several high-amplitude reflectors even in the youngest units. In the northern part of the basin, where the sedimentary section is more condensed, the transition to transparent units is more apparent. In the northern basin, unit C of section I has several closely spaced, medium- to high-amplitude reflectors, while units A and B above have fewer, and lower amplitude, reflectors. This difference between unit C and units A and B is also observed where the basement slopes up to the north near the mid-lake moraine complex (Fig. 6). In this area, unit C more closely resembles section II below than units A and B above. The upper contact of unit C is the FLLS2 distal deposit. Based on the similar transitions in acoustic character in Emerald Bay, Fallen Leaf Lake, and Lake Tahoe, slide EBS1 appears to be correlated with FLLS2 in Fallen Leaf Lake and deposit J in Lake Tahoe. This is a reasonable assumption given the estimated age of ca. 8.6–9.3 ka calculated from core EB2. A slightly greater increase in sedimentation rate than predicted would shift the age of the slide toward the younger age of FLLS2.

Following this stratigraphic interpretation in Cascade Lake, we interpret the youngest, strong reflector that can be traced basin wide as the Tsoyowata Ash horizon (dashed horizon in Fig. 8). This reflector is actually resolved as two closely spaced high-amplitude reflectors in some parts of the basin. This is consistent with the Tsoyowata Ash horizon in Fallen Leaf Lake Chirp data. In Fallen Leaf Lake, two closely spaced high-amplitude reflectors may define the ash layer, with a lower amplitude reflector above marking the top of the FLLS2 turbidite. Several closely spaced, high-amplitude reflectors characterize the unit below this Tsoyowata Ash horizon in Cascade Lake, similar to the Emerald Bay stratigraphy. Using this correlation, slide CLS1 is younger than the FLLS2, and CLS3 is older than FLLS2. Nevertheless, we cannot rule out the presence of a slide associated with the Tsoyowata Ash horizon. There is some evidence that the youngest slide may obscure an older slide (CLS2?) below (Fig. 8). This interpretation of the Tsoyowata Ash horizon results in a sedimentation rate of ~0.39 mm/yr for sediments above the horizon in the deep southern basin. This would generate an age estimate for the younger slide of ca. 5.2 ka. This age is close to the age range of deposit G in Lake Tahoe (5.3–5.6 ka), which was associated with the age of a drowned tree near Baldwin Beach in Lake Tahoe and the MRE on the Rubicon segment of the WTDPF (Smith et al., 2013).

The FLLS3 and FLLS4 slide age ranges are ca. 11.24–11.64 ka and ca. 13.2–16.3 ka, respectively. FLLS3 is synchronous with deposit O in Lake Tahoe, which was dated as 11.1–12.49 ka (Smith et al., 2013). In addition, both event deposits mark the transition between bluish glacial silt and organic laminae below to olive lacustrine silt and clay above. The turbidite component of deposit O was mapped throughout Lake Tahoe above a major liquefaction feature, and the associated debris flow was mapped in the south-central part of the basin (Smith et al., 2013). The older FLLS4 deposit is observed within Fallen Leaf Lake glacial sediments of section II. Although slide deposits older than deposit O were identified in Lake Tahoe, dates were not determined for these slides and it is therefore difficult to correlate FLLS4 to a slide in Lake Tahoe.

We can also estimate the ages of the older slides in Emerald Bay and Cascade Lake based on calculated sedimentation rates and stratigraphic correlations. In Emerald Bay, the previously estimated age of EBS2 is ca. 11.2–11.9 ka, which correlates with FLLS3 and deposit O in Lake Tahoe. The stratigraphy also suggests that this horizon may mark a transition from glacial sediments below to lacustrine sediments above, providing further evidence that the slide is synchronous with FLLS3 and deposit O. If the younger slide is ca. 8 ka and the older slide is ca. 11.5 ka in Emerald Bay, this yields a sedimentation rate between the two slides of ~0.95 mm/yr. This rate is slightly lower than rates determined for younger sediments in Emerald Bay, and is not consistent with the increase in sedimentation rate calculated downcore in EB2. This suggests that either our assumption of increasing sedimentation rates is incorrect, or our stratigraphic correlation is incorrect. An alternative interpretation would be that the transition to glacial sediments is deeper than EBS2, which would make EBS2 younger than FLLS3 and deposit O (solid circles and lines in Fig. 15). It is also plausible that EBS2 represents the transition from glacial sediments; this would indicate that the age of EBS1 is slightly older than FLLS2 and deposit J (hollow circles and dashed lines in Fig. 15). Longer piston cores and more detailed radiocarbon dating are necessary to constrain further the ages of Emerald Bay slide deposits.

CLS3 appears to be synchronous with a transition in seismic stratigraphy. Deposits above the slide horizon appear to drape high onto basin walls, whereas sediments below the horizon are observed only in topographic lows with slight onlap onto basin highs. We interpreted this change to represent the transition from glacially derived sediment input to more pelagic lacustrine sedimentation. A similar shift is observed in Fallen Leaf Lake stratigraphy associated with the top of section II and FLLS3. Assuming that our pick for the Tsoyowata Ash horizon in Cascade Lake is correct and CLS3 is synchronous with FLLS3, we calculate a sedimentation rate between the Tsoyowata Ash horizon and CLS3 of 0.44–0.48 mm/yr. This range is reasonable given the sedimentation rate of ~0.39 mm/yr previously calculated for sediments younger than the Tsoyowata Ash horizon.

Triggering of Slide Deposits

There are several possible triggering mechanisms for the Tahoe Basin slide deposits, including lake-level fluctuations, storms, and earthquakes. There is evidence that Fallen Leaf Lake has undergone significant droughts and major changes in lake level during the mid- to late Holocene; these droughts may have occurred every 650–1150 yr (Kleppe et al., 2011). Submerged paleoshorelines and upright and rooted trees observed below the lake surface suggest that lake level may have dropped 40–60 m below present elevation during the late Holocene (Kleppe et al., 2011). The region has also undergone longer term climatic variability throughout the Holocene (Benson et al., 2002), which may have affected Fallen Leaf Lake sedimentation patterns and induced lake-level fluctuations. Significant drops in lake level may trigger landslides by exposing upper slope deposits to wave action and shifting the location of water and sediment input. Although lake level has fluctuated greatly in Fallen Leaf Lake, we do not think that FLLS1 and FLLS2 were triggered by this mechanism. The submerged trees in Fallen Leaf Lake are dated as ca. A.D. 1250 (Kleppe et al., 2011), but we do not observe major slide events of this age in Fallen Leaf Lake. In addition, lake-level fluctuations likely have occurred with a much shorter recurrence interval than the recurrence interval observed for slides in Fallen Leaf Lake; this evidence, together with coincident

Geosphere, published online on 26 June 2013 as doi:10.1130/GES00877.1

slides in Lake Tahoe, suggests a regional trigger for the slides observed in the lake.

Storms are another possible triggering mechanism for slides in Fallen Leaf Lake. Storms may be associated with flooding and increased sediment input to the lake as well as wave erosion and loading in shallow water. Flooding associated with storms may cause hyperpycnal flows, rapid accumulation, oversteepening, and pore pressure loading near stream mouths, all of which may lead to failures. Furthermore, waves associated with storms may erode nearshore sediment and generate hyperpycnal flows, or may increase pore pressure and weaken slopes due to loading. As with lake-level fluctuations, we anticipate the recurrence interval of major storms to be much shorter than the interval determined for Fallen Leaf Lake slide deposits.

Seismic triggering is also a possible cause of the slides observed beneath Fallen Leaf Lake. Earthquakes may trigger slides by strong shaking, increased pore pressure due to ground motion, gas escape, and downdrop of the hanging wall that influences slope stability and lake level. The Fallen Leaf Lake segment of the WTDPF is directly identified beneath Fallen Leaf Lake and Cascade Lake and presumably extends (and dies) into southern Emerald Bay, as evidenced by localized diverging beds. The source area for FLLS1, FLLS2, and FLLS4 appears to be the steep WTDPF scarp that forms the southern basin wall. The correlation of direct evidence (offset of the MRE horizon) and indirect evidence (FLLS1 deposit) makes a convincing case for earthquake-triggered slides in Fallen Leaf Lake; we extend this logic to the FLLS2. The morphology, source area, and extent of FLLS2 are very similar to FLLS1. Furthermore, FLLS2 is correlated to a significant slide in Lake Tahoe and possibly Emerald Bay and Cascade Lake. Although we lack direct evidence of offset associated with FLLS2, the Tsoyowata Ash horizon appears to diverge slightly toward the southernmost splay of the WTDPF. This splay is at the base of the steeply sloping basin wall, and acoustic artifacts obscure direct imaging of offset horizons. In Emerald Bay, the WTDPF is not imaged due to gas wipeout, but the potentially synchronous slide in Emerald Bay appears to correlate with horizons diverging toward the WTDPF (Fig. 11).

In summary, we infer that FLLS1 and FLLS2 were triggered by an earthquake in the Lake Tahoe Basin for the following reasons. (1) The slides appear to be sourced from the steep slope above the trace of the WTDPF. (2) The observed slide recurrence interval of ~3–4 k.y. is much longer than expected for storm or lake-level fluctuation triggers. (3) The coincident timing of deposits between basins suggests triggering by a regional, rather than local, event. (4) We observe both direct and indirect earthquake evidence for the MREs on the Fallen Leaf (FLLS1) and Rubicon segments (CLS1) of the WTDPF.

Although the evidence is indirect for FLLS3, we postulate that this slide was also triggered by an earthquake. FLLS3 appears to be synchronous with deposit O in Lake Tahoe and possibly with CLS3 and EBS2 (Table 2; Fig. 15). FLLS3 is smaller than the FLLS1 and FLLS2, but this may reflect the short time period after FLLS4, which could have reset slope stability around the lake. In addition, the slide occurred near the transition from glacial sediments to lacustrine sediments, so we cannot rule out triggering by flooding. FLLS4 is intercalated within glacial sediments and does not appear to be correlated to slides in other subbasins.

We also observe slide CLS1 and deformation along the WTDPF estimated to be ca. 5.2 ka in Cascade Lake. This age estimate is speculative, and therefore it is difficult to confirm temporal correlation between this event and the other basins. However, the MRE on the Rubicon segment of the WTDPF and a slide deposit were dated (Smith et al., 2013) as ca. 5.3–5.6 ka.

These slides could have been triggered by a number of faults in the area, but based on our observations, we believe that the WTDPF is the most likely source. Regionally, the Genoa fault may produce strong shaking in the Lake Tahoe Basin. However, the two most recent events (500–600 yr ago and 2.0–2.2 ka; Ramelli et al., 1999) on the Genoa fault are not associated with major slide events we observed in Fallen Leaf Lake, Emerald Bay, or Cascade Lake. The MRE on the Incline Village fault (500 yr ago; Seitz et al., 2005) also does not appear to have triggered slides in these southern subbasins. The WTDPF is the largest fault in the Lake Tahoe Basin and trends through each of the southern subbasins; therefore, an event on the WTDPF has greater potential to trigger slides than the more distant faults. Furthermore, FLLS1 appears to be synchronous with the MRE on the Fallen Leaf Lake segment of the WTDPF, and CLS1 appears to be synchronous with the MRE on the Rubicon segment of the WTDPF, providing evidence that events on the WTDPF have triggered slides.

Paleoseismic Implications

The slide deposits observed in the subbasins of the Lake Tahoe Basin provide indirect evidence for seismic events as old as ca. 11.5 ka and can be used to calculate a recurrence interval for basin-wide shaking events. The interval between the FLLS1 and FLLS2 event is ~3.1 k.y. and the interval between the FLLS3 event and the FLLS4 event is ~3.7 k.y. Therefore, we calculate a closed recurrence interval for the two slide events in Fallen Leaf Lake of ~3.4 k.y.; if the most recent open interval is included, then a recurrence time of 3.8 k.y. is calculated along the Fallen Leaf segment of the WTDPF. Given that these three slides were likely triggered by earthquakes, one might be tempted to include the ca. 5.3 ka Rubicon event, which reduces the recurrence interval to ~2.9 k.y for events on the WTDPF, regardless of whether the event was confined to one segment or ruptured across several. In either case, the MRE occurred ca. 4.5 ka, exceeding the calculated recurrence time. In addition to the direct hazard posed by an earthquake in the Lake Tahoe Basin, seismically triggered slides also pose a threat due to the potential to generate tsunamis (Driscoll et al., 2000).

The slide deposits and observed primary deformation also may help constrain rupture patterns in the Lake Tahoe Basin. We observe direct and/or indirect evidence for four potential seismic events in sediments beneath Fallen Leaf Lake, Cascade Lake, Emerald Bay, and Lake Tahoe (Figs. 15 and 16). The MRE on the Fallen Leaf Lake segment of the WTDPF is dated as 4.57–4.85 ka based on the age of coseismic slide deposits (FLLS1). We suggest that deposit F in northern Lake Tahoe, with a modeled age of 4.07–4.51 ka (Smith et al., 2013), was deposited during the same seismic event, which constrains the event age to be ca. 4.5 ka. In Cascade Lake we observe indirect, and potentially direct, evidence of a ca. 5.2 ka event, which may correlate to direct evidence of the MRE on the WTDPF Rubicon segment and associated slide deposit G in Lake Tahoe, dated as ca. 5.3–5.6 ka (Smith et al., 2013). We observe multiple lines of evidence for an event on the WTDPF ca. 8 ka in Lake Tahoe (Smith et al., 2013), Fallen Leaf Lake, and possibly Emerald Bay and Cascade Lake. We observe only secondary evidence for an event ca. 11.5 ka; this event is represented by slides in Lake Tahoe (Smith et al., 2013) and Fallen Leaf Lake, and possibly Emerald Bay and Cascade Lake.

The geographic distribution of slides illustrated in Figure 16 may suggest that the entire basin underwent shaking ca. 11.5 ka and ca. 8 ka, which might be due to a full rupture along all three segments of the WTDPF. The younger events, however, may reflect segmented rupture. The ca. 5.3–5.6 ka event on the Rubicon segment may have only ruptured the northern and central segments of the WTDPF, whereas a ca. 4.57–4.85 ka event may have ruptured only the Fallen Leaf Lake segment of the WTDPF. Nevertheless, the alternative also needs to be considered; that is, rupture of even one segment of the WTDPF might generate

Geosphere, published online on 26 June 2013 as doi:10.1130/GES00877.1

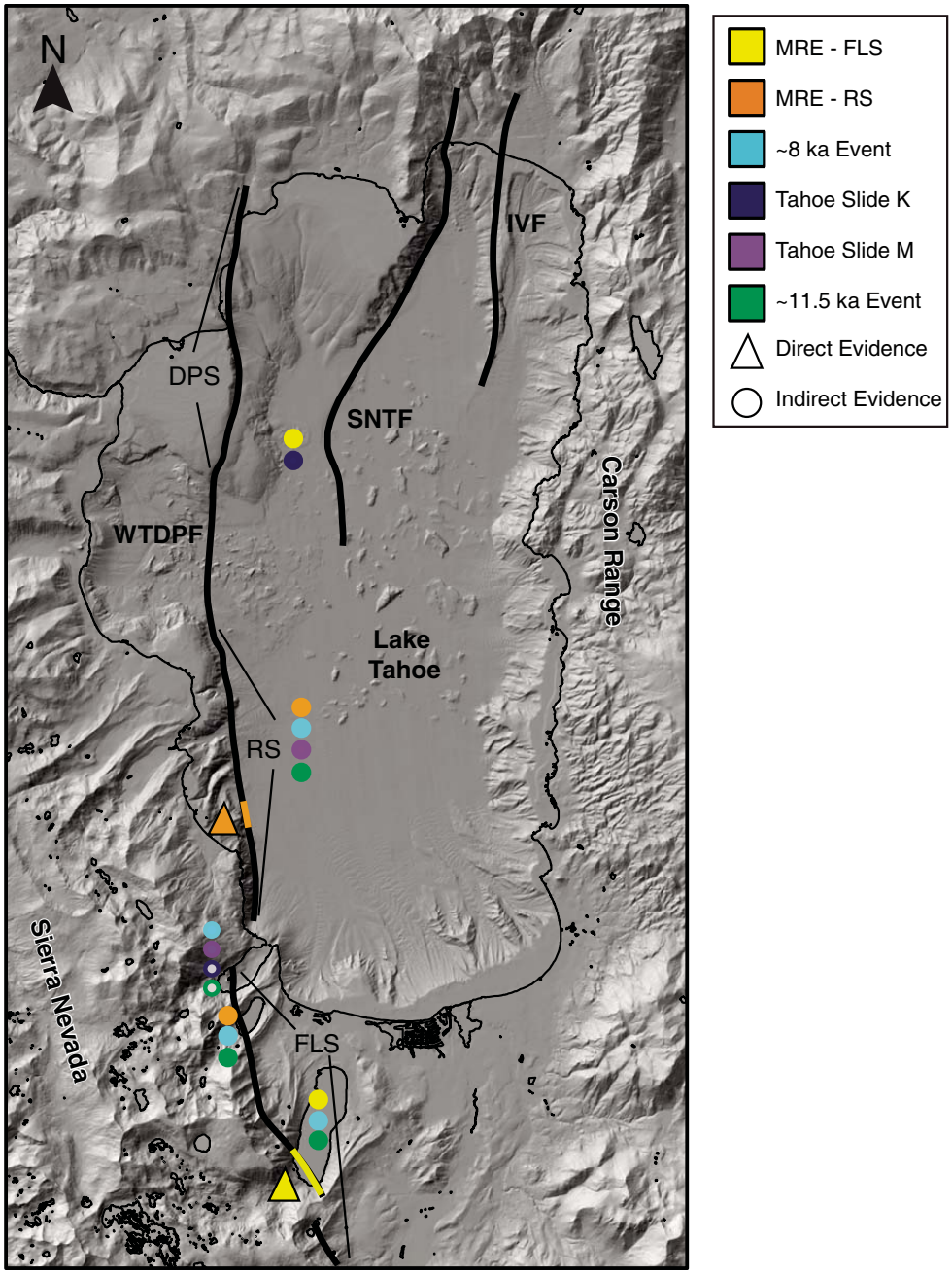

Figure 16. Map of the Lake Tahoe Basin showing direct and indirect evidence of seismic events in the four sub-basins (Lake Tahoe, Fallen Leaf Lake, Emerald Bay, and Cascade Lake). Circles represent slide deposits, colored by their approximate ages. The trace of the West Tahoe–Dollar Point fault (WTDPF) is colored by event age (see legend) and marked with a triangle where direct evidence of faulting is observed. MRE—most recent event; DPS—Dollar Point segment; IVF—Incline Village fault; SNTF—Stateline–North Tahoe fault; FLS—Fallen Leaf segment; RS—Rubicon segment.

Geosphere, published online on 26 June 2013 as doi:10.1130/GES00877.1

sufficient ground motion to trigger failures basin wide. For example, the MRE on the Fallen Leaf Lake segment of the WTDPF might have triggered a slide as far away as the northern part of Lake Tahoe. Additional work is warranted to understand how the segments of the WTDPF accommodate deformation, whether they rupture in concert or alone.

Recent studies of Lidar data and offset moraines suggest that the Fallen Leaf Lake segment of the WTDPF identified in Chirp and Lidar data is equivalent to the Mount Tallac segment of the purported Tahoe-Sierra frontal fault zone (Howle et al., 2012). Difficulties arise with this interpretation, based on both fault architecture and recurrence interval. Our preferred option is that this fault is the southernmost segment of the WTDPF system and the determined fault recurrence interval reported here is more consistent with lower vertical slip rates reported for the WTDPF (0.4–0.8 mm/yr) than the twofold to threefold increase in slip rate reported for the Tahoe-Sierra frontal fault zone (1.1–1.9 mm/yr; Howle et al., 2012). We have mapped the Fallen Leaf Lake segment of the WTDPF in Chirp and Lidar extending from southern Fallen Leaf Lake to Cascade Lake. Diverging beds in Emerald Bay also suggest that this segment may continue and die into Emerald Bay in a number of splays (e.g., Fig. 9). The Rubicon segment of the WTDPF is mapped along the steep western slope from just north of Emerald Bay to McKinney Bay (Fig. 1). The ~2 km step between the Fallen Leaf Lake segment and Rubicon segment is well within the range documented by previous studies (3–4 km; Wesnousky, 2006) for rupture propagation across a stepover.

CONCLUSIONS

Coincident slides in Fallen Leaf Lake, Lake Tahoe, and perhaps Cascade Lake and Emerald Bay support earthquake shaking as the most plausible triggering mechanism. The geographic distribution of the slide events and direct offset evidence further suggests that the segments of the WTDPF may sometimes rupture in concert and other times individually. The recurrence time for events on the Fallen Leaf segment of the WTDPF is ~3–4 k.y., and the time since the MRE (ca. 4.5 ka) exceeds the calculated recurrence time.

Much of our understanding of segment interactions is based on surficial measurements (i.e., Lidar and trenching). The data presented here provide information about earthquake recurrence and how segments interact through longer time intervals. Such data sets combined with surficial measurements will provide an improved understanding of what controls whether ruptures propagate from one segment to another.

ACKNOWLEDGMENTS

This research was supported by National Science Foundation grants OCE-0649410 and EAR-127499, U.S. Geological Survey National Earthquake Hazards Reduction Program grants 10HQPA1000, 06HQGR0064, and 02HQGR0072, and an ExxonMobil student grant. This manuscript was greatly enhanced through thoughtful reviews from Cathy Busby, Paul Umhoefer, Mike Oskin, and Rich Briggs. Radiocarbon ages for the 2010 Fallen Leaf Lake cores were funded by Lawrence Livermore National Laboratory Laboratory Directed Research and Development grant 09-ERI-003. We thank Brig Ebright for his permission to allow us to conduct research on Cascade Lake and Paul Baker for access to a boat ramp on his property. We are indebted to Fire Chief Gary Gerren for access to the Fallen Leaf Lake boat ramp and invasive species boat wash. Generous support from Bill Craven and access to his boat allowed collection of the 2010 multibeam survey. We also thank Shane Romsos and the Tahoe Regional Planning Agency for access to the critical airborne Lidar (light detection and ranging) data collected in 2010. We thank Anders Noren and Kristina Brady from LacCore for adding Fallen Leaf Lake to their busy 2010 coring schedule and for helping us get a high-quality suite of piston cores. Initial core processing, logging, and sampling of the 2010 Fallen Leaf Lake cores were conducted at LacCore. We thank Laurel Stratton for her logistical role in initiating the 2010 coring program and for helping with initial core processing, and Danny Brothers for conversations regarding previously collected Chirp (compressed high intensity radar pulse) profiles and sediment cores.

REFERENCES CITED

Argus, D.F., and Gordon, R.G., 2001, Present tectonic motion across the Coast Ranges and San Andreas fault system in central California: Geological Society of America Bulletin, v. 113, p. 1580–1592, doi:10.1130/0016-7606(2001)113<1580:PTMATC>2.0.CO;2.

Bacon, C.R., 1983, Eruptive history of Mount Mazama and Crater Lake Caldera, Cascade Range, USA: Journal of Volcanology and Geothermal Research, v. 18, p. 57–115, doi:10.1016/0377-0273(83)90004-5.

Bennett, R.A., Wernicke, B.P., Niemi, N.A., Friedrich, A.M., and Davis, J.L., 2003, Contemporary strain rates in the northern Basin and Range Province from GPS data: Tectonics, v. 22, doi:10.1029/2001TC001355.

Benson, L., Kashgarian, M., Rye, R.O., Lund, S.P., Paillet, F.L., Smoot, J.P., Kester, C.L., Mensing, S., Meko, D., and Lindstrom, S., 2002, Holocene multidecadal and multicentennial droughts affecting northern California and Nevada: Quaternary Science Reviews, v. 21, p. 659–682, doi:10.1016/S0277-3791(01)00048-8.

Benson, L.V., May, H.M., Antweiler, R.C., Brinton, T.I., Kashgarian, M., Smoot, J.P., and Lund, S.P., 1998, Continuous lake-sediment records of glaciation in the Sierra Nevada between 52,600 and 12,500 radiocarbon yrs B.P: Quaternary Research, v. 50, p. 113–127, doi:10.1006/qres.1998.1993.

Bischoff, J.L., and Cummins, K., 2001, Wisconsin Glaciation of the Sierra Nevada (79,000–15,000 yr B.P.) as recorded by rock flour in sediments of Owens Lake, California: Quaternary Research, v. 55, p. 14–24, doi:10.1006/qres.2000.2183.

Bronk Ramsey, C., 2009, Bayesian analysis of radiocarbon dates: Radiocarbon, v. 51, p. 337–360.

Brothers, D.S., Kent, G.M., Driscoll, N.W., Smith, S.B., Karlin, R., Dingler, J.A., Harding, A.J., Seitz, G.G., and Babcock, J.M., 2009, New constraints on deformation, slip rate, and timing of the most recent earthquake on the West Tahoe–Dollar Point fault, Lake Tahoe Basin, California: Seismological Society of America Bulletin, v. 99, p. 499–519, doi:10.1785/0120080135.

Clark, D.H., and Gillespie, A.R., 1997, Timing and significance of late-glacial and Holocene cirque glaciation in the Sierra Nevada, California: Quaternary International, v. 38/39, p. 21–38, doi:10.1016/S1040-6182(96)00024-9.

Dingler, J., Kent, G., Driscoll, N., Babcock, J., Harding, A., Seitz, G., Karlin, B., and Goldman, C., 2009, A high-resolution seismic CHIRP investigation of active normal faulting across Lake Tahoe basin, California-Nevada: Geological Society of America Bulletin, v. 121, p. 1089–1107, doi:10.1130/B26244.1.

Dixon, T.H., Miller, M., Farina, F., Wang, H., and Johnson, D., 2000, Present-day motion of the Sierra Nevada block and some tectonic implications for the Basin and Range Province, North American Cordillera: Tectonics, v. 19, p. 1–24, doi:10.1029/1998TC001088.

Driscoll, N.W., Weissel, J.K., and Goff, J.A., 2000, Potential for large-scale submarine slope failure and tsunami generation along the U.S. mid-Atlantic coast: Geology, v. 28, p. 407–410, doi:10.1130/0091-7613(2000)28<407:PFLSSF>2.0.CO;2.

Faulds, J.E., Henry, C.D., and Hinz, N.H., 2005, Kinematics of the northern Walker Lane: An incipient transform fault along the Pacific–North American plate boundary: Geology, v. 33, p. 505–508, doi:10.1130/G21274.1.

Gardner, J.V., Mayer, L.A., and Hughs Clarke, J.E., 2000, Morphology and processes in Lake Tahoe (California-Nevada): Geological Society of America Bulletin, v. 112, p. 736–746, doi:10.1130/0016-7606(2000)112<736:MAPILT>2.0.CO;2.

Goldfinger, C., Morey, A.E., Nelson, C.H., Gutierrez-Pastor, J., Johnson, J.E., Karabanov, E., Chaytor, J., Eriksson, A., and Party, S.S., 2007, Rupture lengths and temporal history of significant earthquakes on the offshore and north coast segments of the northern San Andreas fault based on turbidite stratigraphy: Earth and Planetary Science Letters, v. 254, p. 9–27, doi:10.1016/j.epsl.2006.11.017.

Hammond, W.C., and Thatcher, W., 2004, Contemporary tectonic deformation of the Basin and Range Province, western United States; 10 years of observation with the Global Positioning System: Journal of Geophysical Research, v. 109, no. B8, doi:10.1029/2003JB002746.

Hampton, M.A., Lee, H.J., and Locat, J., 1996, Submarine landslides: Reviews of Geophysics, v. 34, p. 33–59, doi:10.1029/95RG03287.

Henkart, P., 2003, SIOSEIS software: La Jolla, California, Scripps Institution of Oceanography, http://sioseis.ucsd.edu.

Howle, J.F., Bawden, G.W., Schweickert, R.A., Finkel, R.C., Hunter, L.E., Rose, R.S., and von Twistern, B., 2012, Airborne LiDAR analysis and geochronology of faulted glacial moraines in the Tahoe-Sierra frontal fault zone reveal substantial seismic hazards in the Lake Tahoe region, California-Nevada, USA: Geological Society of America Bulletin, v. 124, p. 1087–1101, doi:10.1130/B30598.1.

Hyne, N.J., Chelminski, P., Court, J.E., Gorsline, D.S., and Goldman, C.R., 1972, Quaternary history of Lake Tahoe, California-Nevada: Geological Society of America Bulletin, v. 83, p. 1435–1448, doi:10.1130/0016-7606(1972)83[1435:QHOLTC]2.0.CO;2.

Karlin, R., Noble, P.J., Zimmerman, S.H., Stratton, L., Smith, S.B., Kent, G., Maloney, J., and Driscoll, N.W., 2011, BOLLY Project—Preliminary multi-proxy data from Holocene cores, Fallen Leaf Lake, Tahoe Basin, California, USA: Geological Society of America Abstracts with Programs, v. 43, no. 5, p. 468.

Karlin, R.E., Smith, S., Seitz, G.G., Kent, G.M., and Driscoll, N.W., 2005, Landslides, active faulting, and paleoseismicity in Lake Tahoe: Seismological Research Letters, v. 76, p. 250.

Kent, G.M., and 14 others, 2005, 60 k.y. record of extension across the western boundary of the Basin and Range province: Estimate of slip rates from offset shoreline terraces and a catastrophic slide beneath Lake Tahoe: Geology, v. 33, p. 365–368, doi:10.1130/G21230.1.

Geosphere, published online on 26 June 2013 as doi:10.1130/GES00877.1

Kleppe, J.A., Brothers, D.S., Kent, G.M., Biondi, F., Jensen, S., and Driscoll, N.W., 2011, Duration and severity of Medieval drought in the Lake Tahoe Basin: Quaternary Science Reviews, v. 30, p. 3269–3279, doi:10.1016/j.quascirev.2011.08.015.

Lee, H.J., Greene, H.G., Edwards, B.D., Fisher, M.A., and Normark, W.R., 2009, Submarine landslides of the Southern California Borderland, *in* Lee, H.J., and Normark, W.R., eds., Earth science in the urban ocean: The Southern California Continental Borderland: Geological Society of America Special Paper 454, p. 251–269, doi:10.1130/2009.2454(4.3).

Oldow, J.S., 2003, Active transtensional boundary zone between the western Great Basin and Sierra Nevada block, western U.S. Cordillera: Geology, v. 31, p. 1033–1036, doi:10.1130/G19838.1.

Phillips, F.M., Zreda, M.G., Benson, L.V., Plummer, M.A., Elmore, D., and Sharma, P., 1996, Chronology for fluctuations in late Pleistocene Sierra Nevada glaciers and lakes: Science, v. 274, no. 5288, p. 749–751, doi:10.1126/science.274.5288.749.

Ramelli, A.R., Bell, J.W., dePolo, C.M., and Yount, J.C., 1999, Large-magnitude late Holocene earthquakes on the Genoa fault, west-central Nevada and eastern California: Seismological Society of America Bulletin, v. 89, p. 1458–1472.

Reimer, P.J., and 28 others, 2004, IntCal04 terrestrial radiocarbon age calibration, 0–26 cal kyr BP: Radiocarbon, v. 46, p. 1029–1058.

Rood, D.H., Burbank, D.W., and Finkel, R.C., 2011, Chronology of glaciations in the Sierra Nevada, California, from ^{10}Be surface exposure dating: Quaternary Science Reviews, v. 30, p. 646–661, doi:10.1016/j.quascirev.2010.12.001.

Sarna-Wojcicki, A.M., Lajoie, K.R., Meyer, C.E., Adam, D.P., and Rieck, H.J., 1991, Tephrochronology correlation of upper Neogene sediments along the Pacific margin, conterminous United States, *in* Morrison, R.B., ed., Quaternary nonglacial geology: Conterminous United States: Boulder, Colorado, Geological Society of America, Geology of North America, v. K-2, p. 117–140.

Saucedo, G.J., Little, J.D., Watkins, S.E., Davis, J.R., Mascorro, M.T., Walker, V.D., and Ford, E.W., 2005, Geologic map of the Lake Tahoe Basin, California and Nevada: California Geological Survey Regional Geologic Map no. 4, scale 1:100,000.

Schnellmann, M., Anselmetti, F.S., Giardini, D., McKenzie, J.A., and Ward, S.N., 2002, Prehistoric earthquake history revealed by lacustrine slump deposits: Geology, v. 30, p. 1131–1134, doi:10.1130/0091-7613(2002)030<1131:PEHRBL>2.0.CO;2.

Schweickert, R.A., Lahren, M.M., Smith, K.D., Howle, J.F., and Ichinose, G.A., 2004, Transtensional deformation in the Lake Tahoe region, California and Nevada, USA: Tectonophysics, v. 392, p. 303–323, doi:10.1016/j.tecto.2004.04.019.

Seitz, G.G., Kent, G.M., Dingler, J.A., Karlin, B., and Turner, R., 2005, First paleoseismic results from the Lake Tahoe basin; evidence for three M 7 range earthquakes on the Incline Village fault: Seismological Research Letters, v. 76, p. 239–240.

Seitz, G., Kent, G., Smith, S., Dingler, J., Driscoll, N., Karlin, R., Babcock, J., and Harding, A., 2006, Multi-method paleoseismology; combining on and offshore data to build a basin wide record of earthquakes at Lake Tahoe: Seismological Research Letters, v. 77, p. 274.

Smith, S.B., Karlin, R.E., Kent, G., Seitz, G., and Driscoll, N.W., 2013, Holocene subaqueous paleoseismology of Lake Tahoe: Geological Society of America Bulletin, v. 125, p. 691–708, doi:10.1130/B30629.1.

Strasser, M., Anselmetti, F.S., Faeh, D., Giardini, D., and Schnellmann, M., 2006, Magnitudes and source areas of large prehistoric northern Alpine earthquakes revealed by slope failures in lakes: Geology, v. 34, p. 1005–1008, doi:10.1130/G22784A.1.

Stuiver, M., and Polach, H.A., 1977, Discussion; reporting of ^{14}C data: Radiocarbon, v. 19, p. 355–363.

Surpless, B.E., Stockli, D.F., Dumitru, T.A., and Miller, E.L., 2002, Two-phase westward encroachment of Basin and Range extension into the northern Sierra Nevada: Tectonics, v. 21, p. 2-1–2-10, doi:10.1029/2000TC001257.

Svarc, J.L., Savage, J.C., Prescott, W.H., and Ramelli, A.R., 2002, Strain accumulation and rotation in western Nevada, 1993–2000: Journal of Geophysical Research, v. 107, no. B5, p. ETG 2-1–ETG 2-11, doi:10.1029/2001JB000579.

Tahoe Regional Planning Agency, 2010, Lake Tahoe Basin LiDAR: http://dx.doi.org/10.5069/G9PN93H2 (October 2011).

Uchupi, E., and Ross, D.A., 2000, Early Holocene marine flooding of the Black Sea: Quaternary Research, v. 54, p. 68–71, doi:10.1006/qres.2000.2149.

Unruh, J., Humphrey, J., and Barron, A., 2003, Transtensional model for the Sierra Nevada frontal fault system, eastern California: Geology, v. 31, p. 327–330, doi:10.1130/0091-7613(2003)031<0327:TMFTSN>2.0.CO;2.

Upton, P., and Osterberg, E.C., 2007, Paleoseismicity and mass movements interpreted from seismic-reflection data, Lake Tekapo, South Canterbury, New Zealand: New Zealand Journal of Geology and Geophysics, v. 50, p. 343–356, doi:10.1080/00288300709509841.

U.S. Geological Survey, Coastal and Marine Geology (CMG), Chief Scientist James V. Gardner, 2001, Multibeam mapping of Lake Tahoe, California-Nevada from field activity: L-1–98-LT: http://tahoe.usgs.gov/bath_download.html (October 2011).

Wesnousky, S.G., 2006, Predicting the endpoints of earthquake ruptures: Nature, v. 444, p. 358–360, doi:10.1038/nature05275.

The text and figures from this chapter, in full, is a reprint of the material as it appears in: Maloney, J.M., Noble, P.J., Driscoll, N.W., Kent, G.M., Smith, S.B., Schmauder, G.C., Babcock, J.M., Baskin, R.L., Karlin, R., Kell, A.M., Seitz, G.G., Zimmerman, S., and Kleppe, J.A., 2013, Paleoseismic history of the Fallen Leaf Segment of the West-Tahoe Fault reconstructed from slide deposits in the Lake Tahoe Basin, California-Nevada: Geosphere, v. 9, p. 1065-1090. The dissertation author was the primary researcher and author, and the co-authors listed in this publication directed and supervised the research.

3

Segmentation and step-overs along strike slip fault systems in the inner California borderlands: Implications for fault architecture and basin formation

3.1 ABSTRACT

Reprocessed, industry multichannel seismic reflection and high resolution Chirp data were examined to characterize the geometry and recency of faulting in the inner California borderlands (ICB). Two end-member models have been proposed to explain the deformation observed in the ICB. One model invokes reactivation of detachment faults by the Oceanside Blind Thrust to explain the deformation and margin architecture (e.g., San Mateo/Carlsbad trends). In contrast, the other model explains the deformation by step-overs along the strike-slip fault systems. Several observations in both the southern and central portions of the ICB are more consistent with the step-over model than the regional blind thrust model. For example, regions in the ICB exhibit both tensional and compressional structures across the margin, which is more readily explained by the strike-slip model. Localized compression and extension occurs as predicted at fault bends and step-overs. Furthermore, strike slip fault systems that bound extensional regions exhibit localized normal deformation as they approach the releasing step-overs (i.e., San Diego Bay). In addition, onlapping turbidites reveal that the deformation becomes younger towards the east, an observation not consistent with a westward verging blind thrust fault system. Finally, rotational deformation previously attributed to a splay off the Oceanside Blind Thrust instead appears to be a southward transported gravitational slide deposit. In summary, the nested high-resolution Chirp and multichannel seismic data have provided new constraints on ICB tectonic deformation and margin architecture, and are best explained by step-overs on strike slip fault systems.

3.2 INTRODUCTION

Numerous onshore and offshore studies have vastly improved our understanding of the inner California borderlands (ICB) geology, fault geometry and character, and recency of faulting (Atwater, 1970; Bohannon and Geist, 1998; Crouch, 1979; Crouch

and Suppe, 1993; Darigo and Osborne, 1986; Hogarth et al., 2007; Jackson and Molnar, 1980; Kennedy and Clarke, 1999; Kennedy and Tan, 2005; Kennedy et al., 1975; Kennedy and Welday, 1980; Le Dantec et al., 2010; Legg, 1985; Legg and Kennedy, 1979; Lindvall and Rockwell, 1995; Luyendyk et al., 1991; Magistrale, 1993; Marshall, 1989; Nicholoson et al., 1994; Rivero and Shaw; 2000; 2011; Ryan et al., 2009; Treiman, 1993) (Fig. 1). Nevertheless, debate remains regarding the recent tectonic deformation (late Miocene to Present) of the borderlands; specifically, are active blind thrust systems responsible for the observed faulting and deformation, or are the borderlands predominantly a strike-slip region (Rivero & Shaw 2011; Ryan et al. 2012)?

Here we examine reprocessed, industry seismic reflection data and high resolution compressed high intensity radar pulse (Chirp) data to characterize better the geometry and recency of faulting in the ICB. We observe deformation in both the southern and central portions of the ICB that are more consistent with a predominantly strike-slip style of deformation with localized compression and extension at fault bends and steps. These fault discontinuities appear to control offshore deformation and coastal geomorphology, which has implications for both seismic hazard assessment and nearshore ecosystem resources. With the complex history of the ICB, which has undergone compression, extension, rotation, and translation, combining Chirp and MCS data allows us to observe the interplay between modern and antecedent topography and deformation.

3.3 GEOLOGIC SETTING

The ICB is a geomorphic region offshore southern California and northern Baja, which is characterized by a system of basins and ridges dissected by numerous dextral strike-slip faults (Fig. 1). The ICB has a complex geologic history and has been a major player in the evolution of the western margin of the North American plate (e.g. Bohannon and Geist, 1998; Crouch and Suppe, 1993; Legg, 1985; Nicholson et al.,

1994). As subduction of the Farallon plate beneath western North America waned, the region underwent complex block rotation, extension, and transcurrent faulting (Lonsdale, 1991). During this time (Oligocene to late Miocene?), the ICB experienced extensional deformation as a consequence of Pacific plate capture with its rapid northwest motion relative to the North American plate. This deformation formed a vast system of basins and ridges that still dominates the landscape today. During the late Miocene- early Pliocene, plate motion became more northerly (Atwater and Stock, 1998), the San Andreas transform system stepped landward into the Gulf of California-Salton Trough, and the deformation in the ICB decreased dramatically in magnitude and changed in style, becoming dominantly strike-slip.

At present, the active tectonic processes are controlled by a series of strike-slip fault systems. These include the Newport Inglewood-Rose Canyon (NI-RC) fault zone, Palos Verdes-Coronado Bank fault zone, Santa Cruz-Santa Catalina-San Pedro-San Diego Trough-Bahia Soledad fault zone, and the Santa Cruz-San Clemente-San Isidro fault zone (Fig. 1) (Legg and Kennedy, 1979; Grant and Rockwell, 2002; Grant and Shearer, 2004). Based on geodetic models, over 80 percent of the dextral motion between the Pacific and North American plates is accommodated by onshore faults (Becker et al., 2005; Bennett et al., 1996; Dixon et al., 2000; Meade and Hager, 2005) leaving between 10 and 20 percent (5-10 mm/yr) of the remaining slip budget to be distributed across active structures to the west and offshore. Such an estimate is consistent with long-term slip on the Agua Blanca Fault (5-6 mm/yr) determined from trench sites (Rockwell, 2010).

Recent studies purport that blind thrust faults in the ICB have re-activated extensional detachment surfaces (Rivero and Shaw, 2011; Rivero et al., 2000). The Oceanside Blind Thrust, Thirtymile Blind Thrust, and associated deformation, have been mapped with legacy industry seismic reflection profiles extending from Dana Point to the US-Mexico border (Fig. 2A) (Rivero and Shaw, 2011). The Thirtymile Blind Thrust has

been identified to explain the location of seismicity associated with the 1986 Oceanside earthquake, as well as a partial thrust component of the main shock (Rivero and Shaw, 2011). Conversely, Ryan et al. (2012) suggest that the 1986 earthquake was located in an area of compression associated with a restraining bend in the right-lateral, strike-slip San Diego Trough fault. Additionally, Ryan et al. (2009) put forth an alternative explanation for the observed compressional deformation associated with the Oceanside Blind thrust that involves a clockwise rotating block between the Coronado Bank fault zone and NI-RC fault zone. They observed areas of both extension and compression in seismic data from the ICB and therefore propose that deformation is explained better by rotation versus regional thrust systems.

The major fault zones in the ICB south of Dana Point are the Rose Canyon fault zone, Coronado Bank fault zone, San Diego Trough fault zone, and Descanso fault zone (Fig. 2A). The Rose Canyon fault zone steps onshore near downtown San Diego, continues north along the I-5 corridor, and steps offshore again north of Mount Soledad at the mouth of La Jolla Canyon (LeDantec et al., 2010). The fault zone continues north near the shelf edge and links with the Newport Inglewood fault to the north. The slip rate on the Rose Canyon fault zone is estimated to be ~1.5 mm/yr (Lindvall & Rockwell, 1995; Rockwell, 2010).

The Coronado Bank fault trends ~N30°W and has been mapped from offshore Baja California to the La Jolla Fan valley. The fault zone varies in width and number of splays along strike (Kennedy and Tan, 2005; Legg, 1985; Ryan et al., 2009). Researchers have documented extensional structures along the Coronado Bank fault zone in Loma Sea Valley including conjugate normal faults, “monoclinal downwarping,” and horst-graben structures, with some strands offsetting the seafloor (Legg, 1985; Ryan et al., 2009). Nicholson (1993) and Sorlien (1993) documented Miocene extension on the Coronado Bank fault as an east-dipping normal fault. Rivero et al. (2000) suggested that

the Coronado Bank fault was reactivated as the Oceanside Blind Thrust fault from Dana Point to the US-Mexico border. The Coronado Bank fault has previously been linked to the Palos Verdes fault zone to the north in slip models, but recent evidence suggests that it may not be a through-going fault zone (Ryan et al., 2012). Slip-rates on the Coronado Bank fault have not been directly measured.

The Descanso fault zone is mapped southwest of Point Loma, but the southern continuation is not well understood. The Descanso fault may be an eastern splay of the Coronado Bank fault diminishing near Point Loma as strain is transferred to the Rose Canyon fault, or may be a northern continuation of the Estero fault zone offshore Baja California (Legg, 1985). Several small magnitude (M<4) earthquakes between 1981 and 1997 were located between Coronado Bank and Point Loma, suggesting activity on either the Coronado Bank fault or Descanso fault (Astiz and Shearer, 2000).

Coastal San Diego topography is marked by prominent highs and lows associated with fault systems. Mount Soledad, at ~250 m elevation is a pop-up structure formed by a left bend in the Rose Canyon fault (Moore, 1972), while San Diego Bay is a pull-apart basin formed by a right step from offshore faults to the onshore Rose Canyon fault zone (Kennedy et al., 1979; Moore and Kennedy, 1975). Numerous faults accommodate subsidence in San Diego Bay and from west to east include the Spanish Bight fault, the Coronado fault, and the Silver Strand fault, which are herein referred to as a group – the San Diego Bay faults (Fig. 2A). At an elevation of ~120 m, the Point Loma peninsula is an anomalous topographic high bounded by lows to the north (Mission Bay) and the east (San Diego Bay). Outcrops of the Cretaceous Rosario group are exposed exclusively in coastal San Diego along the coast of Point Loma, the coast of Point La Jolla/Mount Soledad, and on the shelf between La Jolla Canyon and San Diego Bay (Kennedy and Tan, 2005). Despite the similar stratigraphy between Mount Soledad and Point Loma, uplift rates suggest that the topography is controlled by different mechanisms. Dating

of Point Loma marine terraces have yielded uplift rates of ~0.11-0.15 mm/yr, which is comparable to the regional uplift rate of 0.13-0.14 mm/yr, whereas uplift of Mt. Soledad is occurring at a faster rate of ~0.18-0.26 mm/yr (Kern and Rockwell, 1992; Ku and Kern, 1974; Muhs et al., 2002). The exposure of the Cretaceous Rosario group offshore provides habitat for extensive kelp forests at Point Loma and La Jolla, which require hard substrate to grow.

3.4 METHODS

Between 2006 and 2009, over 1000 km of seismic Chirp were acquired between the US-Mexico border and La Jolla Canyon, extending west to Thirtymile Bank (Fig. 2B). The data were acquired using SIO's Edgetech Chirp profiler. The Chirp profiler was operated with a 50 ms swept pulse of 0.7 – 3.0 kHz or 1-6 kHz depending on sediment character and water depth, and provided sub-meter vertical resolution and sub-bottom penetration up to ~50 m. Location accuracy is approximately 10 m. Chirp data were processed using sioseis (sioseis.ucsd.edu) (Henkart, 2003) and imported to Kingdom Suite (http://www.ihs.com) and QPS Fledermaus (http://www.qps.nl/display/fledermaus/main) software packages for interpretation. A nominal water and sediment velocity of 1500 m/s was assumed for all depth conversions in Chirp data.

For interpretation of deeper structure, this study examined legacy multichannel seismic (MCS) profiles from WesternGeco geophysical surveys (Lines from WSD-81; (U.S.G.S), 2006). This data was downloaded on June 12, 2008 in SEG-Y format. Additionally, we present reprocessed 1979 Chevron MCS data (H-17-79 and H-18-79). Reprocessing was conducted in cooperation with Geotrace and has resulted in attenuated multiples, increased vertical resolution, and increased continuity and horizontal resolution.

3.5 RESULTS

3.5.1 Southern ICB - US-Mexico border to La Jolla Canyon

Offshore San Diego Bay, the Coronado Bank fault appears to be a major east-dipping fault that bounds the eastern side of Coronado Bank (Fig. 3). Multiple synthetic and antithetic splays deform acoustic packages in the Loma Sea Valley, forming a broad zone of faulting above the main strand. We observe ~1 second two-way travel time (TWTT) dip-slip offset of deep horizons on the main strand of the Coronado Bank fault imaged in Figure 3. Deformation decreases up-section, but near-seafloor horizons do appear vertically offset. Rollover of the hanging wall into the Coronado Bank fault at this location results in a horst and graben structure in basement rocks south of Point Loma, located along the Descanso fault zone. This style of deformation is limited in extent and changes both to the north and south away from San Diego Bay (Fig. 4). To the south, strands of the Coronado Bank and Descanso fault zones slightly deform sub-horizontal reflectors that fill the Loma Sea Valley and the Descanso fault also slightly deforms the basement (Fig. 4C). Nevertheless, vertical deformation is much less than observed in Figure 4B. To the north of San Diego Bay, the synthetic and antithetic splays of the Coronado Bank fault result in a broad zone of deformation, with little vertical slip observed on the main strand, but increased deformation on the eastern Descanso fault zone (Fig. 4A).

Chirp data image several splays of the Coronado Bank fault and Descanso fault through the Loma Sea Valley (Fig. 5). The main strand of the Coronado Bank fault is not imaged due to acoustic attenuation within the Loma Sea Valley channel and diffraction off the steep Coronado Bank slope. The imaged splays show deformation including chevron folding and lateral variation in sediment thickness across the fault (Figs. 5B & 5C). The most recent offset of acoustic horizons observed on these splays is within ~2 m of the seafloor. Nevertheless, several Coronado Bank fault strands are buried

under chaotic and highly reflective layers that may obscure younger, offset horizons. Although Chirp data fails to image the main Coronado Bank fault strand, a Chirp line does image significant vertical displacement of reflectors within the Loma Sea Valley channel (Fig. 6). Reflectors are folded and dip to the west, toward the eastern edge of the Coronado Bank. Offset of the uppermost horizon in the folded package is ~27 m. The accommodation is filled with sub-horizontal beds that onlap the tilted strata. An acoustically transparent unit mantles both the tilted and sub-horizontal package (Fig. 6).

The Descanso fault zone is also imaged in high-resolution Chirp data. The Descanso fault could not be mapped in the southernmost Chirp lines due to chaotic reflectors and channels associated with the Tijuana River. To the north, offshore southern San Diego Bay, several fault strands are imaged just west of the rocky Cretaceous hardgrounds that extends south from Point Loma (Fig. 7). The Descanso fault zone here is almost 5 km wide with several strands that offset the transgressive surface. The maximum offset observed on the transgressive surface is ~3.8 m, and the shallowest offset occurs at ~46 m water depth. To the north approaching the tip of Point Loma, the Descanso fault zone decreases in width to ~1.4 km and is represented by strands that do not appear to offset the transgressive surface, but strata beneath the transgressive surface are folded and deformed. Fault strands in this segment of the Descanso fault zone offset and deform the Cretaceous Rosario group, as well as younger rocks that make up west dipping foreset beds and wedge deposits at the shelf edge (Figs. 5A & 7A). This deformation is observed to the north along the widest part of the shelf offshore Mission Bay (Fig. 2A).

The Cretaceous Rosario group rocks extend south from Point Loma where they outcrop as a bathymetric high on the seafloor. The outcrop narrows and plunges to the southeast until it becomes completely covered by younger sediments and can be no longer traced in the Chirp data (Fig. 7). When compared with MCS data (Fig. 8),

the Rosario group rocks mapped in Chirp data overlay structural highs in basement topography. In particular, the offshore extension of the Point Loma Rosario group plunges to the south and appears to overly the easternmost horst observed in MCS data in Figures 3 & 4B. A simple cross section across the outcropping Rosario Group in the horst block is shown in Figure 9. In the southern ICB, the interaction between the Coronado Bank fault zone, Descanso fault zone, and the San Diego Bay fault zone plays an important role in the deformation, specifically whether it has an extensional or compressional component.

3.5.2 Central ICB - La Jolla Canyon to Dana Point

Farther north in the central ICB, the Coronado Bank fault zone interacts with the San Mateo, San Onofre, and Carlsbad trends as well as the NI-RC fault zone. Here we present new reprocessed industry MCS data from north to south. The data reprocessing improved reflector coherence and continuity down to ~2.5 seconds TWTT as well as removing the multiple. Approximately 950 line-km of the 1979 Chevron seismic reflection data along twenty nine seismic lines were reprocessed and are shown in Figure 2B. The geometry from the 1979 Chevron Survey (H-18-79) was fully recovered from the archived field data. These legacy multichannel seismic (MCS) data were shot at ~33.5 m spacing to a 96- channel hydrophone streamer with ~33.5 m group spacing, providing a nominal fold of 48 traces per common-midpoint bin. The coarse receiver spacing limits some modern processing approaches for prestack migration, and demultiple approaches due to issues with spatial aliasing; however, the processing scheme employed greatly improved the surficial resolution and continuity of reflectors (upper 2.5 seconds TWTT).

MCS line 4516 is a dip line located off San Clemente (Fig. 2B). A high amplitude basal reflector with a low frequency acoustic character is observed and is interpreted to be acoustic basement (Fig. 10). The acoustic basement shoals from 2+ seconds TWTT in the east to the west where it outcrops/subcrops. Basement in this region of the ICB

is predominately composed of the Catalina Schist (Bohannon and Geist, 1998). The region where the Catalina Schist outcrops off Dana Point is referred to as Schist Ridge. The acoustic basement reflector is offset and fragmented by a series of high angle faults. Toward the center of the basin (near shot 350) the high angle faults are associated with a deformational ridge that offsets both the red and green horizon (e.g., positive flower structure). The onset of deformation in this region is difficult to identify with confidence based on stratal geometry and rotation; however, deformation and rotation of the stratal packages above the dashed red horizon are clearly observed (Fig. 10). The basin stratigraphy has a westward dip that diminishes up section. Toward the east, the San Mateo trend delineates a change in slope and appears to offset the sea floor. Furthermore, the faulted and offset acoustic basement can be observed to the east and appears offset by the San Mateo trend. There is much confusion in the literature regarding the San Mateo, San Onofre, and Carlsbad trends (e.g., Sorlien et al, 2006; Rivero and Shaw, 2011). We employ the following nomenclature based on the strike of the faults and the observed deformation and dip of the seafloor west of the trends. Where the faults are northwest trending and the stratigraphy and seafloor dip to the west, we refer to the structure as the San Mateo trend. The San Onofre trend is where the stratigraphy is flat-lying, but maintains a similar strike to the San Mateo trend. Finally, the Carlsbad trend is where the strike of the fault becomes more northerly the stratigraphy and seafloor remain relatively flat lying to slightly eastward dipping. An important demarcation exists between the San Mateo and San Onofre trends in that deformation appears more recent from the San Mateo trend to the north, while there is no recent deformation observed west of the San Onofre and Carlsbad trends. The different trends are associated with different deformation styles and the observations can be reproduced (Fig. 2A).

Continuing south, MCS line 4520 is roughly offshore the San Onofre Nuclear Generating Station (SONGS; Fig. 2B). The acoustic basement in this region exhibits

less relief than farther north and is best manifested in the seismic data west of the San Onofre trend. The sediment package below the red horizon and above acoustic basement is well laminated and roughly concordant (Fig. 11). Based on correlation with industry wells, these packages are middle Miocene to Pliocene deposits including from oldest to youngest, the San Onofre Breccia, Monterey Formation, San Mateo Formation, Capistrano Formation, Repetto Formation, and lower Pico Formation (Sorlien et al., 2006; Rivero and Shaw, 2011). A rotated block is imaged along the western portion of the profile above acoustic basement with well-imaged internal laminations (Fig. 11). Above the red and green horizons the sediment packages onlap structural highs, are rotated, and deformed; the packages have an overall westward dip. Continuing upsection, the orange horizon separates rotated and deformed sediment below from flat lying, undeformed sediment above. The orange horizon is most likely late Pliocene and separates lower Pico below from middle and upper Pico above (Sorlien et al., 2006). West of the San Onofre trend, the faults are moribund and do not offset the orange reflector. Moving east near the San Onofre trend, the reflectors are folded (anticline-syncline pair), faulted and uplifted. The amount of folding across the San Onofre trend appears slightly greater than that observed across the San Mateo trend in MCS line 4516 (Fig. 10). East of the San Onofre trend, there are a series of eastward dipping faults that may be splays of the NI-RC fault zone, which is observed along the eastern margin (Fig. 11).

Farther south, MCS Line 4522 similar to line 4520 reveals a systematic pattern of deformation that progressively gets younger toward the east (Fig. 12). Above the flat-lying acoustic basement, the rotated block with well-imaged acoustic laminations is onlapped by flat-lying sediments above the green horizon. Farther east, fault structures offset and deform the green and orange horizon. Nevertheless, faults west of the San Onofre trend are dormant as the orange horizon is onlapped by flat-lying reflectors that show no signs of deformation. The stratigraphic packages bounded by the red and

orange horizons appear flat-lying with no regional dip. Near the San Onofre trend, the deformation appears more distributed with less folding and uplift; horizons very close to the seafloor appear offset (Fig. 12). In this region, the dip of the NI-RC fault zone appears slightly steeper.

Farther south, offshore Carlsbad Canyon and south of Crespi Knoll, the Carlsbad trend is a narrow fault zone with a more northerly trend (Fig 2B). Seaward there are two additional faults (no-name faults) that exhibit a similar trend being roughly parallel to the Carlsbad trend (Fig. 2B). In MCS Line 4542, west of the Carlsbad trend, the stratigraphic packages bounded by the red and orange horizon dip to the east with the dip increasing down section (Fig. 13). The faults west of the Carlsbad trend and east of the Coronado Bank fault zone have a normal dip-slip component and do not offset the orange reflector (Fig. 13). Flat-lying reflectors above the orange horizon onlap onto the deformation associated with the Carlsbad trend and more importantly mantle the Carlsbad trend. The deformation associated with the Carlsbad trend has no bathymetric expression in this region (Fig. 13). A strand of the NI-RC fault zone is imaged farther up slope and dips to the west. The basement high toward the west in line 4542 aligns with Coronado Bank farther to the south and faulting in that area appears associated with the Coronado Bank fault zone (Figs. 2A and 2B).

MCS Line 4515 is a strike line that trends parallel the margin and crosses the western portion of MCS lines 4516, 4520, and 4522 (Fig. 2B). Toward the north, the acoustic basement has a diagnostic high amplitude reflector with a low-frequency acoustic character and outcrops/subcrops in the vicinity of Schist Ridge (Fig. 14). Moving south, the acoustic basement exhibits a pronounced change in slope (ramp) between the flat-lying basement to the north and the gently dipping regional basement to the south. There is approximately 2.5 seconds TWTT of relief on the acoustic basement with the greatest depths observed offshore La Jolla (Fig. 2B). The reflectors between the

acoustic basement and red horizon dip north with an increase in dip with depth. Adjacent to the basement, the reflectors exhibit a slight reversal of dip. In east-west profiles (e.g., 4520 & 4522) across this deformed structure, faulted strata within the block dip to the west (Figs. 11 and 12). Moving south along the acoustic basement interface (down section) there appears to be an increase in deformation and acoustic imaging becomes limited. Structures and deformed strata are observed in the overlying carapace that might be indicative of fluid expulsion (Fig. 14). The onlapping packages above the red and green horizon show evidence of minor deformation; with no deformation observed in the flat-lying packages above the orange reflector.

3.6 DISCUSSION

In both the southern and central areas of the ICB studied here, controversy remains regarding the origin of the observed late Pliocene to Present deformational features. In 2000, Rivero and Shaw proposed a new hypothesis that much of the margin deformation was caused by the reactivation of the extensional detachment by the Oceanside Blind Thrust and Thirtymile Blind Thrust. This new idea gained much traction in light of the recent Northridge earthquake. Conversely, other models propose that the deformation patterns are caused by compressional and extensional jogs in the dextral fault systems offshore, or by large block rotation (Ryan et al., 2012; 2009).

3.6.1 Southern ICB – US-Mexico border to La Jolla Canyon

In the southern region of this study, we observe variability in deformational patterns along strike of the major fault zones. As the Coronado Bank fault approaches the San Diego Bay pull-apart basin, we observe a localized increase in dip-slip displacement on the main fault strand with rollover and collapse of the hanging wall seaward of San Diego Bay. The observed dip-slip and hanging wall rollover of the Coronado Bank fault

are directly adjacent to the widest and apparently most active segment of the Descanso fault, as well as the deepest part of the San Diego Bay pull-apart basin as defined by gravity data (Marshall, 1989). The Descanso fault zone narrows and is represented by fewer splays to the north and south. The zone of distributed deformation may be the result of increased dip-slip on the Coronado Bank fault in this region, or may be related to the transfer of strain across the San Diego Bay pull-apart. These data illustrates how slip on major fault strands varies as they approach releasing steps similar to observations in the Salton Sea (Kell et al., in prep).

The localized dip-slip on the Coronado Bank fault has also influenced coastal geomorphology. We propose that the horst and graben structure formed by hanging wall rollover is responsible for the topographic high of Point Loma (Fig. 9). The easternmost horst visible in the MCS data underlies the southern extension of the Point Loma peninsula and is bounded by the Descanso fault to the west and San Diego Bay faults to the east. Subsidence and collapse along these fault zones appears to cause the relief observed across the horst block and associated topographic high of Point Loma. As such, Point Loma and the bathymetric shoal observed offshore are due to differential subsidence to the east and west as opposed to differential uplift. This result is consistent with the finding that uplift rates on Point Loma are not higher than regional rates (Kern and Rockwell, 1992; Muhs et al., 2002). Furthermore, the rough surface on the offshore Cretaceous Rosario group suggests the formation is more resistant than the surrounding rocks, which have been eroded by wave-base erosion during the sea-level transgression. Subsidence and collapse on either side of Point Loma combined with the resistant character of the exposed Cretaceous Rosario group creates the high-standing hardgrounds offshore that provide habitat for the largest kelp forest in California (Parnell, et al., 2006).

Chirp data through the Loma Sea Valley also image recent deformation on strands of the Coronado Bank fault. Deformation is consistent with strike-slip faulting including

chevron folding and lateral variation in sediment thickness across the fault. Significant vertical offset is only observed in a single Chirp profile where the slip is normal and likely late Pliocene in age. A thick package of flat-lying, onlapping strata indicate no recent vertical deformation along this part of the Coronado Bank fault. The Coronado Bank fault was mapped as a reactivated thrust and an extension of the Oceanside Blind Thrust all the way to the U.S.-Mexico border (Rivero and Shaw, 2000; 2011). Chirp and legacy MCS data from the southern ICB presented here image deformation more consistent with predominantly strike-slip faulting.

If the Coronado Bank fault underwent extension primarily during the Miocene as suggested by Sorlien et al. (1993) and Nicholson et al. (1993), the localized hanging wall deformation may have impacted the formation of San Diego Bay as plate motion became more oblique and faults were re-activated as strike-slip. The horst and graben deformation of the basement appears to form the western boundary of San Diego Bay basin. Furthermore, the localized near-surface dip-slip displacement observed in Chirp data along the Coronado Bank fault suggests that the interplay between the Coronado Bank fault and faults within the San Diego Bay pull-apart basin is ongoing. Figure 9 illustrates the relationship between the Coronado Bank fault, Descanso fault, and the San Diego Bay faults as well as their role in controlling coastal topography including Point Loma and San Diego Bay.

Numerous laboratory and numerical models describe the theoretical formation and evolution of pull-apart basins (e.g. Basile and Brun, 1998; Katzman et al., 1995; McClay and Dooley, 1995; Wu et al., 2009), but few field studies have examined the character of bounding faults as they approach releasing bends and step-overs. Offshore San Diego Bay we observe variability in the slip characteristics of major faults as they approach step-overs and influence surrounding geomorphology. Deformation on the Coronado Bank fault may be linked to the formation and ongoing subsidence of the San Diego Bay

pull-apart, but interplay with the Descanso fault, Rose Canyon fault and San Diego Bay faults at depth beneath San Diego Bay is not well understood.

3.6.2 Central ICB – La Jolla Canyon to Dana Point

Rivero and Shaw (2000; 2011) presented several lines of evidence to support their hypothesis regarding the Oceanside blind thrust. First and foremost, faults and folds in the overlying carapace did not offset the Oceanside blind thrust. The second is an outgrowth of the first, and states that the Oceanside blind thrust can be continuously mapped along the margin and is not fragmented by faults. Finally, their structural cross-sections balanced lending support to their interpretation, which suggested approximately 2 – 2.4 km of shortening. Age constraints on the timing of this deformation are poor; however, if the Oceanside blind thrust became active in the late Pliocene, then based on Rivero and Shaw's (2011) reconstructions the contraction rate is approximately 0.5 - 1.5 mm/yr with an attendant uplift rate of approximately 0.27 – 0.40 mm/yr.

The reprocessed MCS data improved reflector continuity and resolution that allowed a sequence stratigraphic process oriented approach to be employed (Christie-Blick and Driscoll, 1995), which places important constraints on the relative timing of deformation across and along the margin. We will first discuss the character of the acoustic basement, then focus on the deformation above the acoustic basement and finally on the timing of deformation across the margin.

In MCS Line 4516, the acoustic basement is fragmented and offset by numerous fault zones (Fig. 10). The positive flower structure observed in the basin is more consistent with steep vertical faults than a low-angle thrust. Along MCS line 4522 and 4520, the acoustic basement is flat lying with much rugosity. On all of the reprocessed lines, it is difficult to trace the Oceanside Blind Thrust landward beyond the San Mateo, San Onofre, and Carlsbad trends (Figs. 11, 12, and 13). One might argue that in the

other legacy MCS data or in depth sections, the Oceanside Blind Thrust appears more continuous and can be traced laterally farther to the east under the margin (e.g., Rivero and Shaw, 2011). The main problem with the legacy data is that during stacking, some refractions were misinterpreted as reflections and improperly stacked. This introduced artifacts into the processed data and the Oceanside Blind Thrust reflections observed in the legacy data could be artifacts. For clarity, we distinguish the detachment from the thrust in the following way: (1) the detachment surface accommodated the Miocene extension along the margin during the reorganization (Bohannon and Geist, 1998), and (2) the thrust is where the detachment has been reactivated in compression. Rivero and Shaw (2011) use these terms interchangeably (see their Fig.2). It is important to note that the detachment has a complicated geometry and may comprise both an east and west-dipping component (Bohannon and Geist, 1998). In our interpretation, the high amplitude reflectors with a low frequency acoustic character are more indicative of a basement surface than an active fault surface (Figs. 10 and 11).

The largest relief on the basement is toward the south, parallel the margin; acoustic basement is >2.5 seconds TWTT offshore La Jolla (Fig. 14). This deep basin corresponds to a gravity low (Smith and Sandwell, 1997). The basin is associated with un-named faults that have a more northerly trend than the other main fault zones and appear to be accommodating transtension across a releasing step between the Coronado Bank Fault and NI-RC fault. This step-over may also explain the dying away of the Coronado Bank Fault to the north. The deformed block above acoustic basement is observed in Figure 14 and the rotated strata and possible drag folding indicate transport towards the south-southwest, into the basin and gravity low. The basin most likely has a composite history recording both Miocene extensional deformation and late Pliocene to Present transtensional deformation. The onlapping strata indicate that rotation and deformation of the block have not occurred since the green horizon (Figs. 11, 12, and 14).

In summary the fragmentation, geometry, and north-south relief on the acoustic basement imaged in the reprocessed data are more consistent with a strike-slip model of the margin than a regional thrust system (Fig. 15). Our observations of the southwest transported deformed block and minimal deformation since the green horizon are also inconsistent with a large block rotation model as proposed by Ryan et al. (2009).

The western limit of the deformation and folding associated with the Oceanside Blind Thrust is termed the Oceanside Thrust breakaway zone (Fig.6 - Rivero & Shaw, 2011). Rivero and Shaw (2011) map the Oceanside Blind Thrust to depths of 5 to 6 km (Fig. 2 – Rivero and Shaw, 2011), which is roughly coincident or slightly inboard of the San Mateo trend and San Onofre trend and outboard of the Carlsbad trend (Fig. 2A) (Fig. 6 - Rivero and Shaw, 2011). The new reprocessed MCS data reveal that the deformation along the breakaway zone is moribund as it is onlapped by late Pliocene flat-lying strata (Fig. 11). Furthermore, deformation west of the San Mateo, San Onofre, and Carlsbad trends also is dormant since the orange horizon (Figs. 11, 12, and 13). Finally, onlapping turbidites reveal that the deformation becomes younger towards the east; an observation not consistent with a westward verging blind thrust fault system – such as the Oceanside Blind Thrust. In summary, the reprocessed MCS data have provided new constraints on ICB tectonic deformation and margin architecture, and are best explained by step-overs on strike slip fault systems.

We observe several changes in deformational patterns moving from north to south through the central borderlands region. West of the San Mateo, San Onofre, and Carlsbad trends, we observe a change from compressional deformation in the north to extensional deformation and divergence in the south (Figs. 10, 11, 12 and 13). In concert, the dip of the stratigraphic units bounded by the red and orange horizons changes dip from west dipping offshore the San Mateo trend, to flat-lying west of the San Onofre trend, to east dipping west of the southern Carlsbad trend. These observations of both transtension and

transpression are difficult to explain by a regional thrust system, such as that proposed by Rivero & Shaw (2000; 2011).

In both the southern and central ICB, the character of faulting varies along strike of major fault zones (Fig. 2A). Evidence from seismic data indicates that some of this variability is caused by transtensional and transpressional jogs along dextral fault systems. In the central ICB, the area defined in Figure 13 appears to be a zone of extension created by a right step from the Coronado Bank fault zone to the NI-RC fault zone. Meanwhile, variations in slip in the southern ICB appear related to the step between offshore faults and the onshore portion of the Rose Canyon fault across San Diego Bay. Both of these step-over zones are characterized by deep basins with associated gravity lows (Marshall, 1989). Given these new interpretations, a pattern emerges in the ICB in which faults trending to the northwest of the regional orientation appear transpressional whereas more northerly trending faults appear transtensional (e.g., un-named central ICB faults and San Diego Bay faults) (Fig. 15).

3.6.3 Recency of faulting

Constraints on the onset and rate of dip-slip deformation on the Coronado Bank fault remain speculative, but the extent of basement deformation in the hanging wall suggests a prolonged period of extension (Fig. 3B). The deformation on the Coronado Bank fault has previously been associated with Miocene extension across the ICB (Nicholson et al., 1993; Sorlien et al., 1993). Nevertheless, the youngest strata resolved in the MCS data appear vertically offset. New evidence from Chirp data within the northern Loma Sea Valley channel also may indicate younger extension along the Coronado Bank fault (Fig. 6). Although sediments in Loma Sea Valley have not been dated, the deformation is likely Pliocene in age or younger based on the depth of the deformation and regional tectonic history. Onlapping sediments above the tilted strata are undeformed,

indicating no deformation since the Pliocene. Additionally, splays of the Coronado Bank fault zone on the slopes of the Loma Sea Valley deform strata within ~2 m of the seafloor that is interpreted to be Pleistocene to Holocene aged sediment. Some slight vertical slip is observed, but deformational patterns indicate predominantly strike-slip displacement on these fault segments.

The most recent event on the Descanso fault zone (transgressive surface offset ~46 mbsf) was less than 9.5 ka using the sea level curve of Fairbanks (1989). We do not observe offset of the seafloor above the fault segments. Nevertheless, mobile Holocene sands overlie the transgressive surface, and currents at these depths would likely smooth any seafloor offset rapidly. The measured transgressive surface offsets (maximum ~3.8 m on Descanso fault) may represent more than one event. The Descanso fault north of the tip of Point Loma does not offset the transgressive surface in any Chirp profile. This suggests that the most recent event on these segments was prior to the Holocene sea-level transgression. Alternatively, these segments may be Holocene active, but small offsets due to strike-slip faulting may not be resolved in the Chirp data. Several recent small magnitude earthquakes were located near the segment of the Descanso fault zone along the shelf edge north of Point Loma (Astiz and Shearer, 2000). Evidence from Chirp data suggests that the Descanso fault is active in the Holocene, and multiple strands of the Coronado Bank fault also appear recently active. These faults should be considered in assessing seismic risk to the San Diego area.

3.7 CONCLUSIONS

New Chirp and reprocessed legacy MCS data place important constraints on the timing and architecture of the offshore deformation along the ICB. Any model of the offshore deformation needs to account for the following observations/results:

(1) Onlapping sequences reveal that the deformation becomes younger toward the

east.

(2) Transport of western rotated blocks observed on MCS lines 4520, 4522, and 4515 (Figs. 11, 12, and 13) is toward the south/southwest, not toward the west.

(3) The Oceanside thrust breakaway zone is moribund and is mantled by flat-lying, onlapping reflectors.

(4) Localized compression and extension occurs as predicted at fault bends and step-overs (i.e., un-named faults).

(5) Strike slip fault systems that bound extensional regions (i.e., San Diego Bay) exhibit localized normal deformation as they approach the releasing step-overs.

(6) The stratigraphic dip changes from a westward dip in the north (e.g., MCS line 4516, Fig. 10) to an eastward dip with divergent reflectors in the south (e.g., MCS line 4542, Fig. 13).

(7) Polarity flips along the NI-RC fault zone.

(8) The lack of deformation in the Late Pliocene/Pleistocene onlapping sequences (e.g., MCS lines 4520, 4522; Figs. 11 & 12) suggest deformation west of the San Mateo, San Onofre, and Carlsbad trends is old (Late Pliocene).

In summary, the timing and style of deformation observed in the ICB is better explained by strike slip fault discontinuities than by a regional thrust system or a large rotating block.

3.8 ACKNOWLEDGEMENTS

Funding for this research was provided by the National Science Foundation (OCE0649410) and Southern California Edison.

The text and figures from this chapter are being prepared for publication in: Maloney, J.M., N.W. Driscoll, G.M. Kent, D.S. Brothers, S. Duke and T. Freeman, In

Prep, Segmentation and step-overs along strike slip fault systems in the inner California borderlands: Implications for fault architecture and basin formation. The dissertation author was the primary researcher and author of the manuscript. The co-authors directed and supervised the research that forms the basis for this chapter.

3.9 REFERENCES

Anderson, J. G., Rockwell, T. K., and Agnew, D. C., 1989, Past and possible future earthquakes of significance to the San Diego Region: Earthquake Spectra, v. 5, no. 2, p. 299-335.

Astiz, L., and Shearer, P. M., 2000, Earthquake locations in the inner Continental Borderland, offshore southern California: Bulletin of the Seismological Society of America, v. 90, no. 2, p. 425-449.

Atwater, T., 1970, Implications of plate tectonics for the Cenozoic tectonic evolution of western North America: Geological Society of America Bulletin, v. 81, p. 3513-3536.

Atwater, T., and Stock, J., 1998, Pacific-North America plate tectonics of the Neogene southwestern United States: An update: International Geology Review, v. 40, no. 5, p. 375-402.

Basile, C., and Brun, J.P., 1998, Transtensional faulting patterns ranging from pull-apart basins to transform continental margins; an experimental investigation: Journal of Structural Geology, v. 21, no. 1, p. 23-37.

Becker, T. W., Hardebeck, J. L., and Anderson, G., 2005, Constraints on fault slip rates of the southern California plate boundary from GPS velocity and stress inversions: Geophysical Journal International, v. 160, no. 2, p. 634-650.

Bennett, R. A., Rodi, W., and Reilinger, R. E., 1996, Global positioning system constraints on fault slip rates in southern California and northern Baja, Mexico: Journal Of Geophysical Research, v. 101, no. B10, p. 21,943-921,960.

Boggs, S., Jr., 1995, Principles of Sedimentology and Stratigraphy, Englewood Cliffs, New Jersey, Prentice-Hall, Inc.

Bohannon, R. G., and Geist, E., 1998, Upper crustal structure and Neogene tectonic development of the California continental borderland: Geological Society of America Bulletin, v. 110, no. 6, p. 779-800.

Christie-Blick, N. and Driscoll, N.W., 1995, Sequence Stratigraphy, Annual Review of Earth and Planetary Science, v. 23, p. 451-478.

Crouch, J.K., 1979, Neogene tectonic evolution of the western Transverse Ranges and the California Continental Borderland: Geological Society of America Bulletin, v. 90, p. 338-345.

Crouch, J. K., and Suppe, J., 1993, Late Cenozoic tectonic evolution of the Los Angeles Basin and inner California borderland; a model for core complex-like crustal extension: Geological Society of America Bulletin, v. 105, no. 11, p. 1415-1434.

Darigo, N. J., and Osborne, R. H., 1986, Quaternary stratigraphy and sedimentation of the inner continental shelf, San Diego County, California: Memoir - Canadian Society of Petroleum Geologists, v. 11, p. 73-98.

Dayton, P. K., 1985, Ecology of kelp communities: Annual Review of Ecology and Systematics, v. 16, p. 215-245.

Dayton, P. K., Currie, V., Gerrodette, T., Keller, B. D., Rosenthal, R., and Ventresca, D., 1984, Patch dynamics and stability of some California kelp communities: Ecological Monographs, v. 54, no. 3, p. 253-289.

Devinny, J. S., and Volse, L. A., 1978, Effects of sediments on development of Macrocystis-pyrifera gametophytes: Marine Biology, v. 48, no. 4, p. 343-348.

Dixon, T., Farina, F., DeMets, C., Suarez-Vidal, F., Fletcher, J., Marquez-Azua, B., Miller, M., Sanchez, O., and Umhoefer, P. J., 2000, New kinematic models for Pacific-North America motion from 3 Ma to present; II, Evidence for a “Baja California shear zone”: Geophysical Research Letters, v. 27, no. 23, p. 3961-3964.

Estes, J. A., and Steinberg, P. D., 1988, Predation, herbivory, and kelp evolution: Paleobiology, v. 14, no. 1, p. 19-36.

Fairbanks, R. G., 1989, A 17,000-year glacio-eustatic sea level record; influence of

glacial melting rates on the Younger Dryas event and deep-ocean circulation: Nature, v. 342, no. 6250, p. 637-642.

Grant, L.B. and Rockwell, T.K., 2002, Northward-propagating earthquake sequence in coastal Southern California: Seismological Research Letters, v. 73, no. 2, p. 461-469.

Grant, L.B. and Shearer, P.M., 2004, Activity of the offshore Newport-Inglewood Rose Canyon fault zone, coastal southern California, from relocated microseismicity: Bulletin of the Seismological Society of America, v. 94, p. 747-752.

Hart, M. W., 1974, Radiocarbon ages of alluvium overlying La-Nacion fault, San-Diego, California: Geological Society Of America Bulletin, v. 85, no. 8, p. 1329-1332.

Henkart, P., 2003, SIOSEIS software. Scripps Institution of Oceanography, La Jolla, California. http://sioseis.ucsd.edu.

Hogarth, L. J., Babcock, J., Driscoll, N. W., Dantec, N. L., Haas, J. K., Inman, D. L., and Masters, P. M., 2007, Long-term tectonic control on Holocene shelf sedimentation offshore La Jolla, California: Geology, v. 35, no. 3, p. 275-278.

Jackson, J., and Molnar, P., 1990. Active faulting and block rotations in the western Transverse Ranges, California: Journal of Geophysical Research, v. 95, p. 22,073-22,0089.

Katzman, R., ten Brink, U. S., and Lin, J., 1995, Three-dimensional modeling of pull-apart basins; implications for the tectonics of the Dead Sea Basin: Journal of Geophysical Research, v. 100, no. B4, p. 6295-6312.

Kennedy, M. P., and Clarke, S. H., 1999, Analysis of late quaternary faulting in San Diego Bay and hazard to the Coronado Bridge: California Division of Mines and Geology Open-File Report, v. 97-10A.

Kennedy, M. P., Clarke, S. H., Greene, H. G., and Legg, M. R., 1979, Recency and character of faulting offshore from metropolitan San Diego, California: California Division of Mines and Geology, p. 37.

Kennedy, M. P., and Moore, G. W., 1971, Stratigraphic relations of upper Cretaceous and

Eocene formations, San Diego coastal area, California: The American Association of Petroleum Geologists Bulletin, v. 55, no. 5, p. 709-722.

Kennedy, M. P., and Tan, S. S., 2005, Geologic Map of the San Diego 30' x 60' Quadrangle, California. Regional Geologic Map Series 1:100,000 scale, Map No. 3: California Geological Survey, California Department of Conservation.

Kennedy, M. P., Tan, S. S., Chapman, R. H., and Chase, G. W., 1975, Character and recency of faulting, San Diego Metropolitan Area, California.

Kennedy, M. P., and Welday, E. E., 1980, Recency and character of faulting offshore metropolitan San Diego, California: California Division of Mines and Geology.

Kern, J. P., and Rockwell, T. K., 1992, Chronology and deformation of Quaternary marine shorelines, San Diego County, California: Annual Field Trip Guidebook. South Coast Geological Society, v. 20, p. 1-7.

Ku, T.-L., and Kern, J. P., 1974, Uranium-Series Age of the Upper Pleistocene Nestor Terrace, San Diego, California: Geological Society of America Bulletin, v. 85, no. 11, p. 1713-1716.

Le Dantec, N., Hogarth, L. J., Driscoll, N. W., Babcock, J. M., Barnhardt, W. A., and Schwab, W. C., 2010, Tectonic controls on nearshore sediment accumulation and submarine canyon morphology offshore La Jolla, Southern California: Marine Geology, v. 268, no. 1-4, p. 115-128.

Legg, M. R., 1985, Geologic structure and tectonics of the inner continental borderland offshore northern Baja California, Mexico: University of California Santa Barbara Ph.D. thesis.

Legg, M. R., and Kennedy, M. P., 1979, Faulting offshore San Diego and northern Baja California, in Abbott, P. L., and Elliott, W. J., eds., Earthquakes and other perils, San Diego region: San Diego, California, San Diego Association of Geologists, p. 29-46.

Lindvall, S. C., and Rockwell, T. K., 1995, Holocene activity of the Rose Canyon fault zone in San Diego, California: Journal of Geophysical Research, v. 100, no. B12, p. 24,121-124,132.

Lonsdale, P.F., 1991, Structural patterns of the Pacific floor offshore of peninsular California, in The Gulf and Peninsular Province of the Californias, AAPG Memoir, v. 47, p. 87-125.

Luyendyk, B.P., 1991, A model for the Neogene crustal rotation, transtension, and transpression in southern California, Geological Society of America Bulletin, v. 103, p. 1528-1536.

Magistrale, H., 1993, Seismicity of the Rose Canyon fault zone near San Diego, California: Bulletin of the Seismological Society of America, v. 83, no. 6, p. 1971-1978.

Marshall, M., 1989, Detailed gravity studies and the tectonics of the Rose Canyon--Point Loma--La Nacion Fault System, San Diego, California: Proceedings, Workshop on "The seismic risk in the San Diego region: Special focus on the Rose Canyon Fault system," June 29-30. Ed. Roquemore, G., p. 80-99.

McClay, K., and Dooley, T., 1995, Analogue models of pull-apart basins: Geology, v. 23, no. 8, p. 711-714.

Meade, B. J., and Hager, B. H., 2005, Block models of crustal motion in Southern California constrained by GPS measurements: Journal of Geophysical Research, v. 110, no. B03403.

Moore, G. W., 1972, Offshore extension of the Rose Canyon Fault, San Diego, California: U. S. Geological Survey Professional Paper, Report: P0800C, p. 113-116.

Moore, G. W., and Kennedy, M. P., 1975, Quaternary faults at San Diego Bay, California: Journal of Research of the U. S. Geological Survey, v. 3, no. 5, p. 589-595.

Muhs, D. R., Simmons, K. R., Kennedy, G. L., and Rockwell, T. K., 2002, The last interglacial period on the Pacific Coast of North America: Timing and paleoclimate: Geological Society of America Bulletin, v. 114, no. 5, p. 569-592.

Nicholson, C., Sorlien, C. C., Atwater, T., Crowell, J. C., and Luyendyk, B. P., 1994, Microplate capture, rotation of the western Transverse Ranges, and initiation of the San Andreas transform as a low-angle fault system: Geology, v. 22, no. 6, p.

491-495.

Nilson, T. H., and Abbott, P. L., 1979, Turbidite sedimentology of the upper Creatceous Point Loma and Cabrillo Formations, San Diego, California, in Abbott, P. L., ed., Geologic excursions in the Southern California area: San Diego, California, Department of Geological Sciences, San Diego State University, p. 139-166.

Parnell, P. E., Dayton, P. K., Lennert-Cody, C. E., Rasmussen, L. L., and Leichter, J. J., 2006, Marine reserve design: optimal size, habitats, species affinities, diversity, and ocean microclimate: Ecological Applications, v. 16, no. 3, p. 945-962.

Rivero, C., and Shaw, J. H., 2011, Active folding and blind thrust faulting induced by basin inversion processes, inner California borderlands, in Shaw, J. H., and Suppe, J., eds., Thrust fault related folding, Volume AAPG Memoir 94, p. 187-214.

Rivero, C., Shaw, J. H., and Mueller, K., 2000, Oceanside and Thirtymile Bank blind thrusts: Implications for earthquake hazards in coastal southern California: Geology, v. 28, no. 10, p. 891-894.

Rockwell, T., 2010, The Rose Canyon Fault Zone in San Diego, Fifth International Conference on Recent Advances in Geotechnical Earthquake Engineering and Soil Dynamics and Symposium in Honor of Professor I.M. Idriss: San Diego, California.

Ryan, H. F., Legg, M. R., Conrad, J. E., and Sliter, R. W., 2009, Recent faulting in the Gulf of Santa Catalina; San Diego to Dana Point: Special Paper - Geological Society of America, v. 454, p. 291-315.

Ryan, H.F., Conrad, J.E., Paull, C.K., and McGann, M., 2012, Slip Rate on the San Diego Trough fault zone, inner California borderland, and the 1986 Oceanside earthquake swarm revisited, Bulletin of the Seismological Society of America, v. 102, no. 6, p. 2300-2312, doi: 10.1785/0120110317.

Smith, W. H. F. and D. T. Sandwell, 1997, Global Seafloor Topography from Satellite Altimetry and Ship Depth Soundings, Science 277: 1956-1962, http://www.sciencemag.org/content/vol277/issue5334/.

Sorlien, C. C., Nicholson, C., Luyendyk, B. P., Legg, M. R., and Anonymous, 1993,

Miocene collapse of the California continental margin: Abstracts with Programs - Geological Society of America, v. 25, no. 6, p. 311.

Treiman, J. A., 1993, The Rose Canyon Fault Zone, Southern California, California Department of Conservation, Division of Mines and Geology.

United States Geological Survey (USGS), 2006, National Archive of Marine Seismic Surveys: West Coast Surveys, accessed September 2009 (http://walrus.wr.usgs.gov/NAMSS/west_coast_surveys.html).

Wakabayashi, J., Hengesh, J.V., and Sawyer, T.L., 2004, Four-dimensional transform fault processes: progressive evolution of step-overs and bends: Tectonophysics, v. 392, p. 279-301.

Walls, C., Rockwell, T. K., Mueller, K., Block, Y., Williams, S., Pfanner, J., Dolan, J. F., and Fang, P., 1998, Escape tectonics in the Los Angeles metropolitan region and implications for seismic risk: Nature, v. 394, no. 6691, p. 356-360.

Wiegand, J. W., 1970, Evidence of a San Diego Bay-Tijuana Fault: Bulletin of the Association of Engineering Geologists, v. 7, no. 2, p. 107-121.

Wu, J. E., McClay, K., Whitehouse, P., and Dooley, T., 2009, 4D analogue modelling of transtensional pull-apart basins: Marine and Petroleum Geology, v. 26, no. 8, p. 1608-1623.

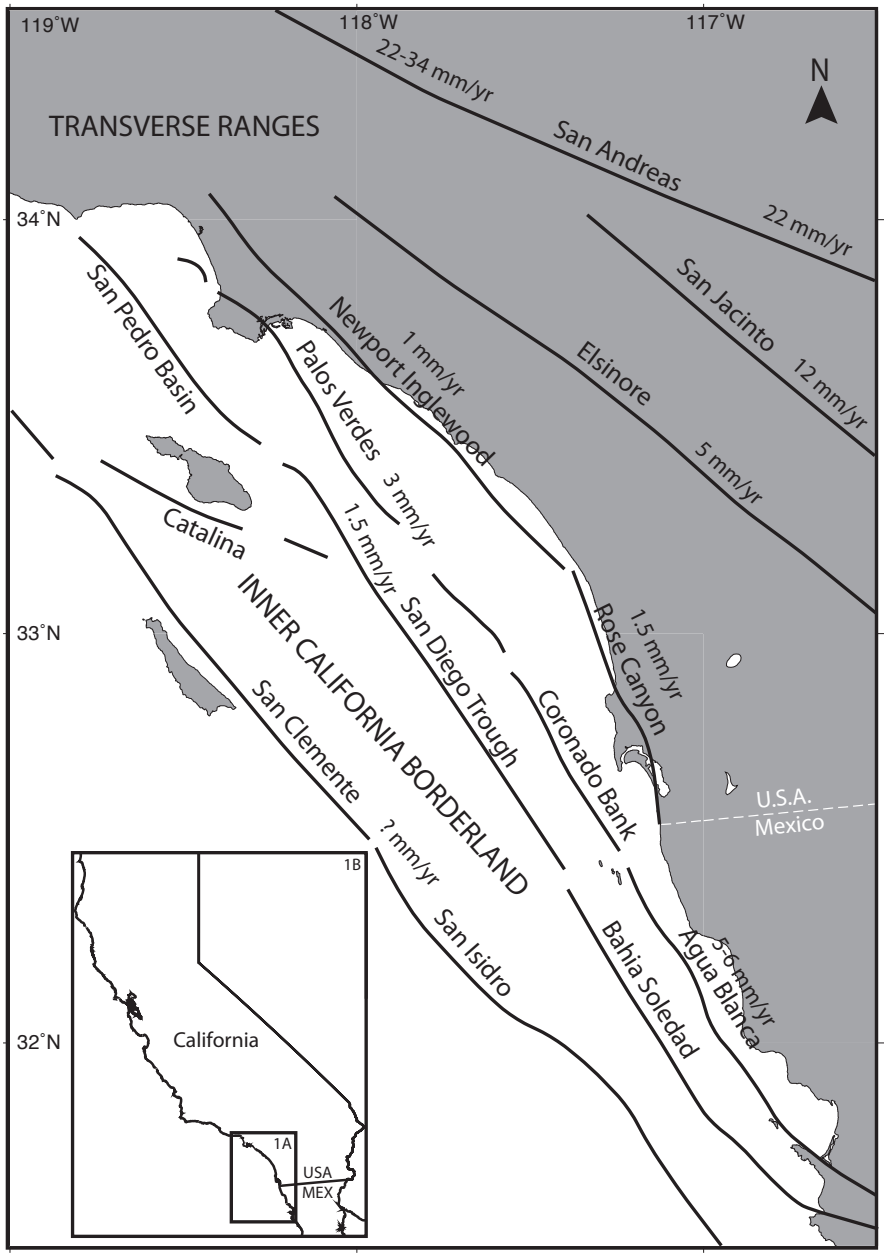

Figure 3-1:(A) Overview of the inner California borderland region. Generalized fault traces and associated slip rates are labeled. Slip rates are from Grant and Shearer (2004), with the exception of the San Diego Trough fault, which is from Ryan et al. (2012). (B) Regional map of California with box illustrating the location of the inner California borderlands shown in Figure 1A.

Figure 3-2: (A) Shaded relief map of the inner California borderlands highlighting major fault zones and purported thrust faults from Rivero and Shaw (2011). Major fault zones from the USGS database are shown in red and labeled: San Diego Trough fault zone (SDTFZ); Coronado Bank fault zone (CBFZ); Descanso fault zone (DFZ); La Nacion Fault Zone (LNFZ); Newport Inglewood-Rose Canyon fault zone (NI-RCFZ); San Mateo trend (SMT); San Onofre trend (SOT); Carlsbad trend (CT). Additionally, San Diego Bay faults are labeled as a group (SDBFZ) and include the Spanish Bight fault, Coronado fault, and Silver Strand fault. The fault surfaces mapped by Rivero and Shaw (2011) of the Thirtymile thrust (green) and Oceanside thrust are shaded and the mapped breakaway zone of the Oceanside thrust is drawn in white and labeled. (B) Shaded relief map showing location of reprocessed MCS, legacy MCS, and high resolution Chirp data used in this study (see inset legend). Faults from the USGS database are shown in red.

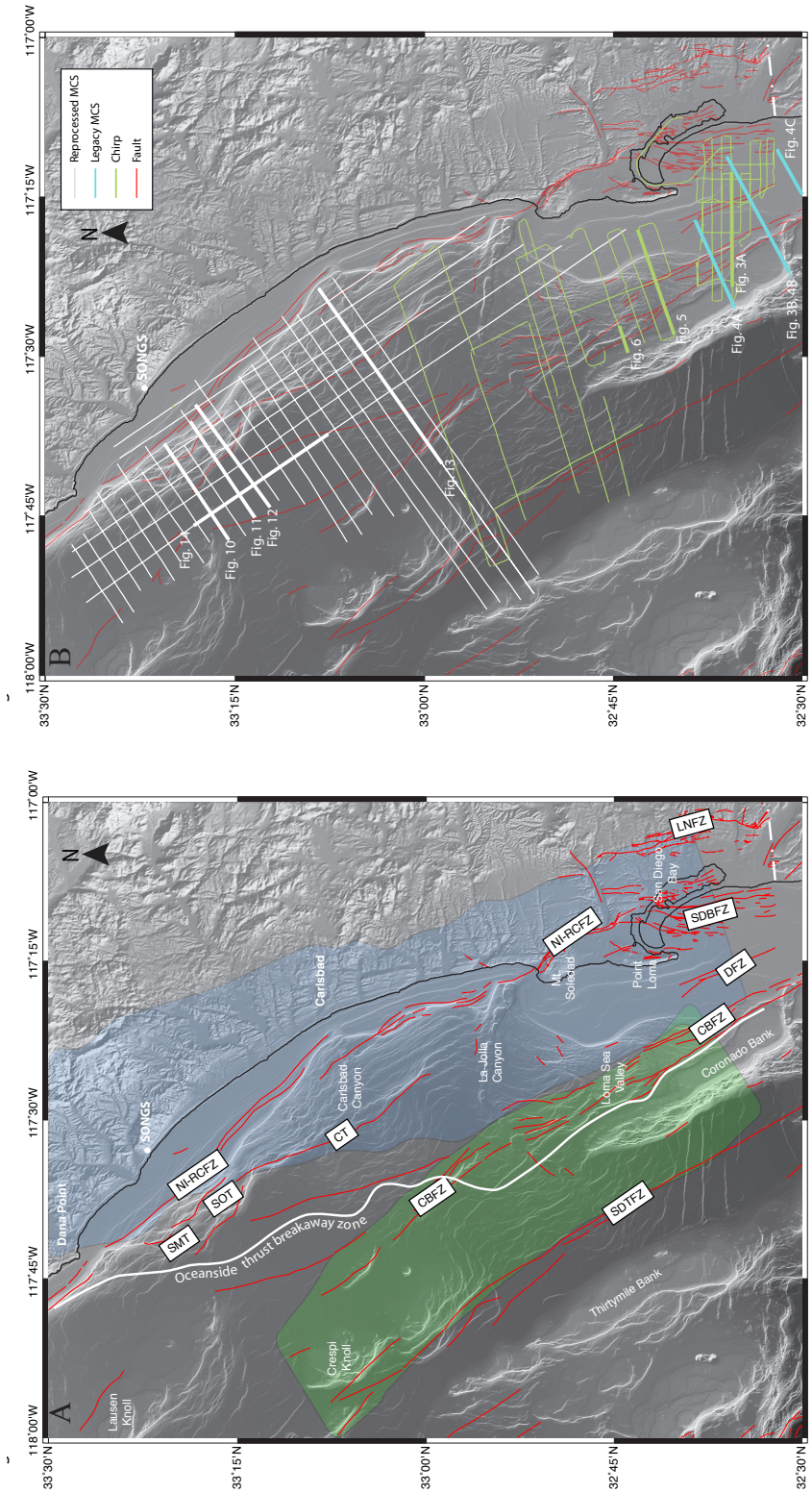
A
B
N
SONGS
Dana Point
Carlsbad
Carlsbad Canyon
La Jolla Canyon
Loma Sea Valley
Point Loma
San Diego Bay
Mt. Soledad
Coronado Bank
Thirtymile Bank
Crespi Knoll
Lausen Knoll
Oceanside thrust breakaway zone
NI-RCFZ
SOT
SMT
CT
CBFZ
SDTFZ
DFZ
SDBFZ
LNFZ
Reprocessed MCS
Legacy MCS
Chirp
Fault
Fig. 3A
Fig. 3B, 4B
Fig. 4C
Fig. 5
Fig. 6
Fig. 10
Fig. 11
Fig. 12
Fig. 13
Fig. 14
117°00'W
117°15'W
117°30'W
117°45'W
118°00'W
33°30'N
33°15'N
33°00'N
32°45'N
32°30'N

Figure 3-3: (A) Interpreted Chirp profile illustrating shallow structure offshore San Diego Bay. Location shown in Figure 2B. Three strands of the Descanso fault zone (DFZ) are observed in the Chirp profile. The blow-up inset illustrates the westernmost strand of the DFZ, which offsets the transgressive surface ~1.5 m. The transgressive surface here is ~62 mbsf. The DFZ is ~5 km wide at this latitude; it is bounded by shallow exposure of Cretaceous rocks in light blue to the east, and to the west by younger rocks characterized by west dipping foresets. The Coronado Bank fault zone (CBFZ) is mapped as four strands running through the Loma Sea Valley. Folding and offset beds characterize the three eastern strands along the slope, whereas the western strand in Loma Sea Valley is inferred based on MCS data and bathymetric expression. (B) Interpreted legacy MCS profile (WSD-81-768) illustrating deep structures offshore San Diego Bay. Profile location is shown in Figure 2B. The DFZ is mapped as a broad zone that offsets basement and bounds a horst and graben structure. An unconformity within the horst and graben structure may represent the boundary between Cretaceous rocks below and younger strata above. The easternmost faults illustrated in the profile are interpreted to be strands of San Diego Bay faults (SDBFZ). The CBFZ consists of a master fault bounding the east side of the Coronado Bank with two antithetic splays (the westernmost DFZ strand also appears antithetic to the main CBFZ strand). Vertical offset of a-a' is ~1 second two-way travel time. Vertical offset decreases up-section, but vertical displacement is still observed in the youngest strata. Abbreviations: G - ghost; M – multiple; TS – transgressive surface; CBFZ – Coronado Bank fault zone; DFZ – Descanso fault zone; SDBFZ – San Diego Bay fault zone.

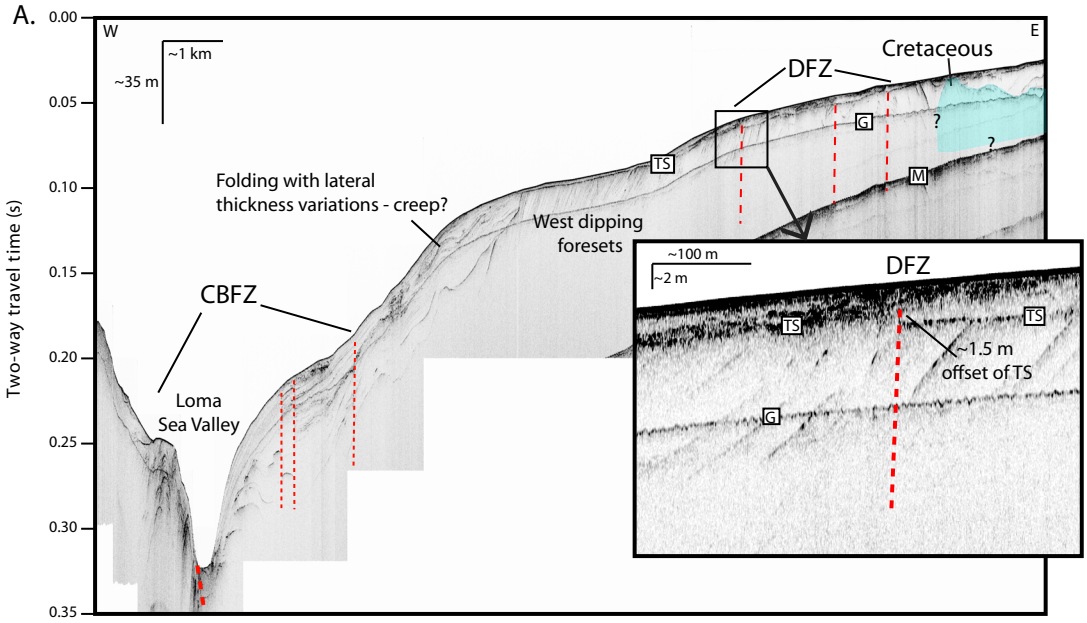
A.
W
E
~1 km
~35 m
Two-way travel time (s)
0.00
0.05
0.10
0.15
0.20
0.25
0.30
0.35
DFZ
Cretaceous
G
TS
M
?
?
Folding with lateral
thickness variations - creep?
West dipping
foresets
CBFZ
Loma
Sea Valley
~100 m
~2 m
DFZ
TS
TS
~1.5 m
offset of TS
G

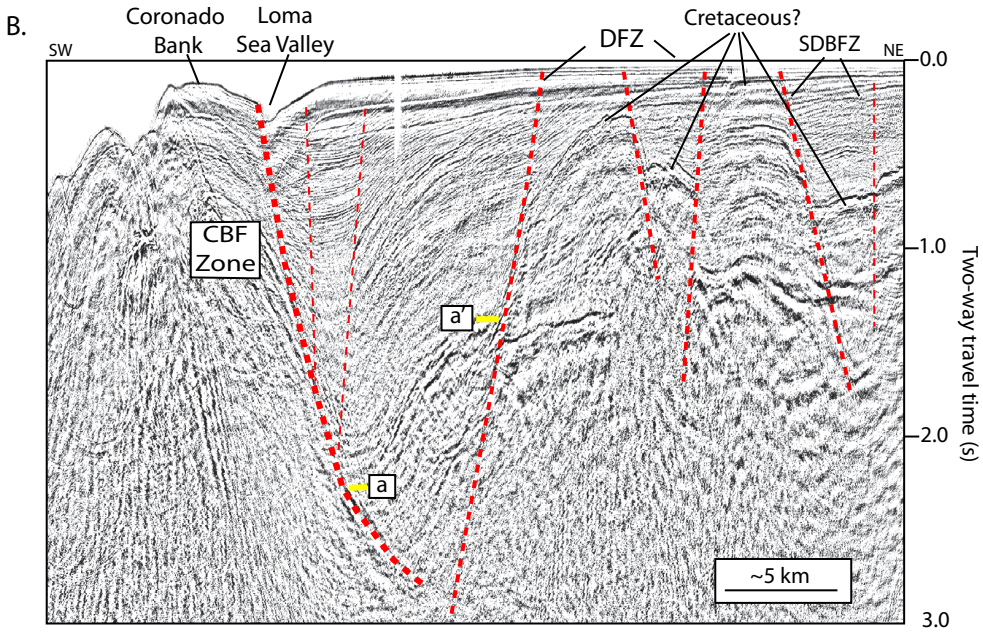
B.
SW
Coronado
Bank
Loma
Sea Valley
DFZ
Cretaceous?
SDBFZ
NE
CBF
Zone
a'
a
~5 km
0.0
1.0
2.0
3.0
Two-way travel time (s)

Figure 3-4: Three interpreted legacy MCS profiles, (A), (B), and (C), showing lateral variations in slip on the Coronado Bank fault (CBFZ) and Descanso fault zone (DFZ) moving north to south through the Loma Sea Valley. Profile locations are shown in Figure 2B. (A) MCS profile WSD-81-764. The synthetic and antithetic splays of the CBFZ result in a broad zone of deformation, with minor dip-slip deformation observed on the main fault strand. Folding on the DFZ indicates a component of vertical motion, which decreases up section. (B) MCS profile WSD-81-768, located directly offshore southern San Diego Bay and exhibiting a significant dip-slip component of displacement. The vertical motion on the CBFZ has resulted in rollover and collapse of the hanging wall block. The DFZ in this profile is associated with the horst and graben structure formed by the CBFZ rollover. A more detailed interpretation of the profile in (B) is provided in Figure 3. (C) MCS profile WSD-81-772. Strands of the CBFZ slightly deform sub-horizontal reflectors that fill the Loma Sea Valley above basement. Deformation occurs along strands of the DFZ, but little vertical offset is observed. Maximum vertical offset of the CBFZ is observed in (B) and decreases both to the north and south. Abbreviations: CBFZ – Coronado Bank fault zone; DFZ – Descanso fault zone.

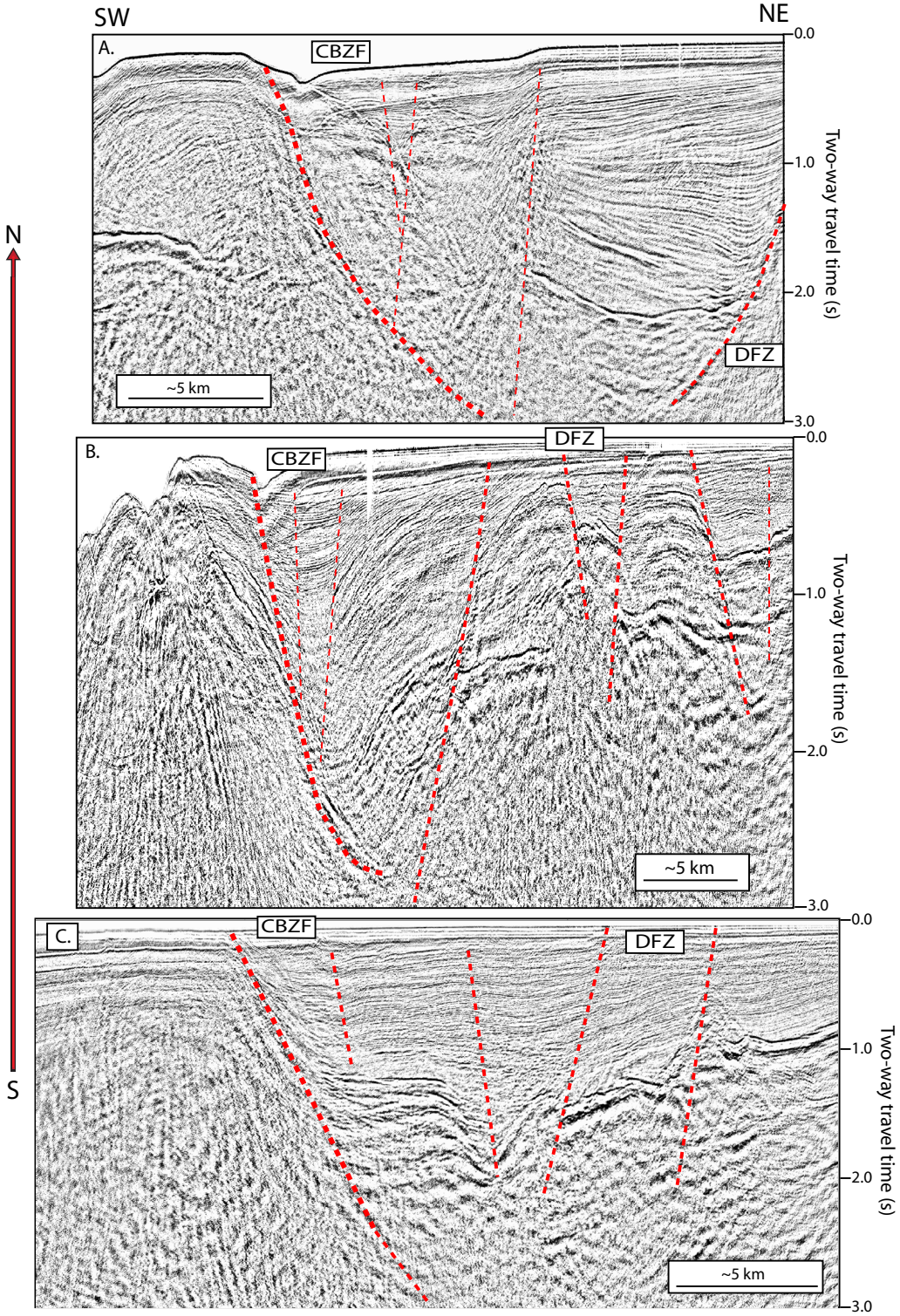
SW
NE
A.
CBZF
DFZ
~5 km
0.0
1.0
2.0
3.0
Two-way travel time (s)
N
S
B.
CBZF
DFZ
~5 km
0.0
1.0
2.0
3.0
Two-way travel time (s)
C.
CBZF
DFZ
~5 km
0.0
1.0
2.0
3.0
Two-way travel time (s)

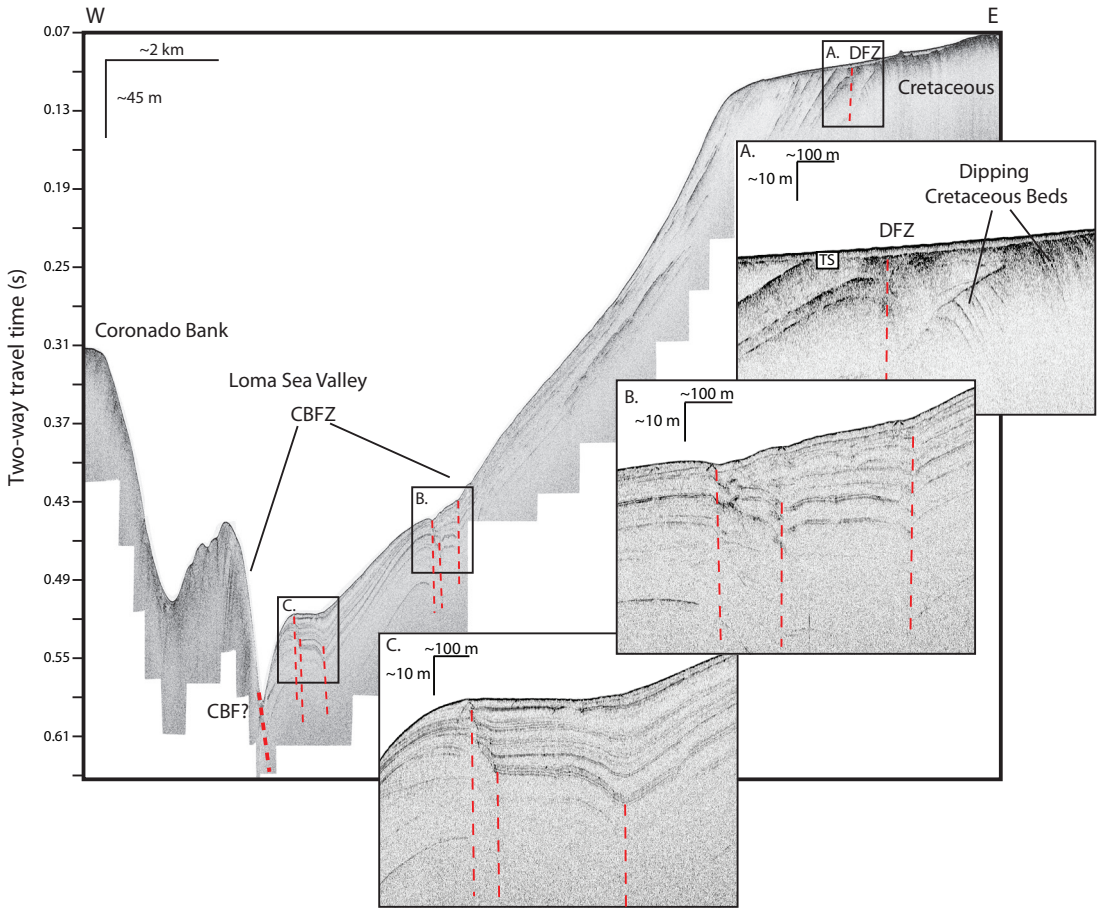

Figure 3-5: Chirp profile across the Coronado Bank fault zone (CBFZ) and Descanso fault zone (DFZ) with insets (A), (B), and (C) showing details of the deformation. Profile location is shown in Figure 2B. (A) The DFZ here deforms horizons near the shelf-edge, but does not offset the transgressive surface. (B) CBFZ splays offset beds very near the seafloor and appears to have a bathymetric expression. (C) CBFZ splays are characterized by folding and lateral variations in bed thickness across faults. Abbreviations: TS – transgressive surface; CBFZ – Coronado Bank fault zone; DFZ – Descanso fault zone.

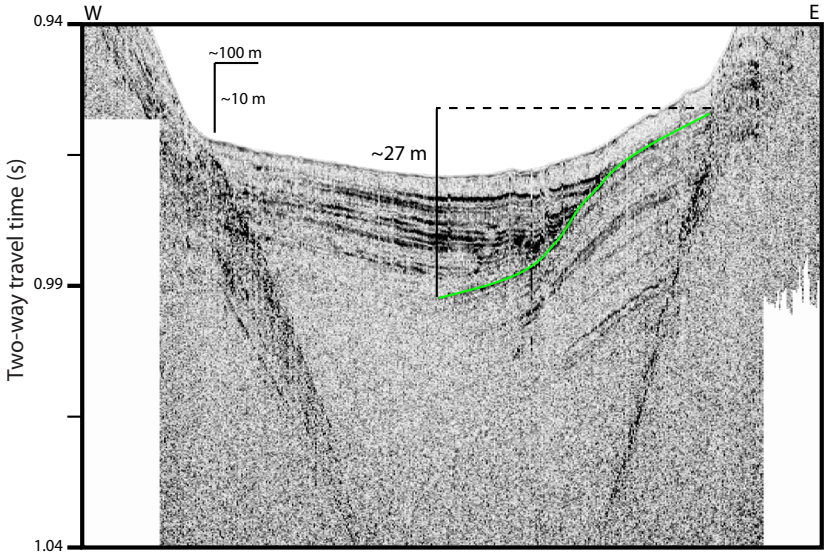

Figure 3-6: Chirp profile across the Loma Sea Valley channel. Profile location is shown in Figure 2B. A package of acoustically laminated strata is vertically offset ~27 m. Above the deformed strata, a package of acoustically laminated, sub-horizontal strata fill accommodation and onlap the folded beds. The onlap surface marks the cessation of deformation and is highlighted in green.

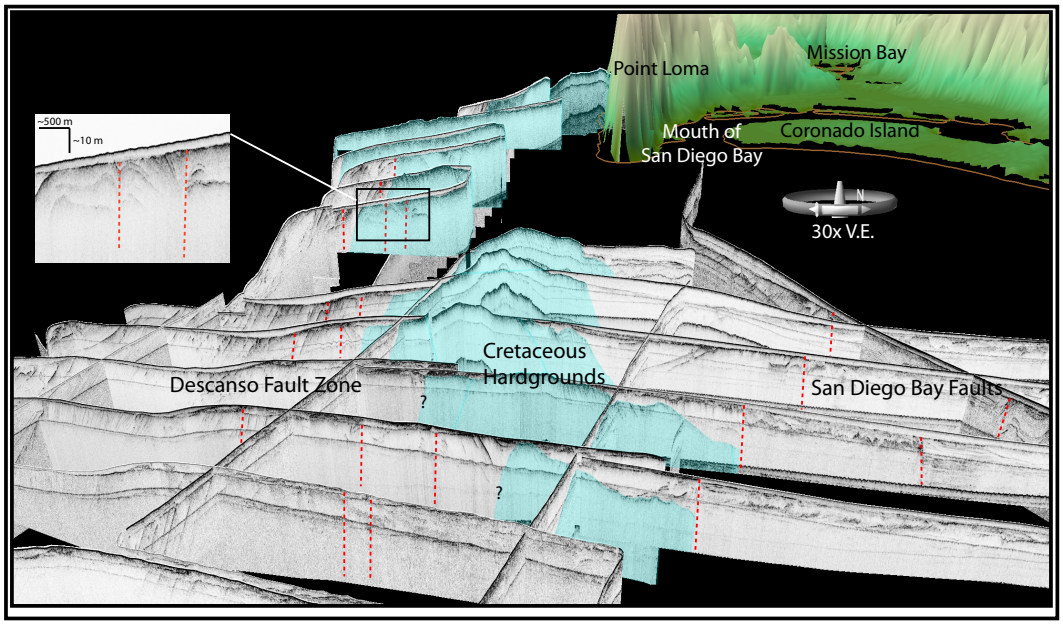

Figure 3-7: Fence diagram of Chirp data looking north and showing lateral extent of Cretaceous Rosario group south and west of Point Loma. The Cretaceous rocks (blue) contain thinly spaced, east dipping beds and rough topography characteristic of the Point Loma Formation observed onshore at Point Loma and in bathymetry data. These rocks appear more resistant than adjacent rocks, which were eroded during sea-level transgression (i.e., abrasion platform; Hogarth et al., 2007). In the Chirp dataset, the Cretaceous rocks are only observed between the Descanso and San Diego Bay fault zones south of Point Loma. Inset shows detail of deformed Cretaceous rocks at the Descanso fault zone. Faults are marked with dashed red lines.

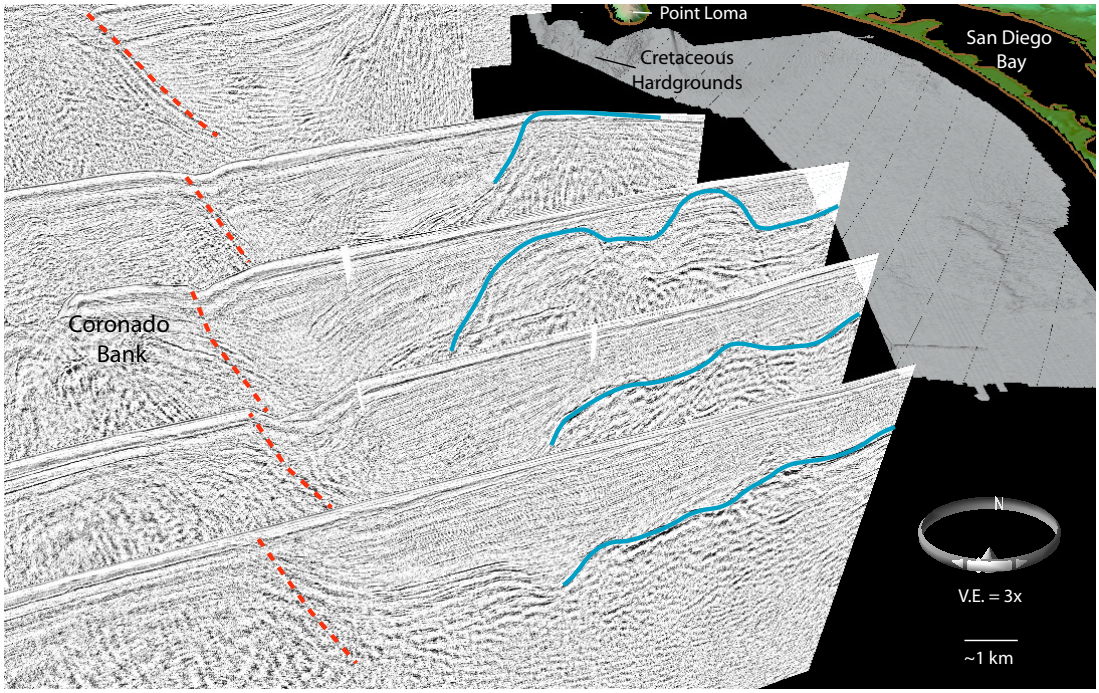

Figure 3-8: Fence diagram of legacy MCS profiles showing basement structure and faulting south of Point Loma. The contact between inferred Cretaceous basement rocks and younger, sedimentary rocks is highlighted in blue. The horst-graben structure is localized offshore San Diego Bay. The relict topographic high in the basement aligns with the outcrops of the Cretaceous rocks imaged in the Chirp data and onshore high at Point Loma shown in Figure 7. The MCS profiles also illustrate lateral changes in vertical displacement along the Coronado Bank fault zone to the north and south away from San Diego Bay. The main strand of the Coronado Bank fault zone is marked in dashed red. Swath bathymetry data were acquired, processed, archived, and distributed by the Seafloor Mapping Lab of California State University Monterey Bay.

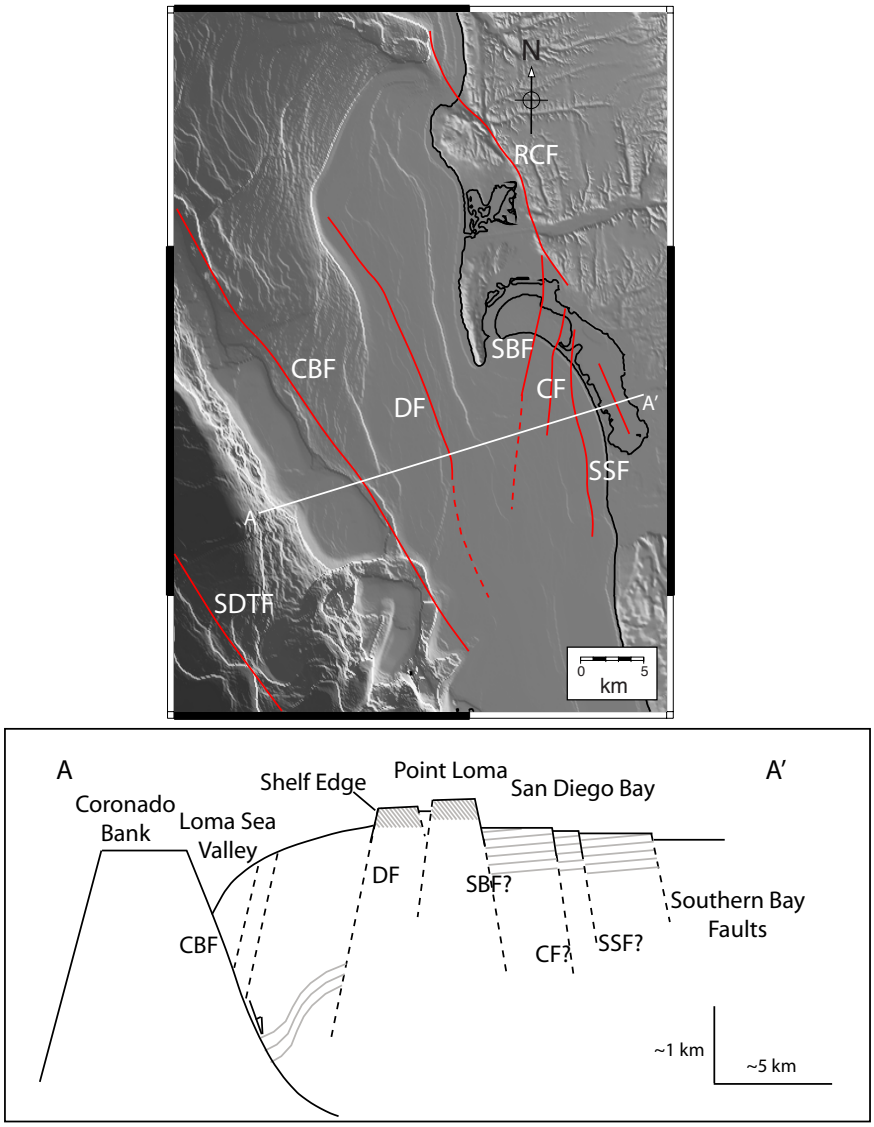

Figure 3-9: Schematic diagram of tectonic structure offshore San Diego Bay. Significant dip-slip displacement on the Coronado Bank fault (CBF) west of San Diego Bay results in a series of horst and graben structures that appear to control the topographic high of Point Loma and the wide shelf offshore Mission Bay. The Point Loma topographic high is bounded by the Descanso fault to the west and the San Diego Bay faults to the east. The San Diego Bay faults include the Spanish Bight fault, Coronado fault, and Silver Strand fault. The rollover geometry of the hanging wall is consistent with the eastward dipping CBF soling at depth, suggesting a possible link to the San Diego Bay pull-apart basin. Abbreviations: SDTF – San Diego Trough fault; CBF – Coronado Bank fault; DF – Descanso fault; SBF – Spanish Bight fault; CF – Coronado fault; SSF – Silver Strand fault; RCF – Rose Canyon fault.

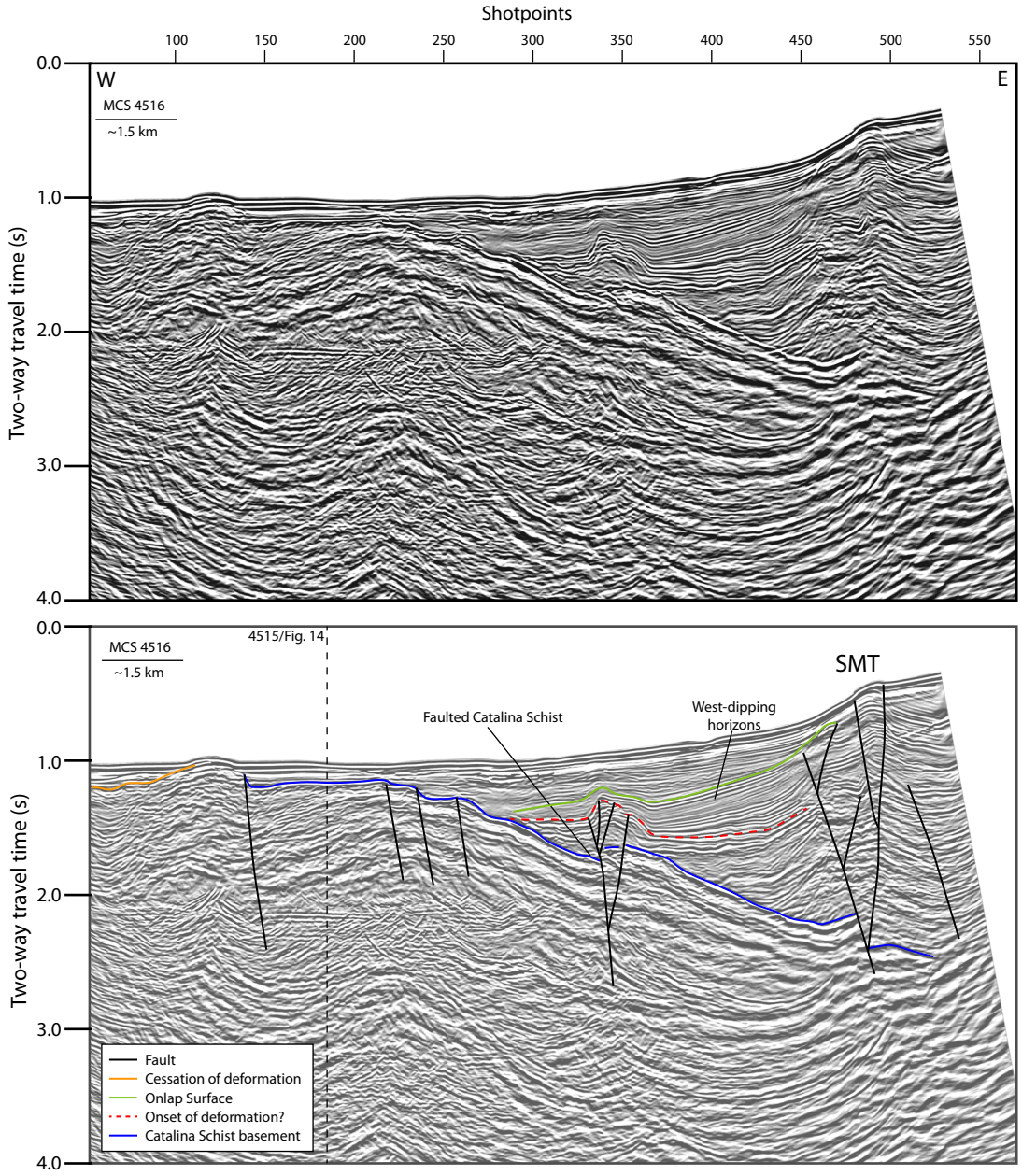

Figure 3-10: Un-interpreted (top) and interpreted (bottom), re-processed MCS Line 4516 illustrating deformation west of the San Mateo trend. Horizons regionally dip to the west and onlap the basement, which is fragmented and offset by several faults. A flower structure offsets the basement near shot 350. Profile location is shown in Figure 2B. See inset legend for interpretation key. Vertical dashed line shows intersection with labeled profile. Abbreviation: SMT – San Mateo trend.

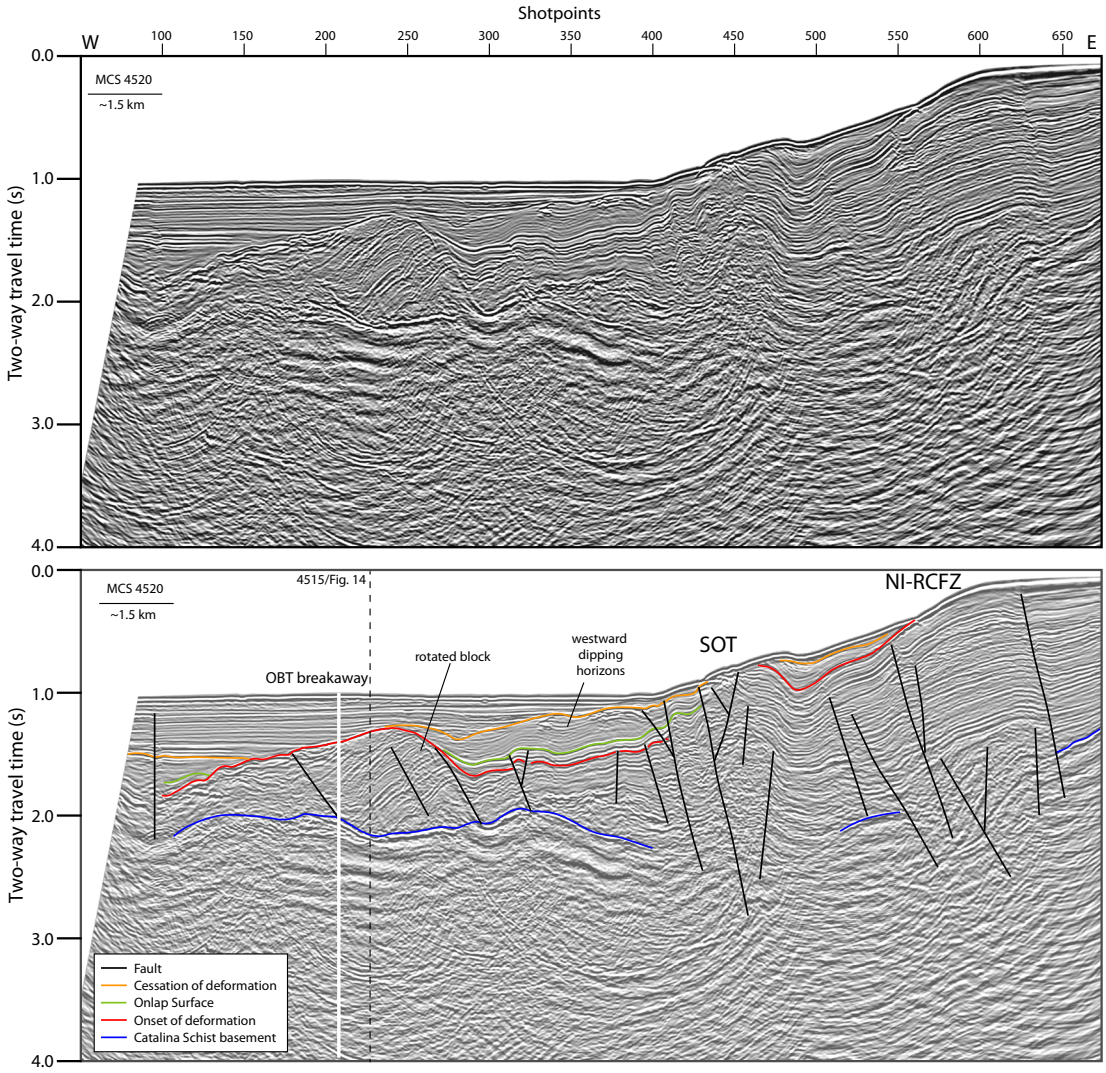

Figure 3-11: Un-interpreted (top) and interpreted (bottom), re-processed MCS Line 4520 illustrating deformation at the San Onofre trend (SOT) and Newport Inglewood-Rose Canyon fault zone. Horizons west of the SOT above the red horizon are regionally flat lying and locally slightly westward dipping. The vertical white line marks the geographic location of the Oceanside Blind Thrust breakaway zone mapped in Rivero and Shaw (2011). Profile location is shown in Figure 2B. See inset legend for interpretation key. Vertical dashed line shows intersection with labeled profile. Abbreviations: SOT – San Onofre trend; NI-RCFZ – Newport Inglewood-Rose Canyon Fault Zone; OBT – Oceanside Blind Thrust.

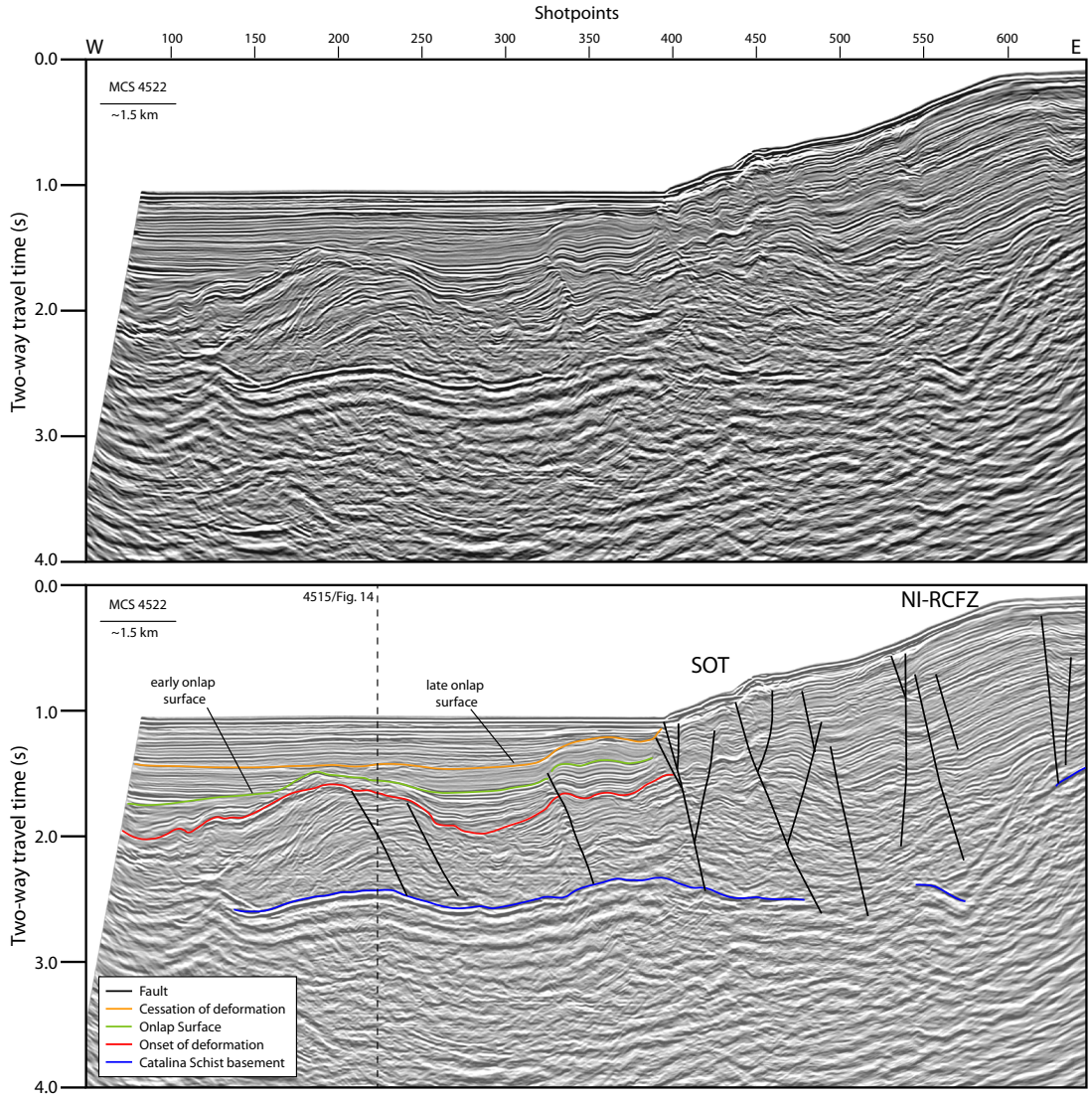

Figure 3-12: Un-interpreted (top) and interpreted (bottom), re-processed MCS Line 4522 illustrating deformation at the San Onofre trend (SOT) and Newport Inglewood-Rose Canyon fault zone. Horizons west of the SOT above the red horizon are regionally flat lying. Note the deformation of the green horizon is younger toward the east. Profile location is shown in Figure 2B. See inset legend for interpretation key. Vertical dashed line shows intersection with labeled profile. Abbreviations: SOT – San Onofre Trend; NI-RCFZ – Newport Inglewood-Rose Canyon Fault Zone.

Figure 3-13: Un-interpreted (top) and interpreted (bottom), re-processed MCS line 4542 illustrating transtensional deformation west of the CT. Note reflectors bounded by the red and orange horizons diverge and dip towards the east. Onlapping reflectors mantle the deformation associated with the Carlsbad trend. Profile location shown in Figure 2B. See inset legend for interpretation key. Abbreviations: CT – Carlsbad trend; NI-RCFZ – Newport Inglewood-Rose Canyon fault zone.

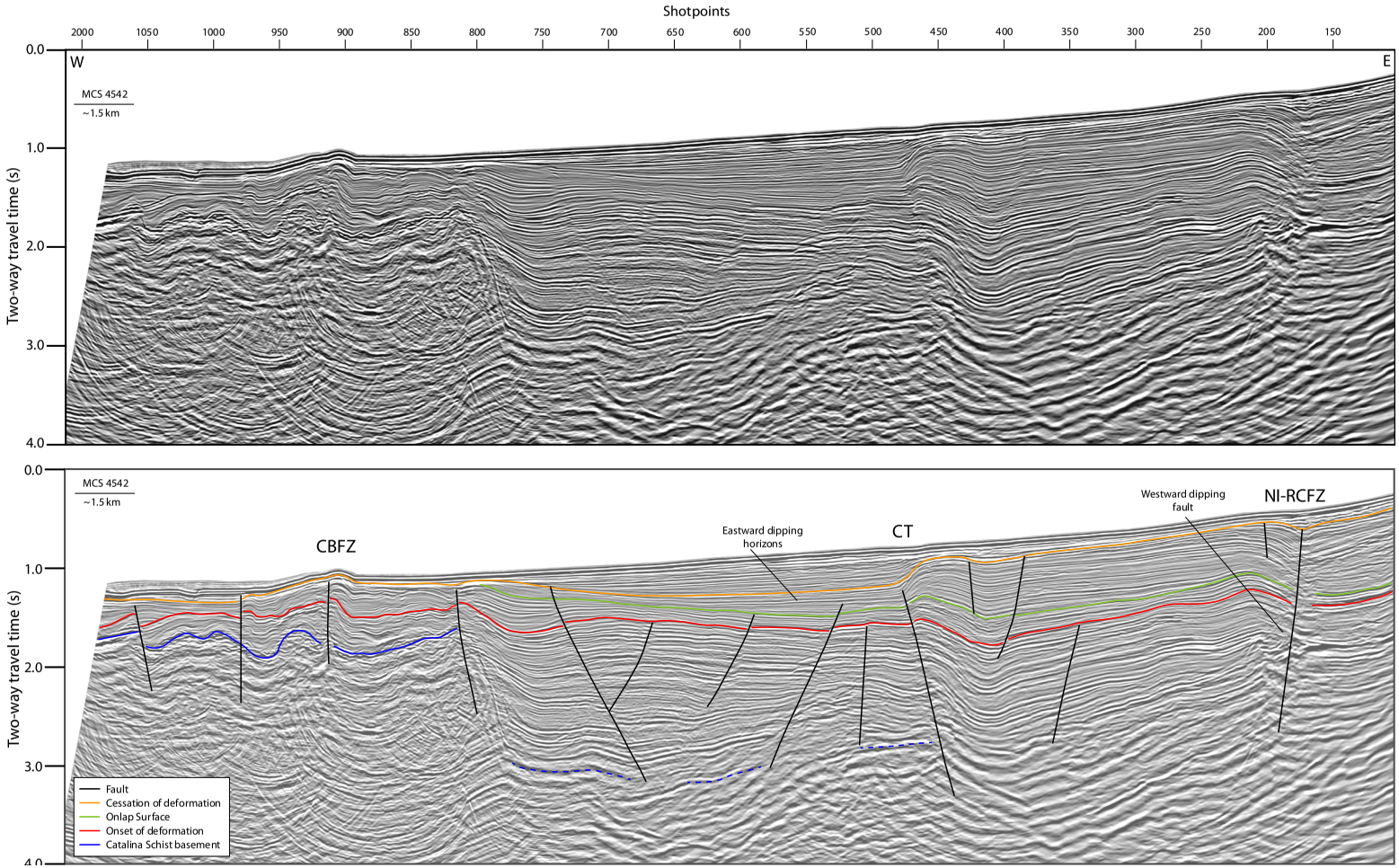
Shotpoints
2000
1050
1000
950
900
850
800
750
700
650
600
550
500
450
400
350
300
250
200
150
0.0
1.0
2.0
3.0
4.0
Two-way travel time (s)
W
E
MCS 4542
~1.5 km
MCS 4542
~1.5 km
CBFZ
Eastward dipping horizons
CT
Westward dipping fault
NI-RCFZ
Fault
Cessation of deformation
Onlap Surface
Onset of deformation
Catalina Schist basement

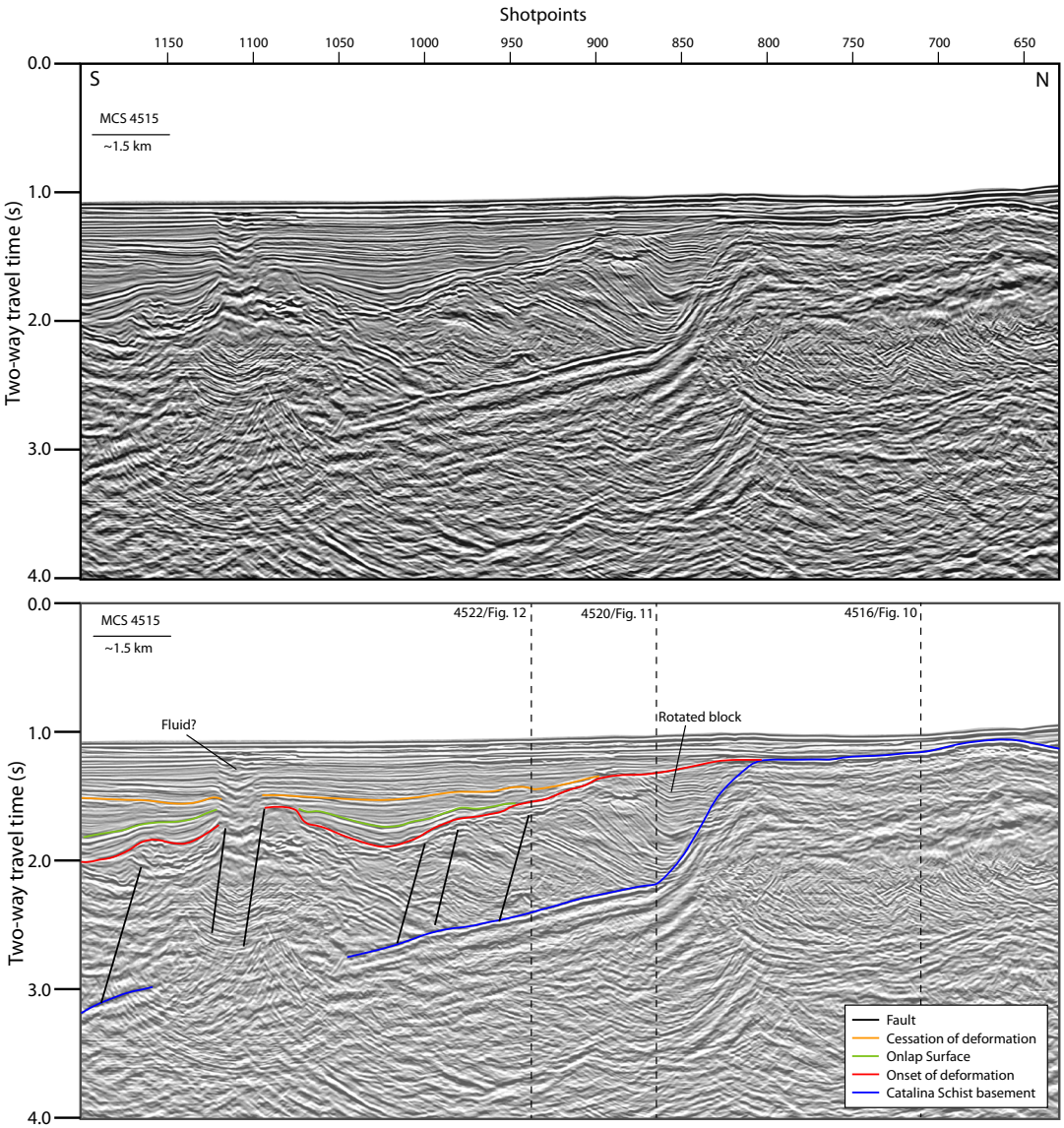

Figure 3-14: Un-interpreted (top) and interpreted (bottom), re-processed MCS line 4515 illustrating acoustic basement relief and the rotated and deformed reflectors. The dip of the reflectors increases with depth and the minor reversal in dip may represent small drag folds. Note the deformation increases down-section and reflector clarity diminishes. The basement dips to the south, away from the high in the north (Schist Ridge). Lens shaped reflections in the overlying carapace between shots 1100-1150 may be recording fluid expulsion. Profile location is shown in Figure 2B. See inset legend for interpretation key. Vertical dashed lines show intersection with labeled profiles.

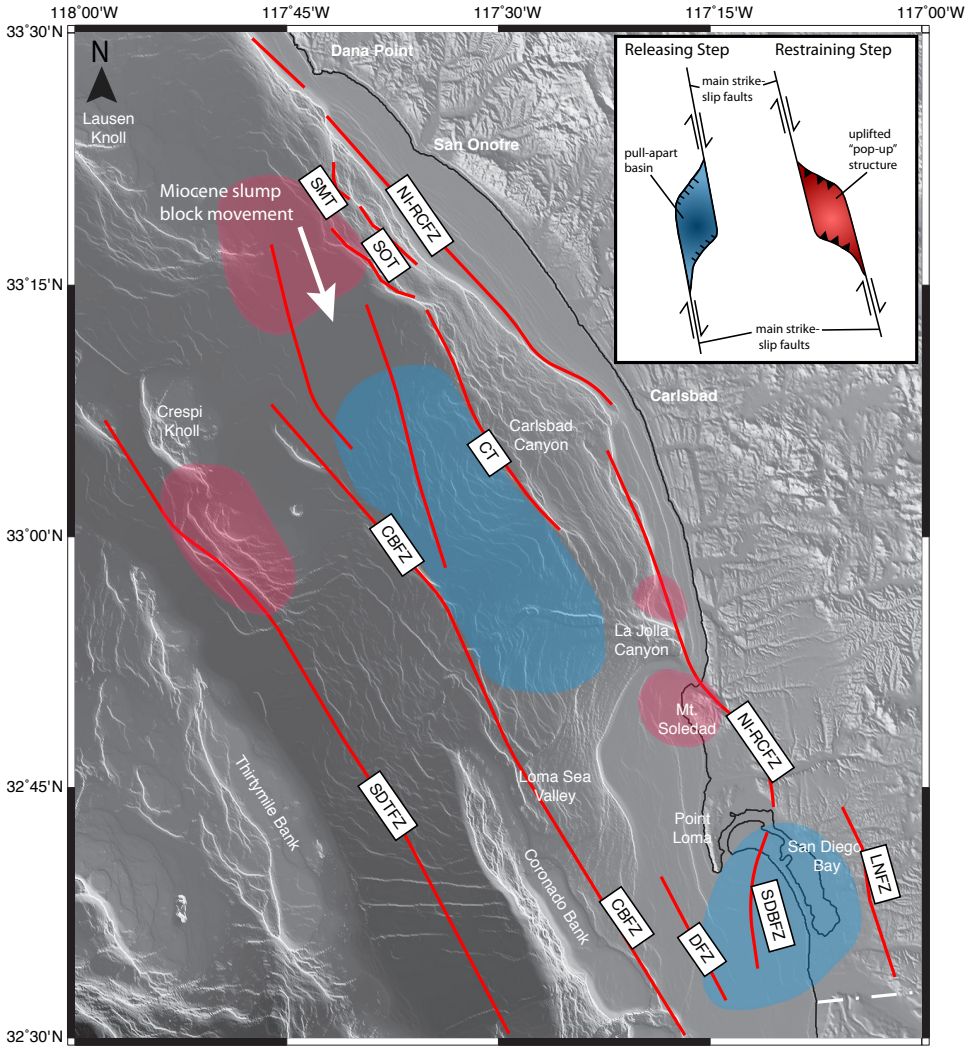

Figure 3-15: Map of the inner California borderlands highlighting areas of transtension (blue) and transpression (red) associated with fault bends and steps. Transpression at bend in San Diego Trough fault zone south of Crespi Knoll was proposed by Ryan et al. (2012). Transpression at bend in Rose Canyon fault zone north of La Jolla canyon was proposed by Hogarth et al. (2007). Evidence for transtension offshore San Diego Bay and north of La Jolla Canyon is detailed in the text. Both appear to be associated with releasing steps along major strike-slip fault zones. Simple models for idealized releasing and restraining bends illustrated in the upper right corner modified from Wakabayashi et al. (2004). Abbreviations: SDTFZ - San Diego Trough fault zone; CBFZ - Coronado Bank fault zone; DFZ - Descanso fault zone; LNFZ - La Nacion Fault Zone; NI-RCFZ - Newport Inglewood-Rose Canyon fault zone; SMT - San Mateo trend; SOT- San Onofre trend; CT - Carlsbad trend; SDBFZ - San Diego Bay faults.

4

Geological constraints on biohabitats: A geophysical characterization of San Diego Bay and adjacent regions, California

4.1 ABSTRACT

Swath bathymetry and high-resolution Chirp data were acquired in San Diego Bay to examine the relationship between geologic substrate exposed at or near the seafloor and related biohabitats. The data reveal important links between geology and biohabitats. For example, south of Ballast Point where the transgressive surface outcrops and exposes hard grounds on the seafloor exist kelp canopies (*Egregia menziesii* and *Macrocystis pyrifera*) not observed in other regions within the bay. Likewise, at the bay mouth the Point Loma Formation outcrops on the seafloor as a horst block that provides substrate for kelps and rockweeds. In addition, the overall density of eelgrass (*Zostera marina*) exhibits depth control along Zuniga Jetty; the density of eelgrass decreases with depth. Nevertheless, secondary controls on eelgrass density are observed and appear to be related to rapid sedimentation associated with sediment spillways in the Zuniga Jetty. Terrestrial sediment input into the bay is low. Regions of modern sediment accumulation near the Embarcadero and south of Ballast Point appear to be caused by anthropogenic sediment reworking related to ship traffic. Recency of offset along existing faults (Spanish Bight, Coronado, and Silver Strand faults), and a newly identified fault (Harbor Island fault), was examined using the Chirp data. These faults have a dip-slip transtensional component and appear to be active in the Holocene, with some exhibiting a bathymetric expression. As such these faults, in all likelihood, play a role in groundwater flux and stream capture of the San Diego River in the past. In summary, these geophysical investigations of San Diego Bay and surrounding regions have yielded new insights into the operative processes that shape the bay as well as providing a quantitative baseline from which future change can be assessed (e.g., rapid sea level rise ≥ 3 mm/yr).

4.2 INTRODUCTION

The near shore region of San Diego is facing increased human pressure

from fisheries, land development and runoff, as well as climate change. Sea level is rising at an unprecedented rate of over 3 mm/yr due to global warming (IPCC, 2007; Rahmstorf, 2007; Pfeffer et al., 2008), raising concerns about the long-term stability of biogenic habitats in bays and estuaries. Our understanding of biological and geological processes in near shore regions remains limited; thus the response of near shore habitats (e.g., beaches, bays, and the inner shelf) to rapid sea level rise is difficult to predict. Understanding the factors that influence and limit the distribution, density, and patchiness of biological habitats in and around San Diego Bay is the critical first step toward developing predictive capabilities. Toward this goal, we have surveyed San Diego Bay and adjacent regions with swath bathymetry and subbottom Chirp (compressed high intensity radar pulse) data to establish a regional baseline to evaluate change in response to a number of forcing factors (Fig. 1).

In San Diego Bay, anthropogenic influence is evident and, as such, the bay provides a laboratory to study how human constructs and natural processes interact to influence circulation, morphology, sediment processes, and ecosystem structure in near shore environments. San Diego bay is a tectonically active pull-apart basin that has undergone major deformation (Rockwell, 2010; Maloney et al., in prep.). Drainage to the bay has been altered through damming of rivers and altered drainage patterns, artificial islands have been constructed, and extensive dredging has removed sediment to maintain open shipping channels (Canada, 2006). Despite all of this overprinting, there are still large areas that are important for understanding the natural links between biology and geology where previous geologic structures and ongoing sediment transport play a role in habitat distribution. Furthermore, the bay provides insights into the tectonic evolution of pull-apart basins (Basile and Brun, 1998; Katzman et al., 1995; McClay and Dooley, 1995; Wu et al., 2009) and how segmentation and step-overs along fault systems can influence the exposed geologic strata on the seafloor and associated biohabitats.

We conducted geophysical surveys of the bay and surrounding region to understand the links between geology and biology and how anthropogenic impacts can alter or overprint these regions in the bay. We also imaged extensive faulting throughout the bay at high resolution to assess potential geohazards posed to the region. With ongoing and predicted future sea level rise (IPCC, 2007; Rahmstorf, 2007; Pfeffer et al., 2008), it is critical to understand the geologic controls on coastal morphology and how these forcing factors impact ecosystem structures.

4.3 BACKGROUND

San Diego Bay is ~25 km long and varies in width between 1-3 km (Fig. 2). The bay is elongated along a trend of ~N10°W, but in the northwest, makes an almost 180° turn such that the mouth opens to the south. The depth of the bay ranges from ~15 m in the dredged shipping channel to < 1 m in the south. The ~100 m high Point Loma peninsula on the western edge of the bay mouth protects the bay from west and northwest waves and storms (Fig. 2). Likewise, the Zuniga Jetty, which extends south from Coronado Island, protects the mouth of the bay along the eastern edge. Coronado Island was originally divided by a shallow channel (the Spanish Bight) into two landmasses, named North Island and Coronado Island. The bight was infilled and a naval base currently occupies what was once North Island, while old Coronado Island is primarily residential. The Silver Strand is a natural barrier beach connecting Imperial Beach to Coronado Island, formed by sediment transport northward from the Tijuana River mouth (Elliott, 1987). Archeological evidence suggests that the Silver Strand formed ~5 ka when the rate of eustatic sea level rise decreased (Masters, 2006).

There are three main drainage channels into San Diego Bay from the east. These are Chollas Creek, Sweetwater River, and Otay River, and together they drain ~700 km2 of combined urban, agricultural, and undeveloped land (Mazor and Schiff, 2007a;

2007b; 2007c). The Sweetwater and Otay rivers are dammed. The bay is considered a Mediterranean, inverse estuary, characterized by freshwater input almost exclusively during the winter with evaporation outpacing input for most of the year (Delgadillo-Hinojosa et al., 2008). This results in hypersalinity and long residence times for water in the bay (Largier et al., 1997). Average rainfall for San Diego is ~25 cm/yr (Largier, 1995). San Diego Bay shows seasonal variability and longitudinal gradients from the mouth to head of the bay in temperature, salinity, and nutrients (Delgadillo-Hinojosa et al., 2008). Over a year long study, with data collection in August, January, May and September, Delgadillo-Hinojosa et al. (2008) measured an overall temperature range of 13.5° C - 24.9° C and a salinity range of 32.27 - 35.86. Seasonal variability in salinity occurs mainly near the head of the bay, with measurements near the mouth remaining constant throughout the year. Estimates of overall residence times for San Diego Bay range from 2 - 100 days (Chadwick and Largier, 1999).

Circulation is driven by tidal pumping and the amount of exchange between the bay and the Pacific Ocean varies with tidal range (Chadwick and Largier, 1999). Currents are strongest at the mouth of the bay (50-100 cm/s) where the tidal influence is greatest, and weakest in the southern bay (<10 cm/s) (Chadwick and Largier, 1999). Modeled transport of suspended fine-grained sediment (2 and 20 micron) out of San Diego Bay is ~4.7 x 107 kg/yr and input from rivers is ~2.25 x 107 kg/yr (Peng and Zeng, 2007).

Humans have been modifying San Diego Bay for over two centuries. In the early 1800s the San Diego River changed course from emptying into Mission Bay to emptying into San Diego Bay (Pourade, 1960). By the early 1850s there was significant concern that sediment input from the San Diego River would endanger use of the bay as a harbor. By 1877, a levee was built diverting flow of the river to Mission Bay permanently (Rambo and Speidel, 1969). In the 1900s San Diego Bay underwent extensive dredging and development projects resulting in loss of ~90% of natural marshland and ~50% of

natural intertidal zone. Harbor and Shelter Islands are both artificially constructed (Fig. 2). The land surrounding the bay is developed into commercial, industrial, and military operations. Dredging of the bay for ship traffic and development has been ongoing since the early 1900s, leaving ~82% of the original bay floor now altered by dredge and fill (Peñafuerte, 2003). Current marine protected areas include parts of the Point Loma peninsula, which is home to the Cabrillo National Monument, and the San Diego Bay National Wildlife Refuge, which encompasses ~2,600 acres of land and water in southern San Diego Bay (Service, 2006).

4.3.1 Regional Tectonics

Coastal San Diego is located at the boundary between the offshore inner California borderlands geologic province and the onshore Peninsular Ranges province (e.g., Bohannon and Geist, 1998; Vedder, 1987). The region is characterized by several strike slip fault systems that accommodate motion between the Pacific and North American plates, and control San Diego geomorphology (Figs. 1 & 2A; Kennedy and Welday, 1980). San Diego Bay is a pull-apart basin formed by a right step from offshore faults to the onshore Rose Canyon fault. The offshore faults involved in the step-over include the Coronado Bank fault and the Descanso fault.

The Descanso and Coronado Bank fault zones parallel one another trending northwest offshore San Diego (Fig. 1). The Descanso fault was mapped between the US-Mexico border and Point Loma (Legg, 1985) and appears associated with a basement horst-graben structure formed by localized dip-slip on the Coronado Bank fault (Maloney et al., in prep.). The Coronado Bank fault may be a southern extension of the Palos Verdes fault zone, but recent surficial evidence suggests this may not be a through-going fault (Ryan et al., 2012); however, the faults may connect at depth in the basement. Another option is that only the northern and southern segments have ruptured recently

with the intervening section being more quiescent (Fig. 1). Deformation in the offshore ICB is accommodated by predominantly strike-slip with localized areas of compression and extension at fault bends and steps. Offshore San Diego Bay, the Coronado bank fault exhibits localized extension that appears associated with the pull-apart basin (Maloney et al. in prep.).

The Rose Canyon fault is the southern extension of the Newport Inglewood fault zone, which is located along the eastern side of Palos Verdes in Los Angeles County and steps offshore and trends along the shelf edge through Orange and San Diego Counties (e.g., Ryan et al., 2009). At Point La Jolla, the Rose Canyon fault steps back onshore at a restraining bend responsible for the Mount Soledad topographic high (Rockwell, 2010). South of Mount Soledad, the fault zone trends ~N20°W and appears to terminate near downtown San Diego. Here, several faults splay into San Diego Bay and accommodate subsidence across the basin. The slip rate on the Rose Canyon fault is ~1.5 mm/yr, with evidence for at least three events during the last ~8 kyr (Lindvall and Rockwell, 1995).

The San Diego Bay basin is ~20 km wide and ~2-3 km deep, and is filled with ~1-3 km thick sedimentary fill with increasing thickness to the south (Marshall, 1989). Fault trends and dips suggest an asymmetric pull-apart with ~10 km separation between the offshore Descanso fault and onshore Rose-Canyon fault. Three north-south trending fault zones extend south from near downtown, cross Coronado Island, and extend offshore. These are the Spanish Bight fault, Coronado fault, and Silver Strand fault. Several un-named faults have also been mapped in the southeastern bay (Fig. 2A). Several faults within the Bay extend to within 2-3 m of the bay floor and are likely Holocene active based on seismic reflection data and radiocarbon dating (Kennedy and Clarke, 1999). To the east, the north-south trending La Nacion fault zone has been interpreted as the eastern boundary of the pull-apart basin. The fault zone is composed of west dipping, anastomosing normal faults with >60 m vertical offset observed in the

Pliocene San Diego Formation (Hart, 1974).

Historic seismicity has been observed in the San Diego Bay vicinity. Astiz and Shearer (2000) located several earthquakes occurring between 1981 and 1997 of M<4 between Coronado Bank and Point Loma, which could be attributed to motion along either the Coronado Bank fault or the Descanso fault. Additional seismicity includes a several small magnitude earthquake clusters recorded beneath San Diego Bay from 1985-1987 (Magistrale, 1993).

4.3.2 Ecosystems

Eelgrass beds are an important component of shallow coastal waters, bays and estuaries. They provide food, refuge, and critical habitat space for many coastal and estuarine species, including commercially relevant fish and shellfish, and are important for nutrient cycling and sediment stabilization (Hemminga and Duarte, 2000). Several studies have documented loss or decline of eelgrass ecosystems worldwide due to human impacts, which include increased sediment and nutrient supply, and fragmentation due to coastal development (e.g., Duarte, 2002; Orth et al., 2006; Short and Wyllie-Echeverria, 1996; Waycott et al., 2009). Efforts at restoring eelgrass habitat often include artificial transplantation, although the success of this method is estimated at only ~30% (Fonseca et al., 1998). Light availability is the major requirement for eelgrass habitat, as they require some of the highest levels of any plant group worldwide (Dennison et al., 1993; Orth, 2006). As such, factors affecting the availability of light are most often studied, while other factors that may influence habitat, such as sediment characteristics, are less well understood (Koch, 2001). Nonetheless, erosional events (Bell, 1999; Hine, 1987; Koch, 2001), variable sedimentation rates (Marba and Duarte, 1995; Koch, 2001; Moore et al., 1993), and bedform structure (Daniell et al., 2009) have been shown to impact eelgrass populations.

4.4 METHODS

Between 2006 and 2012, over 1000 km of seismic Chirp data were acquired in and offshore San Diego Bay (Fig. 2B). The data were collected using SIO's Edgetech Chirp profiler. The Chirp profiler was operated with a 50 ms swept pulse of 1-15 kHz, and provided sub-meter vertical resolution with sub-bottom penetration up to ~50 m. Location accuracy is to within 5 m. Chirp data were processed using sioseis (sioseis.ucsd.edu) (Henkart, 2003) and imported to Kingdom Suite (http://www.ihs.com) and QPS Fledermaus (http://www.qps.nl/display/fledermaus/main) software packages for interpretation. A nominal water and sediment velocity of 1500 m/s was assumed for all depth conversions in Chirp data.

Bathymetric data were acquired in 2012 using a Reson 7125 multibeam system operated at 400 kHz (Figs. 2 & 3) with a nominal vertical resolution of ~2.5 cm. Positions were calculated through a real time kinematic GPS system, providing centimeter lateral position accuracy. Data positions were determined using the Geoid99 model and are referenced to the NAVD88 vertical datum. Data were processed using Caris HIPS and SIPS software, and interpreted with IVS Fledermaus and ArcGIS software packages. In order to visualize the distribution of eelgrass and kelp plants, these signals were not removed from the bathymetric data to make a bare Earth model.

4.5 RESULTS

4.5.1 Sedimentary Processes

We observe several anthropogenic sedimentary features in the bay including dredge scours, cable trenches, pipelines, and shoals. Most scour features are observed within the dredged channel (e.g., Fig. 3A). A prominent set of linear, cross-channel trenches is observed trending north-northeast north of the Coronado Bridge between downtown San Diego and Coronado Island (Fig. 3A). A major pipeline was mapped

along the bay side of Shelter Island that extends from the channel on the east side of Shelter Island, along the length of Shelter Island, and then bends around the southern end of the island, crosses the channel into Shelter Island Harbor, and continues up to the edge of data coverage near the Point Loma peninsula (Fig. 3B). The pipeline is imaged as a thin continuous feature often observed at the bottom of a topographically low trench (Fig. 3B). A triangular shaped shoal also is located at the southern end of Shelter Island, possibly an extension of fill used to build the island (Fig. 3B). There are also several areas with evidence of anthropogenic sediment re-working. The deepest part of the bay is adjacent to the naval submarine berths (Fig. 3C). Similar round, deep pits are also located near the other major piers around the bay (Figs. 3A, 3B). For example, at the cruise ship terminal, deep pits are observed between the piers and just to the west of the docks the seafloor exhibits semi-circular scours (Fig. 3D). To the north of the cruise ship terminal a ~2 m thick sediment depocenter mantles the most recent dredge surface (Figs. 3D & 4). In Chirp data, the dredge surface is a high amplitude, roughly horizontal reflector. The transparent unit above the dredge surface forms the depocenter, which is bounded on the north and east sides by the steep dredge walls (Fig. 4).

Despite the extensive anthropogenic alterations to the bay, several natural sediment features are also observed. For example, localized bedforms are found throughout the bay. Large-scale bedforms are located near the mouth of the bay, south of the Zuniga Jetty and east of the shipping channel (Fig. 3E). These bedforms are ~20 m wavelength, ~0.2-0.4 m height, are fairly linear, and trend southwest-northeast. They are slightly asymmetrical with the steep stoss side facing towards the southeast. Just north of the jetty on the east side of the channel there is a small patch of roughly symmetrical, large wavelength bedforms within an eelgrass bed (~50 m wavelength, ~0.4-0.8 m height) (Fig. 3C). Smaller bedforms are located both on the east and west side of the shipping channel near the bay mouth. East of the shipping channel, ~5-30 m wavelength

and ~0.1-0.4 m high, symmetrical bedforms are observed at ~12 m water depth with their axis trending east-west (Fig. 3E). West of the shipping channel, east-west trending, ~4-6 m wavelength, >0.5-0.1 m high symmetrical bedforms are observed south of Ballast Point, in ~6 m water depth (Fig. 3C). The bedforms on the west side of the channel die away approaching the shore at Point Loma where the seafloor exhibits a rougher, blockier character. In Chirp profiles across this area, the transgressive surface, represented by a strong, planar reflector, shoals to the west. A thick sediment lens is located adjacent to the dredged channel where the transgressive surface deepens (Fig. 5). A marked increase in sediment thickness occurs where the dip of the transgressive surface changes. The sediment deposit is acoustically transparent and thickens north toward Ballast Point reaching a maximum thickness of ~7 m (Fig. 5). On the surface of the deposit bedforms are ~10-15 m wavelength and ~0.2 m height (Fig. 3C). Another prominent set of bedforms is located between two Coronado Bridge pilings and extends parallel to the channel ~570 m. The bedforms form a strip parallel to the shipping channel with a maximum width of 35 m, with a wavelength of ~5 m and height of ~0.1-0.3 m (Fig. 3F). The crests of the bedforms trend east-west, perpendicular to the channel, and they appear symmetrical.

Paleochannels are also mapped throughout the bay and offshore Coronado Island and Silver Strand (Fig. 2B). The channels are characterized by a rough, irregular, channel-shaped horizon below the transgressive surface, and are filled with both thinly laminated and transparent to chaotic acoustic packages (Fig. 6).

4.5.2 Tectonics

Faults observed in Chirp data are mapped in Figure 2A. The Spanish Bight fault is mapped as two strands that diverge from Coronado Island to the north. The western strand trends north-south and the east strand trends N25°E. Direct offset of horizons at

the fault is difficult to measure, but the fault is identified by highly deformed strata with folded and tilted horizons (Fig. 4). In profiles on the north side of the shipping channel, we observe vertical down to the east offset of the transgressive surface (~0.5 m) and the seafloor (~0.4 m) above at the western fault strand (Fig. 4). Chirp profiles also image the Spanish Bight fault farther south at the edge of the shipping channel (Fig. 7). Here, the western strand appears to diverge upwards into two splays that both offset the seafloor. Horizons are highly deformed by the splays and a small wedge appears rotated (Fig. 7). The eastern strand is mapped out of the channel and offsets horizons below the seafloor down to the east, but does not offset the seafloor. West of the Spanish Bight fault, a previously unmapped fault was identified south of Harbor Island trending roughly north-south (Fig. 4). The fault zone is made up of several splays; offset horizons are identified approximately 2 m below the seafloor.

The seaward extent of some bay faults can be mapped offshore Coronado Island and the Silver Strand. For example, a splay of the Spanish Bight fault can be traced laterally offshore for ~7 km with a trend of ~N14°E (Fig. 8). The fault offsets the transgressive surface with a down to the east sense of slip. Maximum offset is approximately 1.2 m at a minimum water depth of ~16.7 m. At the southern extent, the fault appears to border the Cretaceous Rosario Group extending south from Point Loma. Offshore the paleochannels appear to be fault controlled (Fig. 6).

Three continuous fault strands are mapped as part of the Coronado fault zone (Fig. 9). The northern and central strands are subparallel and trend N30°E while the southern strand trends north-south (Fig. 2A). The northern strand is identified by downward folded horizons towards the fault (Fig. 9). The uppermost deformed horizon is ~2.6 m below the seafloor. The central strand is also marked by deformed horizons and exhibits some down to the west vertical offset. The depth to the most recent offset is difficult to define because of the extensive deformation, but the seafloor does not appear offset. Vertical offset is

also observed on the southernmost strand. Offset is observed as both down to the east and down to the west with the youngest offset horizon ~1.6 m below the seafloor. Maximum observed offset at the strand is ~3.7 m.

Previous mapping of the Silver Strand fault through the bay have the fault oriented roughly north-south (Kennedy and Tan, 2005). In Chirp data, two continuous strands are mapped in this vicinity, but they trend N58°W (Figs. 2B & 10). There appears to be slight vertical offset on the fault, but it is primarily identified by folding and deformation. Additionally, in the vicinity of the Silver Strand fault zone, a high amplitude, chaotic acoustic unit obscures detailed imaging below. The youngest offset observed is ~ 1 m below the seafloor. We also observe complex faulting in the vicinity of the Coronado Bridge with two distinct, continuous fault strands that trend N32°W. These faults also exhibit dip-slip motion and most recent offsets occur at variable depths. Offset on these strands reaches ~5 m (Fig. 11).

4.5.3 Biological Observations

We observe variations in the density and patterns of eelgrass and kelps within areas of San Diego Bay. Although diving was not performed as part of this effort, some of the vegetation was examined from the vessel and correlated to the bathymetric signals in real time. Additionally, comparisons between bathymetric signals were correlated to previously mapped eelgrass and kelp distributions to build confidence in identifying the plants imaged in the bathymetric and backscatter data (NAVFAC, 2011). Figure 3C illustrates the acoustic, bathymetric signal produced by a known patch of eelgrass (NAVFAC, 2011). Acoustic, backscatter data was also used to identify plants (Fig. 12).

The acoustic signal associated with eelgrass is observed in locations throughout the bay, primarily in shallow areas. A large eelgrass bed is located between the shipping channel and Zuniga Jetty (Fig. 3C). In the bathymetry data, the eelgrass is imaged as

a rough seafloor that reaches ~0.6-0.8 m above surrounding smooth seafloor. Zostera marina grows from the shallowest depths out to ~ 5.5 m water depth. The eelgrass becomes increasingly patchy with depth. Within the regional distribution of eelgrass there are some internal bare patches (Fig. 3C). One patch is tongue shaped oriented roughly east-west and located adjacent to the Zuniga Jetty at ~4 m water depth. The other patch is north of the jetty in ~3 m water, is also tongue shaped, and is filled with ~50 m wavelength bedforms. Within the bare patch, there are east-west oriented bedforms with ~50 m wavelength (Fig 3C).

East of Point Loma, acoustic backscatter data image two distinct types of plants. One was imaged as semi-circular bright spots (Fig. 12A) while the other was imaged as long thin bright spots that often extended high into the water column (Fig12B). The long thin bright spots were commonly associated with sightings of long feathery kelp in the water that were identified as Egregia menziesii. These kelp plants were only imaged close to Point Loma and were not observed elsewhere in the bay. The circular bright spots are also located in very shallow water (~3 m) just east of Point Loma. In bathymetry data, these patches look similar to eelgrass, though are much patchier. Eelgrass beds have previously been mapped in this area (NAVCO, 2011).

4.6 DISCUSSION

4.6.1 Sedimentary Processes

Much of San Diego Bay has been anthropogenically altered; its shorelines sediment distribution, and seafloor morphology. The sharp edges of dredged channels, linear cable trenches, and scour marks typical of the dredging process are all observed in the bay. Furthermore, anthropogenic forcing in the bay appears to play an important role in circulation patterns, sediment redistribution, and habitat patchiness.

The largest anthropogenic redistribution of sediment in the bay appears to be

associated with the cruise ship terminal and naval submarine base. At the cruise ship terminal, seafloor roughness and semi-circular patterns on the seafloor may be associated with propeller motion scraping and stirring up sediment. The re-suspended sediment is then re-deposited to the north in the corner of the dredged area because as the cruise ships exit the pier they turn clockwise and shunt all the re-suspended sediment northward (Fig. 3D and Fig. 4). The smooth seafloor on top of the thick sediment package indicates a primarily depositional environment contrasting with the scoured and rough erosional surface just to the south adjacent to the terminals (Fig. 3D). Approximately 2 m of sediment has been deposited above the dredge surface (Fig. 4).

The deepest point in San Diego Bay, adjacent to the naval submarine bays at Ballast Point was likely created by submarine operations eroding and re-suspending sediment (Fig. 3C). Some of this sediment would then become entrained in tidal currents and re-deposited elsewhere. We interpret the thick sediment deposit south of Ballast Point to be a constructional drift deposit created by swift tidal pumping through the narrow channel between Ballast Point and Coronado Island interacting with more quiescent water as the flow expands laterally just south of Ballast Point (Fig. 5). Some of the sediment entrained in the water column by the C-Tractor tugs towing the submarines likely contributes to this deposit. The diminishing thickness to the south indicates the deposit formed more on the ebb than the flood tide, and the topography of the deposit indicates it is constructional in nature (Figs. 3C and 5). .

Other anthropogenic alterations are important for considering circulation patterns within the bay. For example, the pipeline and shoal at the mouth of Shelter Island harbor could be playing an important role in bay circulation (Fig. 3B); inhibiting circulation in and out of Shelter Island harbor. Hull paint and the lack of tidal flushing in and out of the Shelter Island harbor would contribute to the build-up of high concentrations of copper in the water (Blake et al., 2004).

The bedforms located under and south of the Coronado Bridge appear tidally controlled (Fig. 3F). The symmetric shape is consistent with an oscillatory tidal current. The isolation of the bedforms in a thin ribbon is likely associated with the predominant path of large ships through the bridge pilings. Large cargo and military ships generally go under the span of the Coronado Bridge along the northern edge of the dredged channel; a path marked by the bedforms. The propeller swash from the ships could be winnowing out fine grain sediments, leaving behind sands that more readily form bedforms (e.g., Southard and Boguchwal, 1990).

South of Ballast Point, the transgressive surface shoals from the shipping channel towards Point Loma and appears to control the morphological features on the seafloor (Fig. 5). Closest to Point Loma, rough and blocky seafloor features are found where the transgressive surface appears to subcrop or outcrop near the seafloor. As the transgressive surface plunges to the east, the sediment deposit above thickens, and bedforms on the seafloor are observed. The transgressive surface is ~9 m deep at the channel edge (Fig. 5). Based on the sea level curve of Fairbanks (1989) and the depth of the transgressive surface, inundation occurred at ~5.5 ka. The differential accumulation of sediment near the Embarcadero and south of Ballast Point is very high yet extremely localized (Figs. 3C and 3D).

4.6.2 Tectonics

In some locations, the Spanish Bight fault appears to offset the seafloor (Figs. 4 & 7). The offset may be recording real slip on the fault, but could also result from fluid flow along the fault mobilizing unconsolidated sediment. Near the southern shore, offset of the seafloor appears more convincing because of the folded and tilted horizons between the two fault strands (Fig. 7). Towards the northern shore, the western strand offsets the dredge surface below the seafloor (Fig. 4). Given the offset of the dredge surface and

seafloor, the Spanish Bight fault appears to have been active recently.

The Spanish Bight fault and the newly identified fault (Harbor Island fault) trend north and project out of the bay towards Lindbergh Field (Fig. 4). Prior to permanent re-routing, the San Diego River has historically alternated flow from Mission Valley either west to Mission Bay or south to San Diego Bay, in the area of modern Harbor Island. Given the dip-slip component on the faults in the area of Harbor Island, these faults may be capable of altering the course of the river by stream capture and may help explain the migration of the San Diego River between Mission Valley and San Diego Bay through time.

The 7 km segment of the Spanish Bight fault zone mapped offshore offsets the transgressive surface as shallow as ~16.7 m below seafloor (Fig. 8). Based on a eustatic sea level curve and the assumption that the offset post-dated the formation of the transgressive surface, this constrains the age of the most recent event to be younger than 7.5 ka (Fairbanks, 1989). The 1.2 m offset of the transgressive surface is overlain by mobile Holocene sands, which would likely relax and thus erase any seafloor offset. Therefore, the most recent event on this strand may be younger than 7.5 ka. If the maximum 1.2 m offset resulted from one earthquake, the slip rate on this fault is ~0.16 mm/yr and the potential magnitude of the most recent event was ~M6.35 (7 km length and 15 km depth of fault zone -Wells and Coppersmith, 1994). This may be an underestimate because it only accounts for the vertical offset on a transtensional fault.

The shallow depths of offset on the Coronado and Silver Strand faults also suggest that these faults are active in the Holocene and vertical offsets demonstrates a component of dip-slip motion (transtension) on the faults. The transtensional faults also may play an important role in groundwater transport and flux of freshwater to the bay.

4.6.3 Biological Discussion

Light availability (related to depth and water clarity) and nutrient supply are the most important controls on eelgrass distribution (Hauxwell et al. 2003), but substrate characteristics also influence eelgrass habitats (Orth 1977). Patterns in eelgrass distribution appear controlled by sediment processes in some areas of the bay. For example, west of Zuniga Jetty, we observe patchiness in eelgrass habitat that does not appear to be depth or nutrient controlled because the patches occur within a regionally continuous zone that is mostly covered with eelgrass. These barrens areas are likely the result of mechanical benthic disturbance due to human activities. A bare patch located adjacent to Zuniga Jetty may be related to sediment spilling through the jetty from the east that constantly blankets the area (Fig. 3C). A bare patch farther north from the jetty is characterized by bedforms suggesting this zone may have coarser sediment than surrounding areas and greater current velocities. The bare patch is just south of the narrowest part of the mouth of the bay between Ballast Point and Coronado Island, and adjacent to a slight outward jog in the Coronado Island shoreline with a groin. Tidal currents through the narrow passage would be enhanced and could potentially winnow out fine sediments in the eelgrass free patch (Fig. 3C).

On the east side of Point Loma, patterns in kelp growth appear controlled by the shoaling of the transgressive surface towards the peninsula (Figs. 3C and 5). As the transgressive surface shoals, the younger sediment package above thins and exposes the underlying hardgrounds that are rockier. Multibeam data indicates that hardground outcrops at the seafloor are not as continuous as on the west side of Point Loma, which may result in the different ecosystem characteristics observed in the major Point Loma kelp forest offshore (Fig 12). The highly turbid and protected environment within the Bay likely limits the distribution of *Macrocystis pyrifera* (North et al. 1986). The semi-circular bright patches observed in backscatter data (Fig. 12A) appear to be eelgrass

based on previous mapping and acoustic characteristics. The patchier nature of this area compared with the east side of the shipping channel, might be related to the rockier substrate at this location. It may also be possible that the eelgrass near Point Loma is a different species than near Zuniga jetty that is more commonly found in rockier areas (i.e., *Phyllospadix*; Turner, 1985), or that we are imaging other species of brown algae (i.e., *Sargassum muticum* or *Cystoseira osmundacea*; Norton, 1977; Abbott and Hollenberg, 1976). Additional groundtruthing is required to determine the nature of the imaged plants.

4.7 CONCLUSIONS

Anthropogenic forcing plays a major role in sediment processes and consequent morphology in San Diego Bay. With minimal terrestrial input, shipping activities in the bay appear to be the major driver of sediment reworking and differential deposition. Symmetric bedforms throughout much of the bay are consistent with oscillatory tidal pumping, which is an important process for bay circulation and flushing. Faults mapped in the bay appear transtensional and several appear active in the Holocene. Dip slip motion on bay faults, in particular the Spanish Bight and Harbor Island faults could play an important role in groundwater flow and may have altered the course of the San Diego River by stream capture. Furthermore, paleochannels and faulting through the Silver Strand could create weak zones that could lead to breakthrough during the rapid sea level rise and astronomical high tides. The geology of the bay, both natural and anthropogenic has important links to eelgrass and kelp habitats.

Future work needs to be conducted to understand better the impact of anthropogenic structures and sediment re-working on bay circulation and contamination. Dating of sediments within the bay would provide insights into the earthquake history on active faults to assess seismic risk to the cities of San Diego and Coronado. Modeling of

predicted future sea level rise using bathymetry and Chirp data presented here also would elucidate potential hazards and assist in preparing for future impacts. Furthermore, this study provides a baseline for future work on eelgrass and kelp habitats in the bay, which will be important for ecosystem management plans in response to rapid sea level and increase storminess.

4.8 ACKNOWLEDGEMENTS

We would like to thank E. Aaron for immeasurable field assistance and R. Switzer and T. Martin for multibeam data processing assistance.

The text and figures from this chapter are being prepared for publication in: Maloney, J.M., Driscoll, N.W., Babcock, J.M, Anderson, T. and Parnell, P.E., In Prep, Geological constraints on biohabitats: A geophysical characterization of San Diego Bay and adjacent regions, California. The dissertation author was the primary researcher and author of the submitted work. The co-authors directed and supervised that research, which forms the basis for this chapter.

4.9 REFERENCES

Abbott, I.A., and Hollenberg, G.J., 1976, Marine Algae of California, Stanford University Press, Stanford, CA.

Astiz, L., and Shearer, P.M., 2000, Earthquake locations in the inner Continental Borderland, offshore southern California: Bulletin of the Seismological Society of America, v. 90, no. 2, p. 425-449.

Basile, C., and Brun, J.P., 1998, Transtensional faulting patterns ranging from pull-apart basins to transform continental margins; an experimental investigation: Journal of Structural Geology, v. 21, no. 1, p. 23-37.

Bell, S.S., Robbins, B.D., and Jensen, S.L., 1999, Gap dynamics in a eelgrass landscape: Ecosystems, v. 2, no. 6, p. 493-504.

Bohannon, R.G. and Geist, E., 1998, Upper crustal structure and Neogene tectonic development of the California continental borderland: Geological Society of America Bulletin, v. 110, p. 779-800.

Canada, L.A., 2006, “Sitting on the Dock of the Bay:” 100 years of photographs from the San Diego Historical Society: The Journal of San Diego History, San Diego Historical Society Quarterly, v. 52, no. 1 & 2, Eds. Engstrand, I.H.W. and McClain, M.

Chadwick, D.B., and Largier, J.L., 1999, The influence of tidal range on the exchange between San Diego Bay and the ocean: Journal of Geophysical Research, v. 104, no. C12, p. 29,885-829,899.

Daniell, J.J., Harris, P.T., Hughes, M.G., Hemer, M., and Heap, A., 2008, The potential impact of bedform migration on eelgrass communities in Torres Strait, northern Australia: Continental Shelf Research, v. 28, no. 16, p. 2188-2202.

Delgadillo-Hinojosa, F., Zirino, A., Holm-Hansen, O., Hernandez-Ayon, J.M., Boyd, T.J., Chadwick, B., and Rivera-Duarte, I., 2008, Dissolved nutrient balance and net ecosystem metabolism in a Mediterranean-climate coastal lagoon: San Diego Bay: Estuarine Coastal and Shelf Science, v. 76, p. 594-607.

Duarte, C.M., 2002, The future of eelgrass meadows: Environmental Conservation, v. 29, no. 2, p. 192-206.

Fairbanks, R.G., 1989, A 17,000-year glacio-eustatic sea level record; influence of glacial melting rates on the Younger Dryas event and deep-ocean circulation: Nature, v. 342, no. 6250, p. 637-642.

Fonseca, M.S., Kenworthy, W.J., and Thayer, G.W., 1998, Guidelines for the conservation and restoration of eelgrasses in the United States and adjacent waters: National Oceanic and Atmospheric Administration (NOAA) Coastal Ocean Office.

Hart, M.W., 1974, Radiocarbon Ages Of Alluvium Overlying La-Nacion Fault, San-Diego, California: Geological Society Of America Bulletin, v. 85, no. 8, p. 1329-1332.

Hauxwell, J., Just C., and Ivan V., 2003, Eelgrass Zostera Marina Loss in Temperate

Estuaries: Relationship to Land-derived Nitrogen Loads and Effect of Light Limitation Imposed by Algae: Marine Ecology Progress Series, v. 247, no. 1, p. 59–73.

Hemminga, M.A., and Duarte, C.M., 2000, Eelgrass Ecology, Cambridge, Cambridge University Press.

Henkart, P., 2003, SIOSEIS software. Scripps Institution of Oceanography, La Jolla, California. http://sioseis.ucsd.edu.

Hine, A.C., Evans, M.W., Davis, R.A., and Belknap, D.F., 1987, Depositional response to eelgrass mortality along a low-energy, barrier-island coast, West-central Florida: Journal of Sedimentary Petrology, v. 57, no. 3, p. 431-439.

Intergovernmental Panel on Climate Change (IPCC), 2007, The Physical Science Basis: Contribution of Working Group I to the Fourth Assessment Report of the Intergovernmental Panel on Climate Change, Eds. S. Solomon et al., Cambridge University Press, Cambridge.

Katzman, R., ten Brink, U.S., and Lin, J., 1995, Three-dimensional modeling of pull-apart basins; implications for the tectonics of the Dead Sea Basin: Journal of Geophysical Research, v. 100, no. B4, p. 6295-6312.

Kennedy, M.P., and Clarke, S.H., 1999, Analysis of late Quaternary faulting in San Diego Bay and hazard to the Coronado Bridge: California Division of Mines and Geology Open-File Report, v. 97-10A.

Kennedy, M.P., and Welday, E.E., 1980, Recency and character of faulting offshore metropolitan San Diego, California: California Division of Mines and Geology.

Koch, E.M., 2001, Beyond light: Physical, geological, and geochemical parameters as possible submersed aquatic vegetation habitat requirements: Estuaries, v. 24, no. 1, p. 1-17.

Largier, J.L., 1995, San Diego Bay Circulation - A study of the circulation of water in San Diego Bay for the purpose of assessing, monitoring and managing the transport and potential accumulation of pollutants and sediment in San Diego Bay.

Largier, J.L., Hollibaugh, J.T., and Smith, S.V., 1997, Seasonally Hypersaline Estuaries in Mediterranean-climate Regions: Estuarine, Coastal and Shelf Science, v. 45, p. 789-797.

Legg, M.R., 1985, Geologic structure and tectonics of the inner continental borderland offshore northern Baja California, Mexico: University of California Santa Barbara Ph.D. thesis.

Lindvall, S.C., and Rockwell, T.K., 1995, Holocene activity of the Rose Canyon fault zone in San Diego, California: Journal of Geophysical Research, v. 100, no. B12, p. 24,121-124,132.

Magistrale, H., 1993, Seismicity of the Rose Canyon fault zone near San Diego, California: Bulletin of the Seismological Society of America, v. 83, no. 6, p. 1971-1978.

Maloney, J.M., Driscoll, N.W., Kent, G.M., and Brothers, D.S., in prep., Segmentation and step-overs along strike slip fault systems in the inner California borderlands: Implications for fault architecture and basin formation.

Marba, N., and Duarte, C.M., 1995, Coupling of eelgrass (Cymodocea-nodosa) patch dynamics to subaqueous dune migration: Journal of Ecology, v. 83, no. 3, p. 381-389.

Marshall, M., 1989, Detailed gravity studies and the tectonics of the Rose Canyon--Point Loma--La Nacion Fault System, San Diego, California: Proceedings, Workshop on “The seismic risk in the San Diego region: Special focus on the Rose Canyon Fault system,” June 29-30. Ed. Roquemore, G., p. 80-99.

Masters, P.M., 2006, Holocene sand beaches of Southern California: ENSO forcing and coastal processes on millennial scales: Palaeogeography, Palaeoclimatology, Palaeoecology, v. 232, no. 1, p. 73-95.

Mazor, R.D. and Schiff, K., 2007a, Surface water ambient monitoring program (SWAMP) report on the Otay Hydrologic Unit: Technical Report 527, prepared for the California Regional Water Quality Control Board, San Diego Region (Region 9). Southern California Coastal Water Research Project.

Mazor, R.D. and Schiff, K., 2007b, Surface water ambient monitoring program (SWAMP) report on the Pueblo San Diego Hydrologic Unit: Technical Report 527, prepared for the California Regional Water Quality Control Board, San Diego Region (Region 9). Southern California Coastal Water Research Project.

Mazor, R.D. and Schiff, K., 2007c, Surface water ambient monitoring program (SWAMP) report on the Sweetwater Hydrologic Unit: Technical Report 527 prepared for the California Regional Water Quality Control Board, San Diego Region (Region 9). Southern California Coastal Water Research Project.

McClay, K., and Dooley, T., 1995, Analogue models of pull-apart basins: Geology, v. 23, no. 8, p. 711-714.

North, W.J., Jackson, G.A., and Manley, S.L., 1986, Macrocystis and Its Environment, Knowns and Unknowns: Aquatic Botany, v. 26, p. 9–26.

Norton, T.A., 1977, The growth and development of Sargassum muticum (Yendo) Fensholt: Journal of Experimental Marine Biology and Ecology, v. 25, no. 1, p. 41-53.

Orth, R.J., 1977. The importance of sediment stability in seagrass communities. In Coull BL(ed) Ecology of Marine Benthos, University of South Carolina Press, Columbia, p281-300.

Orth, R.J., Carruthers, T.J.B., Dennison, W.C., Duarte, C.M., Fourqurean, J.W., Heck, K.L., Hughes, A.R., Kendrick, G.A., Kenworthy, W.J., Olyarnik, S., Short, F.T., Waycott, M., and Williams, S.L., 2006, A global crisis for seagrass ecosystems: Bioscience, v. 56, no. 12, p. 987-996.

Peñafuerte, G.S., 2003, Military mission and the environment; the Navy in San Diego Bay in ed. Garbaciak Jr., S., Dredging ‘02: Key Technologies for Global Prosperity, http://dx.doi.org/10.1061/40680(2003)123

Peng, J., and Zeng, E.Y., 2007, An integrated geochemical and hydrodynamic model for tidal coastal environments: Marine Chemistry, v. 103, no. 1-2, p. 15-29.

Pfeffer, W.T., Harper, J.T., and O’Neel, S., 2008, Kinematic constraints on glacier contributions to 21st-century sea-level rise: Science, v. 321, p. 1340-1343.

Pourade, R.F., 1960, The Explorers 1492-1774, Union-Tribune Publishing Company, Copley Press.

Rahmstorf, S., 2007, A semi-emperical approach to projecting future sea-level rise: Science, v. 315, p. 368-370.

Rambo, C.E. and Speidel, W.C., 1969, A case study of estuarine sedimentation in Mission Bay-San Diego Bay, California, Prepared for U.S. Department of the Interior, Federal Water Pollution Control Administration, Contract no. 14-12-425. Marine Advisers, Inc., La Jolla, California.

Rockwell, T., 2010, The Rose Canyon Fault Zone in San Diego, Fifth International Conference on Recent Advances in Geotechnical Earthquake Engineering and Soil Dynamics and Symposium in Honor of Professor I.M. Idriss: San Diego, California.

Ryan, H.F., Conrad, J.E., Paull, C.K., and McGann, M., 2012, Slip rate on the San Diego Trough Fault Zone, Inner California Borderland, and the 1986 Oceanside Earthquake Swarm Revisited: Bulletin of the Seismological Society of America, v. 102, no. 6, p. 2300-2312.

United States Fish and Wildlife Service (USFWS), 2006, San Diego Bay National Wildlife Refuge, Sweetwater Marsh and South San Diego Bay Units: Final Comprehensive Conservation Plan and Environmental Impact Statement Summary. Downloaded 5/6/2011 from http://www.fws.gov/sandiegorefuges/new/ccp/ccp.htm.

Short, F.T., and Wyllie-Echeverria, S., 1996, Natural and human-induced disturbance of eelgrasses: Environmental Conservation, v. 23, no. 1, p. 17-27.

Turner, T., 1985, Stability of rocky intertidal surfgrass beds; persistence, preempton, and recovery: Ecology, v. 66, no. 1, p. 83-92.

Vedder, J. G., 1987, Regional geology and petroleum potential of the southern California border-land, in, Scholl, D. W., Grantz, A., and Vedder, J. G., eds., Geology and resource potential of the continental margin of western North America and adjacent ocean basins—Beaufort Sea to Baja California: Houston, Texas, Circum-Pacific Council for Energy and Mineral Re- sources, Earth Science Series, v. 6, p. 403–447.

Waycott, M., Duarte, C.M., Carruthers, T.J.B., Orth, R.J., Dennison, W.C., Olyarnik, S., Calladine, A., Fourqurean, J.W., Heck, K.L., Hughes, A.R., Kendrick, G.A., Kenworthy, W.J., Short, F.T., and Williams, S.L., 2009, Accelerating loss of eelgrasses across the globe threatens coastal ecosystems: Proceedings of the National Academy of Sciences of the United States of America, v. 106, no. 30, p. 12377-12381.

Wells, D.L., and Coppersmith, K.J., 1994, New Empirical Relationships among Magnitude, Rupture Length, Rupture Width, Rupture Area, and Surface Displacement: Bulletin of the Seismological Society of America, v. 84, no. 4, p. 974-1002.

Wu, J.E., McClay, K., Whitehouse, P., and Dooley, T., 2009, 4D analogue modelling of transtensional pull-apart basins: Marine and Petroleum Geology, v. 26, p. 1608-1623.

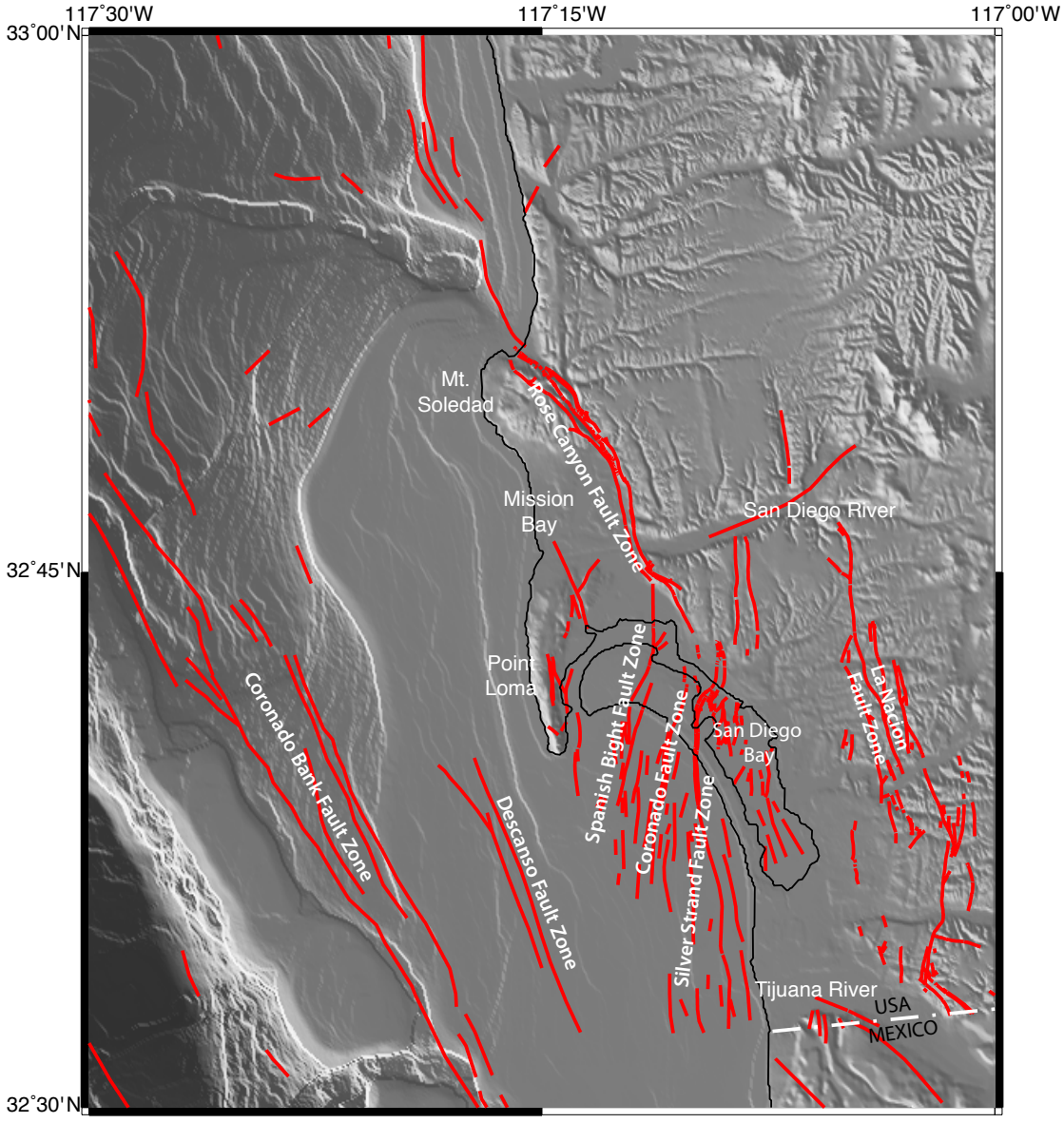

Figure 4-1: Regional map of San Diego showing major fault zones and morphologic features. Major fault zones are labeled.

Figure 4-2: (A) Map of San Diego Bay showing collected bathymetry data, Chirp track lines (white), previously mapped faults (green), and faults mapped in this study (black). Abbreviations: HIF – Harbor Island Fault; SBF – Spanish Bight Fault; CF – Coronado Fault; SSF – Silver Strand Fault. (B) Map of San Diego Bay showing collected bathymetry data, Chirp track lines (white), and locations of Chirp figures shown in the paper. Mapped paleochannels are also shown in yellow. Abbreviations: HIF – Harbor Island Fault.

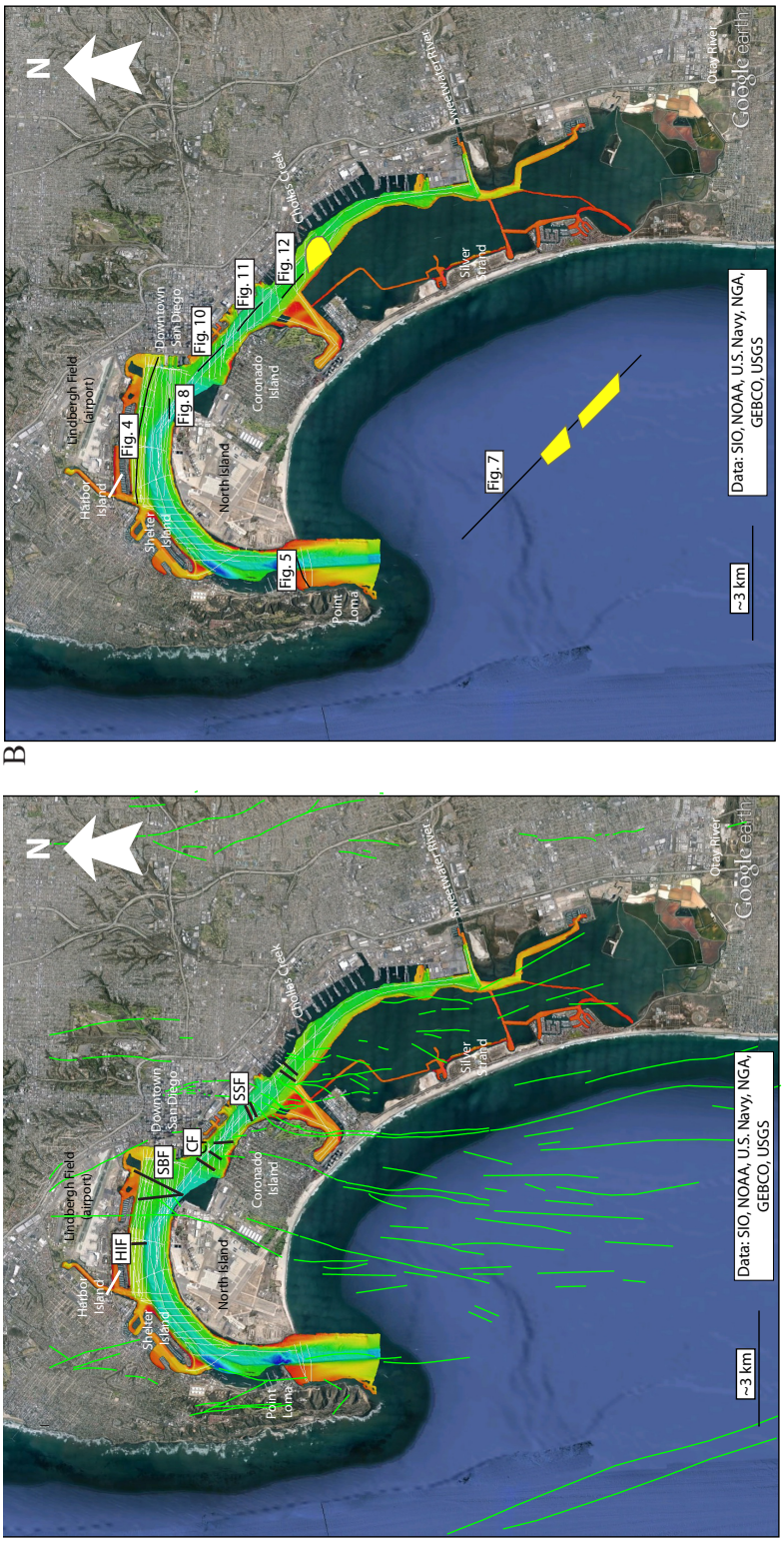
A
B
N
HIF
SBF
CF
SSF
Fig. 4
Fig. 5
Fig. 7
Fig. 8
Fig. 10
Fig. 11
Fig. 12
Harbor Island
Lindbergh Field (airport)
Shelter Island
Downtown San Diego
North Island
Coronado Island
Point Loma
Chollas Creek
Silver Strand
Sweetwater River
Otay River
~3 km
Data: SIO, NOAA, U.S. Navy, NGA, GEBCO, USGS
Google earth

Figure 4-3: Map of San Diego Bay showing collected bathymetry data and locations of blow-up figures.
(A) Bathymetry illustrating the morphology of the shipping channel, dredge scours, cross-channel trenches, and deep pits interpreted to result from shipping traffic.
(B) Bathymetry from near Shelter Island showing the triangular shoal extending north from the island, the long pipeline, which runs along the entire length of the island, and deep pits associate with the Scripps Marine Facility.
(C) Bathymetry from near the mouth of San Diego Bay illustrating several features described in detail in the text.
(D) Bathymetry from near the cruise ship terminal showing sediment scour and re-working.
(E) Bathymetry from the mouth of the bay showing several bedforms of various scales.
(F) Bathymetry near Coronado Bridge showing a ribbon of bedforms.

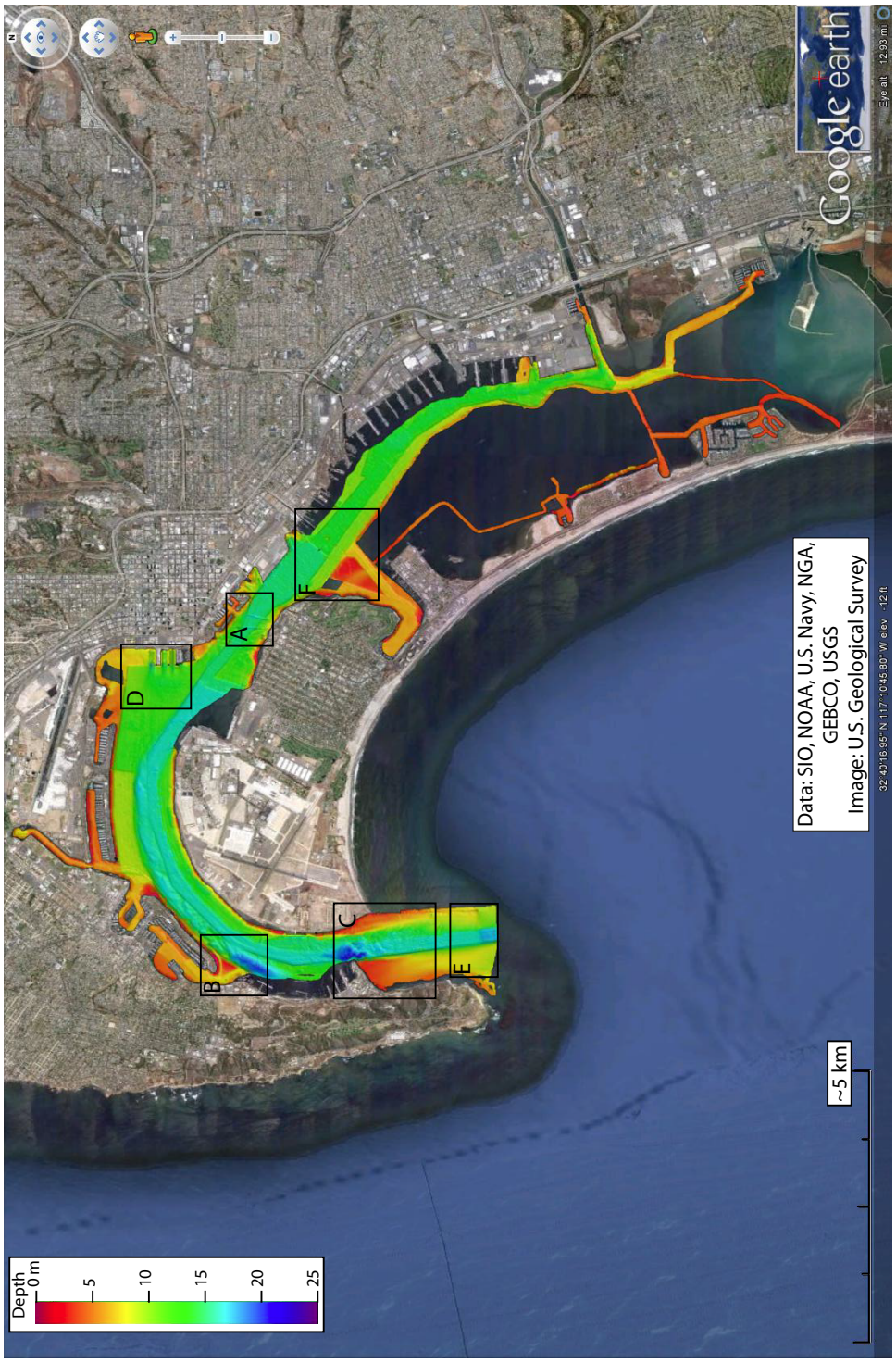
Depth
0 m
5
10
15
20
25
~5 km
A
B
C
D
E
F
Data: SIO, NOAA, U.S. Navy, NGA, GEBCO, USGS
Image: U.S. Geological Survey
Google earth

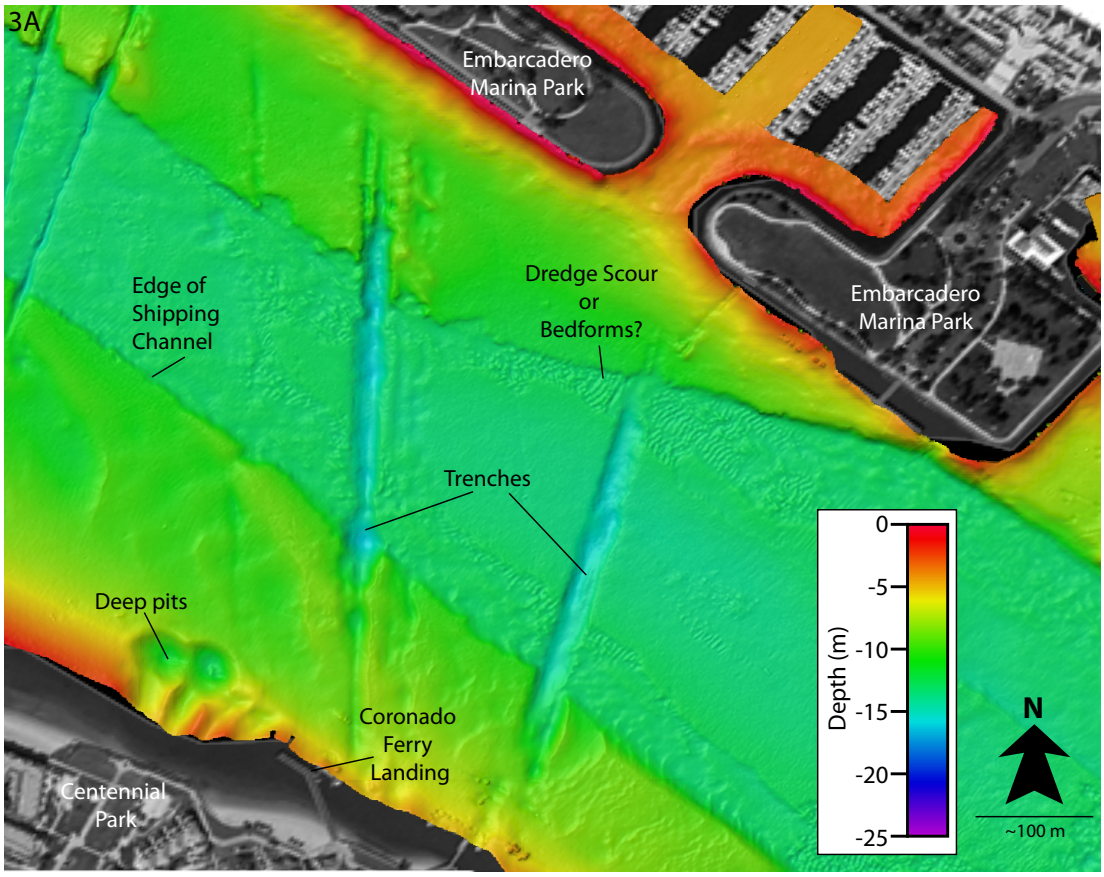

Figure 4-3:(A) Bathymetry illustrating the morphology of the shipping channel, dredge scours, cross-channel trenches, and deep pits interpreted to result from shipping traffic.

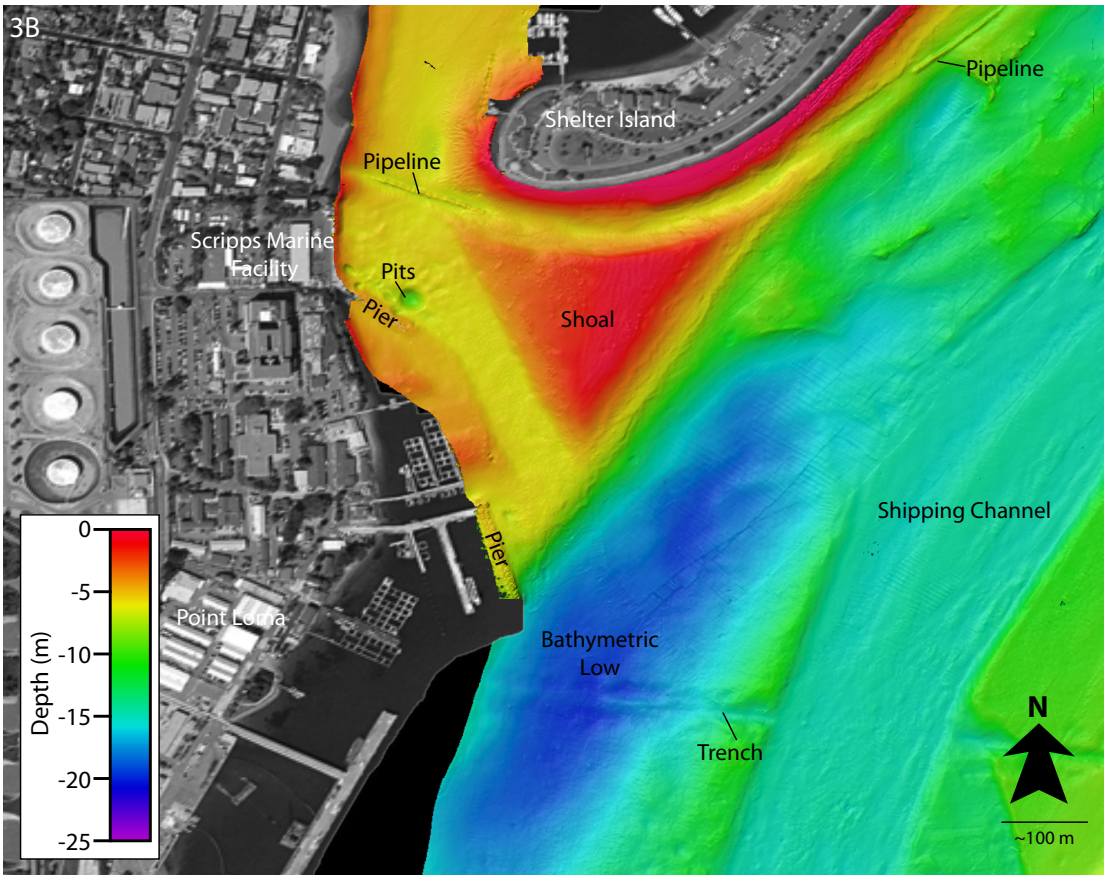

Figure 4-3: (B) Bathymetry from near Shelter Island showing the triangular shoal extending north from the island, the long pipeline, which runs along the entire length of the island, and deep pits associate with the Scripps Marine Facility.

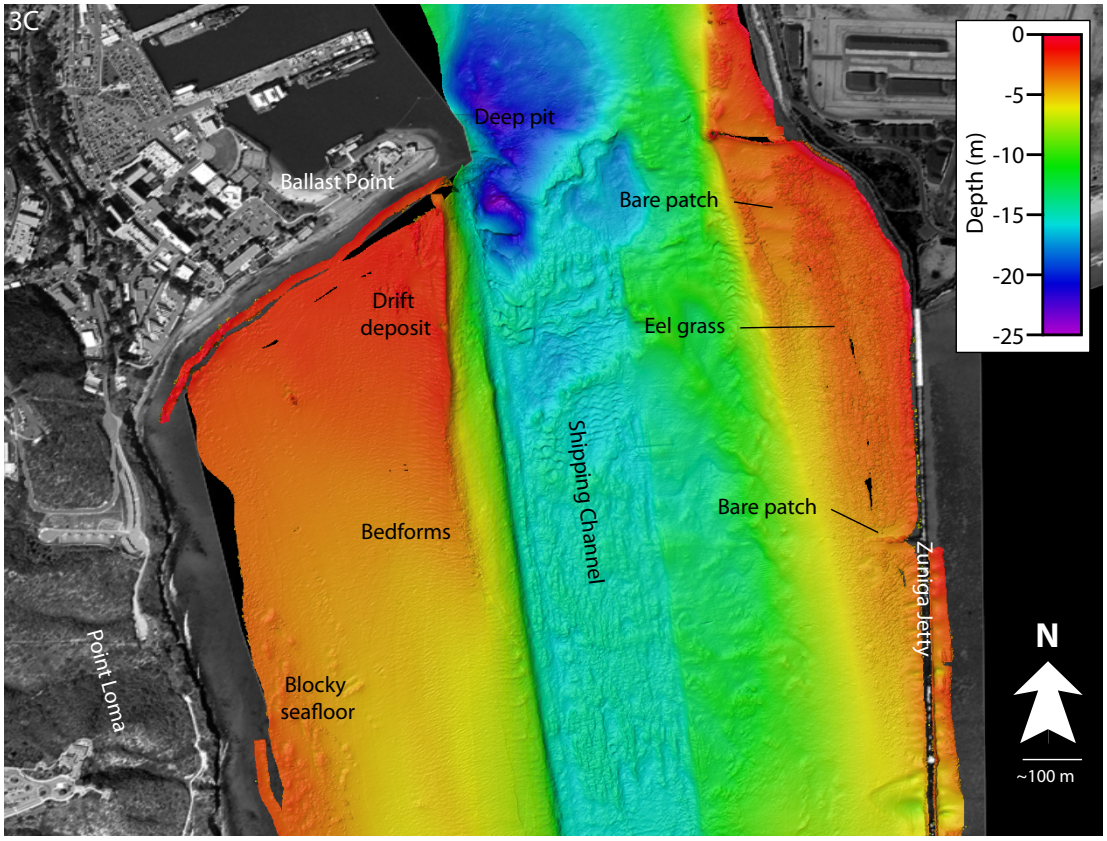

Figure 4-3: (C) Bathymetry from near the mouth of San Diego Bay illustrating several features described in detail in the text.

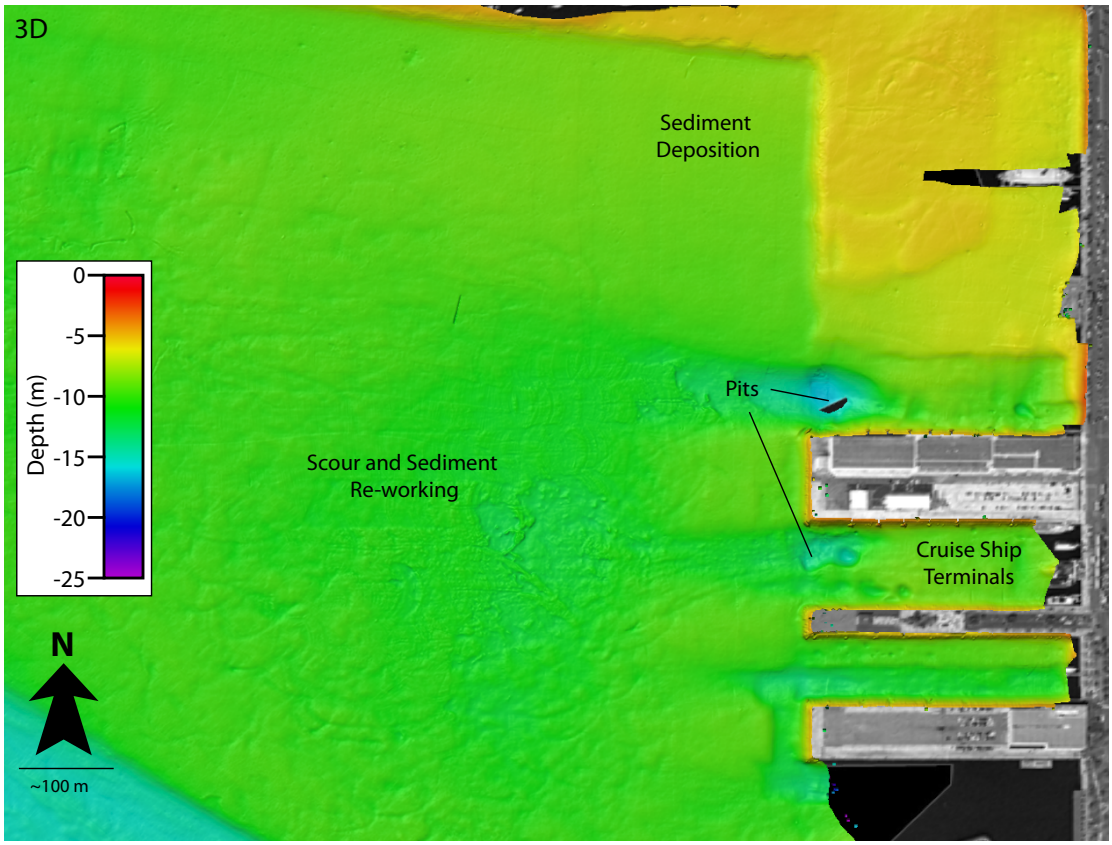

Figure 4-3: (D) Bathymetry from near the cruise ship terminal showing sediment scour and re-working.

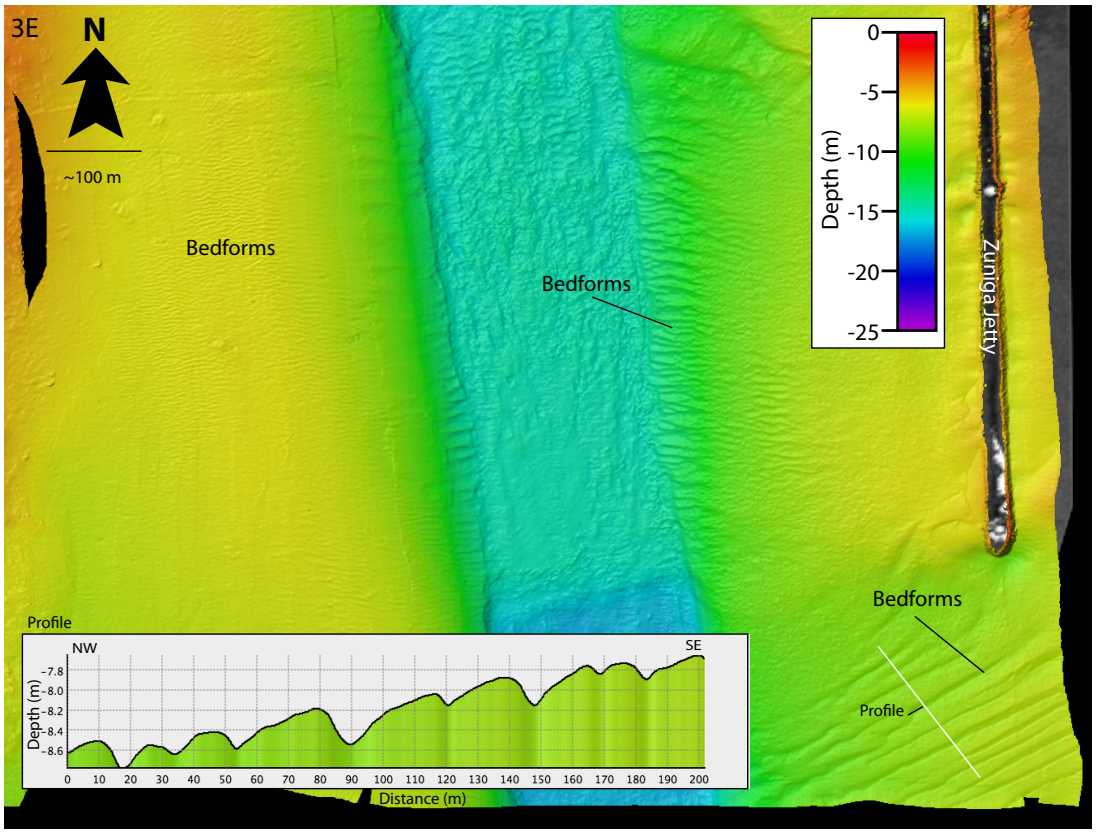

Figure 4-3: (E) Bathymetry from the mouth of the bay showing several bedforms of various scales.

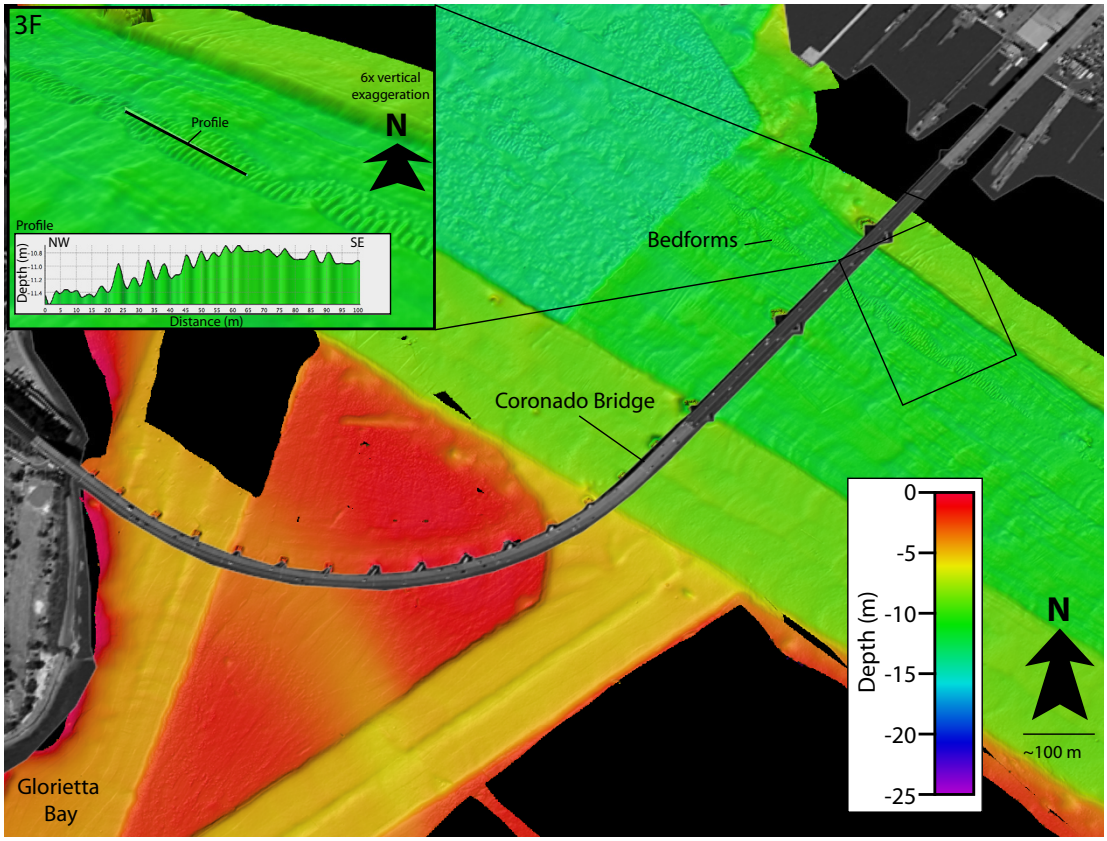

Figure 4-3: (F) Bathymetry near Coronado Bridge showing a ribbon of bedforms.

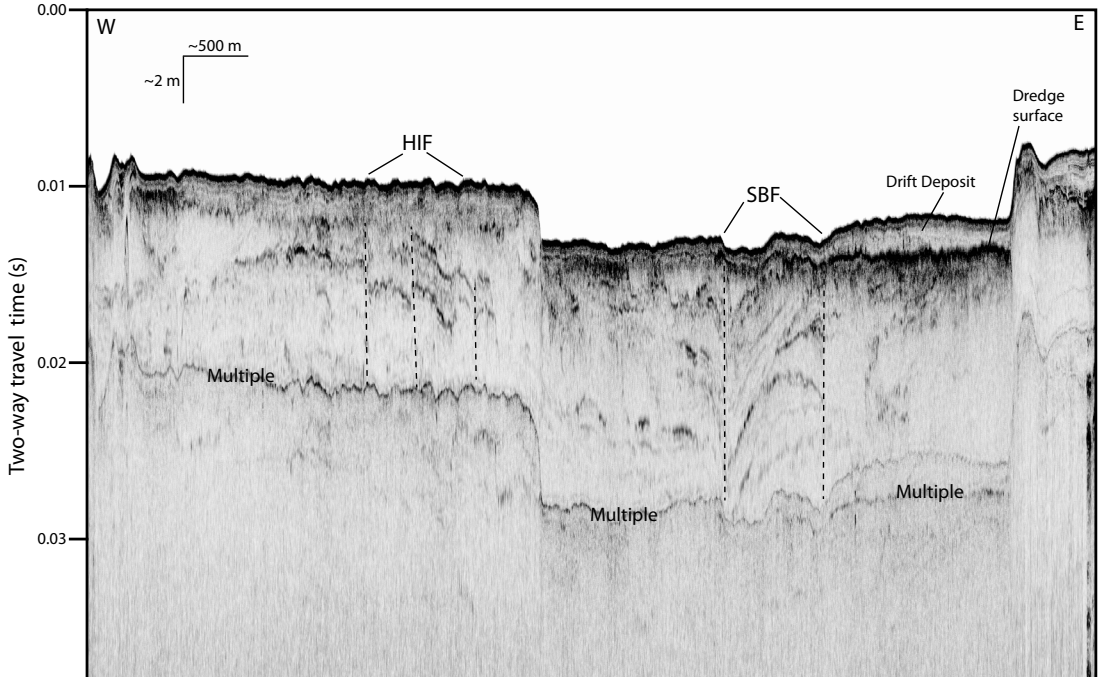

Figure 4-4: Chirp profile imaging deformation on the newly mapped Harbor Island fault (HIF) and the Spanish Bight fault (SBF). In this region, the SBF appears to offset the dredge surface and the seafloor over the western strand. Also imaged is the sediment lens mantling the dredged surface north of the cruise ship terminals. Location is shown in Figure 2B. Abbreviations: HIF – Harbor Island fault; SBF – Spanish Bight fault.

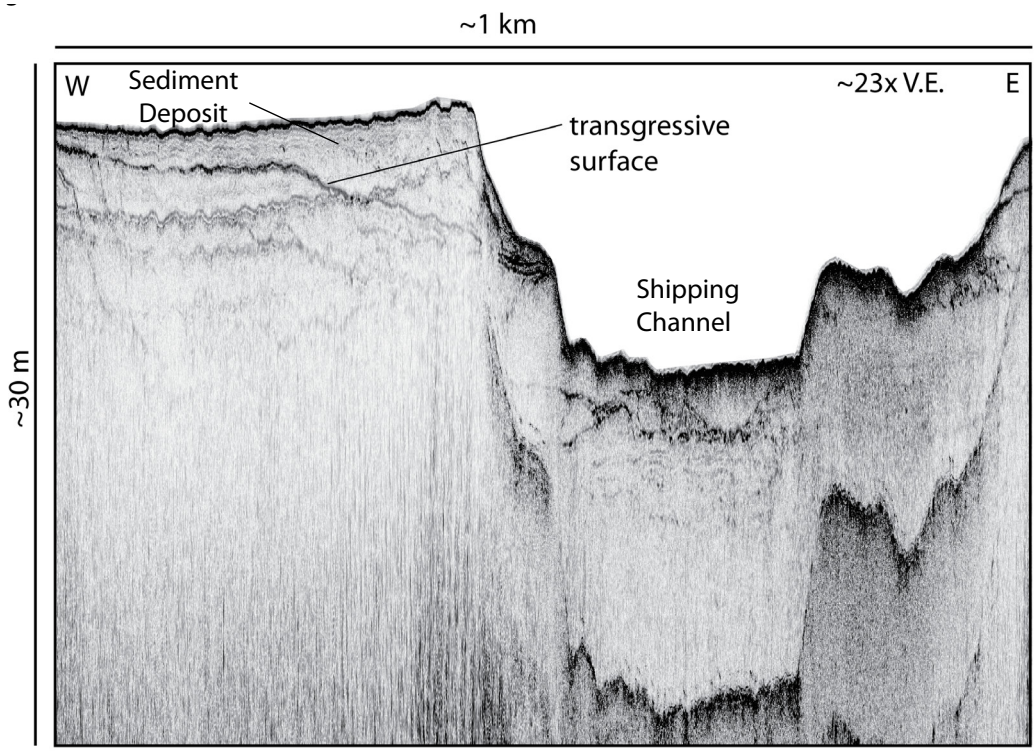

Figure 4-5: Chirp profile illustrating the shoaling of the transgressive surface towards Point Loma away from the shipping channel as well as the constructional sediment deposit south of Ballast Point. Location is shown in Figure 2B.

Figure 4-6: Chirp profile offshore the Silver Strand showing paleochannels and strands of the Spanish Bight fault (SBF) and Coronado fault (CF) where they extend offshore. The SBF appears to offset the transgressive surface at this location. Location is shown in Figure 2B. Abbreviations: G – ghost; M – multiple; TS – transgressive surface; SBF – Spanish Bight Fault; CF – Coronado Fault.

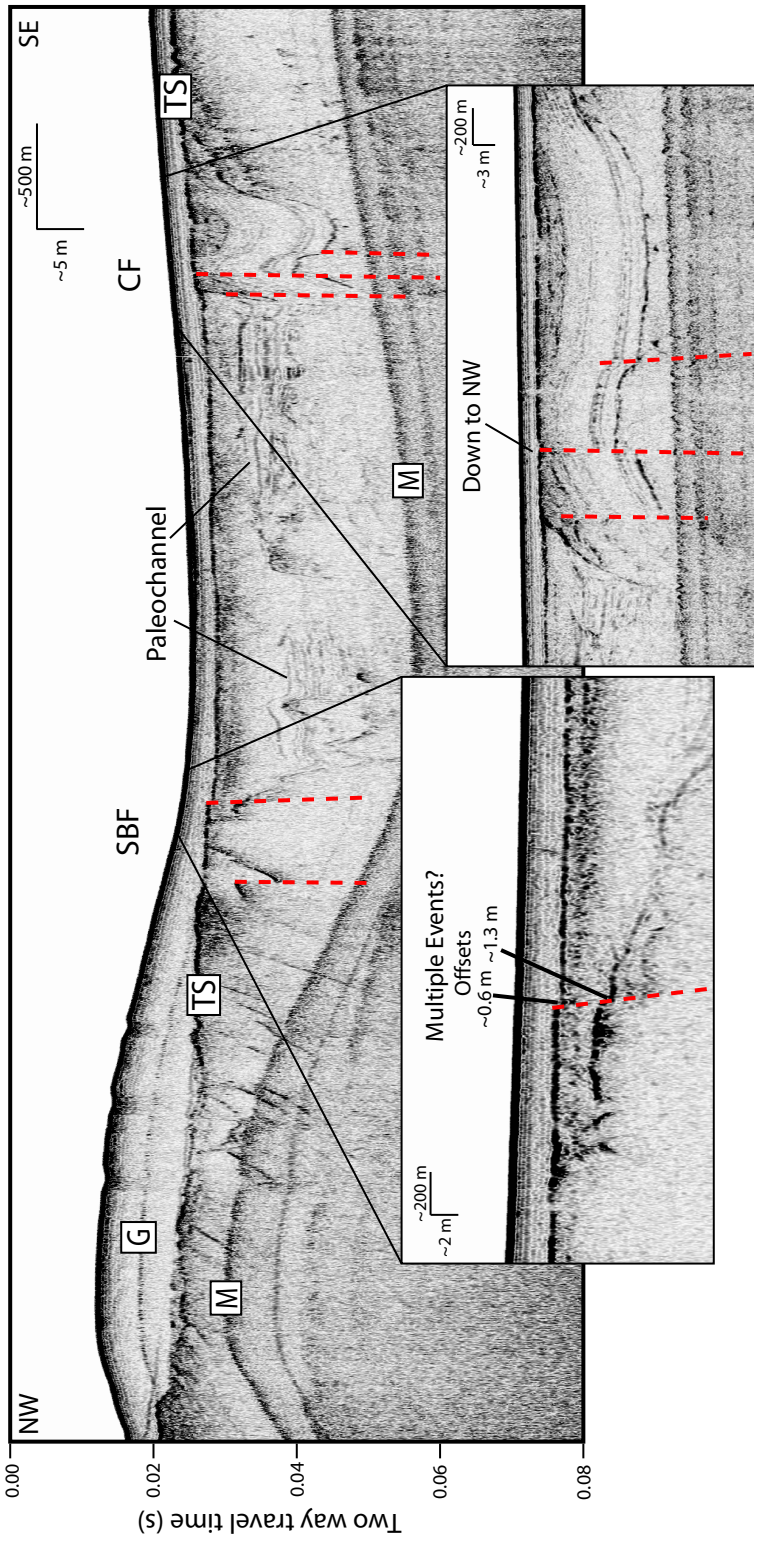
NW
SE
SBF
CF
Paleochannel
G
M
TS
TS
M
~500 m
~5 m
~200 m
~2 m
Multiple Events?
Offsets
~0.6 m ~1.3 m
~200 m
~3 m
Down to NW
0.00
0.02
0.04
0.06
0.08
Two way travel time (s)

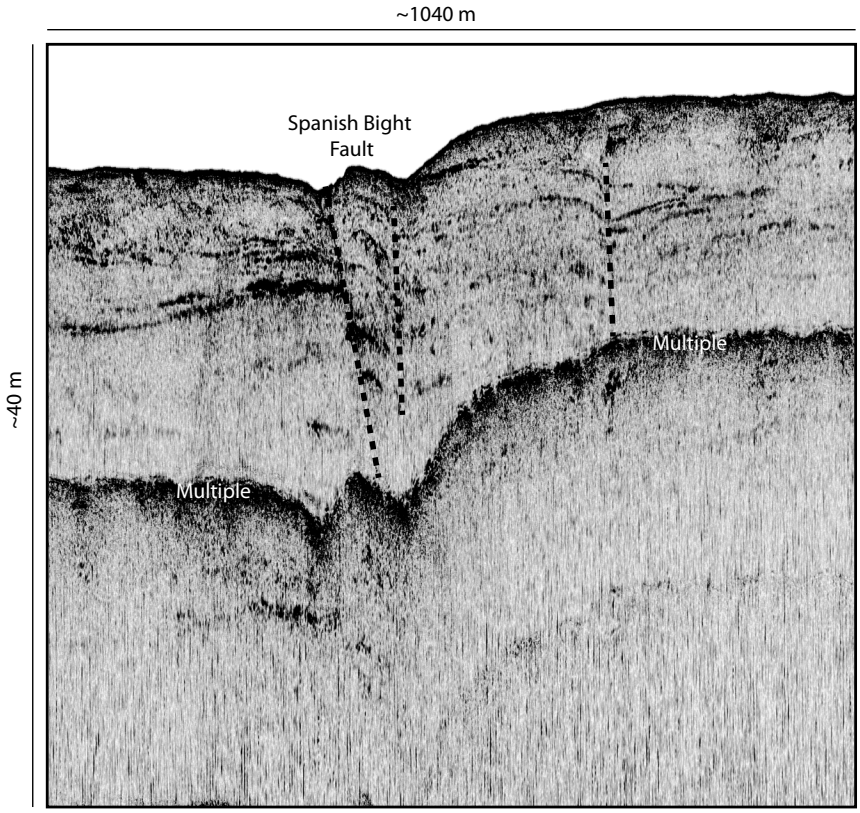

Figure 4-7: Enlarged Chirp profile showing the Spanish Bight fault where the western strand diverges towards the surface into two splays, forming a rotated wedge. The splays offset the seafloor at the edge of the shipping channel. The eastern strand also deforms horizons outside the channel, but does not appear to offset the seafloor. Location is shown in Figure 2B.

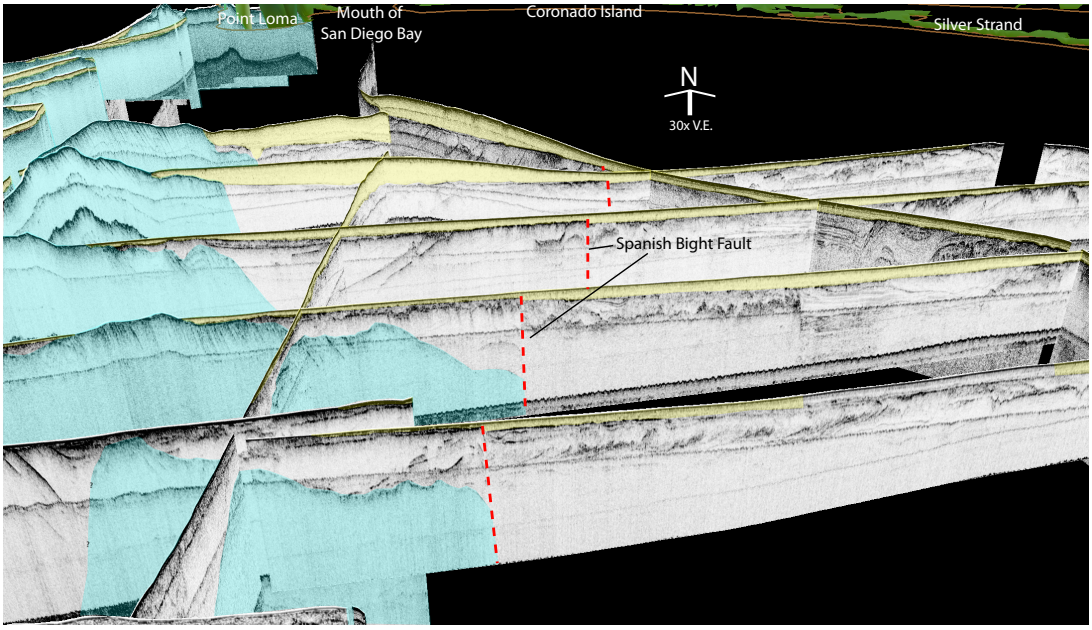

Figure 4-8: Fence diagram showing Chirp data offshore the Silver Strand with the ~7 km mapped segment of the Spanish Bight fault (dashed red). Yellow is Holocene sediments above the transgressive surface, blue is Cretaceous hardgrounds extending south from Point Loma.

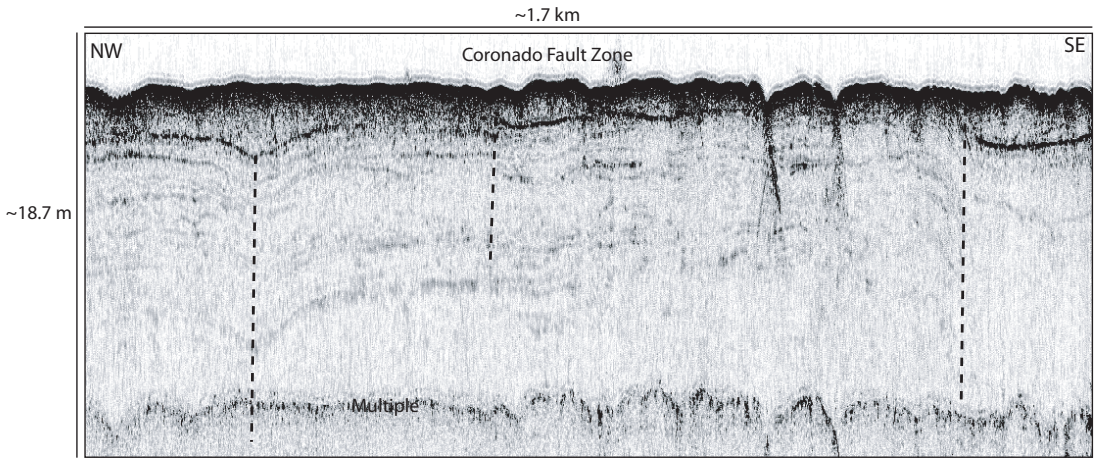

Figure 4-9: Chirp profile showing three strands of the Coronado Bank fault (dashed). Location is shown in Figure 2B.

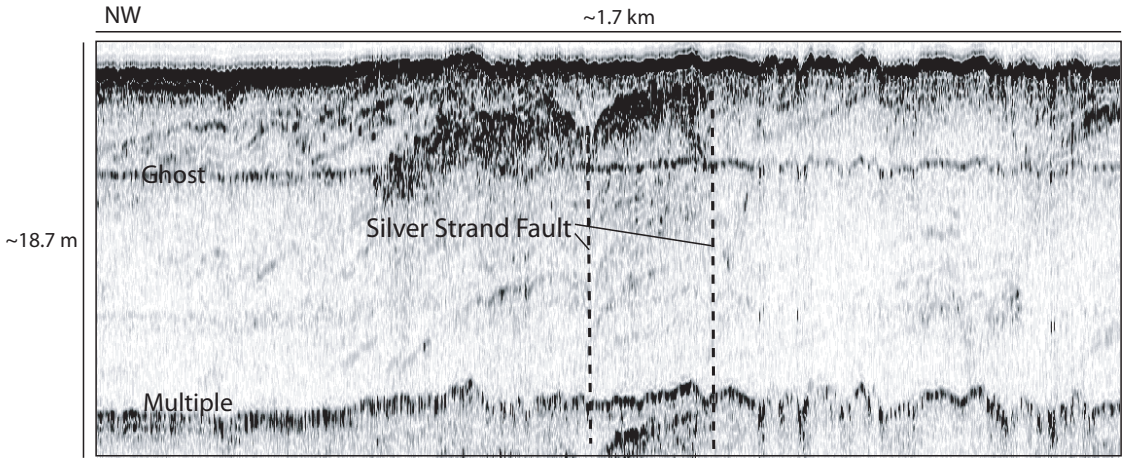

Figure 4-10: Chirp profile showing deformation at the Silver Strand fault (dashed). Location is shown in Figure 2B.

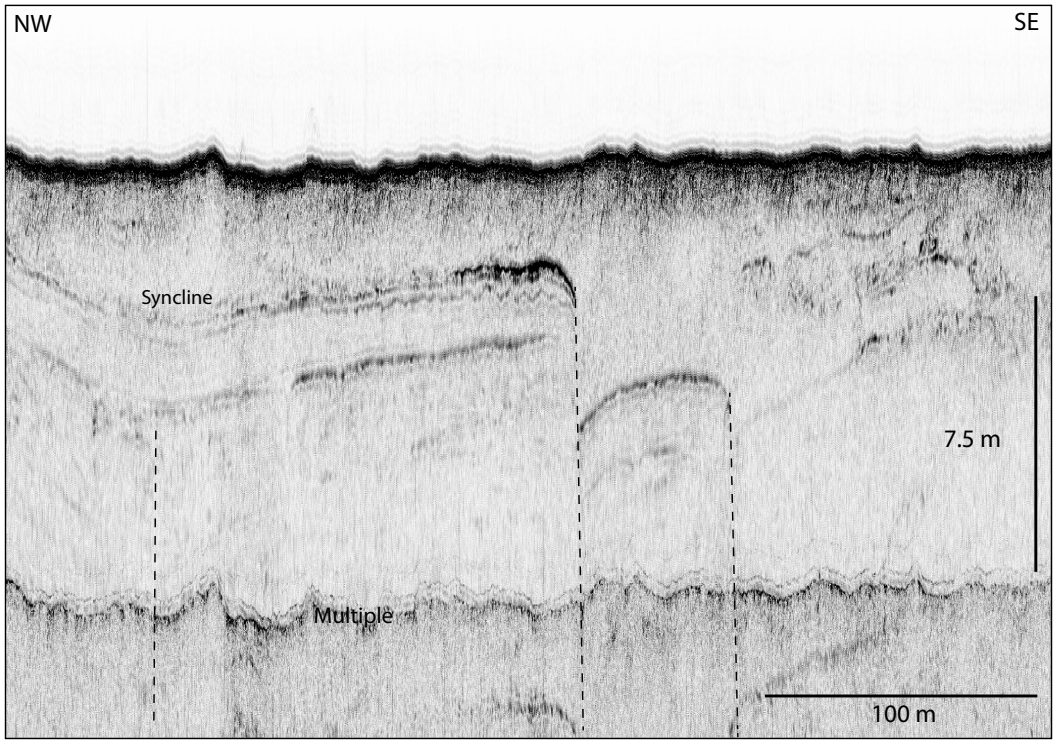

Figure 4-11: Chirp profile showing offset of horizons on faults (dashed) just south of Coronado Bridge. Location is shown in Figure 2B.

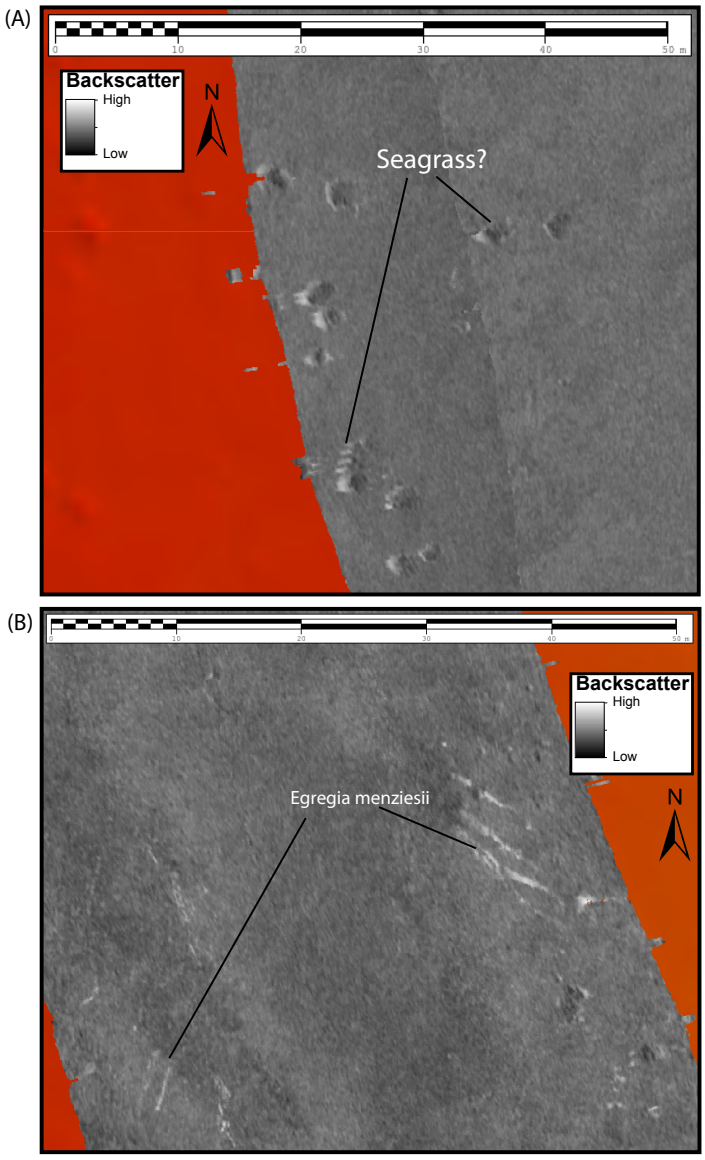

Figure 4-12: Backscatter data from the east side of Point Loma showing two different types of plants imaged in the area. (A) Semi-circular bright spots and (B) Thin, elongated bright spots.

Appendix A

Transpressional segment boundaries in strike slip fault systems offshore southern California: Implications for fluid expulsion and seep habitats

A.1 ABSTRACT

The importance of fluid flow, and its control on seep habitats, has long been appreciated at convergent margins, but the importance in strike-slip systems remains poorly understood. Here, for the first time, we present geophysical, geochemical, and biological data from a newly discovered methane seep in the inner California borderlands (ICB) to examine the interplay between fluid expulsion and restraining bends or step-overs along strike-slip fault systems. These segment boundaries may have important controls on the location of seeps in the ICB, and other margins that are controlled by strike slip faulting (e.g., Greece, Sea of Marmara). Strike-slip systems may have a more variable distribution of fluid expulsion sites compared to fluid flow at convergent margins, which may lead to an increase in seep habitat diversity. Understanding the interplay between tectonic deformation and fluid expulsion along strike-slip margins will provide important insights into the complex evolution of these ecosystems.

A.2 INTRODUCTION

Cold seeps have been recognized on both passive and active margins (e.g., Silver et al., 2000; Paull et al., 1985; Hovland and Judd, 1988). On active margins, faults create permeable conduits that allow methane and other hydrocarbons to migrate upwards and seep from the seafloor (Hein et al., 2006; Paull et al., 2008; Ranero et al., 2008) providing the foundation for chemosynthetic ecosystems. The controls on fluid seepage at convergent margins are fairly well understood (e.g., Le Pichon et al., 1992; Moore and Vrolijk, 1992; Carson & Screaton, 1998). In subduction settings, oceanic sediments from the subducted slab are extensively compressed and deformed. Compaction of sediments within the wedge leads to increased pore fluid pressure and both dispersed flow, with localized fluid expulsion at faults, mud volcanoes, and diapirs. Shallow biogenic and deep thermogenic sources of methane are both observed at these margins (Moore and

Vrolijk, 1992). Controls on fluid seepage in strike-slip settings are less well understood, and the role of fault segment boundaries in controlling seep distribution has yet to be fully examined.

Several methane seeps offshore southern California have recently been identified (e.g., Torres et al., 2002; Hein et al., 2006, Paull et al., 2008). This geomorphic province, known as the inner Continental borderlands (ICB), is characterized by a system of basins and ridges, and extensive strike-slip faulting. The ICB may accommodate up to ~20% of the ~50 mm/yr right-lateral motion between the Pacific and North American plates (Bennett et al., 1996; Becker et al., 2005; Meade and Hagar, 2005). Here, we investigate a pop-up structure located at a bend in the San Diego Trough Fault (SDTF), south of Crespi Knoll, where we discovered an active methane seep (Del Mar Seep) (Fig. 1A). Ryan et al. (2012) identified the pop-up structure, as well as two small zones over the pop-up indicative of fluid seepage in the bathymetry data. We present new geophysical, geochemical, and biological data from the active Del Mar Seep. This seep provides an ideal opportunity to examine the role of localized fault segment boundaries on fluid expulsion and the implications for regional ecology.

A.3 METHODS

Data were collected during two cruise efforts aboard the R/V Melville in July and December 2012. Multibeam and backscatter data were collected with the hull-mounted Kongsberg EM122 at a frequency of 12 kHz and Chirp data were collected with the hull-mounted Knudsen 3.5 kHz sub-bottom echosounder. Data were processed and interpreted using the following software packages: Caris Hips & Sips, IVS Fledermaus, ArcGIS, sioseis, and Kingdom Suite. A nominal 1500 m/s sound velocity was used to convert travel-time to depth for all Chirp data. Reprocessed 1979 Chevron MCS data (H-17-79 and H-18-79) were also examined to identify deep structures and fluid flow pathways

associated with the seep.

Three site surveys were conducted with the Scripps' ROV Trident. The ROV was navigated using Tracklink software, and locations are accurate to ~25 m. ROV video was examined and general habitat zones were identified and mapped by linking timestamps with navigation files. The manipulator arm was used to acquire rock and biological grab samples. A 4.5 cm diameter push core was deployed with the manipulator arm and returned ~7 cm of sediment from an orange bacterial mat in the active portion. This core was not sectioned and sampled for quantitative analysis, but geochemical and microbiological measurements were performed.

Due to limitations on the number of ROV push cores, multicores also were collected near the seep site (Fig. 3). For macrofaunal abundance, the upper 5 cm was preserved unsieved in four different vertical fractions (0-1,1-2, 2-3, 3-5) and the >5 cm fraction was sieved on a 0.3-mm mesh (July fractions: 5-7,7-10; December fractions: 5-10, 10-15). All fractions were preserved in 8% buffered formalin and re-sieved in the laboratory on a 0.3-mm mesh. A replicate core was sectioned in the same manner, but sorted live for macrofaunal isotope and ethanol preservation. For geochemistry, cores were sectioned in five different vertical fractions (0-3, 3-5, 5-7,7-10 and 10-15). Sediments were squeezed and pore waters were sampled for methane concentration, δ13CCH4, and alkalinity.

A.4 RESULTS

A.4.1 Geophysical Data

Geophysical evidence for the seep was identified in backscatter and CHIRP data (Fig. 1). Two areas of high backscatter correspond to areas of acoustic wipe-out in the sub-bottom CHIRP data (Figs. 1B & 1C). These areas are herein referred to as Eastern Seep (ES) and Western Seep (WS). The area of high backscatter for the ES and WS is

~0.15 km2 each. ES is located at the crest of an anticline and WS is located ~1200 m down-dip to the southwest (Fig. 1B). Both areas appear to be associated with faulting (Fig. 1C). At WS, the seafloor is offset ~2.25 m and the deepest observable horizon is offset ~9.75 m. At ES, we observe folding and faulting, but discrete offset of horizons is difficult to detect due to the acoustic wipe-out.

Re-processed MCS data image deeper structure across the San Diego Trough near the location of the seep (Fig. 2). We observe several strands of the SDTF extending to and offsetting acoustic basement and compressional folding between the eastern and western strands at the latitude of the seep (Fig. 2A). The western strand appears to reach very near the seafloor and reflectors to the west diverge towards the fault. The folding generates bathymetric relief and shallow reflectors onlap the anticline to the west. In a profile just to the south of the seep, we observe bright reflectors at the western SDTF strand (Fig. 2B). In the southern profile, there is less compressional folding and the eastern SDTF strand is imaged as a positive flower structure. The bright spots are not observed in profiles to the north. We do not observe deformed stratigraphy at the Thirtymile Bank detachment.

A.4.2 Biological Data

An ROV survey revealed that the ES area is characterized by areas of carbonate rubble substrate, sparse clam beds, and possible faint white microbial mats. We did not observe signs of active seepage, such as dense clams beds, extensive bacterial mats, or active venting. Nevertheless, this was an exploratory ROV dive and a more dense gridding of ROV transects might reveal these characteristics in areas not targeted by our survey.

Two ROV dives were completed on the WS area. Here we identified several different habitat zones. Zone 1 represents the active seep area where we observed thick orange, yellow, and white bacterial mats, dense clam beds, complex carbonate structures,

and gas bubbles actively venting from the seafloor. Zone 2 is clam beds dominated by large vesicomyid clams. Higher density clam patches with faint white microbial mats characterize Zone 3. In Zone 4, we observed low-density clam patches and some patches of slight sediment discoloration. Whelks, burrows in soft sediment, bathysiphon (foraminifera) tubes, and isolated, single clams were observed in Zone 5. Zone 6 is also soft sediment, but ophiuroids visually dominate the fauna. The extent of these zones for the area covered by the ROV survey is mapped in Figure 3.

Two live vesicomyid clams (~8 cm length) were collected with the ROV and appear similar to those observed in the densest clam beds of the ROV video. Additional samples collected via ROV or multicore characteristic of methane seeps include the frenulate *Siboglinum* sp., the tube worm *Escarpia* sp., another species of vesicomyid clam (3 cm length) worms, filamentous bacteria, dorvilleid and ampharetid polychaetes, provannid gastropods, and folliculinid ciliates. *Siboglinum* and the small vesicomyid collected from the multicores had δ13C in the range of 33.5‰ to -40‰.

A.4.3 Geochemistry Data

The pore water from sediment collected within the most active region of the seep has a methane concentration of 51.3 μmol of methane/L-sediment slurry and an alkalinity of 4.52 mM. The methane had a δ13C of -60.4‰. Porewater collected from the edge of the seep (e.g., less active region) had a similar methane isotope signature as the active mat core (δ13C of -59.4‰), but the alkalinity and methane concentration were lower (2.61 ± 0.1 mM, ~20 μmol of methane/L-sediment slurry, respectively).

Results from a methane sensor test (CONTROS Hydro™ CH4 Sensor, http://www.contros.eu/hydroc-ch4-hydrocarbon-methane-sensor.html) across the seep, towed ~80 m off the seafloor, indicated a 2-3x background level concentration of methane in the area of the seep (Steve Constable, personal communication). Due to a calibration

problem, absolute methane concentrations were not available.

A.5 DISCUSSION AND CONCLUSIONS

We interpret the ES to be an inactive seep with potentially some diffuse flow as indicated by sparse clams and faint sediment discolorations. The amount of carbonate rubble observed in ROV video suggests that this was at one time an area of active fluid expulsion. Faulting at the crest of the anticline appears to have created a conduit for gas migration. Additionally, the anticline would tend to focus fluid migration towards the crest, as is commonly observed in hydrocarbon traps (e.g., Biddle & Wielchowsky, 1994). The site may no longer be active due to capping by authigenic carbonates, source depletion, or complex fault-fluid interactions. The wipe-out in the Chirp data indicates that gas is likely still present in the sediments below the seafloor.

The WS area is a currently active methane seep with a small zone of focused fluid flow surrounded by areas of potentially diffuse flow. Active venting and extensive, thick microbial mats are observed only in a small area (2000 m2) in the southern part of the WS (Zone 1, Figure 3). The seep is located along an active fault that vertically offsets the seafloor and appears to record multiple events down-section. The surface trace of the fault is confined to the area of the acoustic wipe-out in Chirp data (Figure 1C). Additionally, bright spots observed along the western strand of the SDTF in MCS data are indicative of fluid flow along the major fault strands near the Del Mar seep location, and the style of deformation also indicates a zone of compression along a predominantly strike-slip fault (Fig. 2A).

The low δ13C values of the Siboglinid and vesicomyid indicate that these organisms are using chemosynthetic sources of carbon, which is not surprising since these taxa are known to harbor sulfide-oxidizing bacteria. The δ13C signature of porewater methane suggests that the methane at this seep was biogenically produced through CO2

reduction; however, δD concentrations are needed to confirm this hypothesis (Whiticar, 1999; Strapoc et al., 2011).

The biogenic source of methane is not unexpected given the high productivity of the Southern California Bight. ROV video of bubbles venting from the seafloor and the 2-3x background increase in methane in the water column above the seep indicate that there is an excess of gas reaching the seafloor that is not being used by microbes. Microbial and biological assemblages identified at the seep are typical of cold seep settings.

The geology controlling the fluid expulsion at the Del Mar Seep appears to be related to faulting and compression at a restraining step in the San Diego Trough Fault Zone (Fig. 1). This type of localized control on fluid seepage in strike slip settings has yet to be investigated. Rapid sedimentation, tectonic compression, mineral dehydration, or hydrocarbon generation are processes that can generate fluid overpressure at depth (Bray & Karig, 1985; Carson & Screaton, 1998). Overpressurized fluids migrate upward to the seafloor along permeable conduits (Hill et al., 2004). In a strike-slip tectonic setting, local variations may promote or suppress fluid expulsion at the seafloor and control seep distribution. Due to the nature of strike-slip faulting, there are localized areas of increased compression or extension at fault bends and steps. At restraining bends and steps, increased tectonic compression and deformation may promote fluid migration to the seafloor compared to the surrounding area. This appears to be the case for the Del Mar seep characterized here, and the Santa Monica Basin seeps investigated by Hein et al. (2006) and Paull et al. (2008). Both seep locations are characterized by folded and faulted strata at restraining bends. Other localized controls on seeps in the ICB could be related to erosion (e.g., Eichhbul et al., 2000; Naehr et al., 2000; Paull et al., 2008) or deposition (e.g., increased sedimentation at submarine fans).

In strike-slip settings, we propose that fluid flow is focused at restraining bends

and that it is more likely that seeps are located at these bends rather than along releasing bends. Therefore, the complexity of fault geometry and fault segmentation patterns in the ICB could play a major role in the distribution of seeps and their connectivity to one another as well as to regional ecological patterns. Additionally, the impact of these bends on the constancy and rates of fluid flow is not well understood. Although the geochemistry and biology of this site appear similar to other seeps, due to the localized geologic control there may be differences regarding fluid flow dynamics, which could impact biological recruitment and ecological succession through time.

The patterns of seep distribution and fluid flow across the ICB, as controlled by the tectonic setting, may play an important role for regional ecology. Methane seeps increase the heterogeneity of continental margin habitats and influence margin biodiversity, which are both important for ecosystem functions and have implications for resource management (Snelgrove et al., 2004; Danovaro et al., 2008; Levin et al., 2010]. Due to their novel metabolic activities, seep bacteria and archaea have extremely high rates of in situ primary production relative to the surrounding deep sea. They perform important and only partially understood roles in biogeochemical cycling, and provide both food and habitat for dense animal assemblages, which contribute to regional biodiversity patterns along continental margins (Levin, 2005, Cordes et al., 2010]. The East Pacific continental margin is dominated by convergent tectonics, but in the latitudes from Baja to Mendocino, the tectonic setting is characterized by strike-slip faulting. This area is ecologically productive and is a hydrocarbon-producing region, but the controls on fluid migration and expulsion at the seafloor differ from convergent margins, which are characterized by extensive regional tectonic compaction and deep fluid sources. In the ICB, the location of seeps appears somewhat dependent upon localized fault interactions.

Further investigation of seeps located at fault segment boundaries may elucidate spatial and temporal patterns of fluid migration and expulsion, and how they impact

patterns of regional productivity and biodiversity. These areas also are interesting in terms of understanding the relationship between seismic activity and fluid expulsion. The Del Mar Seep is located near the epicenter of the 1986 Oceanside earthquake and fluid appears to be migrating along an active fault. Fault segment boundaries have been shown to influence earthquake rupture propagation (i.e., Wesnousky, 2006; Oglesby & Mai, 2012). Segment boundaries add complexity to the little understood relationship between seismicity and fluid migration. Additional investigations into the relationship between restraining bends, fluid flow, and seep habitats are warranted.

A.6 ACKNOWLEDGEMENTS

The authors would like to thank the Melville crew and scientific party of SDCoastEx, especially Monika Krach, Sigrid Katz, Adriana Garcia, Valerie Sahakian, Rachel Marcuson, Drew Cole, and Jay Turnbull. This research was supported by a UC Ship Funds grant.

The text and figures from this appendix are being prepared for publication in: Maloney, J.M., B.M. Grupe, A. Pasulka, C.A. Frieder, L.A. Levin, K. Dawson, D. Case, and N.W. Driscoll, In Prep, Transpressional segment boundaries in strike-slip fault systems offshore southern California: Implications for fluid expulsion and seep habitats. The dissertation author, second author, and third author were the primary researchers, and the dissertation author was the primary author of the manuscript. The co-authors assisted with the research that forms the basis for this chapter.

A.7 REFERENCES

Becker, T. W., J. L. Hardebeck, and G. Anderson (2005), Constraints on fault slip rates of the southern California plate boundary from GPS velocity and stress inversions, Geophys. J. Int., 160(2), 634-650, doi:10.1111/j.1365-246X.2004.02528.x.

Bennett, R. A., W. Rodi, and R. E. Reilinger (1996), Global positioning system

constraints on fault slip rates in southern California and northern Baja, Mexico, J. Geophys. Res., 101(B10), 21943-21960, doi:10.1029/96JB02488.

Biddle, K. T., and C. C. Wielchowsky (1994), Hydrocarbon Traps, AAPG Mem., 60, 219-235.

Bray, C. J., and D. E. Karig (1985), Porosity of sediments in accretionary prisms and some implications for dewatering processes, J. Geophys. Res., 90(B1), 768-778, doi:10.1029/JB090iB01p00768.

Carson, B., and E. J. Screaton (1998), Fluid flow in accretionary prisms: evidence for focused, time-variable discharge, Rev. Geophys., 36(3), 329-351, doi:10.1029/97RG03633.

Cordes, E. E., M. R. Cunha, J. Galeron, C. Mora, K.O. Roy, M. Sibuet, S. Van Gaever, A. Vanreusel, and L. Levin (2010), The influence of geological, geochemical, and biogenic habitat heterogeneity on seep biodiversity, Mar. Ecol., 31, 51-65, doi:10.1111/j.1439-0485.2009.00334.x.

Danovaro, R., C. Gambi, A. Dell'Anno, C. Corinaldesi, S. Fraschetti, A. Vanreusel, M. Vincx, and A.J. Gooday (2008), Exponential decline of deep-sea ecosystem functioning linked to benthic biodiversity loss, Curr. Biol., 18(1), 1-8, doi:10.1016/j.cub.2007.11.056.

Eichhubl, P., H. G. Greene, T. Naehr, and N. Maher (2000), Structural control of fluid flow: offshore fluid seepage in the Santa Barbara Basin, California, J. Geochem. Explor., 69-70, 545-549, doi:10.1016/S0375-6742(00)00107-2.

Hovalnd, M. and A.G. Judd (1988), Seabed Pockmarks and Seepages, Graham and Trotman, Norwell, MA.

Le Pichon, X., K. Kobayashi, and Kaiko-Nankai Scientific Crew (1992), Fluid venting activity within the eastern Nankai Trough accretionary wedge: A summary of the 1989 Kaiko-Nankai results, Earth Planet. Sci. Lett., 109, 303-318, doi:10.1016/0012-821X(92)90094-C.

Levin, L. A. (2005), Ecology of cold seep sediments: Interactions of fauna with flow, chemistry and microbes, CRC Press-Taylor & Francis Group, Boca Raton, FL.

Levin, L. A., G. F. Mendoza, J. P. Gonzalez, A. R. Thurber, and E. E. Cordes (2010), Diversity of bathyl macrofauna on the northeastern Pacific margin: the influence of methane seeps and oxygen minimum zones, Mar. Ecol., 31, 94-110, doi: 10.1111/j.1439-0485.2009.00335.x.

Meade, B. J., and B. H. Hager (2005), Block models of crustal motion in southern California constrained by GPS measurements, J. Geophys. Res., 110(B03403), doi:10.1029/2004JB003209.

Moore, J. C., and P. Vrolijk (1992), Fluids in accretionary prisms, Rev. Geophys., 30(2), 113-135, doi:10.1029/92RG00201.

Naehr, T. H., D. S. Stakes, and W. S. Moore (2000), Mass wasting, ephemeral fluid flow, and barite deposition on the California continental margin, Geology, 28(4), 315-318, doi:10.1130/0091-7613(2000)28.

Oglesby, D. D., and P. Mai (2012), Fault geometry, rupture dynamics and ground motion from potential earthquakes on the North Anatolian Fault under the Sea of Marmara, Geophys. J. Int., 188(3), 1071-1087, doi:10.1111/j.1365-246X.2011.05289.x.

Paull, C.K., A. J. T. Jull, L. J. Toolin, T. Linick (1985), Stable isotope evidence for chemosynthesis in an abyssal seep community, Nature, 317, 709-711, doi:10.1038/317709a0.

Paull, C. K., W. R. Normark, W. Ussler III, D. W. Caress, and R. Keaten (2008), Association among active seafloor deformation, mound formation, and gas hydrate growth and accumulation within the seafloor of the Santa Monica Basin, offshore California, Mar. Geol., 250, 258-275, doi:10.1016/j.margeo.2008.01.011.

Ranero, C.R., I. Grevemeyer, H. Sahling, U. Barckhausen, C. Henson, K. Wallmann, W. Weinrebe, P. Vannucchi, R. von Huene, K. McIntosh (2008), Hydrogeological system of erosional convergent margins and its influence on tectonics and interplate seismogenesis, Geochem. Geophys. Geosyst., 9(3), doi:10.1029/2007GC001679.

Ryan, H. F., J. E. Conrad, C. K. Paull, and M. McGann (2012), Slip rate on the San Diego Trough Fault Zone, Inner California Borderland, and the 1986 Oceanside Earthquake Swarm Revisited, Bull. Seismol. Soc. Am., 102(6), 2300-2312,

doi:10.1785/0120110317.

Silver, E., M. Kastner, A. Fisher, J. Morris, McIntosh, K., and D. Saffer (2000), Fulid flow paths in the Middle America Trench and Costa Rica margin, Geology, 28, 679-682, doi: 10.1130/0091-7613(2000)28<679:FFPITM>2.0.CO;2.

Snelgrove, P. V. R., M. C. Austen, S. J. Hawkins, T. Iliffe, R. T. Kneib, L. A. Levin, J. M. Weslawski, R. B. Whitlatch, and J. R. Garey (2004), Ecosystem services provided by marine sedimentary biota and their vulnerability to anthropogenic disturbance, in Sustaining Biodiversity and Ecosystem Services in Soils and Sediments, edited by D. Wall, pp. 161-192, Island Press, Covelo, CA.

Strapoc, D., M. Mastalerz, K. Dawson, J. Macalady, A. V. Callaghan, B. Wawrik, C. Turich, and M. Ashby (2011), Biogeochemistry of Microbial Coal-Bed Methane, Annu. Rev. Earth Planet. Sci., 39, 617-656, doi:10.1146/annurev-earth-040610-133343.

Torres, M. E., J. McManus, and C. Huh (2002), Fluid seepage along the San Clemente Fault scarp: basin-wide impact on barium cycling, Earth Planet. Sci. Lett., 203, 181-194, doi:10.1016/S0012-821X(02)00800-2.

Wesnousky, S. G. (2006), Predicting the endpoints of earthquake ruptures, Nature, 444, 358-360, doi:10.1038/nature05275.

Whiticar, M. J. (1999), Carbon and hydrogen isotope systematics of bacterial formation and oxidation of methane, Chem. Geol., 161, 291-314, doi:10.1016/S0009-2541(99)00092-3.

Figure A-1: (A) Regional map of the inner California borderlands with major fault zones drawn in black (USGS, 2006). Red lines show location of multichannel seismic (MCS) profiles in Figure 2. White box outlines area shown in Figure 1B. (B) Acoustic backscatter over seep area showing high backscatter zones at the western seep (WS) and eastern seep (ES). Red lines are faults mapped in the Chirp data. The white line corresponds to the Chirp profile shown in Figure 1C. (C) Chirp profile across WS and ES, which are imaged as areas of acoustic wipeout. Dashed red lines are inferred faults. Acoustic horizons across the WS are offset.

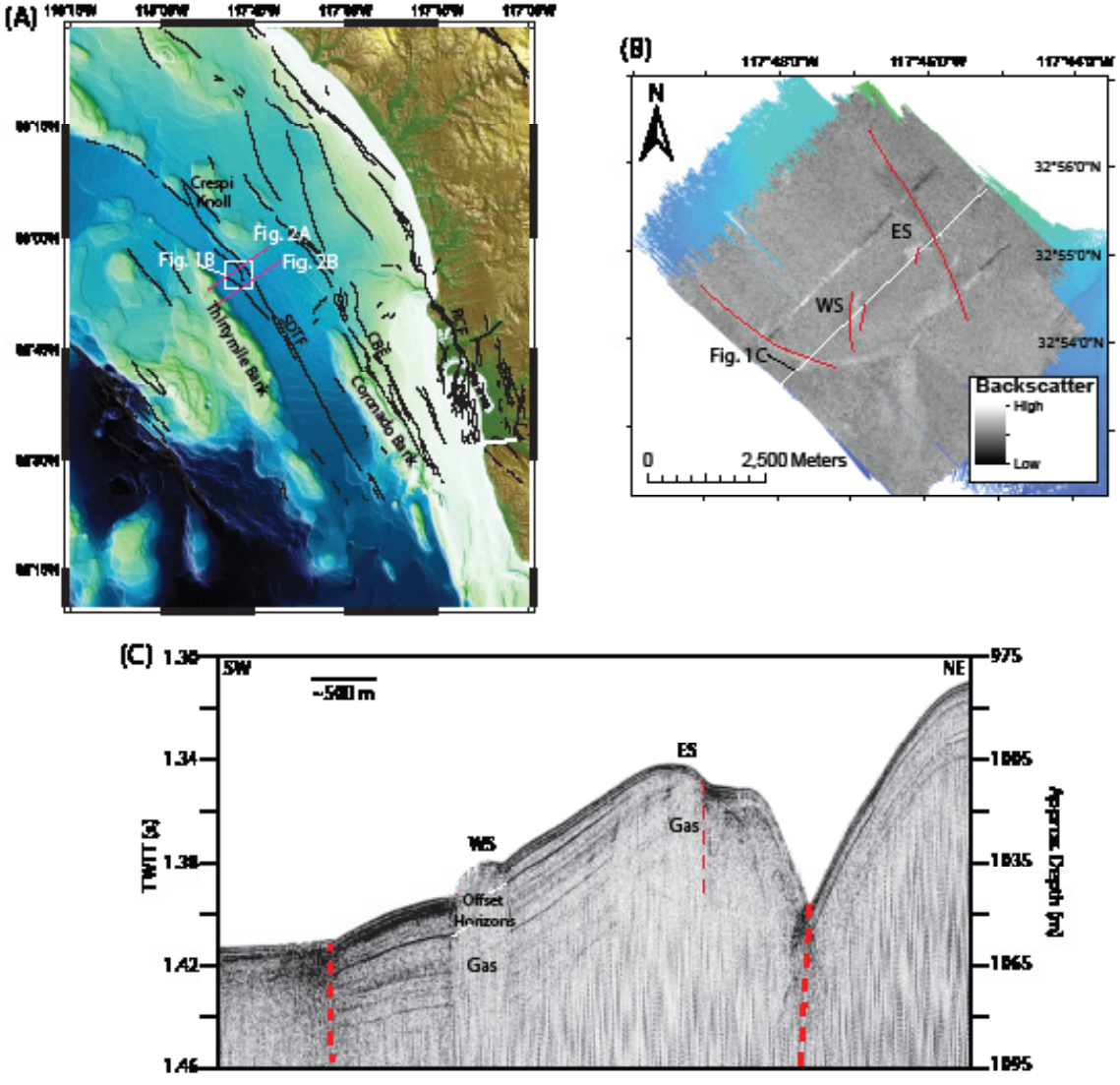
(A)
Crespi Knoll
Fig. 2A
Fig. 1B
Fig. 2B
Thirtymile Bank
SDTF
CBF
Coronado Bank
(B)
N
ES
WS
Fig. 1C
32°56'0"N
32°55'0"N
32°54'0"N
Backscatter
High
Low
0
2,500 Meters
(C)
SW
NE
~500 m
ES
WS
Gas
Offset Horizons
Gas
TWTT (s)
Approx. Depth (m)
1.30
1.34
1.38
1.42
1.46
975
1885
1935
1985
1995

Figure A-2: (A) MCS profile 4540 across the San Diego Trough, through the seep area. The interpreted basement is drawn as a blue horizon. Faults are marked as black solid lines. At this latitude, anticlinal folding is observed between the western and eastern strands of the San Diego Trough fault (SDTF). The youngest horizons appear to onlap the anticline on the west. Strands of the SDTF also appear to offset the basement. Location of profile is shown in Figure 1A. (B) MCS profile 4544 located just to the south of the seep. The interpreted basement is drawn in blue and faults are drawn in solid black. In this profile deformation along the SDTF zone is less compressional and a flower structure at the eastern SDTF is indicative of strike-slip faulting. Bright spots at depth near the western SDTF indicate the presence of fluids beneath the seafloor in this region.

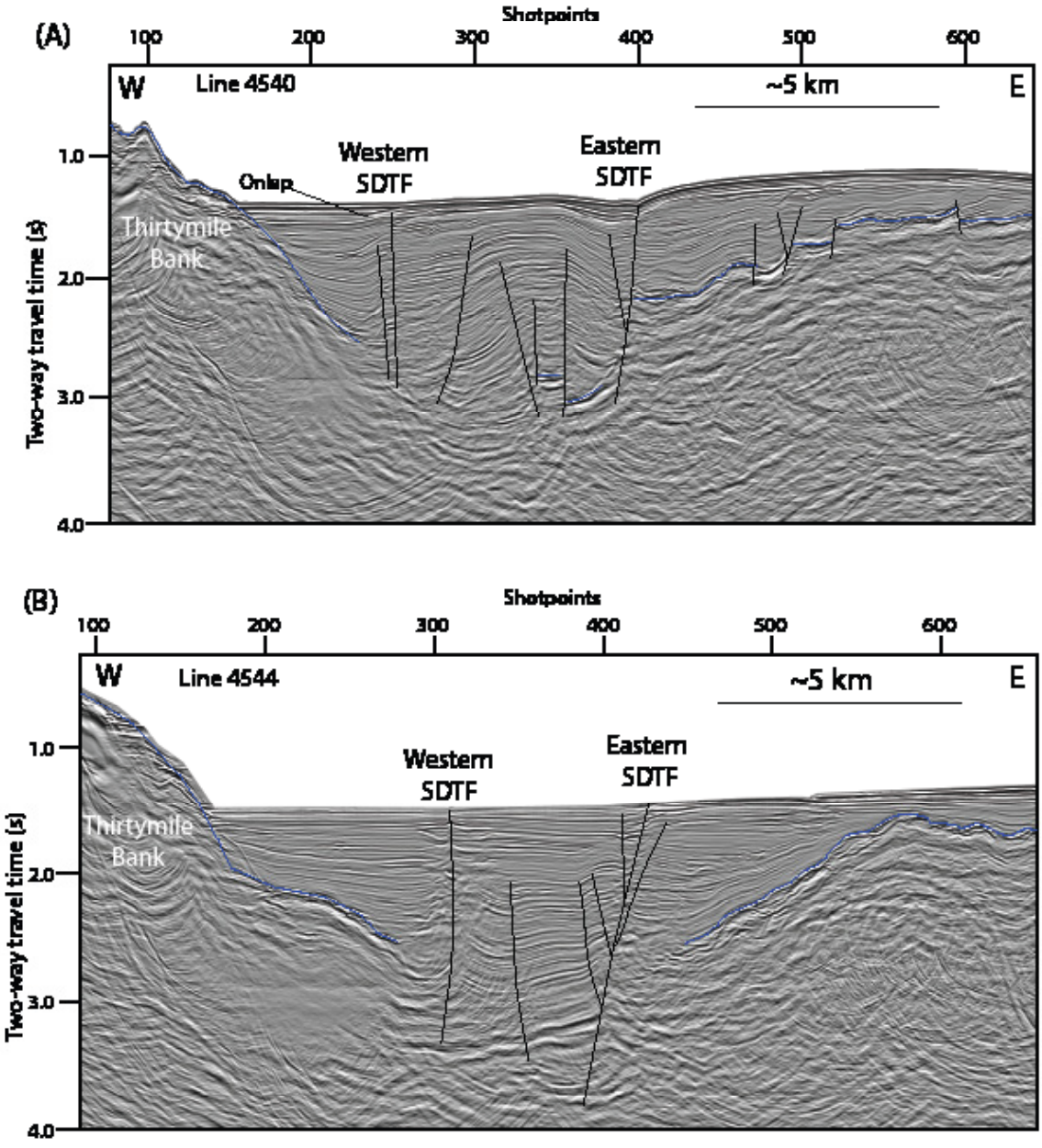
(A)
Shotpoints
100
200
300
400
500
600
W
Line 4540
~5 km
E
Western
SDTF
Eastern
SDTF
Onlap
Thirtymile
Bank
Two-way travel time (s)
1.0
2.0
3.0
4.0
(B)
Shotpoints
100
200
300
400
500
600
W
Line 4544
~5 km
E
Western
SDTF
Eastern
SDTF
Thirtymile
Bank
Two-way travel time (s)
1.0
2.0
3.0
4.0

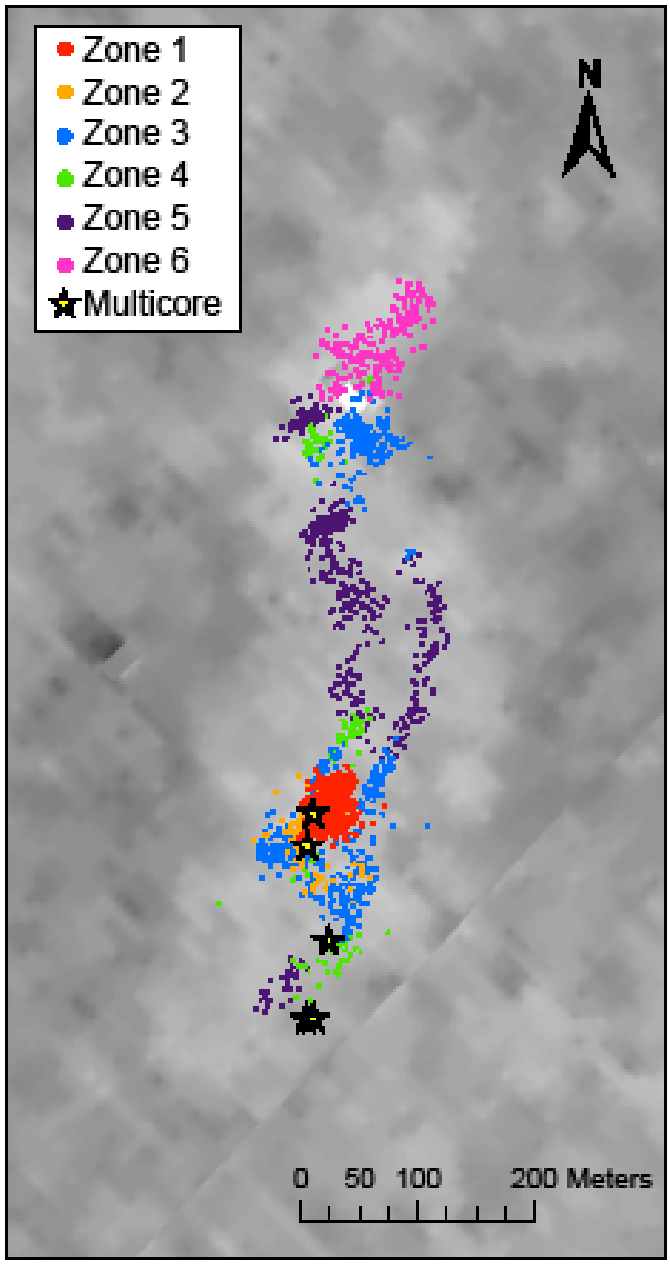

Figure A-3: Close up on western seep (WS) backscatter data with results from the ROV video survey and multicore locations overlain. See inset legend for identification of ecological zones. A description of each zone is detailed in the text.

Appendix B

Strike-slip Faulting along the Wassuk Range of the northern Walker Lane, Nevada

Strike-slip faulting along the Wassuk Range of the northern Walker Lane, Nevada

Shaopeng Dong [1,2], Gulsen Ucarkus[3], Steven G. Wesnousky[2], Jillian Maloney[3], Graham Kent[4], Neal Driscoll[3], Robert Baskin[5]

[1]Key Laboratory of Active Tectonics and Volcanoes, Institute of Geology, China Earthquake Administration, Beijing, China (dshaopeng@gmail.com)

[2]Center for Neotectonics Studies, University of Nevada, Reno, Reno, NV, USA. (wesnousky@unr.edu)

[3]Scripps Institution of Oceanography, University of California at San Diego, La Jolla, CA, USA (gucarkus@ucsd.edu; ndriscoll@ucsd.edu; jmaloney@ucsd.edu)

[4]Nevada Seismological Laboratory, University of Nevada, Reno, Reno, NV, USA (gkent@unr.edu)

[5]U.S. Geological Survey, West Valley City, UT, USA (rbaskin@usgs.gov)

Abstract

A strike-slip fault is observed outboard and subparallel to the Wassuk rangefront within the central Walker Lane. Recessional shorelines of pluvial Lake Lahontan that reached its highstand about 15,475 ± 720 cal. yr B.P. are displaced about 14 m and yield a right-lateral slip-rate estimate approaching 1 mm/yr. The strike-slip fault trace projects southeastward toward the eastern margin of Walker Lake that is ~15 km to the southeast. The trace is obscured in this region by recessional shorelines features

that record the historical dessication of the lake caused by agricultural practices. High resolution seismic CHIRP profiles acquired in Walker Lake reveal ~20,000 years of stratigraphy that is tilted westward approximately 20 - 30 m to the Wassuk rangefront, consistent with about 1.0 - 1.5 mm/yr (20 - 30 m /20,000 yrs) of vertical displacement on the main rangebounding normal fault. Direct evidence of the northwest trending right-lateral strike-slip fault is not observed, though superimposed upon the west dipping strata are a set of folds and faults trending N35°E, conjugate to the trend of the strike-slip fault observed to the north. The pattern and trend of folding and faulting beneath the lake is not simply explained. It is perhaps recording development of Riedel shears in a zone of northwest directed strike-slip. Regardless of their genesis, the faults and folds appear to have been inactive during the last ~10,500 yrs B.P. These observations begin to reconcile what has been a mismatch between geodetically predicted deformation rates and geological fault slip rate studies along the Wassuk rangefront, and provides another example of strain partitioning between predominantly normal and strike-slip faults that occurs in regions of oblique extension such as the Walker Lane.

Keywords: Wassuk Range fault; Walker Lane; dextral strike-slip; seismic CHIRP, LiDAR, Riedel shear zone

INTRODUCTION

The Wassuk Range is a north-trending ~80-km-long mountain block within the central Walker Lane (Figures 1 and 2), which is an ~100 km wide zone of discontinuous active faults and disrupted topography that trends along the east flank of the Sierra Nevada. Based on geodesy, up to one-fifth of the right-lateral relative plate motion between the Pacific and North America plates is accommodated east of the Sierra Nevada, with the majority localized within the Walker Lane (Bennett et al., 1999; Hammond and Thatcher, 2007; Thatcher et al., 1999). The eastern escarpment of the Wassuk Range is steep, abrupt, and bounded by a normal fault just west of Walker Lake (Figure 2). Here we present both terrestrial and lacustrine observations to show the presence of a strike-slip fault system outboard and subparallel to the range front that may accommodate ~1 mm/yr of right-lateral motion. This observation begins to reconcile an existing mismatch between geodetically predicted deformation rates compared to geologically determined slip rates reported from studies along the range-bounding fault (Bormann et al., 2012). The high resolution CHIRP profiles also document an ongoing thickening of sediments into the Wassuk normal fault; a deformed unconformity places a minimum bound of vertical motion of ~20 -30 m over the past 20,000 yrs B.P., or a vertical slip rate approaching 1.0 - 1.5 mm/yr, nearly twice the rate published from paleoseismic studies (Bormann et al., 2012). Together, these observations also provide another example of the partitioning of slip between primarily normal and strike-slip faults that occur in regions of oblique

extension.

OBSERVATIONS

Terrestrial

The characteristics of the strike-slip fault system are elucidated with LiDAR data reported and processed by Lopes and Smith (2007) and a section of a 1:40,000 scale low-sun angle photograph. The LiDAR digital elevation map (DEM) defines a lineament that sits east and strikes subparallel to the rangefront (Figure 3). The entirety of the lineament is located below the pre-historic highstand of pluvial Lake Lahontan that filled the basin to an elevation of ~1330 m at ~13,070 ± 60 ^{14}C B.P. (e.g., Adams and Wesnousky, 1998) or about 15,475 ± 720 cal. yr B.P. (Briggs and Wesnousky, 2004). Below the ~1330 m pluvial highstand and above the ~1262 m latest Holocene highstand of the lake mapped by House and Adams (2012, 2013), the lineament cuts wave-washed surfaces of pluvial Lake Lahanton and alluvial fan deposits developed since that time and is defined by the presence of alternate facing scarps along strike, which are typically associated with strike-slip displacement. The lineament continues southeastward from the ~1262 m shoreline for about 1 km as an alignment of vegetation. Continuing yet farther southeast with a slight change in azimuth, and below the ~1252 m historical highstand of the lake (Adams (2007), a distinct lineament in the LiDAR imagery is also present (Figure 3b). Though the LiDAR reports horizontal and vertical positional accuracies of ~1 m and 13-20 cm,

84 respectively, field observation indicates the lineament is an artifact of LiDAR
85 processing errors (e.g., swath stitching misalignment).
86 An enlarged portion of a 1:40,000 scale Nevada Bureau of Mines and Geology
87 low-sun angle photo of the fault trace where it cuts recessional shorelines of Lake
88 Lahontan is shown in Figure 4a. The fault trace cuts from northwest to southeast
89 across the central portion of the image. Several of the tonal bands resulting from
90 shadows cast by the recessional shoreline beach ridges are offset right-laterally across
91 the trace. To measure the amount of offset the airphoto was georeferenced to existing
92 USGS DRGs and Orthophotoquads encompassing the site. The dashed line pairs on
93 Figure 4b are along interpreted piercing point lines that follow the 3 most distinct
94 tonal contrasts. The right-lateral offset of the tonal lineaments across the fault range
95 from 11.7 to 15.2 m with an average of 13.5 m. Additionally, we used a backpack
96 GPS system to survey along our interpretation by eye of the crests and swales of a
97 number of beach ridges (dotted line pairs in Figure 4c). The range of 4 offsets
98 measured in this way range from 12.3 m to 14.3 m, with an average of 13.9 m. Figure
99 4d additionally shows the LiDAR image at the same scale as Figures 4b and 4c. In
100 this case, the offsets observed in the low-sun angle image are not clearly evident in
101 the LiDAR image.
102 The offset shorelines postdate the highstand of pluvial Lake Lahontan (15,475 ±
103 720 cal. yr B.P). Dividing the ~14 m offset of the shorelines by the age of the
104 highstand yields a minimum fault slip rate equal to ~0.9 mm/yr. The calculation of

fault slip rate assumes the total offset is due to multiple earthquakes and the uncertainty bars exclude the uncertainty associated with where in the period of time the postulated offsets occurred.

Submarine CHIRP Survey

Methods

About 200 line-km of seismic CHIRP (Compressed High Intensity Radar Pulse, acoustic variant) data were acquired in Walker Lake in 2012 and 2013 (Figure 5). The survey employed Scripps Institution of Oceanography's Edgetech SUBSCAN CHIRP profiler and was operated with a 50 ms swept pulse of 1-15 kHz, which provides decimeter vertical resolution with sub-bottom penetration >60 m. All data were digitally recorded in JSF format (converted to SEG-Y format) with real-time GPS navigation, providing location accuracy to within 5 m. Data were processed using SIOSEIS (Henkart, 2003) and imported to Kingdom Suite and IVS Fledermaus software packages for interpretation. A nominal water and sediment velocity of 1500 m/s is assumed for all depth and sediment thickness conversions.

Lines D01L02 was designed to traverse across two existing cores acquired in the lake (12-m-long and 50-m-long; Benson, 1988; Bradbury et. al., 1989, Benson et al, 1991) to correlate the lithostratigraphy and seismic stratigraphy (Figure 6). Detailed analyses of both cores were performed including radiocarbon age dating (Benson, 1988; Bradbury et. al., 1989, Benson et al, 1991), which allowed us to determine the

age of the reflectors imaged in the CHIRP data as well as lake history (Figure 6). These data provide important age constraints for the deformational events imaged in the CHIRP profiles. Accordingly, an unconformity associated with the orange horizon in Figure 6 is interpreted to be approximately 20,000 yrs B.P. and the age of the green horizon to be ~10,500 yrs B.P. In the shallowmost sedimentary section, an interpolation of C14–dated samples from the 12-m-long Benson et al. (1991) sediment core places the age of the blue horizon (erosional unconformity) at 3000 yrs B.P. and yellow horizon at approximately 3900 yrs B.P. The distinct acoustic character of these reflectors allows for robust correlation of these horizons around the CHIRP seismic grid (e.g., Figures 7 and 8)

Results

Characteristic track lines that best illustrate the structure and stratigraphy observed in the lake sediments are presented: lines D01L02 (Figure 6), D01L01 (Figure 7) and D02L13 (Figure 8). All three line cross the lake in the east-west direction (Figure 5). There are several notable features observed in the CHIRP data. First and foremost, west-east profiles are marked by a strong divergence of sedimentary packages toward the Wassuk normal fault to the west. Superimposed on this westward tilt are broad folds, some faulted, with diminished amplitude upsection. The seismic imagery also reveals two erosional unconformities that appear to be related to periodic dessication of Walker Lake throughout the late Pleistocene and

Holocene; these fiduciary markers (orange, ~20 ka, blue, ~3.9 ka) also help place bounds on vertical slip-rate across the Wassuk fault.

The divergence, rotation and systematic increase in dip with depth of reflectors observed along the western portion of the lake (Figures 6 and 7) are consistent with the presence of down-to-the-east normal fault along the Wassuk rangefront (e.g., Borman et al., 2012). In this regard, the most recent deformation event preserved in the lake stratigraphy is recorded by an ~2.5-m-thick wedge of sediment above the blue horizon (cyan wedge, Figure 6), which is dated at approximately 3000 yrs B.P. Bormann et al. (2012) recognized at least one surface displacement during this period of time along the rangefront fault at Rose Creek, and thus it is possible these events correlate. Imaging structures closer to the western-most portion of the lake was precluded by gas (Figure 6).

The orange horizon exhibits a regional dip that increase towards the west near the core sites (Figure 6). The observed regional tilt to the west is ~20 - 30 m. Given the orange horizon marks an erosional unconformity that was originally horizontal, the tilting would suggest a vertical component of displacement along the Wassuk Range front on the order of 1.25 ± 0.25 mm/yr or more (20 -30m / 20,000 yrs). This value is more than twice that interpreted from displaced terrestrial deposits along the rangefront fault (~0.2 – 0.8 mm/yr - Borman et al., 2012; Figure 2). The difference in the estimated slip rate may reflect that the rates reported in each study are averaged over different periods of time or the limited data available to document the age of

offset features in each study.

The deepest reflectors (red horizon and below) exhibit tight synclinal folds: one in the case of line D01L02 (Figure 6) and three in line D01L01 (Figure 7). The layers of this deeper fold are concordant and maintain constant thickness. The easternmost limb of the easternmost fold in each section is truncated by an erosional unconformity (late Pleistocene, ~20 ka) marked for clarity in Figure 6 by an orange horizon that is most pronounced toward the east. This erosional unconformity is most likely due to wave-base erosion during an episode of lower lake level, potentially near Tioga glacial maximum.

The synclinal fold appears to continue up section above the erosional unconformity, but with diminshed amplitude. No folding is observed above the green horizon, which marks a distinct surface with stratigraphic onlap (Figure 6). The deepest basal reflectors are offset by a fault (f_1) along the easternmost fold on all three lines (Figures 6, 7 and 8). The different pattern of throw along this fault (f_1) (note: a different down thrown side is observed in D01L01 (Figure 7) with respect to D01L02 (Figure 6) and D02L13 **(**Figure 8) is consistent with strike-slip deformation. Deformation observed along this fault does not offset the orange horizon. In line D01L01 (Figure 7), both of the two synclines are offset at their eastern limbs with the cessation of deformation delineated by the green horizon (early Holocene, ~10.5 ka). Deduced age constraints for the orange and green horizons post-date the last deformational event associated with the deep folds and fold-related faults observed in

all three lines at about ~20 ka (f_1) (Figure 6) and 10.5 ka yrs B.P. (f_2 and f_3) (Figure 7).

The location and orientation of fault and fold axes determined by mapping of these features through the entire CHIRP dataset is summarized in Figure 5. The fault oreintations and fold axes are oriented about N35°E. The faults are discontinuous, reach in length no more than 2-5 kilometers and exhibit a en echelon character in map view (Figure 5).

The CHIRP profiles also record lake level fluctuations of Walker Lake in the late Quaternary that are consistent with several core studies (Benson, 1988; Benson et al., 1991). Benson (1988) reports high lake levels between 12–15 ka yrs B.P., which correlates to the acoustically transparent layer (homogeneous fine-grained sediments) below the green horizon (~10.5 ka). The green horizon is an onlap surface that separates the acoustically transparent high-stand deposits below from the acoustically laminated onlapping sediments above. The high amplitude reflectors within the acoustically laminated sequence are coarse layers emplaced during low-lake level conditions (e.g., Brothers et al., 2012; Figure 6). Some high-amplitude sequences are also observed above the orange layer suggesting another low lake level stand that correlates with a desiccation period between 15–20 ka (Benson, 1988). Furthermore, the transparent layer below the orange horizon correlates to the high-stand reported as >20 ka (Figure 6). The acoustic character and erosional surfaces (i.e., orange and blue horizon) observed in the CHIRP data appears to confirm the lake environment history

as presented by Benson (1988) in terms of lake elevation and facies predictions from the late Pleistocene through Holocene, placing greater confidence in our chronostratigraphic famework.

A notable acoustic feature observed in the CHIRP data appears to be linked to distribution of tufas/bioherms in Walker Lake (Figures 5 and 8). The pattern is well documented in line D02L13 (Figure 8), where carbonate growth has resulted in a rough hummocky surface that obscures the sediments below. The attenuation of acoustic energy from the hummocky horizon is significantly different than acoustic attenuation by gas (Figures 6, 7, and 8). Acoustically gas in the subsurface has a blotchy return and obscures reflectors beneath it. The hummocky surface has a marked change in roughness and a sharp acoustic impedance contrast. The distribution of the hummocky acoustic return is shown in Figure 5.

DISCUSSION AND CONCLUSION

Geodesy shows at the latitude of the Wassuk range that right-lateral strain accumulation across the width of the Walker Lane is equivalent to 6–7 mm/yr, with a lesser component distributed across the Wassuk rangefront. The Wassuk Range is oriented oblique to the shear field. As a result, it may be expected that both normal and strike-slip components of displacement are required to accommodate the ongoing shear. Prior geological estimates of fault slip rate are few and focused on the component of normal displacement along the range–bounding fault (Bormann et al.,

2012). They have suggested the vertical late Pleistocene slip rate along the rangefront is up to ~0.7 mm/yr. Our observations of the divergence, rotation and systematic increase in dip with depth of reflectors observed along the western portion of the lake suggest the vertical rate may be twice this value. An additional ~1.1 ± 0.4 mm/yr of right-lateral strike-slip parallel to the rangefront is required by geodesy to account for the entirety of the geodetic strain field (Wesnousky et al., 2012). The terrestrial and lacustrine observations we have put forth here are quite suggestive that this additional ~1.1 ± 0.4 mm/yr may all or in large part be accounted for by slip on this strike-slip fault system outboard the rangefront. The observed offset of the remnant Lake Lahontan shorelines is on the order of 12 to 15 m. Dividing this value by the age of the Lake Lahontan highstand yields a slip rate approaching 1 mm/yr or greater. The rate assumes the offset is the result of 2 or more earthquakes. Lesser offsets of these presumed events are not documented along the trace.

The partitioning of oblique deformation between subparallel normal and strike-slip faults was first noted by (Fitch, 1972) in his study of oblique convergence at plate boundaries; subsequently it has been frequently observed in both transtensional and transcompressional environments (Jones and Wesnousky, 1992; Wesnousky and Jones, 1994). In this particular case, it is analogous to the pairing of the Owens Valley and Sierran rangefront faults farther south in the Walker Lane. Projection of the strike-slip fault ~15 km southeastward toward Walker Lake is problematic. The trace is obscured over this distance by recessional shorelines

features that record the historical dessication of the lake caused by agriculture in the region. Direct evidence for the existence of a northwest directed right-lateral strike-slip fault is not present in the CHIRP profiles, although superimposed upon the west dipping strata are a set of folds and faults aligned along a N35°E trend, conjugate to the trend of the strike-slip fault observed to the north. While the presence of the faults and folds illustrate the presence of tectonic deformation within the lake, the pattern and trend of folding and faulting beneath the lake is not simply explained. It is perhaps recording development of Riedel shears in a zone of northwest directed strike-slip. While illustrative of late Pleistocene displacement, the faults and folds appear to have been inactive during the last ~10,500 yrs B.P. If it is assumed that the onshore and submarine traces share the same earthquake history (i.e., that large earthquakes along the dextral strike-slip fault are driving deformation in the Riedel shear zone), it would imply that the 12 to 15 meters of offset observed onshore occurred during the same short period of time, perhaps due to a punctuated period of earthquakes lasting no more than ~5,000 years.

ACKNOWLEDGEMENTS:

Center for Neotectonics Contribution No. 65. Funding for the seismic CHIRP survey on Walker Lake was provided by the Southern California Earthquake Center, award SCEC-10166. We also thank Danny Brothers for an internal USGS review and Ernest Aaron for his mob/demob efforts.

REFERENCES:

Adams, K. D., and Wesnousky, S. G., 1998, Shoreline processes and the age of the Lake Lahontan highstand in the Jessup embayment, Nevada: Geological Society of America Bulletin, v. 110, no. 10, p. 1318-1332.

Adams, K. D. , 2007, Late Holocene sedimentary environments and lake-level fluctuations at Walker Lake, Nevada, USA, Geological Society of American Bulletin, 119, 126-139.

Arrowsmith, J. R., 1995, Coupled tectonic deformation and geomorphic degradation along the San Andreas Fault System [Ph.D]: Stanford University.

Bennett, R.A., Davis, J.L., and Wernicke, B.P., 1999, Present-day pattern of Cordilleran deformation in the western United States: Geology, v. 27, p. 371–374.

Benson L. V., 1988, Preliminary paleolimnological data for Walker Lake subbasin, California and Nevada, USGS Water Resources Investigations Report 87-4258, p. 1-50.

Benson, L. V., P. A. Meyers and R. J. Spencer, 1991, Change in the size of Walker Lake during the past 5000 years, Palaeogeography, Palaeoclimatology, Palaeoecology, 81, p. 189-214.

Bormann, J. M., Surpless, B. E., Caffee, M. W., and Wesnousky, S. G., 2012, Holocene Earthquakes and Late Pleistocene Slip-Rate Estimates on the Wassuk Range Fault Zone, Nevada: Bulletin of the Seismological Society of America, v.

102, no. 4, p. 1884-1891.

Bradbury, J. P., R. M. Forester, R. S. Thompson, 1989, Late Quaternary paleolimnology of Walker Lake, Nevada, Journal of Paleoliomnology, v. 1, p. 249-267.

Briggs, R. W., and Wesnousky, S. G., 2004, Late Pleistocene fault slip rate, earthquake recurrence, and recency of slip along the Pyramid Lake fault zone, northern Walker Lane, United States: Journal of Geophysical Research-Solid Earth, v. 109, no. B8.

Brothers, D., D. Kilb, K. Luttrell, N. Driscoll and G. Kent, 2011, Loading of the San Andreas Fault by flood-induced rupture of faults beneath the Salton Sea Nature Geoscience V. 4, N.7: 486 – 492

Eisses, A., A. Kell, G. Kent, N. Driscoll, R. Baskin, K. Smith, R. Karlin, J. Louie, and S. Pullammanappallil, 2013, New constraints on slip-rates, recurrence intervals, and strain partitioning beneath Pyramid Lake, Nevada, Geosphere, in review.

Fitch, T. J., 1972, Plate convergence, transcurrent faults, and internal deformation adjacent to southeast Asia and western Pacific. : Journal of Geophysical Research, v. 77, no. 23, p. 4432-4442.

Hammond, W. C., and Thatcher, T., 2007, Crustal deformation across the Sierra Nevada, northern Walker Lane, Basin and Range transition, western United States ,easure with GPS, 2000-2004, Journal of Geophysical Research, v. 112, no. B054211, doi: 10.1029/2006JB004625.

316 Henkart, P., 2003, SIOSEIS, software: Scripps Institution of Oceanography, La Jolla,
317 California.
318 House, P. K. and K. D. Adams, 2012, Preliminary geologic map of the northern part
319 of the lower Walker River area, Mineral County, Nevada, Nevada Bureau of
320 Mines and Geology 1:24,000 scale Open File Map 10-12.
321 House, P. K. and K. D. Adams, 2013, Preliminary geologic map of the southern part
322 of the lower Walker River area, Mineral County, Nevada, Nevada Bureau of
323 Mines and Geology 1:24,000 scale Open File Map 09-13.
324 Jones, C., and Wesnousky, S., 1992, Variations in strength and slip rate along the San
325 Andreas fault system: Science, v. 256, no. 5053, p. 83-86.
326 Lopes, T. J., and Smith, J. L., 2007, Bathymetry of Walker Lake, West-Central
327 Nevada: United States Geological Survey Scientific Investigations Report, v.
328 2007-5012, p. pp. 25.
329 Thatcher, W., Foulger, G.R., Julian, B.R., Svarc, J., Quilty, E., and Bawden, G.W.,
330 1999, Present-day deformation across the Basin and Range province,
331 western United States: Science, v. 283, p. 1714–1718.
332 Wesnousky, S. G., Bormann, J. M., Kreemer, C., Hammond, W. C., and Brune, J. N.,
333 2012, Neotectonics, geodesy, and seismic hazard in the Northern Walker Lane
334 of Western North America: Thirty kilometers of crustal shear and no strike-slip?:
335 Earth and Planetary Science Letters, v. 329, p. 133-140.
336 Wesnousky, S. G., and Jones, C. H., 1994, Oblique slip, slip partitioning, spatial and

temporal changes in the regional stress field, and the relative strength of active faults in the Basin and Range, western United States: Geology, v. 22, no. 11, p. 1031-1034.

FIGURE CAPTIONS

Figure 1. Tectonic map showing the location of the Wassuk Range within the Walker Lane (shaded). Range-bounding fault of the Wassuk Range shown as thick black line with hachures on hanging wall. The majority of ~50mm/yr of northwest directed Pacific plate motion is taken up by the San Andreas and Walker Lane fault systems.

Figure 2. Rangebounding fault along Wassuk Range shown as dark line. GPS measured displacement field (red arrows emanating from small white circle) plotted with respect to an assumed stable Sierra Nevada block. Orientation and increasing length of arrows to northeast shows shear is oriented obliquely to the Wassuk Range. Shown in white boxes are geologically determined values of fault-normal extension (black-upper text), geodetic estimates of fault-normal extension (magenta-middle text) and geodetic estimates of fault parallel strike-slip (blue-lower text) rates reported in Wesnousky et al (2012). Two-headed arrows schematically show ranges of same values and correspond in arrangement and color to the values in boxes. The geologically determined extension rate arrows are placed adjacent to the sites of studies. The dash white box shows extent of Figure 3a. Dashed blue line is historical

(~1880) highstand shoreline of Walker Lake as marked in Figure3a.

Figure 3. Portions of LiDAR imagery from Lopes and Smith (2007) along west flank of Wassuk Range. Extent of this image is shown by small box in Figure 2. a) White arrows point to location of fault trace outboard of the main rangefront. Walker Lake today sits about 11 km south of the label of the 1214 m contour. Area in box is enlarged in b). Fault trace (white arrows) extends southward below the 1880 highstand of Walker Lake as a lineament (black arrows) in the Lidar imagery. Though the LiDAR reports horizontal and vertical positional accuracies of ~1 m and 13-20 cm, respectively, field observation indicates the lineament is an artifact of LiDAR processing errors. Small white box in (b) shows extent of aerial photo image shown in Figure 4.

Figure 4. a) Fault trace cuts from northwest to southeast across the low-sun angle photograph from Nevada Bureau of Mines and Geology and shows right-lateral offset of tonal bands (shadows) that trend along the orientation of preserved recessional beach berms and bars of pluvial Lake Lahontan. Location is shown by small box in Figure 3b. b) Enlarged portion within dashed box of (a) shows different piercing lines defined by tonal contrasts (dash lines) used to estimate the fault offset. c) White dots are backpack GPS survey points along lines interpreted in the field to follow the crest and swales of the most evident recessional shoreline features. One northern survey

spot has been annotated as shown. The lineament between two red arrows shows the fault trace. Estimates of the offsets taken from these transects are annotated. d) LiDAR image of same area as (b) and (d) extracted from data set of Lopes and Smith (2007).

Figure 5. Topographic and bathymetric map of the Walker Lake region. Contour interval is 2 m. Legend highlights track lines from the CHIRP survey (black), core location (yellow), Wassuk Fault (red), offshore antithetic fault (red dashed), fold axes (blue) and tufa/bioherm deposits (orange).

Figure 6. Uninterpreted (top) and interpreted CHIRP seismic profile D01L02 across Walker Lake. Ages of horizons are estimated by interpolating C14–dated samples from Core WL84-8 (Benson, 1988; Benson et al., 1991) and WL84-4 (Bradbury et al., 1989). Faults are shown in black, sedimentary horizons in various colors. Key stratigraphic horizons are also annotated. Location of the CHIRP profile is shown in Figure 5. The vertical scale was converted from two-way travel time to meters using a nominal velocity of 1500 m/s. Horizontal scale bar is shown. Vertical exaggeration is 65X.

Figure 7. Uninterpreted (top) and interpreted CHIRP seismic profile D02L01 across Walker Lake. Location of the CHIRP data is shown in Figure 5. Faults are shown in

400 black, sedimentary horizons in various colors. See text for discussion. Horizontal
401 scale bar is shown. Vertical exaggeration is 65X.
402
403 Figure 8. Uninterpreted (top) and interpreted CHIRP seismic profile D02L01 across
404 Walker Lake. Location of the CHIRP data is shown in Figure 5. Faults are shown in
405 black, sedimentary horizons in various colors. Location of tufa/bioherms are
406 highlighted. See text for discussion. Horizontal scale bar is shown. Vertical
407 exaggeration is 65X.

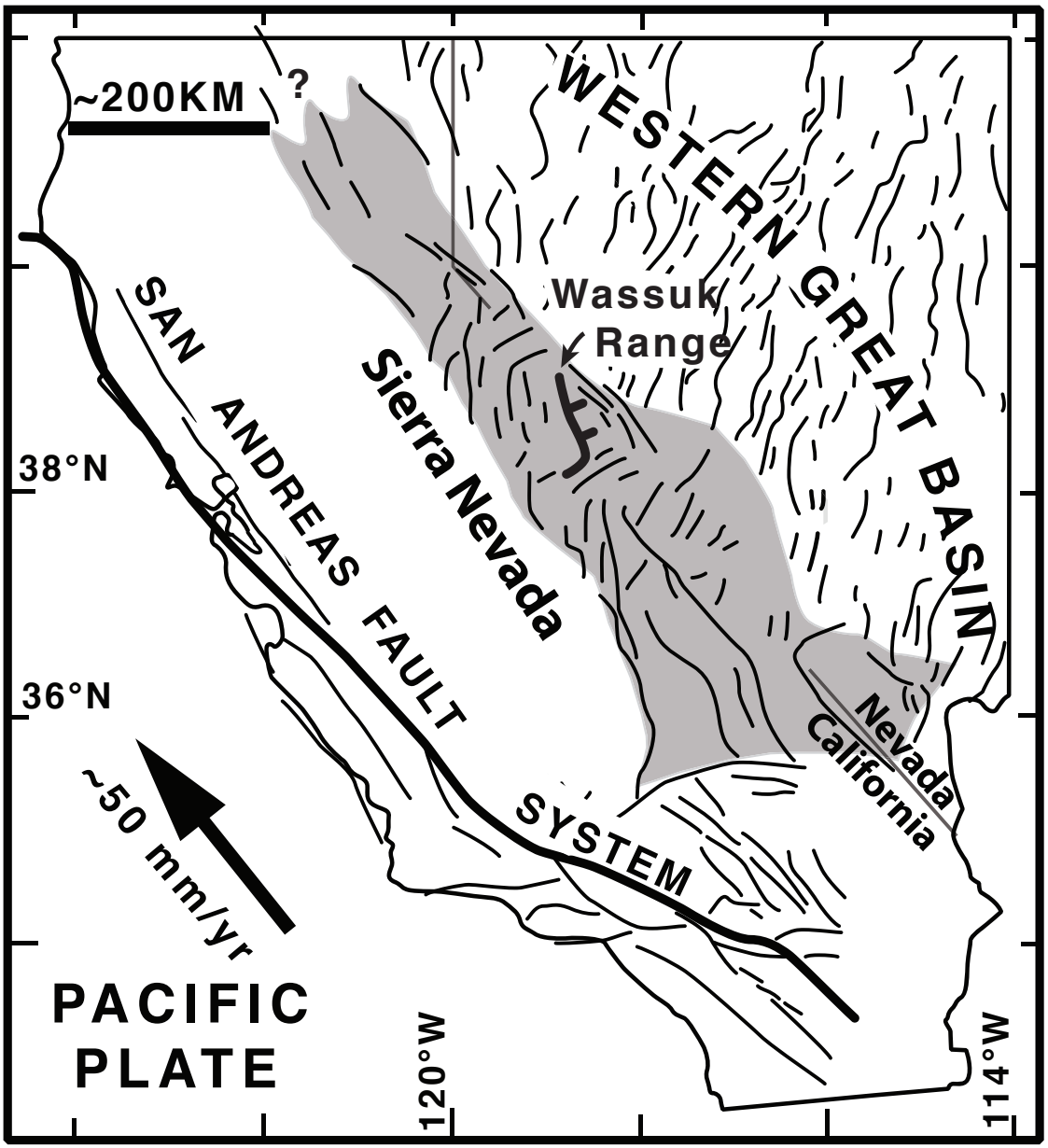
~200KM
?
WESTERN GREAT BASIN
Wassuk
Range
SAN ANDREAS FAULT
Sierra Nevada
38°N
36°N
Nevada
California
SYSTEM
~50 mm/yr
PACIFIC
PLATE
120°W
114°W

Figure 1

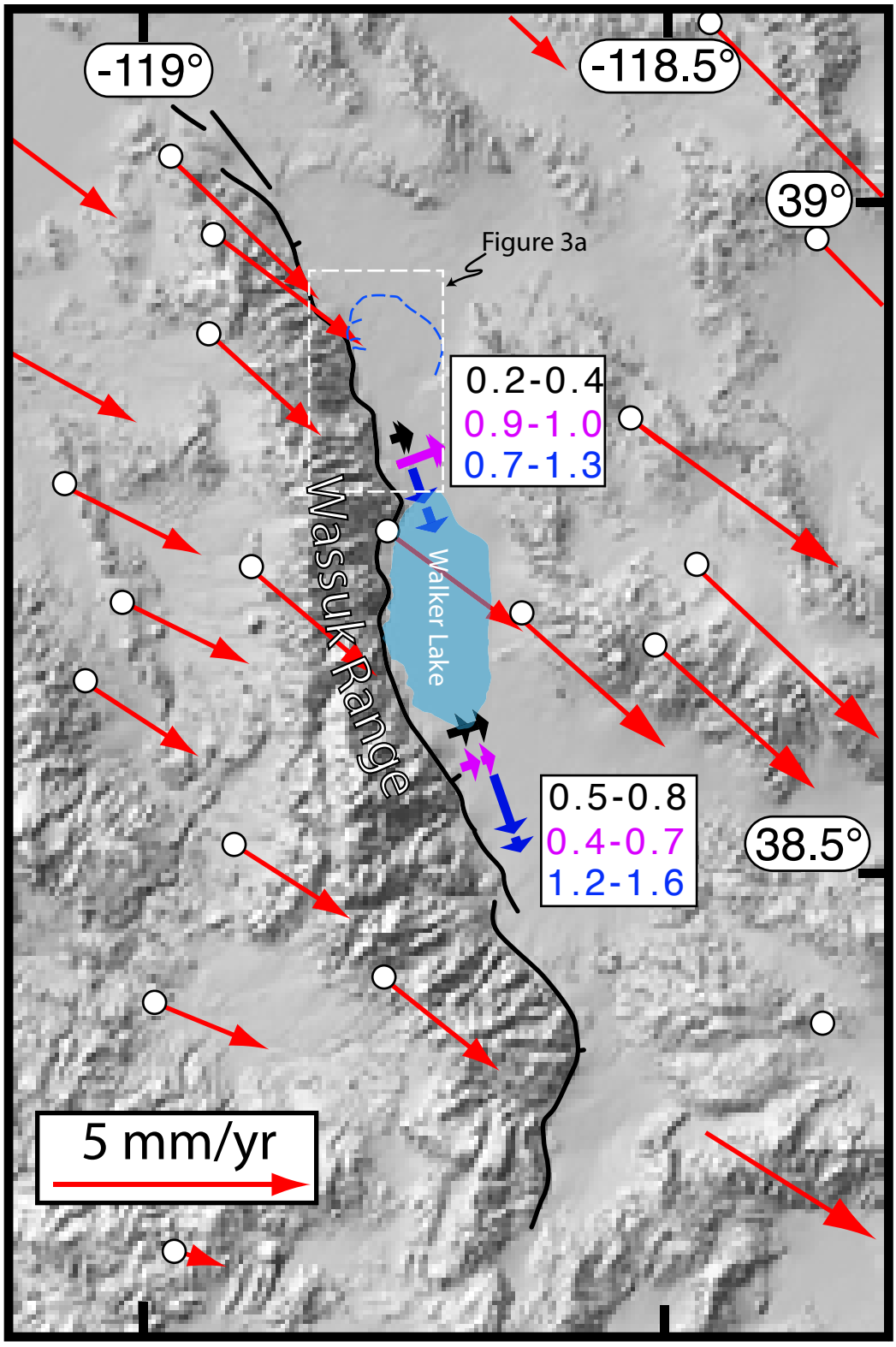
-119°
-118.5°
39°
38.5°
Figure 3a
0.2-0.4
0.9-1.0
0.7-1.3
0.5-0.8
0.4-0.7
1.2-1.6
Wassuk Range
Walker Lake
5 mm/yr

Figure 2

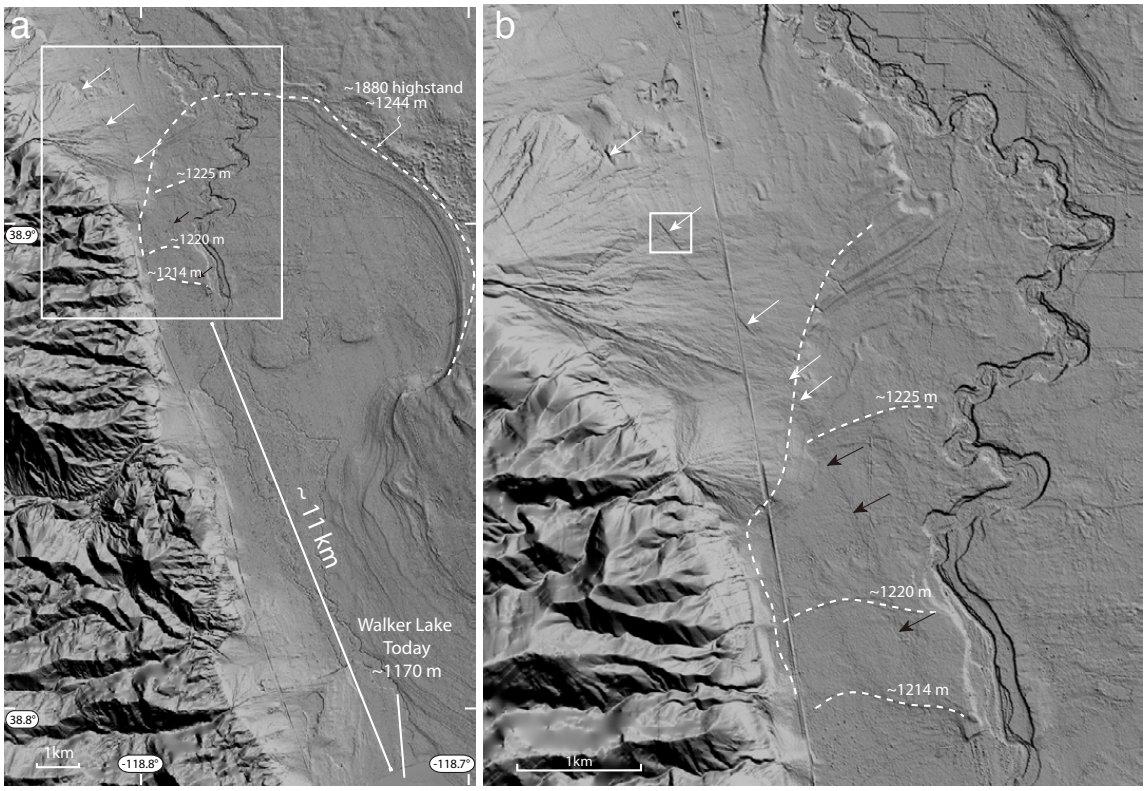
a
~1880 highstand
~1244 m
~1225 m
~1220 m
~1214 m
38.9°
~ 11 km
Walker Lake
Today
~1170 m
38.8°
1km
-118.8°
-118.7°
b
~1225 m
~1220 m
~1214 m
1km

Figure 3

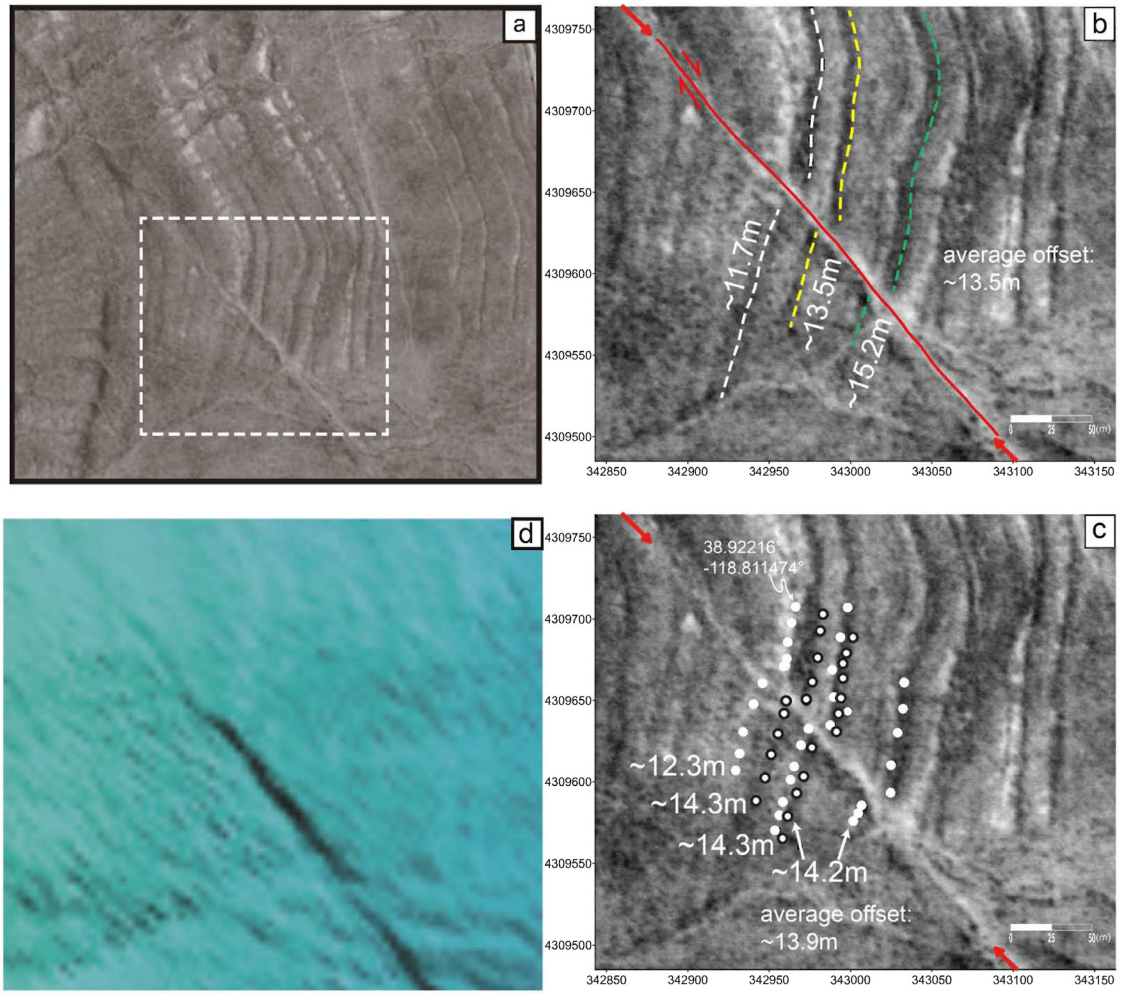
a
b
c
d
4309750
4309700
4309650
4309600
4309550
4309500
342850
342900
342950
343000
343050
343100
343150
~11.7m
~13.5m
~15.2m
average offset:
~13.5m
38.92216°
-118.811474°
~12.3m
~14.3m
~14.3m
~14.2m
average offset:
~13.9m

Figure 4

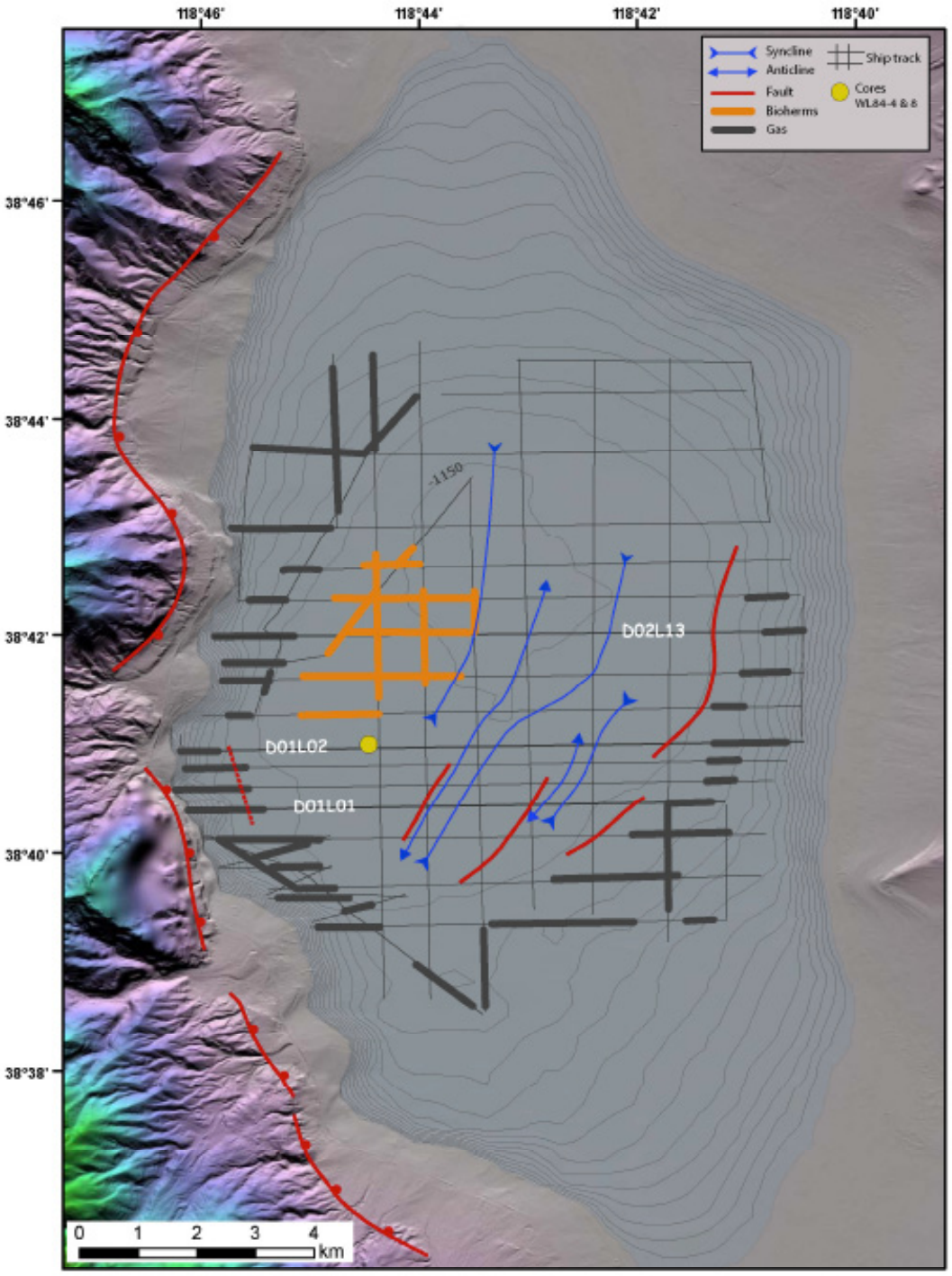
118°46'
118°44'
118°42'
118°40'
38°46'
38°44'
38°42'
38°40'
38°38'
Syncline
Anticline
Fault
Bioherms
Gas
Ship track
Cores
WL84-4 & 8
-1150
D02L13
D01L02
D01L01
0 1 2 3 4
km

Figure 5

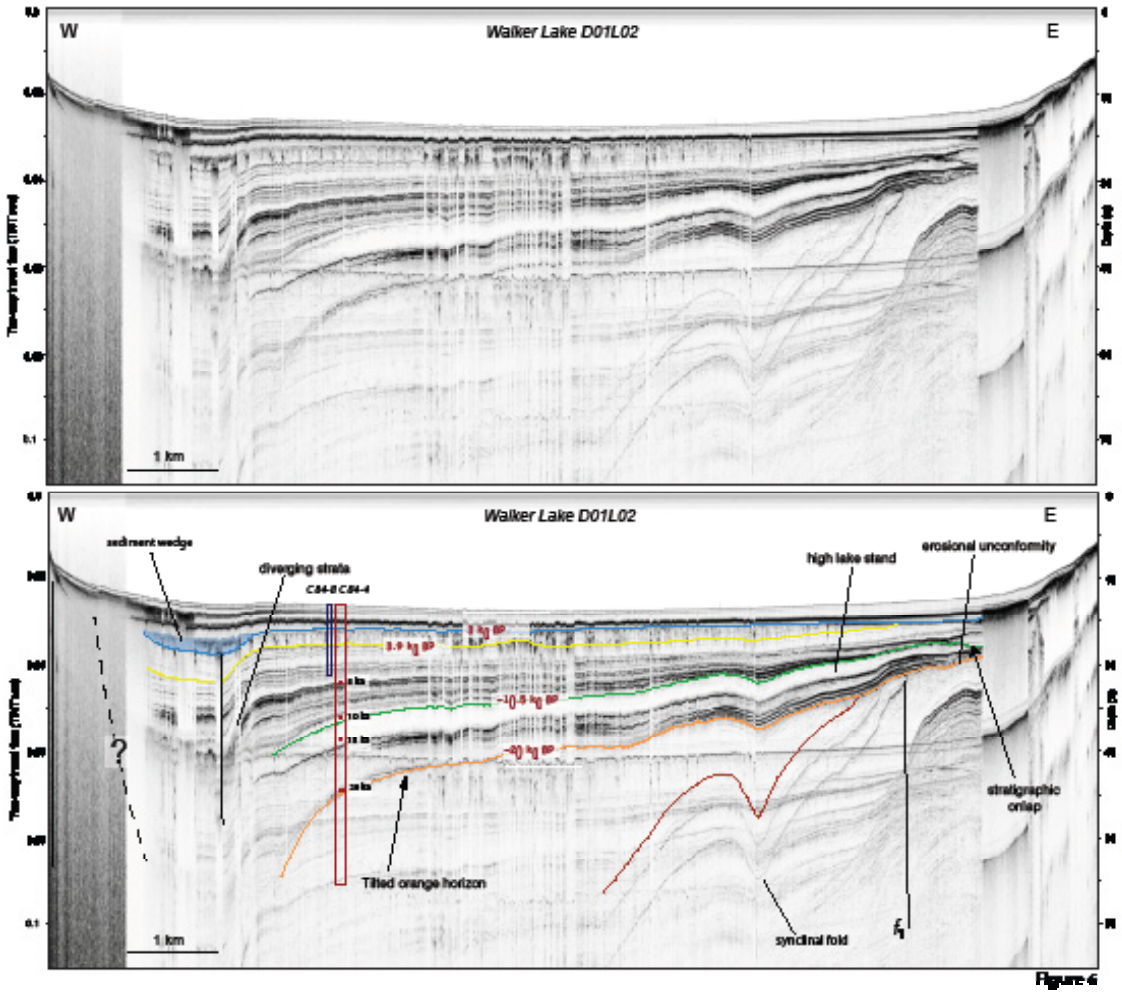
W
Walker Lake D01L02
E
1 km
W
Walker Lake D01L02
E
sediment wedge
diverging strata
high lake stand
erosional unconformity
stratigraphic onlap
Tilted orange horizon
synclinal fold
1 km

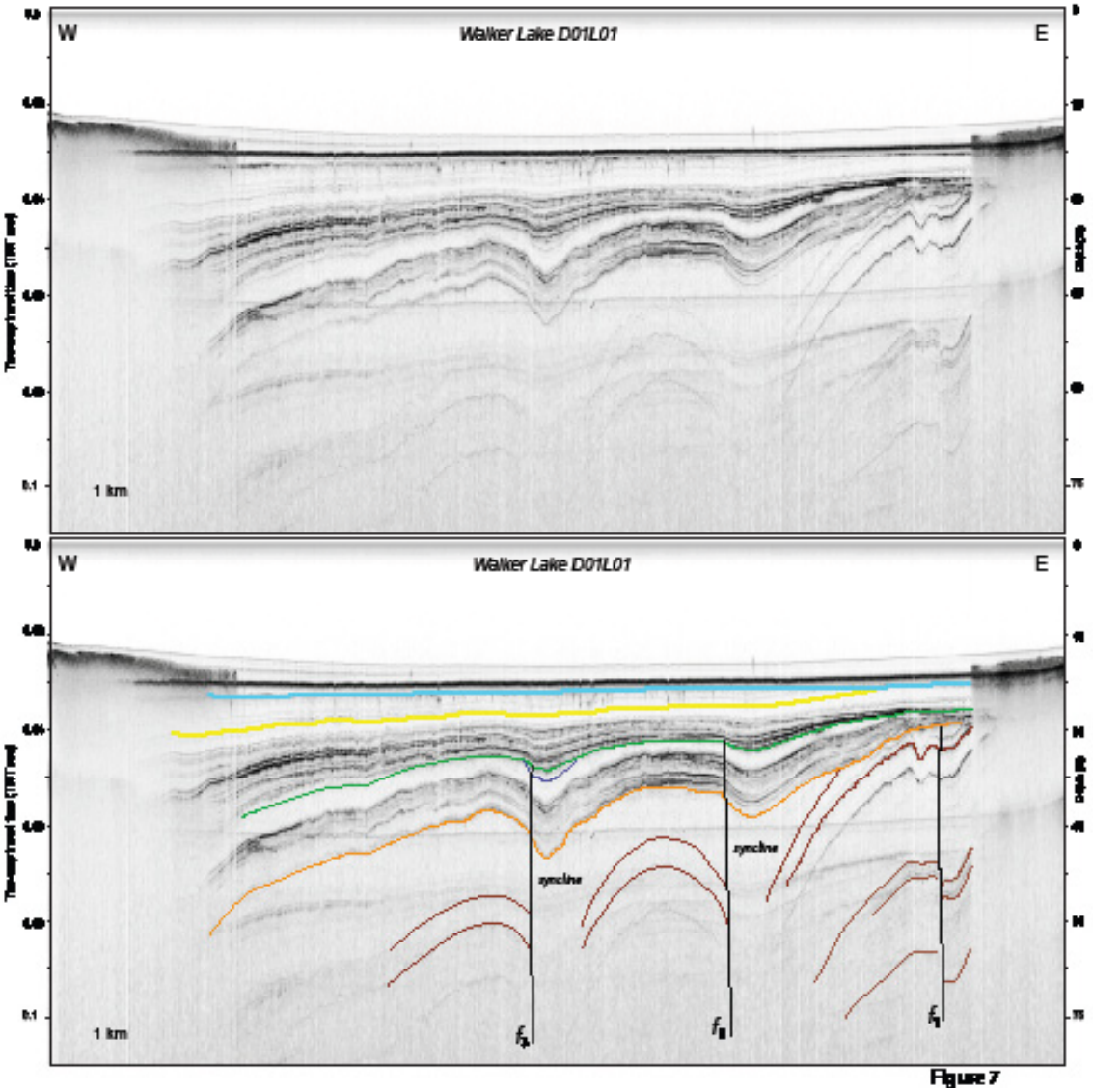
W
Walker Lake D01L01
E
1 km
W
Walker Lake D01L01
E
syncline
syncline
1 km

Figure 7

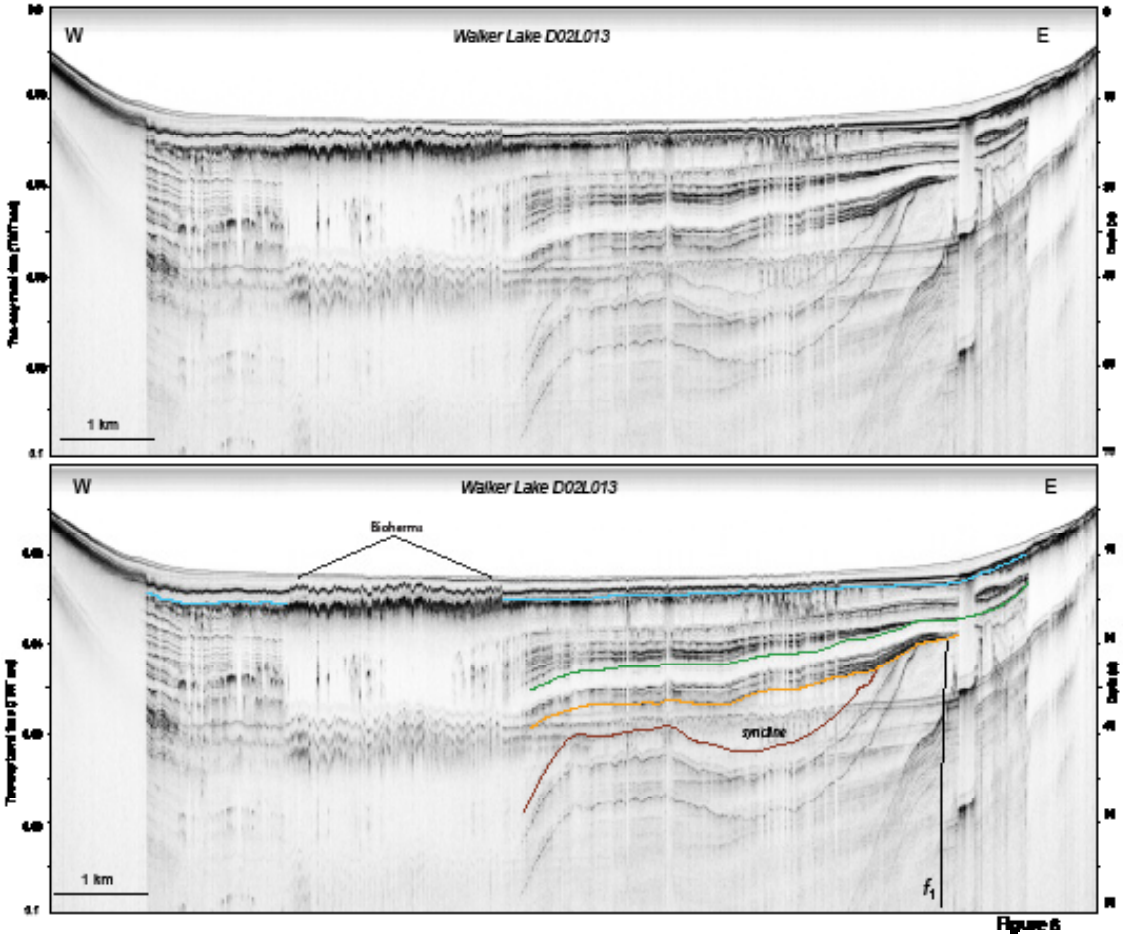

The text and figures from this appendixare being prepared for publication in: Dong, S., G. Ucarkus, S.G. Wesnousky, J. Maloney, N.W. Driscoll, G. Kent, and R. Baskin, In Review, Strike-slip Faulting along the Wassuk Range of the northern Walker Lane, Nevada: Geosphere. The dissertation author was involved in aquisition, processing and interpretation of the data that forms the basis of this chapter.

Appendix C

Sea level and substrate control on kelp forest habitats offshore southern California since the last glacial maximum

C.1 ABSTRACT

Sea level rise since the last glacial maximum (LGM, ~18 k.y.) has resulted in the dramatic transformation of coastal environments, including changes in coastal geomorphology, sediment dispersal, and substrate composition. These changes have undoubtedly impacted ecosystems occupying important near shore habitats (i.e., kelp forests, marshland, mangroves, and coral reefs), yet the impact of past sea level change on temperate marine ecosystems is not well understood. Little is known about how the availability and patterns of benthic habitat evolve with sea level change, or how rates of sea level change might also impact habitat distribution. While many other factors influence ecosystem health, including nutrient supply and temperature, determining the spatial availability of benthic habitat throughout a sea level cycle provides a baseline for understanding the distribution and patchiness of near shore ecosystems. Here, we attempt to quantify these changes in two ways. First, we use bathymetric data from the U.S. east and west coasts to compare how eustatic sea level cycles impact the size and shape of temperate coastal habitats associated with passive versus active margins. Second, we examine a high-resolution subbottom Chirp dataset offshore San Diego to interpret the tectonic and sedimentary evolution of a temperate coastal region and associated ecological transitions associated with the most recent glacial-interglacial cycle. At present with a highstand of sea level, the largest kelp forests in California exist offshore Point Loma and Mount Soledad due to the presence of uplifted Cretaceous hardgrounds. Since the LGM, sea level has risen approximately 120 m and kelp forest size and patchiness appears to have varied greatly through time as the slope and shelf morphology and geologic substrate (e.g., hardgrounds) were inundated.

C.2 INTRODUCTION

Over the past ~2.6 Ma global climate has fluctuated between glacial and

interglacial periods due to patterns in the characteristics of earth's orbit and climatic feedbacks (Milankovitch cycles) (Milankovitch, 1941). These cycles change ecological patterns as organisms migrate, adapt, or become extinct due to changes in climate and habitat. Several researchers have studied these ecological patterns in terrestrial habitats (e.g., Hewitt, 2000; Davis and Shaw, 2001), but less is known about marine ecosystems. Marine ecosystems are impacted by changes in temperature, nutrient supply, and ocean currents. Additionally important for these ecosystems, is that sea level varies ~120 m over a single sea-level cycle and the rates of sea-level rise and fall also vary throughout a cycle (e.g., Fairbanks, 1989; Lambeck and Chappell, 2001).

In the ocean, primary producers form the base of near shore ecosystems such as kelp forests, coral reefs, mangroves, and marshes. The two major physical controls on primary production are light and nutrients (Lalli & Parsons, 2006). Nutrient availability depends on several factors including terrestrial input and oceanic circulation patterns, whereas light availability depends on how deep photosynthetically active radiation can penetrate through the water column. The euphotic zone is where there is sufficient light to support plant growth (Lalli & Parsons, 2006). In clear ocean water, the maximum depth of photosynthetically active radiation is around 150 m; however, in turbid coastal waters the depth decreases markedly. Measurements of global irradiance indicate that some benthic algae can live at depths >200 m (Gattuso et al., 2006). Nevertheless, benthic coastal ecosystems with high diversity and productivity are generally limited to < 50 m water depth. For example, reef building corals, kelp forests, mangroves, and seagrass habitats are all restricted to this shallow, near shore zone (Lalli and Parsons, 2006), herein referred to as the coastal euphotic zone.

The coastal euphotic zone (0-50 m below sea level (mbsl)) migrates with changing sea level over glacial-interglacial cycles and because of the morphology of the shelf and slope, the size and shape of the coastal euphotic zone also changes with sea

level (Fig. 1). Sea level changes can have a large impact on ecosystems in the coastal euphotic zone. For example, it has been shown in coral reefs, that the ecosystem response to sea level will either "keep-up," "catch-up," or "give-up" (Davies and Montaggioni, 1985). The influence of sea level change on coral reefs has been documented in several locations (e.g., Blanchon and Shaw, 1995; Cabioch et al., 2008; Pandolfi, 1999). In addition to light requirements, the distribution of productive coastal habitats is controlled by substrate characteristics. For example, kelp forest habitats require hard substrate to exist, while eelgrass habitats require sediment. Seafloor substrate characteristics are subject to change with sea level due to antecedent geology and variations in patterns of erosion and deposition. Variability in baseline requirements of both light and substrate characteristics may have impacted temperate ecosystems as sea level has risen and fallen repeatedly across continental margins.

Much work has been done to understand eustatic controls on depositional processes using sequence stratigraphic models (e.g., Posamentier & Vail, 1988a; 1988b; Christie-Blick & Driscoll, 1995; Hill & Driscoll, 2008). As sea level rises and falls, accommodation is created and filled, and accordingly the margin undergoes periods of erosion and deposition. The physiography of the shelf and slope plays a role in the distribution and thickness of the sedimentary sequences, as well as in the amount of habitat available to benthic organisms within the coastal euphotic zone.

Others have approached studies of marine ecosystem evolution over glacial cycles using measurements of sea level change and bathymetry, and conceptual models of coastal substrate change (e.g., Graham et al., 2003). Here, for the first time, we incorporate Chirp (compressed high intensity radar pulse) subbottom seismic data to observe how actual substrate characteristics offshore San Diego may have varied throughout a sea level cycle, and how these changes may regulate kelp forest ecosystems.

Offshore La Jolla and Point Loma are two of the largest kelp forests in California

(Parnell et al., 2006; Fig. 2). Kelp is the general term used to describe several species of large brown algae in the orders Laminariales and Fucales. These algae form dense forests in shallow, subtidal, and temperate environments of the Pacific, Atlantic, and Southern Oceans, but are most diverse in the North Pacific (Estes and Steinberg, 1988). Some kelps can grow on sandy bottoms; however, most require hard substrata to survive to maturity (Dayton, 1985). Additionally, sedimentation and scour can cause significant damage to kelp gametophytes and young plants (Dayton, 1985). The kelp forests offshore San Diego grow on exposed submarine bedrock, reefs, and associated cobbles (Parnell et al., 2006) made up of the Cretaceous Rosario group (Kennedy and Tan, 2005).

How has habitat space for these kelp forests changed with sea level? What are the rates of change in available surface area? How have these changes impacted the organisms constrained to the coastal euphotic zone? Determining the substrate and spatial availability of habitat based on light penetration is a limiting factor in ecosystem health and may play a role in controlling ecosystem distribution, density, and patchiness.

C.3 GEOLOGIC BACKGROUND

The area offshore San Diego is part of the inner California borderland, which is a geomorphic region offshore southern California and northern Baja characterized by a system of basins and ridges and extensive strike-slip faulting. In the vicinity of San Diego, important geomorphic features include the La Jolla Canyon, Coronado Bank, Loma Sea Valley, Mount Soledad, Point Loma, and San Diego Bay (Fig. 2). Emery (1952) and Emery et al. (1952) extensively sampled and characterized the surficial geology of this region. Rock samples from Coronado Bank indicate primarily consolidated sedimentary rocks with little sediment cover (Emery, 1952b). The Coronado Bank fault zone extends through the Loma Sea Valley, which is filled with Miocene-modern sediments above the Catalina Schist basement. Cretaceous rocks and Holocene

sediments are mapped on the shelf between La Jolla Canyon and San Diego Bay (Kennedy and Tan, 2005). South from San Diego Bay, sediments are predominantly fine sand offshore the Silver Strand grading into medium-coarse sand offshore the Tijuana River (Emery, 1952a). Outcrops of the Cretaceous Rosario group are exposed exclusively in coastal San Diego along the coast of Point Loma, the coast of Point La Jolla, and on the shelf between La Jolla Canyon and San Diego Bay (Kennedy and Tan, 2005). The two major formations in these areas are the Campanian marine sandstone and shale Point Loma Formation, and the Maestrichtian conglomerate and sandstone Cabrillo Formation (Kennedy and Moore, 1971; Nilson and Abbott, 1979).

C.4 METHODS

Between 2006 and 2009, over 1000 km of Chirp seismic data were acquired from the U.S.-Mexico border north to La Jolla Canyon, and extending west to Coronado Bank (Fig. 2). All surveys employed SIO's Edgetech Chirp profiler. The Chirp profiler was operated with a 50 ms swept pulse of 0.7 – 3.0 kHz or 1-6 kHz depending on sediment character and water depth, and provided sub-meter vertical resolution and sub-bottom penetration up to ~50 m. Location accuracy is to within 10 m. Chirp data were processed using sioseis (sioseis.ucsd.edu) (Henkart, 2003) and imported to Kingdom Suite (ihs.com) and QPS Fledermaus software packages for interpretation. A nominal water velocity of 1500 m/s was assumed for all depth conversions.

We used bathymetry data from the National Geophysical Data Center's 3 arc-second U.S. Coastal Relief Model (NOAA, 2011), which was downloaded in netCDF grid format for use with the Generic Mapping Tools (GMT) (http://gmt.soest.hawaii.edu). Based on the eustatic sea-level curve of Fairbanks et al. (1998), and available bathymetry data, we calculated the surface area of the seafloor within the coastal euphotic zone (0 to 50 mbsl) at various sea level stands.

For the comparison of the U.S. east and west coasts, surface area calculations were preformed for selected whole grids (Table 1). Care was taken to ensure that grids used in each calculation encompassed topography ranging from above sea level to less than 170 m. Each grid was mapped to check that boundaries were entered correctly and that grids were free from obvious errors. Boundaries for all grids are listed in the Table 1. Using GMT, we isolated the bathymetry grid surface between 0 and -50 m, -60 and 110 m, and between -120 and -170 m, representing the modern coastal euphotic zone, the coastal euphotic zone when sea level was 60 m below present sea level, and the coastal euphotic zone during the LGM at 120 m below present sea level, respectively. We then completed a surface area calculation for each zone using GMT's grdvolume algorithm.

The accuracy of surface areas measured in this study is limited by the resolution and grid spacing of the bathymetry data (3 arc-second), differential uplift and subsidence rates, and error associated with the GMT algorithm for calculating surface area from a gridded surface. Additionally, modern surface area includes modern inlets, bays, and estuaries, which may be missed in paleobathymetry due to subsequent erosion or deposition.

In order to minimize errors associated with isostatic glacial uplift, we only analyzed areas between 45°N and 45°S. We did not account for water load adjustments; however, we estimate these to be small relative to the eustatic component of sea-level change. The west coast is tectonically active and localized uplift may influence sea level fluctuations. In southern California, however, regional uplift rates are ~0.13-0.14 mm/yr, which is minor compared to eustatic sea level variability (Kern and Rockwell, 1992; Ku and Kern, 1974; Muhs et al., 2002).

C.5 RESULTS

C.5.1 East vs. West coast

Surface area calculations indicate differences in coastal euphotic zone surface area variability between the U.S. east and west coasts associated with sea level change. Figure 3 illustrates changes in surface area of the coastal euphotic zone for the east and west coasts of the U.S. since ~18 k.y. BP compared to the eustatic sea level curve and rate of sea level change since the LGM. For the east coast we calculate a gentle increase in surface area from ~18 - 12 k.y. BP, followed by a slightly steeper increase from 12 - 9.5 k.y. BP, and then a sharp rise in surface area until ~6 k.y. BP. From 18 k.y. BP to present, the surface area of the coastal euphotic zone for this section of the U.S. east coast increased by ~114,000 square kilometers, which represents a percent change of ~2040%. On the west coast, coastal euphotic zone surface area increased between ~18 – 11.5 k.y. BP, with an increase in the rate of change approaching ~11.5 k.y. BP. A plateau in surface area is observed between ~11.5 – 10 k.y. BP, followed by a slight decline from ~10 – 8 k.y. BP, a slight increase from ~8 - 6 k.y. BP, and a relatively constant surface area from ~6 k.y. BP to present. From 18 k.y. BP to present, the surface area of the coastal euphotic zone for this section of the U.S. west coast increased by ~10,400 square kilometers, which represents a percent change of ~140%.

C.5.2 San Diego kelp forests

In the San Diego kelp forest study area, which is bounded by coordinates shown in Table 1, we followed the same procedures as the east vs. west coast surface area comparison and tracked the change in surface area of the coastal euphotic zone since the LGM (Fig. 4). The surface area increased gradually between ~18 – 12.5 k.y. BP. Between ~12.5 – 11.5 k.y. BP, a steeper increase in surface area is observed, followed by another period of more gradually increasing surface area. An intermediate peak in surface area

is centered ~9.5 k.y. BP, followed by a decrease in surface area from ~9.5 – 8 k.y. BP. Surface area again increases until ~6.5 k.y. BP, when a gradual decrease is observed, which continues until present.

After determining the continuous change in surface area for the region, we then selected three different sea level stands for detailed analysis of the coastal euphotic zone substrate during each given time period. The three sea level stands analyzed are present sea level (0 mbsl), sea level ~10 k.y. BP (60 mbsl), and sea level during the LGM (120 mbsl, ~18 k.y. BP). The surface area of the coastal euphotic zone from each sea level stand is listed in Table 2. At ~10 k.y. BP, the surface area was ~66.3% of modern and at the LGM the surface area was ~24.9% of modern. The geographic distribution of the coastal euphotic zone during modern, ~10 k.y. BP, and LGM sea level stands are illustrated in Figure 5.

In Chirp data, we examined the characteristics of the substrate within the coastal euphotic zone at each of the three sea level stands (Fig. 6). Figure 7 is a dip line across the margin from near the coast to Coronado Bank that illustrates the acoustic stratigraphy typical of the region. A description of the acoustic character, extent, and interpretation of the six acoustic units observed in Chirp data is provided in Table 3.

At modern sea level, there are three major kelp forest locations within the study region; offshore Point La Jolla, offshore Point Loma, and north of the Tijuana River mouth (Figs. 2 & 5A). We lack Chirp data from within these forests, but it is known that the kelp forests offshore Point La Jolla and Point Loma grow on rocky substrate associated with the Cretaceous Rosario group (Parnell et al., 2006; Kennedy and Tan, 2005). Multibeam data from around the Point Loma kelp forest also reveal expansive rocky outcrops of dipping beds (Fig. 8). The kelp forest north of the Tijuana River grows on low relief, unconsolidated, cobble deposits and is ephemeral, periodically covered by sediment (Parnell, personal communication). There is a much larger surface

area available within the 0-50 m zone that is not currently occupied by kelp forests. Examination of the Chirp data reveals that transparent, Holocene sediments of Unit 1 mantle much of the zone west of the Silver Strand (Fig. 9, Table 3). The Holocene sediment is deposited above the transgressive surface. Below the transgressive surface, Chirp data image several filled channels and dipping beds. South of Point Loma, the rocky hardgrounds beneath the modern kelp forest are exposed as an offshore high that extends and deepens to the south until it is overlain by sediments. This unit represents the Cretaceous Rosario group of Unit 6 (Table 3). West of the mouth of the Tijuana River, Chirp data image chaotic acoustic character at shallow penetration depths due to signal attenuation. The Holocene sand, Unit 6, is not imaged blanketing the transgressive surface in this area, nor are the deeper units with internal structure (Units 4-6).

At ~10 k.y. BP (60 mbsl), the coastal euphotic zone was predominately located on the shelf (Figs. 5 & 7). Beneath this zone across the shelf Chirp data image a strong acoustic reflector representing the transgressive surface (Fig. 7). Below the transgressive surface we observe Units 3 and 6, and above we observe Units 1 and 2 (Fig. 7, Table 3). The extent and thickness of Unit 1 is mapped in Figure 9.

During the LGM, the coastal euphotic zone was restricted to a narrow strip on the upper slope just below the shelf edge and to areas around the Coronado Bank (Figs. 5, 6 & 7). In Chirp data, the zone around the shelf corresponds to wedge deposits along the shelf edge (Unit 5). The Chirp data over Coronado Bank had limited penetration and, as such, the stratigraphy was not imaged very deeply. We do observe some steeply dipping reflectors just below the seafloor (Fig. 7). Some of the LGM coastal euphotic zone would occur around the upper reaches of the Loma Sea Valley where Chirp data image Unit 4 (Figs. 5 & 7).

C.6 DISCUSSION

C.6.1 East vs. West coast

Variation in the trends of surface area for the coastal euphotic zone between the U.S. east and west coasts are controlled by variations in margin physiography and characteristics of the eustatic sea level curve. On the U.S. east coast, the surface area of the coastal euphotic zone has increased since the LGM with a few rate variations. The first rate increase is closely correlated with the beginning of meltwater pulse 1A (Fig. 3). The rate increase is only slight, and after a first pulse lasting the duration of the meltwater pulse, appears to maintain a relatively constant rate until ~9.5 k.y. BP. After the meltwater pulse related rate increase, the subsequent increased rate appears associated with shelf-slope morphology. The rate increase occurs when sea level is ~90 m below present (Fig. 3). At this sea level, the coastal euphotic zone north of Cape Hatteras is just shallow of the shelf-slope break, while south of Cape Hatteras, portions of the coastal euphotic zone are still on the steeper slope. Due to this morphology, between 12 – 9.5 k.y. BP, the coastal euphotic zone widens north of Cape Hatteras, while it remains fairly constant south of Cape Hatteras, resulting in a slightly increased rate of surface area increase. The second increase in rate at ~9.5 k.y. BP occurs at a sea level of ~45 m below present and is likely due to a combination of an increased sea level rise associated with meltwater pulse 1B and shelf-slope morphology. At ~45 m sea level, the coastal euphotic zone is rising onto the shelf south of Cape Hatteras and as such is widening rapidly throughout the entire grid. This seems to explain the rapid rise in surface area that continues even after rates of sea level rise have decrease after meltwater pulse 1B. The rate of surface area change decreases ~6 k.y. BP and is likely due to both a decrease in rate of sea level rise at this time, as well as to the entire coastal euphotic zone being located on the gently sloping shelf.

The U.S. west coast has a much less dramatic rise in coastal euphotic zone surface

area since the LGM. The rate of surface area change is fairly constant since the LGM with the exception of a rapid rise corresponding to meltwater pulse 1A at ~11.5 k.y. BP. Following the meltwater pulse there is slight plateau and then decline in surface area from ~11.5 – 8 k.y. BP. This corresponds to sea levels of ~75 – 25 m below present sea level. At these depths, in several areas of the coast there is slight steepening of the shelf towards the shoreline. As sea level is rising, the trailing edge of the coastal euphotic zone was advancing faster than the leading edge, thereby narrowing the width of the zone. Additionally, during this time the surface area on offshore banks and islands diminishes. Following the decline in surface area, a slight increase in area is followed by a long plateau since ~6 k.y. BP, which is associated with the decline in rate of sea level rise.

Although different areas of the country experienced the same eustatic sea level rise since the LGM, the response of the coastal euphotic zone has varied due to shelf and slope morphology. Passive margins, like the U.S. east coast exhibit low LGM/Modern surface area ratios because they are generally characterized by wide gently dipping shelves and high gradient slopes. During sea level highstands when the coastal euphotic zone is primarily located on the shelf, the low shelf gradient extends the coastal euphotic zone far from the coast resulting in a large surface area. At the LGM (-120 mbsl), when the entire coastal euphotic zone is located on the steeper slope, the coastal euphotic zone is a very narrow strip with comparatively much smaller surface area. Additionally, the east coast remains relatively constant in slope from the coastal plains out to the shelf-slope break and at modern sea level several large bays and estuaries are located in coastal areas. This morphology results in a consistent increase in surface area, after the coastal euphotic zone is completely located above the shelf-slope break. In contrast, on the Pacific coast of the U.S., the shelf is narrower, resulting in a higher LGM/Modern surface area ratio in this region. The active rocky coastlines on the west coast also create more variability in the size of the coastal euphotic zone once sea level rises above the shelf-

slope break.

These observations have implications for ecosystem evolution of glacial-interglacial sea level cycles on the east vs. west coast. The gentle slope of the east coast would require organisms to travel farther distances for a given amount of sea level rise compared to the west coast. Variations in available habitat between the LGM and modern period are not as pronounced on the west coast as on the east coast. This could have implications for how, and if, species are able to adapt to sea level fluctuations on each coastline. Particularly on north-south oriented coastlines, as temperature gradients changed and available space decreased to a thin strip, migration of organisms following the changing temperature gradients would have been greatly impacted.

C.6.2 San Diego kelp forests

The characteristics of the surface area chart for the kelp forest study area are influenced by both characteristics of the sea level curve and margin physiography (Fig. 4). The steep increase in surface area ~12 k.y. BP corresponds to the rapid sea level rise associated with meltwater pulse 1A. The peak in surface area ~9.5 k.y. BP corresponds to meltwater pulse 1B. Rapid sea level rise appears responsible for the rapid surface area rise up to the peak. The decline after the peak appears to be associated with shelf morphology. This time period corresponds to sea level depths of -55 m at the beginning of meltwater pulse 1B to -35 m at the end of meltwater pulse 1B. The coastal euphotic zone is entirely on the shelf at this point. The surface area increases as sea level advances and widens the coastal euphotic zone, particularly in the wide, gently sloping shelf offshore the Silver Strand. The decrease in surface area is related to a steep step in the bathymetry data between ~45-30 m offshore. As the leading edge of the coastal euphotic zone reaches the steep step, surface area decreases while the trailing edge moves landward faster than the leading edge. The step is created by hardgrounds offshore Point

Loma and Point La Jolla. In higher resolution bathymetry data, the step is imaged but is not as dramatic as in the 3 arc-second bathymetry used here (Dartnell et al., 2007). Therefore, the peak is likely real, but may be slightly exaggerated in Figure 4. Following the brief decline, surface area again increases, mostly due to the widening of the euphotic zone offshore Silver Strand and into San Diego Bay and then plateaus with a slight decrease starting ~6 k.y. BP associated with the decline in rate of sea level rise at the same time period.

During the LGM, the surface area of the coastal euphotic zone was greatly reduced to a narrow strip along the shelf edge, with some larger areas on modern offshore banks and islands. Although the total surface area was much smaller, it appears from the Chirp data that the coastal euphotic zone during the LGM was dominated by rocky substrate (Figs. 6 & 7). Examination of the Chirp data indicates that offshore rocky banks and islands would have provided suitable habitat for kelp forests and in most areas along the shelf edge, the older wedge deposits (Unit 5) also may provide a hard substrate for kelp forest ecosystems.

At ~60 m below present sea level (~10 k.y. BP), the coastal euphotic zone was larger than during the LGM, but smaller than at present. Nevertheless, Chirp data reveal that the coastal euphotic zone at this time may have provided significantly greater rocky substrate than both during LGM and modern sea levels. The ~10 k.y. BP coastal euphotic zone is located across the mid-shelf. Chirp data image the stratigraphy of the mid-shelf region and reveal it is predominantly rocky hardgrounds below the transgressive surface (Units 3 & 6), with relatively thin transgressive lag and modern sand deposits above (Units 1 & 2). The sediment deposits above the transgressive were deposited subsequent to the sea level rise across the shelf. As such, these deposits would have been absent during the ~10 k.y. BP sea-level stand at 60 m, leaving the rocky hardgrounds as the surficial geology during that time. This rocky surficial geology would likely have

persisted throughout the entire steep rise in sea level, as any surficial sediment deposits would have been reworked by wave-base erosion of the rising seas.

During modern sea level, kelp forests are restricted to small areas of the available coastal euphotic zone where rocks are exposed at the seafloor. The substrate in the coastal euphotic zone during modern sea level appears to be made up of three main units - Cretaceous bedrock outcrops (Unit 6), transparent Holocene marine sediments (Unit 1), and chaotic deposits near the Tijuana River mouth. The Holocene sand deposits (Unit 6) mantle much of the transgressive surface, except where hardgrounds are exposed by tectonic processes. Mount Soledad and Point La Jolla are uplifted due to a restraining bend in the Rose Canyon fault zone and Point Loma is an exposed horst related to dip-slip faulting on the offshore Coronado Bank fault (Maloney et al., in prep). These are both locations of large, long-lived kelp forests. The kelp forest offshore the Tijuana River may be associated with coarse-grained deposits from the river, but also appears located adjacent to a jog in the coastline. This is a more ephemeral kelp forest because mobile marine sands may occasionally blanket the coarse substrate.

Visualizing the change in coastal euphotic zone surface area over the past 18 k.y. (Fig. 4), illustrates that the available surface area was at a minimum during the LGM and a maximum around 6 k.y. BP, with a small decline since 6 k.y. BP. Overall, between the LGM and 6 k.y. BP, the surface area increased, with variable rates and one short period of decline. In the southern California borderlands, it appears that the time of rising sea level (~11.5 – 6 k.y. BP) provided the most rocky habitat for kelp forests as compared to the LGM and the post-6 k.y. BP decrease in rate of sea level rise. During this time, the coastal euphotic zone was stepping landward across the shelf. Due to the gentler slope of the shelf, more area was available than during the LGM when the coastal euphotic zone was restricted to the steeper slope. On the shelf, Chirp data reveal predominantly rocky hardgrounds beneath the transgressive surface (Fig. 7) that would have been exposed

during sea level transgression as wave based erosion created rocky shorelines. Once sea-level rise slowed, marine sand deposits began to accumulate on the shelf, decreasing available habitat for kelp forests. This timeline is also in agreement with archeological evidence that shorelines went from rocky to sandy ~4500 yrs BP (Masters & Gallegos, 1997).

Although it appears that coastlines were mostly rocky from the LGM to ~6 k.y. BP, providing suitable habitat for kelp forests, these ecosystems still may have struggled during the LGM because of climate deterioration as well as its duration due to the small surface area available within the coastal euphotic zone. As temperature gradients changed and available space decreased to a thin strip leading into the LGM, migration and dispersal of organisms may have been greatly impacted.

As sea level rose inundating the shelf, the coastal euphotic zone expanded and was predominantly located across rocky substrates. Provided kelp forests could migrate fast enough to keep up with sea level rise, this may have been the most productive time for these ecosystems. As sea level rise stalled around 6 k.y. BP and marine sands began to mantle the rocky hardgrounds, the available area for kelp forests were again reduced in size and constrained to bathymetric highs with outcropping hard substrates. We propose that the most thriving kelp forests would have existed between ~11.5 – 6 k.y. in the area offshore San Diego.

C.7 CONCLUSIONS

The impacts of shelf-slope morphology on ecosystem evolution, as well as substrate characteristics for a specific ecosystem – kelp forests, have been examined with geophysical and geological approaches. Variability exists in response to sea level rise between the U.S. east and west coasts due to characteristic morphologies of passive versus active margins. The ecosystems thriving on each margin may have had to adapt

differently to “keep-up” with changing sea levels. Undoubtedly, future sea level rise will impact these two coastlines differently. In the San Diego area, despite surface area being reduced at lower sea levels, substrate characteristics indicate that more suitable habitat was available for kelp forest prior to deposition of Holocene sands, between ~11.5-6 k.y. BP. Modeling of currents and nutrient fluxes would add additional insight into ecosystem evolution since the LGM and combined with this baseline mapping of sea level and substrate, would provide a more robust reconstruction of biohabitats in the region. These types of studies are important for understanding how ecosystems have adapted to global change in the past, so that we might prepare better for future change.

C.8 REFERENCES

Blanchon, P., and Shaw, J., 1995, Reef Drowning during the last deglaciation – evidence for catastrophic sea-level rise and ice-sheet collapse: Geology, v. 23, no. 1, p. 4-8.

Cabioch, G., Montaggioni, L., Frank, N., Seard, C., Salle, E., Payri, C., Pelletier, B., and Paterne, M., 2008, Successive reef depositional events along the Marquesas foreslopes (French Polynesia) since 26 ka: Marine Geology, v. 254, no. 1-2, p. 18-34.

California Department of Fish and Game (CADFG), 2008, MarineBIOS, BIO_CA_Kelp2008, Layer ID 21.

Christie-Blick, N., and Driscoll, N. W., 1995, Sequence stratigraphy: Annual Review of Earth and Planetary Sciences, v. 23, p. 451-478.

Dartnell, P., Normark, W. R., Driscool, N. W., Babcock, J. M., Gardner, J. V., Kvitek, R. G., and Iampietro, P. J., 2007, Multibeam bathymetry and selected perspective views offshore San Diego, California: U.S. Geological Survey Scientific Investigations Map 2959, 2 sheets.

Davies, P.J., Montaggioni, L.F., 1985, Reef growth and sea-level change: the environmental signature: Proceedings of the Fifth International Coral Reef Congress, Tahiti, v. 3, p. 477–511.

Davis, M. B., and Shaw, R. G., 2001, Range shifts and adaptive responses to Quaternary climate change: Science, v. 292, no. 5517, p. 673-679.

Dayton, P. K., 1985, Ecology of kelp communities: Annual Review of Ecology and Systematics, v. 16, p. 215-245.

Emery, K.O., 1952, Continental shelf sediments of southern California: Geological Society of America Bulletin, v. 63, p. 1105-1108.

Emery, K.O., Butcher, W.S., Gould, H.R., and Shepard, F.P., 1952, Submarine geology off San Diego, California: The Journal of Geology, v. 60, p. 511-548.

Estes, J. A., and Steinberg, P. D., 1988, Predation, herbivory, and kelp evolution: Paleobiology, v. 14, no. 1, p. 19-36.

Fairbanks, R. G., 1989, A 17,000-year glacio-eustatic sea level record; influence of glacial melting rates on the Younger Dryas event and deep-ocean circulation: Nature, v. 342, no. 6250, p. 637-642.

Gattuso, J. P., Gentili, B., Duarte, C. M., Kleypas, J. A., Middelburg, J. J., and Antoine, D., 2006, Light availability in the coastal ocean: impact on the distribution of benthic photosynthetic organisms and their contribution to primary production: Biogeosciences, v. 3, no. 4, p. 489-513.

Graham, M. H., Dayton, P. K., and Erlandson, J. M., 2003, Ice ages and ecological transitions on temperate coasts: TRENDS in Ecology & Evolution, v. 18, no. 1, p. 33-40.

Henkart, P., 2003, SIOSEIS software. Scripps Institution of Oceanography, La Jolla, California. http://sioseis.ucsd.edu.

Hewitt, G., 2000, The genetic legacy of the Quaternary ice ages: Nature, v. 405, no. 6789, p. 907-913.

Hill, J. C., and Driscoll, N. W., 2008, Paleodrainage on the Chukchi shelf reveals sea level history and meltwater discharge: Marine Geology, v. 254, p. 3-4.

Kennedy, M. P., and Moore, G. W., 1971, Stratigraphic relations of upper Cretaceous and Eocene formations, San Diego coastal area, California: The American Association of Petroleum Geologists Bulletin, v. 55, no. 5, p. 709-722.

Kennedy, M. P., and Tan, S. S., 2005, Geologic Map of the San Diego 30' x 60' Quadrangle, California. Regional Geologic Map Series 1:100,000 scale, Map No. 3: California Geological Survey, California Department of Conservation.

Kern, J. P., and Rockwell, T. K., 1992, Chronology and deformation of Quaternary marine shorelines, San Diego County, California: Annual Field Trip Guidebook. South Coast Geological Society, v. 20, p. 1-7.

Kern, J. P., and Warme, J. E., 1974, Trace Fossils and Bathymetry of the Upper Cretaceous Point Loma Formation, San Diego, California: Geological Society of America Bulletin, v. 85, no. 6, p. 893-900.

Lalli, C. M., and Parsons, T. R., 2006, Biological Oceanography: An Introduction, Second Edition, Oxord, Elsevier Butterworth-Heinemann.

Lambeck, K., Chappell, J., Smith, J., and Uppenbrink, J., 2001, Sea level change through the last glacial cycle: Science, v. 292, no. 5517, p. 679-686.

Masters, P.M. and Gallegos, D.R., 1997, Environmental change and coastal adaptations in San Diego County during the Middle Holocene in eds. Erlandson, J.M., Glassow, M.A., The Archaeology of the California Coast during the Middle Holocene p. 11–21, UCLA Institute of Archaeology.

Milankovitch, M., 1941, Canon of insolation and the ice-age problem: translated from German: Israel Program for Scientific Translations, Jerusalem, 1969.

Muhs, D. R., Simmons, K. R., Kennedy, G. L., and Rockwell, T. K., 2002, The last interglacial period on the Pacific Coast of North America: Timing and paleoclimate: Geological Society of America Bulletin, v. 114, no. 5, p. 569-592.

Nilson, T. H., and Abbott, P. L., 1979, Turbidite sedimentology of the upper Creatceous Point Loma and Cabrillo Formations, San Diego, California, in Abbott, P. L., ed., Geologic excursions in the Southern California area: San Diego, CA, Department of Geological Sciences, San Diego State University, p. 139-166.

NOAA National Geophysical Data Center, U.S. Coastal Relief Model, Retrieved February 2011, http://www.ngdc.noaa.gov/mgg/coastal/crm.html.

Pandolfi, J. M., 1999, Response of Pleistocene coral reefs to environmental change over long temporal scales: American Zoologist, v. 39, no. 1, p. 113-130.

Parnell, P. E., Dayton, P. K., Lennert-Cody, C. E., Rasmussen, L. L., and Leichter, J. J., 2006, Marine reserve design: optimal size, habitats, species affinities, diversity, and ocean microclimate: Ecological Applications, v. 16, no. 3, p. 945-962.

Posamentier, H. W., Jervey, M. T., and Vail, P. R., 1988, Eustatic controls on clastic deposition; I, Conceptual framework: Special Publication - Society of Economic Paleontologists and Mineralogists, v. 42, p. 109-124.

Posamentier, H. W., and Vail, P. R., 1988, Eustatic controls on clastic deposition; II, Sequence and systems tract models: Special Publication - Society of Economic Paleontologists and Mineralogists, v. 42, p. 125-154.

Table C-1: List of grids used in surface area calculations with range coordinates and total calculated surface.

Study Area	Grid*	Range	Total Surface Area (km^2)
US East Coast	se_atl_crm_v2.nc	31°N - 40°N, 68°W - 85°W	864453
US West Coast[#]	southern_calif_crm_v6.nc	32°N - 37°N, 114°W - 124°W	419959
	central_pacific_crm_v7.nc	37°N - 44°N, 117°W - 127°W	472127
San Diego Kelp Forest	southern_calif_crm_v6.nc	32°30'N - 32°59'N, 117°W - 117°36'W	3016

Table C-2: Surface area of kelp forest study area at selected sea level stands.

Time Period	Depth Range (mbsl)*	Surface Area (km2)	Percent of Modern (%)
Modern	0-50	316.1	100.0
~10 k.y. BP	60-110	209.5	66.3
Last Glacial Maximum	120-170	78.6	24.9

*Relative to modern sea level

Table C-3: Extent and description of stratigraphic units observed in the Chirp data along with interpretation for each unit.

Table 3: Description of acoustic packages observed in Chirp data

Name	Extent	Acoustic Character	Interpretation
Unit 1	shelf adjacent to the San Diego coast; thickest at depocenter south of SD bay mouth (max. ~12 m); thickest at midshelf between Pt. La Jolla and Pt. Loma (Fig. 9)	transparent; basal contact is high amplitude continuous reflector that represents an unconformity above tilted and eroded rocks	Holocene marine sands
Unit 2	restricted to lows in the underlying topography; usually conicides with a shoreline angle	generally transparent, but contains some chaotic and wavy, discontinuous reflectors; basal contact is planar and represents unconformity with tilted strata below, top is truncated by high amplitude reflector; east of Point Loma, the basal unit is rough and channel-shaped	Transgressive lag and channel fill deposits
Unit 3	south of Point Loma from the midshelf to shelf edge	west dipping reflectors with variable thickness and acoustic character; truncated and planed flat at upper surface, basal contact below penetration depth	Pleistocene foresets
Unit 4	gently dipping slope between the steeper shelf edge and Loma Sea Valley	alternating transparent and reflective layers; subparallel layers onlap onto steep shelf slope; reflectors diverge away from the slope and converge towards the valley; variable thickness; often laterally discontinuous; appears to coalesce with unit 5 at more gentle slopes	Pliocene-Holocene marine deposits
Unit 5	shelf edge; missing from steepest slopes west of Mission Valley	wedge shaped; acoustly transparent with some sloping and chaotic reflectors; in northern profiles the toe of the unit appears to downlap unit 4, but in the south the unit appears to coalesce downslope into unit 4	Wedge and Slump deposits
Unit 6	shelf between La Jolla and Point Loma; extending as submerged peninsula south from Point Loma	uneven, rough upper contact; shallow signal penetration; south of Point Loma thinly spaced, east dipping reflectors; between La Jolla and Point Loma, faulted and folded reflectors	Cretaceous Rosario group

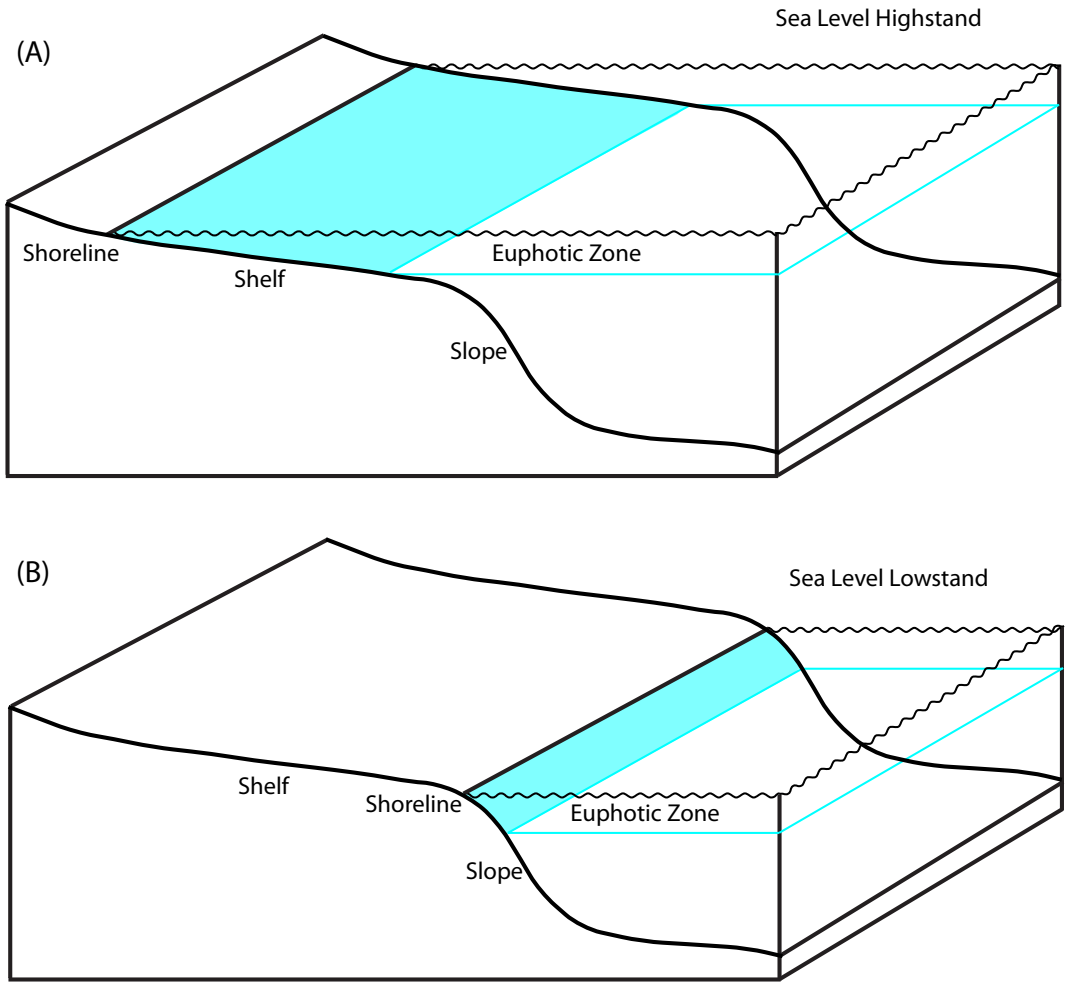

Figure C-1: Generalized shelf and slope morphology at end-member high-stand (A) and low-stand (B) of sea level. The blue line delineates the euphotic zone and blue shading highlights where it intersects benthic habitats (coastal euphotic zone). When sea level is above the shelf/slope break as in (A), the gently dipping shelf allows for a wide swath of habitat within the coastal euphotic zone. When sea level falls below the shelf/slope break, the higher gradient slope results in a much narrower swath of habitats within the coastal euphotic zone.

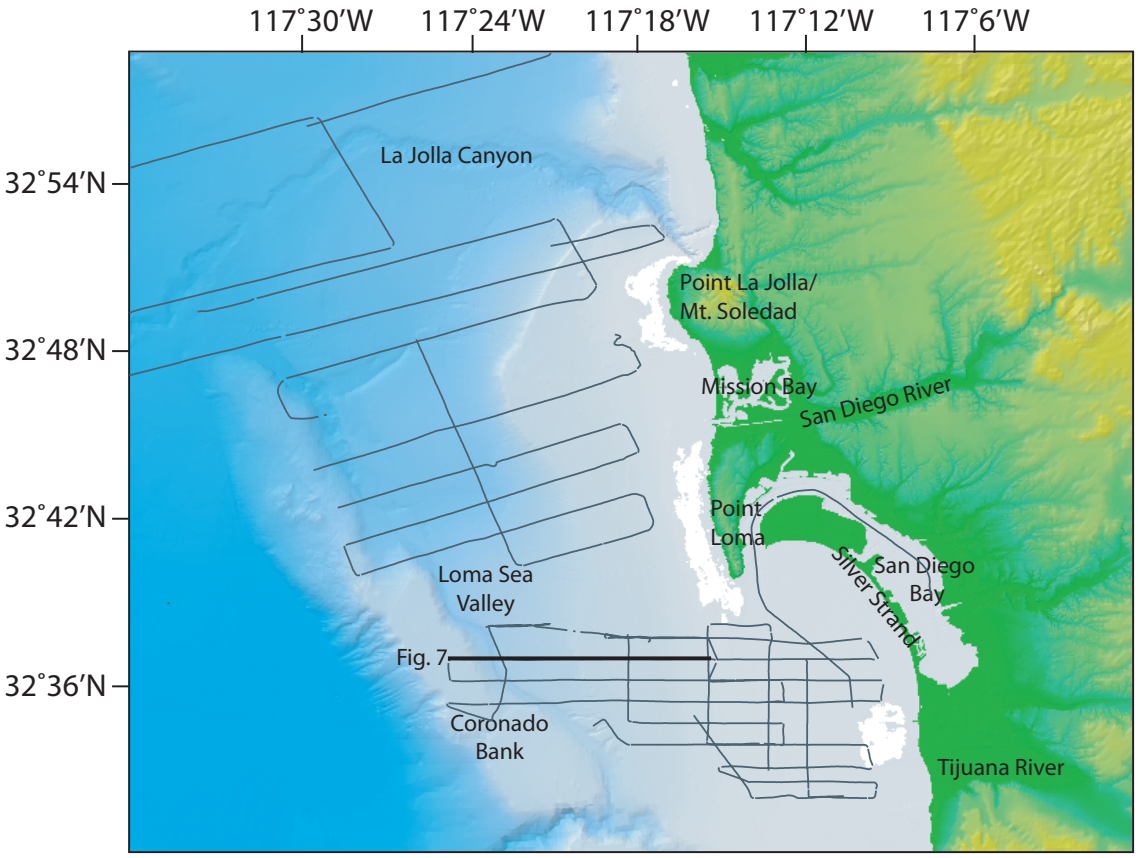

Figure C-2: Shaded relief map of kelp forest study region. Modern kelp canopy is mapped in white (CADFG, 2008) and Chirp lines are shown in dark gray. Thick black line shows location of Figure 7.

Figure C-3: Comparison of eustatic sea-level curve (A), rate of sea-level change (B), and surface area of the coastal euphotic zone on the east and west coasts of the U.S. (C). All ages are ^{14}C k.y. BP. Approximate constraints on meltwater pulses 1A and 1B are shaded in gray. (A) Eustatic sea-level curve reproduced from Fairbanks (1989). (B) Rate of sea-level change approximated using Fairbanks (1989) sea level curve by simple slope calculations over ~50 year intervals. (C) Coastal euphotic zone surface area measurements for designated areas of the U.S. east (blue) and west (red) coasts. Details discussed in text.

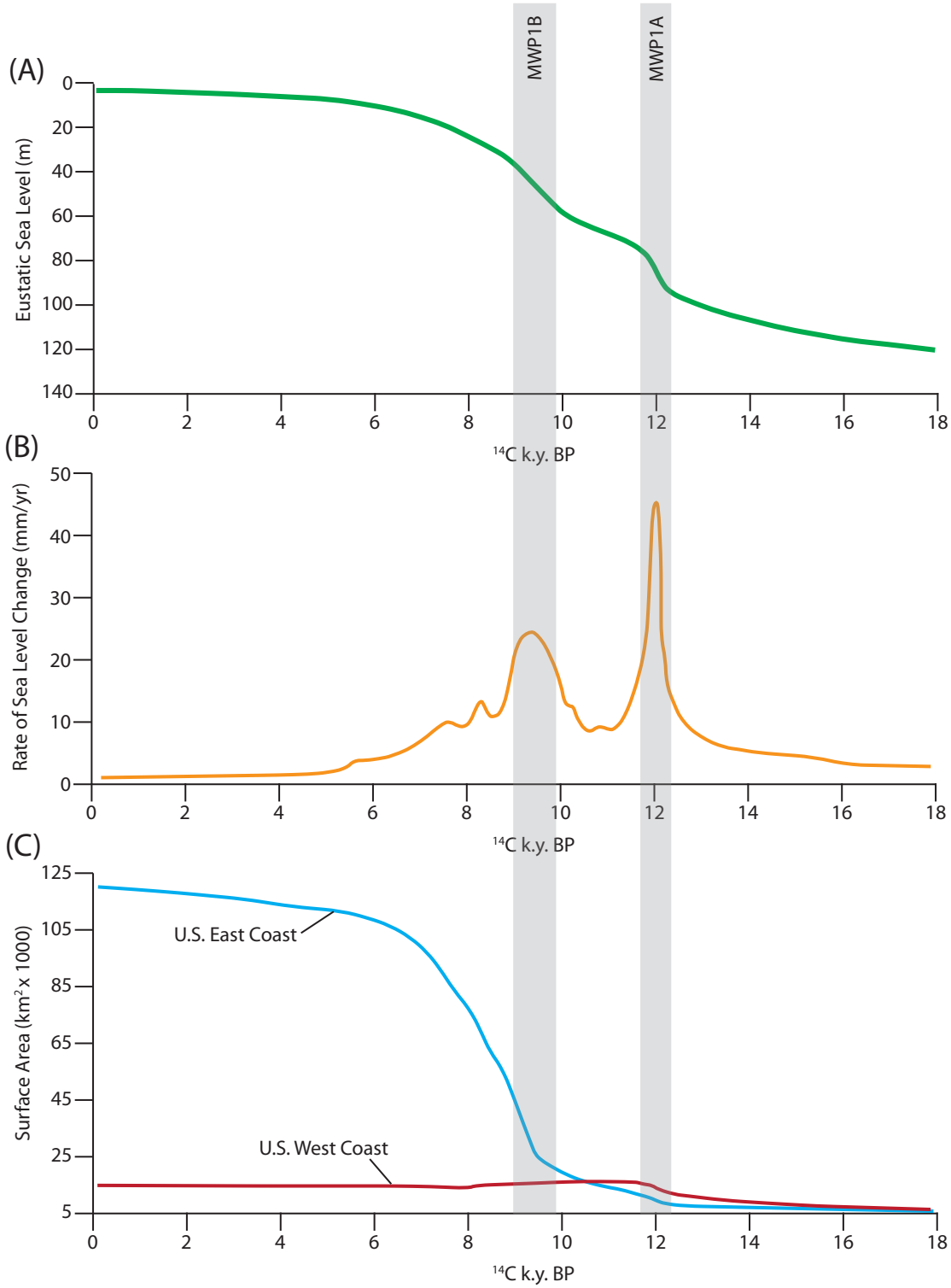
(A)
MWP1B
MWP1A
Eustatic Sea Level (m)
0
20
40
60
80
100
120
140
0
2
4
6
8
10
12
14
16
18
14C k.y. BP
(B)
Rate of Sea Level Change (mm/yr)
50
40
30
20
10
0
14C k.y. BP
(C)
Surface Area (km2 x 1000)
125
105
85
65
45
25
5
U.S. East Coast
U.S. West Coast
14C k.y. BP

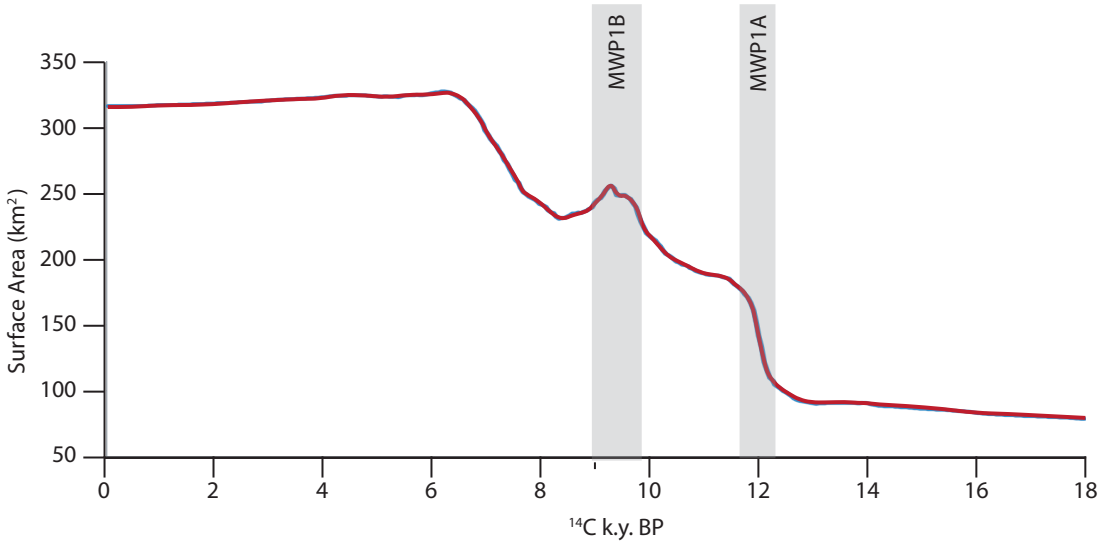

Figure C-4: Chart of coastal euphotic zone surface area vs. time (in ^{14}C k.y. BP) from 18 k.y. BP to present in the area defined for the San Diego kelp forest study area (see Table 1 for geographic bounds).

Figure C-5: (A) Map of modern coastline and bathymetry. Colored swath highlights the coastal euphotic zone at present sea level. The white overlay represents actual kelp canopy coverage data from 2008 (CADFG, 2008). (B) Map of coastline and bathymetry at ~10 k.y. BP. Colored swath highlights the coastal euphotic zone (60-110 m below present sea level). (C) Map of coastline and bathymetry of kelp study area at the LGM. Colored swath highlights the coastal euphotic zone (120 m (red) -170 m (blue) below present sea level).

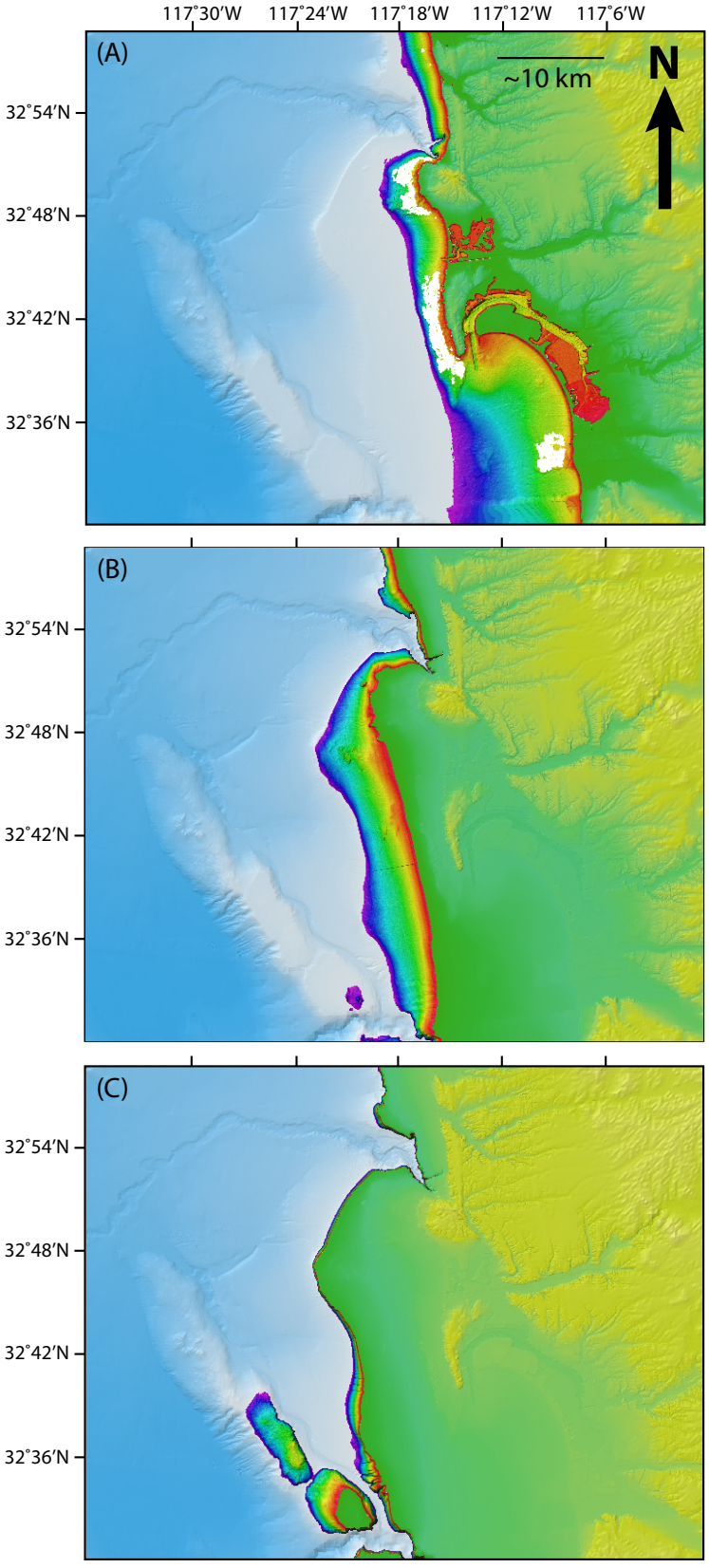
117°30′W
117°24′W
117°18′W
117°12′W
117°6′W
(A)
~10 km
N
32°54′N
32°48′N
32°42′N
32°36′N
(B)
32°54′N
32°48′N
32°42′N
32°36′N
(C)
32°54′N
32°48′N
32°42′N
32°36′N

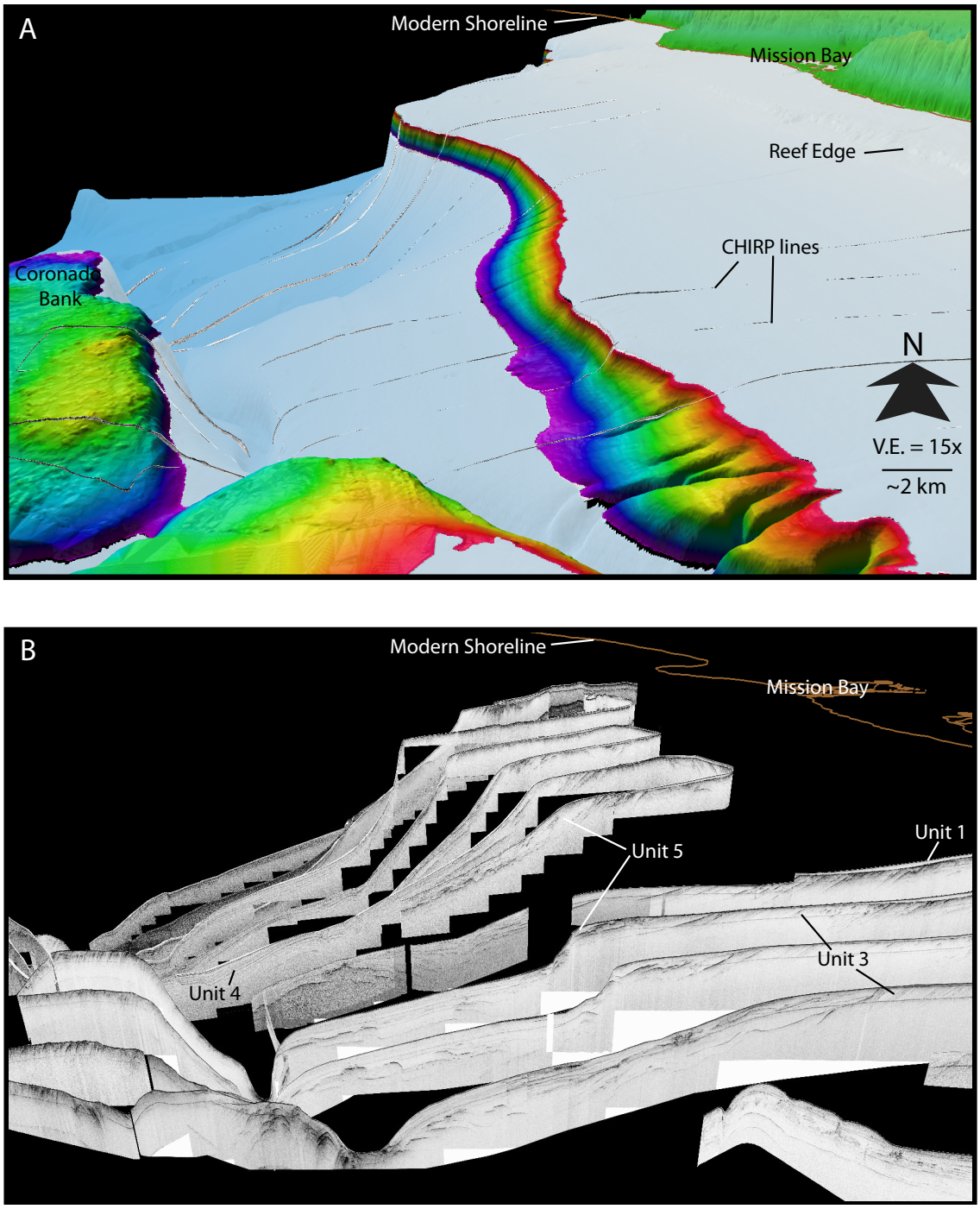

Figure C-6: (A) Coastline and bathymetry offshore San Diego during LGM at sea-level -120 m below present sea level. Gray lines are the tops of Chirp lines shown in (B). Colored swath highlights the coastal euphotic zone during the LGM. Modern Mission Bay is labeled and the modern shoreline is outlined in brown for reference. (B) Same as in (A), but bathymetry removed to reveal Chirp data below seafloor.

Figure C-7: Uninterpreted and interpreted Chirp dip line across the margin from near the coast to Coronado Bank that illustrates the acoustic stratigraphy typical of the region. A description of the acoustic character, extent, and interpretation of the six acoustic units observed in Chirp data is provided in Table 3. Units 1, 2, 5, and 6 are colored in the interpreted profile (see inset legend) and Units 3 and 4 are labeled. Two shaded areas highlight the extent of the coastal euphotic zone at different time periods. Light green represents the coastal euphotic zone ~10 k.y. BP when sea level was ~60 m below present. The light purple zone highlights the coastal euphotic zone during the LGM when sea level was ~120 m below present sea level. Faults are dashed in red. Location of Chirp profile is shown in Figure 2.

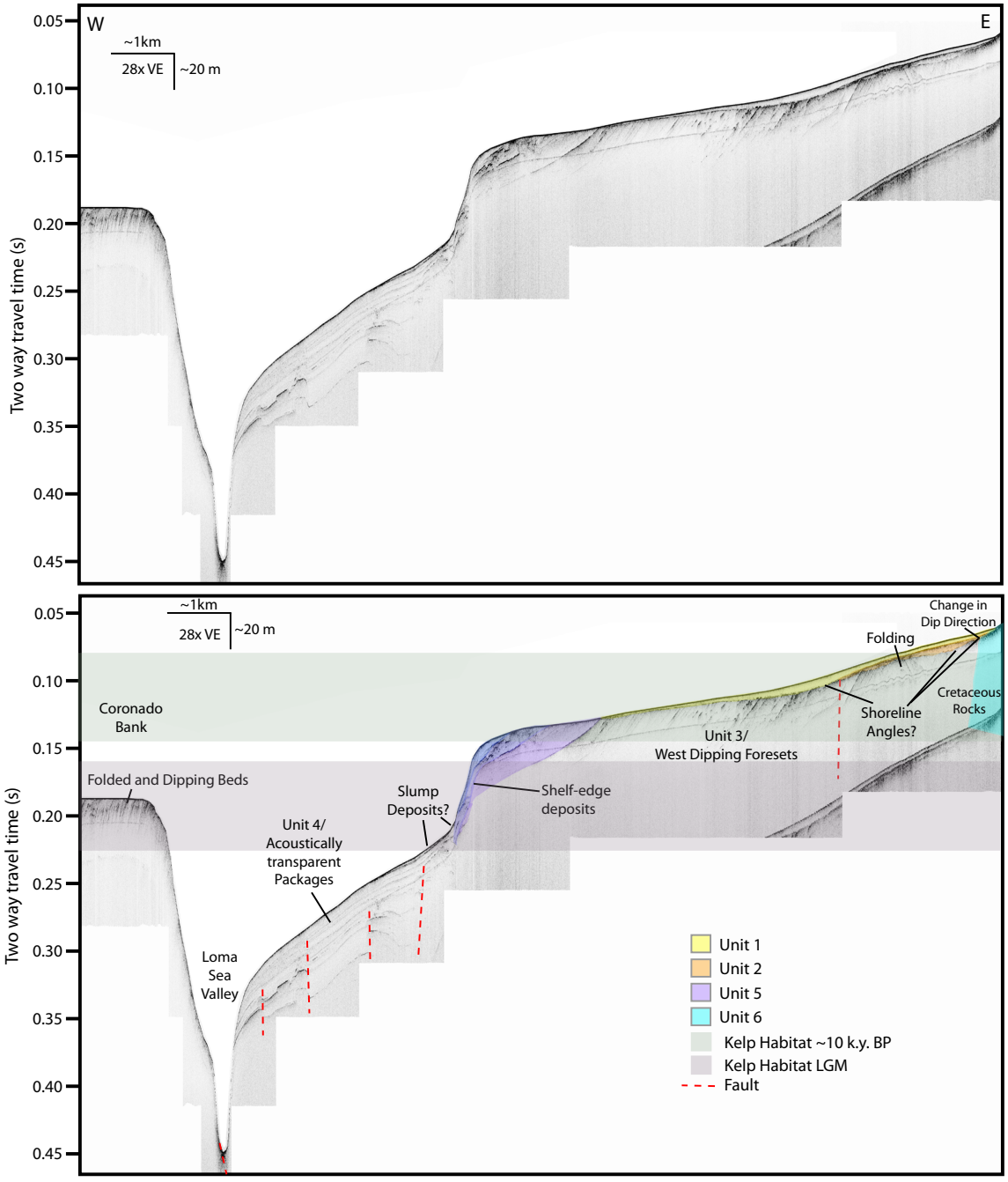
W
E
~1km
28x VE
~20 m
Two way travel time (s)
0.05
0.10
0.15
0.20
0.25
0.30
0.35
0.40
0.45
Coronado Bank
Folded and Dipping Beds
Unit 4/ Acoustically transparent Packages
Slump Deposits?
Shelf-edge deposits
Unit 3/ West Dipping Foresets
Folding
Change in Dip Direction
Shoreline Angles?
Cretaceous Rocks
Loma Sea Valley
Unit 1
Unit 2
Unit 5
Unit 6
Kelp Habitat ~10 k.y. BP
Kelp Habitat LGM
Fault

Figure C-8: Multibeam bathymetry offshore Point Loma collected in 2012 using a Reson 7125 system operated at 400kHz and with real-time kinematic navigation. Grid resolution is 0.5 m. Dipping beds represent the Cretaceous Rosario group, which makes up much of the substrate beneath the Point Loma kelp forest.

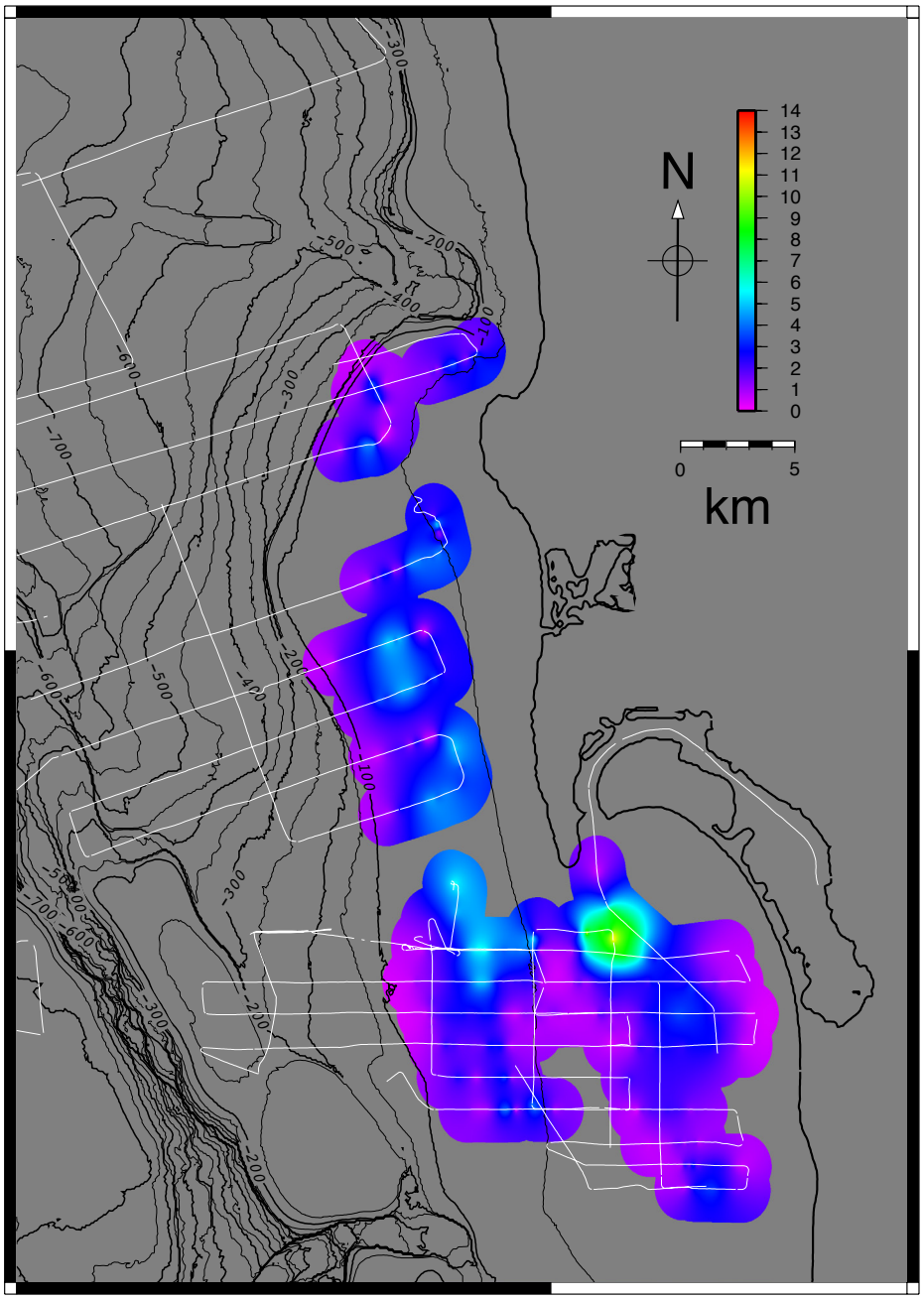

Figure C-9: Isopach map of the Holocene deposits (Unit 1) as mapped in Chirp data.